

Hybrid bioengineering of tubular constructs for esophagus by melt-drawing and 3D bioprinting

Tan, Yu Jun

2018

Tan, Y. J. (2018). Hybrid bioengineering of tubular constructs for esophagus by melt-drawing and 3D bioprinting. Doctoral thesis, Nanyang Technological University, Singapore.

<http://hdl.handle.net/10356/73186>

<https://doi.org/10.32657/10356/73186>



**NANYANG
TECHNOLOGICAL
UNIVERSITY**

**HYBRID BIOENGINEERING OF TUBULAR
CONSTRUCTS FOR ESOPHAGUS BY MELT-
DRAWING AND 3D BIOPRINTING**

TAN YU JUN

**SCHOOL OF MECHANICAL AND
AEROSPACE ENGINEERING**

2017

**HYBRID BIOENGINEERING OF TUBULAR
CONSTRUCTS FOR ESOPHAGUS BY MELT-
DRAWING AND 3D BIOPRINTING**

TAN YU JUN

School of Mechanical and Aerospace Engineering

A thesis submitted to Nanyang Technological University in
partial fulfilment of the requirement for the degree of
Doctor of Philosophy

2017

Acknowledgements

The author has put in great effort for this dissertation. However, it would not have been possible without the kind support and help of many individuals and organizations. The author would like to extend her sincerest thanks to all of them.

Firstly, the author would like to express her endless thanks and gratitude to her supervisors Assoc. Prof. Leong Kah Fai and Assist. Prof. Yeong Wai Yee, who have been extremely patient and provided valuable support to the author. Their support and guidance greatly contribute to the success of the dissertation.

The author highly appreciates the Research Fellows at the Singapore Centre for 3D Printing (SC3DP), Dr. Tan Xipeng and Dr. An Jia who have continually motivated and guided the author throughout the dissertation work. Their encouragement and guidance have enhanced the author's skills and experiences in research.

The author would also like to express heartfelt gratitude towards Assoc. Prof. Chian Kerm Sin who has enthusiastically shared his vast experiences and expert knowledge with the author. His invaluable guidance enriched the author's research experiences.

The author is particularly grateful to Miss Heng Chee Hoon who has provided the logistics support throughout the experiments. The author would also like to thank Miss Koh Joo Luang, Ms Sandy Seah, Mr Leong Kwok Phui, Ms Yong Mei Yoke for their kind assistance in the machines operation in the laboratories.

The author appreciates her fellow lab mates, Ratima Suntornnond, Edgar Tan Yong Sheng, Sitthisang Sonthikan, Ng Wei Long, and Lee Jia Min who have

continuously shared their experiences with the author. The author thanks all her final year project (FYP) students who have worked hard to led to the development of a new melt-drawing machine and the provoked discoveries of new knowledge.

The author is grateful for the use of resources in SC3DP funded by National Research Foundation (NRF), Singapore. The author wants to express her gratitude to Assoc. Prof. Yoh-ichi Tagawa and his students from Graduate School of Bioscience and Biotechnology, Tokyo Institute of Technology who have provided training and resources during her three-month research exchange in his laboratory, particularly to learn cell culture techniques.

Last but not least, the author would also like to take this opportunity to express her deepest gratitude to her parents and siblings for their endless support and love.

Publications

Journal papers:

- (1) **Tan Y.J.**, Tan X.P., Yeong W.Y., Tor S.B., Hybrid microscaffold-based 3D bioprinting of multi-cellular constructs with high compressive strength: A new biofabrication strategy. *Sci. Rep.* **2016**, 6:39140.
- (2) **Tan Y.J.**, Tan X.P., Yeong W.Y., Tor S.B., Additive manufacturing of patient-customizable scaffolds for tubular tissues using the melt-drawing method. *Materials* **2016**, 9, 893.
- (3) **Tan Y.J.**, Yeong W.Y., Tan X.P., An J., Chian K.S., Leong K.F., Characterization, mechanical behavior and *in vitro* evaluation of a melt-drawn scaffold for esophageal tissue engineering. *J. Mech. Behav. Biomed. Mater.* **2016**, 57, 246–59.
- (4) **Tan Y.J.**, Leong K.F., An J., Chian K.S., Tan X.P., Yeong W.Y., Fabrication and *in vitro* analysis of tubular scaffolds by melt-drawing for esophageal tissue engineering. *Mater. Lett.* **2015**, 159, 424-427.
- (5) Behr J-M, **Tan Y.J.**, An J., Irvine S.A., Leong K.F., Chua C.K., Zussman E., Venkatraman S., Non-linear elasticity and compliance matching of PLCL dip-coated tubes with melt-drawn fibers. *Acta Biomater.* Ready for submission.
- (6) **Tan Y.J.**, Tan X.P., Yeong W.Y., Tor S.B., Characterization of microscaffold-based 3D bioprinted constructs. Under preparation.

Conference papers:

- (1) **Tan Y.J.**, Chian K.S., Leong K.F., Fabricating patient-customizable tubular scaffolds from biodegradable polymer, 2nd International Conference on Progress in Additive Manufacturing, 2016. **Best Paper Award.**
- (2) **Tan Y.J.**, An J., Foo Y.S., Yeong W.Y., Leong K.F., Solvent-free melt-drawing of aligned poly (L-lactide-co-caprolactone) microfibers into tubular scaffold for esophageal tissue engineering, 1st International Conference on Progress in Additive Manufacturing, 2014.

Table of contents

Acknowledgements	i
Publications	iii
Table of contents	v
List of nomenclature, abbreviations, and symbols	x
List of tables	xiv
List of figures	xv
Abstract	xxi
Chapter 1. Introduction.....	1
1.1 Background	1
1.2 Tissue engineering: Requirements and key challenges.....	2
1.3 Objectives	5
1.4 Scope	5
1.5 Dissertation organization	6
Chapter 2. Literature review	9
2.1 Esophagus.....	9
2.1.1 Musculature and mucosa	10
2.1.2 Variations among human esophagus.....	12
2.2 Tissue engineering of tubular organs.....	18
2.2.1 Requirements: Microenvironment and cell behavior	18
2.2.2 Strategies: Additive, subtractive, and formative fabrication	22
2.3 Tissue engineering of musculature: Biomimetic fibers for cell alignment	31

2.3.1	Fibrous scaffolds for cell alignment	33
2.3.2	Fibrous scaffold fabrication techniques	36
2.4	Tissue engineering of mucosa: Biomimetic scaffolds for epithelium stratification.....	38
2.4.1	Esophageal mucosa tissue engineering	38
2.4.2	3D bioprinting methods	41
2.4.3	Cell sources for 3D bioprinting.....	45
2.5	Summary	47
 Chapter 3. Bioengineering of esophageal musculature: Fabrication of elastic, aligned microfibrous scaffold		
		49
3.1	Introduction: Techniques and biomaterials evaluation	49
3.2	Materials and methods	51
3.2.1	Materials and sample preparations	51
3.2.2	Thermal and rheological analysis	52
3.2.3	Melt-drawing process	53
3.2.4	Gel permeation chromatography.....	55
3.2.5	Scanning electron microscopy	56
3.2.6	Scaffold density	56
3.2.7	Cell culture and cell seeding.....	56
3.2.8	Statistical analysis.....	61
3.3	Results	62
3.3.1	Tubular microfibrous scaffold formation	62
3.3.2	Thermal and rheological properties.....	63
3.3.3	Melt-drawn tubular microfibrous scaffolds	64
3.3.4	Biocompatibility and cell alignment.....	67
3.4	Discussion	73

3.5	Summary	78
 Chapter 4. Bioengineering of esophageal musculature:		
	Customization of tubular scaffolds.....	80
4.1	Introduction: Mechanical properties and dimensions.....	80
4.2	Materials and methods	80
4.2.1	Crystallinity analysis	80
4.2.2	Tensile testing for PLC rings	82
4.2.3	Planar tensile testing.....	84
4.2.4	Scaffold fabrication with varying dimensions	86
4.2.5	Statistical Analysis	86
4.3	Results	86
4.3.1	Crystalline structure and crystallinity.....	86
4.3.2	Tensile properties of PLC rings.....	89
4.3.3	Scaffolds' planar tensile properties.....	92
4.3.4	Customization of scaffold dimensions	94
4.4	Discussion	95
4.5	Summary	105
 Chapter 5. Bioengineering of esophageal mucosa: A new bioink for		
	3D bioprinting.....	108
5.1	Introduction: A new bioink.....	108
5.2	Materials and methods	112
5.2.1	Materials	112
5.2.2	Porous microsphere fabrication.....	113
5.2.3	Hydrogel preparation	114
5.2.4	Characterization techniques	114

5.2.5	Biocompatibility testing	115
5.3	Results and discussion.....	116
5.3.1	Porous microspheres.....	116
5.3.2	Thermoresponsive AC blend hydrogel	124
5.3.3	Cell attachment and viability.....	127
5.4	Summary	130
 Chapter 6. Bioengineering of esophageal mucosa: A 3D bioprinting		
	strategy	131
6.1	Introduction: A novel 3D bioprinting method	131
6.2	Materials and methods	133
6.2.1	Bioprinting process.....	133
6.2.2	Mechanical evaluation	134
6.2.3	Cell culture	135
6.3	Results	139
6.3.1	Bioprinted constructs.....	139
6.3.2	Mechanical properties	140
6.3.3	Cell viability and proliferation	141
6.4	Discussion	149
6.5	Summary	154
 Chapter 7. Overall summary, conclusions and future work		
7.1	Summary	156
7.2	Conclusions.....	159
7.3	Future work	160
References.....		166
Appendices		I

Appendix A: Biomechanical properties of human esophagus	I
Appendix B: Rheological results for PLC at various temperatures.....	II
Appendix C: GPC report for pristine and melt-drawn PLC.....	III
Appendix D: L929 cell alignment on PLC scaffolds	V
Appendix E: Calculations of the initial cell numbers needed before bioprinting of a 1 mm ³ construct.....	VI
Appendix F: 3D bioprinted constructs	VIII

List of nomenclature, abbreviations, and symbols

4'-6-Diamidino-2-phenylindole	(DAPI)
Agarose-collagen blend hydrogel	(AC blend hydrogel)
Alizarin red S solution	(ARS)
Angular speed	(ω)
Arginyl-glycyl-aspartic acid	(RGD)
Atomic-force microscopy	(AFM)
Attenuated total reflectance	(ATR)
Bovine serum albumin	(BSA)
Cell-laden microspheres	(CLMs)
Computed tomography	(CT)
Computer aided design	(CAD)
Degree of crystallinity	(X_c)
Density	(ρ)
Deoxyribonucleic acid	(DNA)
Dichloromethane	(DCM)
Differential scanning calorimeter	(DSC)
Double-distilled water	(ddH ₂ O)
Dulbecco's modified Eagle's medium	(DMEM)
Dulbecco's phosphate-buffered saline	(DPBS)
Enthalpy of fusion	(ΔH_f)
Epidermal growth factor	(EGF)
Ethanol	(EtOH)
Ethanolic sodium hydroxide	(EtOH–NaOH)
Extracellular matrix	(ECM)

Fetal bovine serum	(FBS)
Final fiber diameter	(D)
Flow activation energy	(E _a)
Fourier transform infrared	(FTIR)
Full width at half maximum	(FWHM)
Fused deposition modelling	(FDM)
Gas constant	(R)
Gastrointestinal tract	(GI tract)
Gel permeation chromatography	(GPC)
Glass transition temperature	(T _g)
Glycosaminoglycans	(GAGs)
Gravitational constant	(g)
Human mesenchymal stem cells	(hMSCs)
Inverted optical microscope	(OM)
L-lactide	(LA)
Magnetic resonance imaging	(MRI)
Materials constant	(A)
Melt height	(h)
Melt temperature at melt-holder	(T)
Melt-drawing speed	(v)
Melting temperature	(T _m)
Mesenchymal stem cells	(MSCs)
Number-average molecular weights	(M _n)
Optical coherence tomography	(OCT)
Optical microscope	(OM)

Orifice diameter	(d)
Phosphate-buffered saline	(PBS)
Poly(D,L-lactide-co-glycolide)	(PLGA)
Poly(L-lactide-co- ϵ -caprolactone)	(PLC)
Poly(L-lactide)	(PLLA)
Poly(vinyl alcohol)	(PVA)
Poly(ϵ -caprolactone)	(PCL)
Polydimethylsiloxane	(PDMS)
Polydispersity indices	(PDI)
Polyglycolic acid	(PGA)
Poly lactides	(PLA)
Propidium iodide	(PI)
Radius of mandrel	(r)
Rotations per minute	(RPM)
Scanning electron microscope	(SEM)
Selective laser sintering	(SLS)
Shear stress	(s)
Shear viscosity	(h)
Small intestine submucosa	(SIS)
Smooth muscle actin	(SMA)
Sodium hydroxide	(NaOH)
Standard deviation	(SD)
Stereolithography apparatus	(SLA)
Thermally induced phase separation	(TIPS)
Thermogravimetric analyzer	(TGA)

Tissue culture polystyrene	(TCPS)
Tissue engineering	(TE)
Transforming growth factor $\beta 1$	(TGF- $\beta 1$)
Transverse speed	(v_t)
Ultimate tensile strengths	(UTS)
Ultraviolet	(UV)
Urinary bladder mucosa	(UBM)
Vascular endothelial growth factors	(VEGFs)
Velocity gradient of shear flow	(dv/dx)
Velocity of polymer melt exiting orifice (v_0)	
Water-in-oil-in-water	(w/o/w)
Weight-average molecular weights	(M_w)
X-ray diffraction	(XRD)
Zero-shear viscosity	(η_0)
ϵ -caprolactone	(CL)

List of tables

Table 1. Comparison on measurements of architectural layer thickness in OCT and histology images of an <i>ex vivo</i> normal esophagus specimens [46]	14
Table 2. Various materials for esophageal tissue engineering.....	30
Table 3. Tensile properties of the fabricated scaffolds as compared to the native esophagus.....	94
Table 4. Comparison between the tissue spheroids and the cell-laden microspheres in their usage in 3D bioprinting.....	110

List of figures

Figure 1.1 Schematic illustration of implantation of a tissue engineered esophagus after an esophagectomy. The figure is modified from Tan <i>et al.</i> [11].	2
Figure 2.1 Cross-sectional view of an esophagus.....	9
Figure 2.2 (a) OCT images of human esophagus showing epithelium (ep or SE), lamina propria (LP), muscularis mucosa (MM), submucosa (SM) and muscularis externa (MP) [46,47]. (b) Phase-contrast X-ray CT image illustrating 3D views of esophagus [48]......	13
Figure 2.3 Modulus of esophagus in comparison with other tissues and tissue culture polystyrene (TCPS). Esophagus is more elastic in circumferential direction to accommodate normal food bolus of ~10 mm.	16
Figure 2.4 Requirements for tissue engineering scaffolds.....	19
Figure 2.5 Illustration on the classification of tissue engineering approaches. .	23
Figure 2.6 Classification of materials for engineering scaffolds	24
Figure 2.7 Graphical illustration of the material selection based on the modulus and tensile strength matching to the native tissue [100]	24
Figure 2.8. Classification of different fibrous scaffold fabrication techniques based on the form of raw materials.....	37
Figure 2.9 Bovine esophagus showing the mucosal folding [206]	39
Figure 2.10. Schematic illustration of the conventional TE of flat membrane and the new 3D bioprinting approach for epithelium regeneration	42
Figure 2.11. Schematic illustration of the use of MSC to seed on decellularized donor esophagus [18]	46
Figure 3.1. (a) Illustration of the melt-drawing device (b) Fiber drawing using the device.	53
Figure 3.2. Schematic illustration of (a) front view, and (b) side view of the melt-drawing process	55
Figure 3.3. Melt-drawn PLGA, PCL and PLC. PLGA and PCL was melt-drawn into loose fibers but the PLC remained as an intact tube.....	62
Figure 3.4. Illustration of circumferential extensibility of a melt-drawn PLC scaffold.....	62
Figure 3.5. TGA results with heating rate of 5 °C/min showing thermal degradation temperature of PLC.....	63

Figure 3.6. DSC results with heating rate of 5 °C/min showing thermal properties of PLC.....	63
Figure 3.7. Dynamic frequency sweep test of PLC at 150 °C. Inset illustrates the zero-shear viscosities at different temperatures.....	64
Figure 3.8. Melt-drawing ability of PLC at different temperatures and melt-drawing speeds. Note: “Drawable but not sustainable drawing” means that the fibers can be drawn, but sometimes the fibers break during fabrication.	65
Figure 3.9. Representative tubular scaffold fabricated by melt-drawing. This scaffold has diameter of 30 mm, width of 20 mm and thickness of 130 mm.....	65
Figure 3.10. SEM micrographs and fiber diameter distribution of melt-drawn scaffolds $V_{0.24}$, $V_{0.47}$, $V_{0.94}$, $V_{1.88}$, and $V_{3.77}$. Inset illustrates the sample taken from the tubular scaffolds for SEM.	66
Figure 3.11. (a) OM images of L929 cell growth and distribution on $V_{0.94}$ scaffold for day 1, 3 and 6. (b) Real-time cell proliferation of L929 on the scaffolds $V_{0.47}$ and $V_{3.77}$. (c) Cell proliferation on the scaffolds $V_{0.47}$ and $V_{0.94}$ comparing to TCPS. Inset: water contact angle of PLC scaffold.	68
Figure 3.12. Live/dead staining of L929 after 6 days of culture on TCPS, PLC flat sheet, $V_{0.94}$, and $V_{3.77}$ scaffolds.	69
Figure 3.13. SEM images showing the L929 cell adhesion on the scaffolds with the different melt-drawing speeds after 6 days of culture.....	70
Figure 3.14. (a) Live(green)/dead(red) staining and (b) SEM images of myoblasts C2C12 cultured on $V_{0.94}$ for 3 days. (c) Confocal microscope images showing F-actin and DAPI nucleus staining of C2C12 cultured on $V_{0.94}$ for 7 days.....	71
Figure 3.15. (a) SEM images and (b) confocal microscopy showing C2C12 cells infiltration into $V_{0.94}$ scaffolds after culturing for 7 days. Note: confocal microscope images showing F-actin (green) and DAPI (blue) nucleus staining.	72
Figure 3.16. Immuno-staining of hMSCs cultured on (a) TCPS control and (b) microfibers. (c) SEM image of the hMSCs on the microfibers.	73
Figure 3.17. Effect of melt-drawing speeds on the fiber diameters from theoretical and experimental results; and (b) linear relationship of fiber diameters with melt-drawing speeds obtained from experiments.	76
Figure 4.1. Illustration of fabrication process of various ring samples for circumferential tensile testing.	82
Figure 4.2. (a) Classification of three different types of samples fabricated for planar tensile testing. (b) Illustration of samples preparation for circumferential and longitudinal samples for planar tensile testing (c) Planar tensile testing process for flat scaffold samples.....	85

Figure 4.3. FTIR spectra of PLC flat sheet and melt-drawn PLC samples.	87
Figure 4.4. XRD patterns for pristine PLC pellets and melt-drawn PLC	88
Figure 4.5. DSC thermograms of the pristine PLC pellets and the melt-drawn PLC samples	89
Figure 4.6. Engineering stress–engineering strain curves for PLC rings with varying melt-drawing speeds. Note: A _{3.77} and B _{3.77} refer to the same set of samples.....	90
Figure 4.7. Engineering stress–engineering strain curves for dry and moisturized PLC rings with varying melt-drawing speeds.....	90
Figure 4.8. Histograms showing the comparison of (a) UTS, (b) tangent modulus at 40% elongation, and (c) elongation properties of the PLC rings (dry and moisturized) with varying melt-drawing speeds.....	91
Figure 4.9. Cyclic tensile engineering stress–engineering strain curves for PLC rings with varying melt-drawing speeds. The results were shown separately, where each red line shows the first cycle and each green line shows the 10 th cycle.	92
Figure 4.10. (a) Schematic illustrations and SEM images illustrating the fiber arrangement of different samples. Planar tensile stress-strain results of the 10L_0.7 mm/s, 20L_0.7 mm/s and 5L_0.7 mm/s+30L_4.0 mm/s samples in (b) circumferential and (c) longitudinal directions.....	93
Figure 4.11. Pictures of scaffolds fabricated with different inner diameters (ranging from 2.5 mm to 30 mm) and different lengths (ranging from 12 mm to 45 mm).....	94
Figure 4.12. Relationship between crystallinity (predicted from DSC) and melt-drawing speed. Crystallinity of the pristine PLC pellets is included (with horizontal dotted lines) for comparison.	99
Figure 4.13. Schematic illustration of the structural evolution of PLC after melt-drawing and air cooling.	100
Figure 4.14. Relationship between (a) Young’s modulus, (b) UTS, and (c) maximum elongation with samples’ crystallinity.	102
Figure 5.1. SEM image of human buccal epithelial cell TR146 cultured on V _{0.94} scaffold.....	108
Figure 5.2. Schematic and pictorial illustration on the fabrication of porous PLGA microspheres.....	117
Figure 5.3. SEM images of PLGA microspheres fabricated by different parameters. The optimized parameter is indicated in the red box.	119

Figure 5.4. SEM images of (a) the optimized pre-treated microspheres and (b) their cross-sections.....	120
Figure 5.5. SEM images of the EtOH-NaOH treated microspheres by using different parameters. The optimized parameter is indicated in red box.	120
Figure 5.6. SEM images of (a) the optimized EtOH-NaOH treated microspheres and (b) their cross-sections	121
Figure 5.7. Schematic showing the relationship between the microsphere size selection and its effect on the 3D bioprinting	122
Figure 5.8. (a) SEM images of PLGA microspheres after 1, 3, 5, and 7 week(s) of hydrolytic degradation in PBS at 37 °C. (b) Graph showing the weight loss of microspheres (n=3) with the weeks of hydrolytic degradation.....	123
Figure 5.9. DSC results showing T_g of amorphous PLGA at ~50 °C.....	123
Figure 5.10. (a) Pictures showing the incubated and freeze-dried 1.5 mg/ml collagen, 1.5 wt/v% agarose, and AC blend hydrogels prior to SEM imaging. (b) SEM images showing the microarchitecture of the hydrogels.	125
Figure 5.11. OM images of C2C12 cast in AC blend hydrogels with (a) 1.5 mg/ml collagen and 1.5 wt/v% agarose and (b) 0.5 mg/mL collagen and 2 wt/v% agarose, after 1 and 3 day(s) of culture.....	126
Figure 5.12. L929 cells cultured on cylindrical AC blend hydrogel and collagen with initial diameter (D_0) of 15.0 mm. D_{10} is the final diameter of the cells-hydrogel constructs.	127
Figure 5.13. SEM images showing (a) the PLGA microspheres and (b) the CLMs. The size distribution histograms of the microspheres and the CLMs are shown below the respective SEM images.	128
Figure 5.14. Day 7 L929 cell viabilities on PLGA microspheres, 1.5 mg/mL collagen, 1.5 wt/v% agarose and AC blend hydrogel.....	129
Figure 5.15. Day 14 L929 cell viabilities on PLGA microspheres, 1.5 mg/mL collagen, 1.5 wt/v% agarose and AC blend hydrogel.....	129
Figure 6.1. Schematic illustration of the bioprinting process.	131
Figure 6.2. Schematic of an automated bioprinting system. Inset shows the OM image of the micropipette tip.	132
Figure 6.3. Pictures demonstrating a 3D printed tubular construct with gelatin (transparent) as support. Construct was printed on superfrost plus microscope slides with a dimension of 25 mm×75 mm.....	139
Figure 6.4. (a) Picture of a 3D printed tubular construct with gelatin (transparent) as support. (b) SEM image illustrates the microarchitecture of the printed construct.....	140

Figure 6.5. Compressive stress-compressive strain curves for the AC blend hydrogel, the loosely packed samples, and the bioink. Pictures on the right show the representative samples used for compression tests.	140
Figure 6.6. (a) Picture showing the representative sample used for tensile tests. SEM image illustrates the surface of the sample. (b) Tensile stress-strain curves for the bioink, the inset shows a picture of a fractured sample. (c) SEM images showing fracture surface of the samples.	141
Figure 6.7. Fluorescence images of L929 cells labelled by green fluorescent cell linker PKH67GL cultured on (a) TCPS, (b) PLGA microspheres, and (c) printed construct.	142
Figure 6.8. SEM images of the printed construct using L929 cells.	142
Figure 6.9. (a) Photograph of a bioprinted ring using C2C12. (b) Fluorescence images of printed ring constructs with L929, A10, TR146 and C2C12 cells.	143
Figure 6.10. Fluorescence image reveal patterning of L929 cells (green) together with C2C12 cells (red) side-by-side achieved by printing.	144
Figure 6.11. (a) Real time cell viability and proliferation of printed 3D constructs. (b) 3D cell viability within the printed construct on the day 2, 7, and 14 of culture after printing shows the cell growth over 14 days.	144
Figure 6.12. L929 cell viability on day 2, 7 and 14 of culture after printing.	145
Figure 6.13. Fluorescence microscopy and SEM pictures of (a) TR146 epithelial cultured on microspheres and (b) bioprinted TR146 CLMs and cultured for 2 weeks. Cells are indicated by the arrows.	146
Figure 6.14. Fluorescence microscopic images of C2C12 tagged with red fluorescence (a) cultured on TCPS, AC blend hydrogel and PLGA microspheres (b) bioprinted into ring.	147
Figure 6.15. (a-c) Fluorescence microscopic images of A10 smooth muscle cells that were cultured on PLGA microspheres, bioprinted construct and TCPS. (d) SEM microscopic images of A10 bioprinted into ring. Cells were indicated by the arrows.	148
Figure 6.16. Live/dead imaging of hMSCs cultured on PLGA microspheres and TCPS (control).	148
Figure 6.17. Fluorescence microscopic images showing Cy3 labeled CD44 (red), AlexaFluor 488 labeled CD31 (green), and DAPI nuclear staining (blue) for the hMSCs on control (TCPS) and bioprinted construct. Photographs of the ARS stained (red) osteo-differentiated cells on the TCPS and the bioprinted constructs.	149
Figure 6.18. Schematic illustration of prediction of the cell growth patterns in bioprinted constructs.	151

Figure 7.1. A prototype combining melt-drawn PLC fibrous scaffold with the bioprinted PLGA microspheres. The bioprinted layers 1 and 2 are to mimic the folded epithelium and the underlying connective tissues, respectively.....	158
Figure 7.2. Rendered design (left) and picture (right) of the melt-drawing machine being newly designed.	162
Figure 7.3. Illustrations and SEM images showing melt-drawn PLC (left), PCL (right) and hybrid co-melt-drawing of PLC and PCL.....	163
Figure 7.4. (a) Illustration of beads printing for the bioprinting of nervous CLMs in the future. (b) OM and (c) pictures of the printed beads.	164

Abstract

Tissue engineering (TE) offers an important alternative for surgical replacement of diseased or traumatized esophagus. The TE replacement can replicate the native esophagus in shape and performance. This dissertation describes the fabrication and characterization of two key components in esophageal TE, i.e. the muscle and the epithelium. Two different additive fabrication techniques are investigated due to the inherent diversity in structure of an esophagus. Customizations of dimension and mechanical properties are made possible by the additive fabrication, which are vital factors for implantation across ages and genders. Tubular poly(L-lactide-co- ϵ -caprolactone) (PLC) scaffold is fabricated by a melt-drawing method to mimic the structure of circular muscles. The microfibrinous solid scaffold serves as exterior of the TE replacement, which is strong and elastic circumferentially to accommodate bolus. Moreover, it consists of highly aligned microfibers in the circumferential direction with a uniform distribution of fiber diameters, which allows the muscle cells to grow along the fiber alignment direction. The crystallinity of PLC fibers increases with an increasing melt-drawing speed due to the strain-induced crystallization. The modulus and the strength are increased with an increase in crystallinity of the PLC scaffold. Tensile properties of the tubular scaffold are comparable to those of the human esophagus in the circumferential direction, which also can be fine-tuned by adjusting the melt-drawing fabrication parameters. Furthermore, tubular scaffolds with varying diameters and lengths are fabricated. In addition, 3D bioprinting is employed to regenerate a layer of cell-laden, folded epithelium in a lumen of esophagus. A new bioink using cell-laden microspheres (CLMs) with a thin encapsulation of agarose-collagen blend hydrogel (AC blend hydrogel) is

introduced. Highly porous microspheres provide high specific surface areas for anchorage-dependent cells to attach, infiltrate and proliferate before printing. AC blend hydrogel allows a good printability of CLMs, with immediate gelation of the construct upon printing on the chilled build platform. Tightly packed construct is bioprinted with high stacking ability using a micropipette extrusion-based method. The mechanical strength of the bioprinted construct is considerably enhanced when compared to that with just AC blend hydrogel. The bioprinted cells proliferate and maintain high viability for up to 2 weeks. *In vitro* performance of individual components of a hybrid esophageal TE construct is successfully illustrated. The hybrid bioengineering of muscle cell-seeded exterior tubular scaffold and 3D bioprinted interior folded epithelium in the lumen have taken a great step towards functional esophageal TE.

Chapter 1. Introduction

1.1 Background

Esophageal carcinoma affects more than 450 000 people in the world annually and the number of incidence is increasing each year [1]. The 2016 statistics from American Cancer Society show that lifetime risk of esophageal cancer in the United States is $\sim 1/125$ in men and $\sim 1/435$ in women [2]. It is one of the most frequent cause of cancer-related deaths with 5-year survival rate of 15-25% [1,3]. Clinical treatments such as radiation are life-preserving, but they are associated with a marked impairment in quality of life. Complications such as esophageal stricture, spinal cord myelopathy, skin erythema, hair loss, mucositis, malnutrition, and fibrosis are common complications after the radiation treatments [4]. Meanwhile, palliative treatment e.g. esophageal stenting is a means to relieve symptoms, such as pain and trouble swallowing, but it is not expected to cure the cancer [5].

Surgical resection (esophagectomy) for the treatment of cancer, atresia, and trauma is considered as the gold-standard treatment, but could result in circumferential, full-thickness, and long-segment loss of the esophagus [6,7]. Autologous tissue grafts from the stomach and colon can be used to bridge the gap for lumen continuity [1]. However, removing intestine or stomach from their normal positions in the body is less than desirable. Moreover, these treatments might fail to restore the peristaltic function. Complications such as reflux, leaks, strictures, ischemia, and postprandial pain were found in 9–60% of patients, and the associated mortality is $\sim 12\%$ [7].

Transplantation from deceased donor is another viable solution to restore normal organ functions, providing better quality of life and longer survival [8]

although there are risks for acute to chronic rejection. Nevertheless, there is a severe shortage of human donor organs. Furthermore, almost every patient who receives an allogeneic organ transplant must take immunosuppressant drugs to prevent the rejection of transplanted organs and tissues. These life-long medications come with morbidity [8]. Many attempts have been made to develop materials such as elastomers (Tygon), polyethylene terephthalate (Dacron), and polytetrafluoroethylene (Teflon) [9] for artificial esophageal prostheses. Unfortunately, there were several possible complications such as stenosis, stricture, or anastomotic leakage [9]. Alternatives to autologous or allogenic organ transplants are thus urgently needed.

1.2 Tissue engineering: Requirements and key challenges

An excellent solution would be to engineer a biodegradable tubular segment in combination with autologous cells to be implanted as illustrated in Figure 1. This tube created from tissue engineering (TE) techniques would eventually be replaced by a normal tissue [10]. Replacement with structural integrity and normal function can be made possible. Tissue engineered replacement can eliminate the need to harvest replacement tissues from the

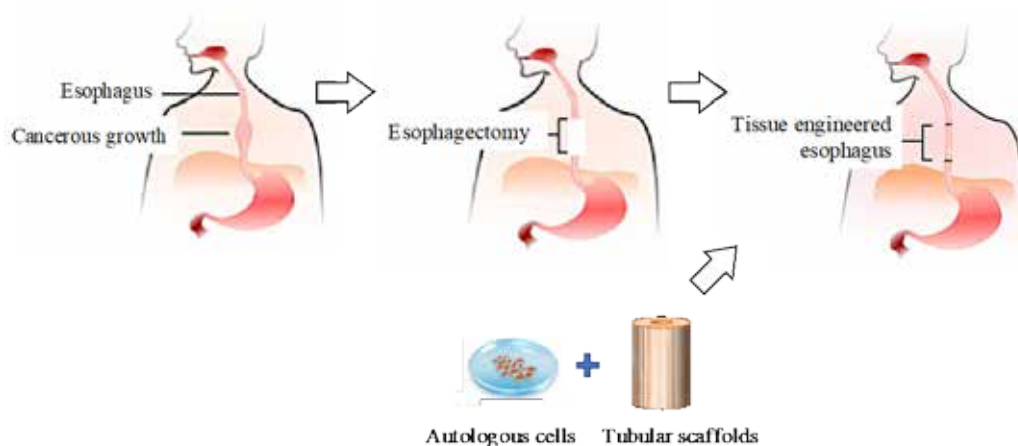


Figure 1.1 Schematic illustration of implantation of a tissue engineered esophagus after an esophagectomy. The figure is modified from Tan *et al.* [11].

patient's own body, would reduce the number of surgeries, be readily available, likely reduce the surgery-related mortality and morbidity, and improve long-term functional outcome.

The regeneration of some organs, such as trachea, heart valve, dermis, and bladder, has reached advanced translational stages in the past few decades [12,13], yet regenerative medicine applied to the esophagus is still in its infancy. The reported TE approaches involve the tissue-specific approach, especially for epithelium [14] and muscle [15] regeneration. Other studies involve innervation, vascularization, sphincter bioengineering, lymphatic and esophageal gland reconstruction [6]. Different types of scaffolds (e.g. decellularized matrices [16–18], synthetic and natural scaffolds [19–21]) and cell sources (e.g. epithelium [22,23], smooth muscle [15] and mesenchymal stem cells (MSCs) [18]) have been evaluated for their capacity to repair or restore the esophagus functions.

Based on extensive experiences in the regeneration of trachea [24], an ideal replacement of the esophagus should meet several criteria i.e. (i) with suitable dimensions and shapes; (ii) flexible circumferentially but rigid enough to maintain a lumen; (iii) with surface suitable for epithelium regeneration; and (iv) easy to handle and insert into the body. There are more challenges in esophagus regeneration because of the intrinsic heterogeneity in its structure. Muscle layers, for example, are important in the TE of esophagus so that peristalsis will be possible [25]. Besides the criteria mentioned above, key challenges of esophageal regeneration are described in the following sections. This dissertation aims to address these challenges.

Musculature

In the regeneration of muscularis externa layer of the esophagus, the scaffold should fulfill the necessary mechanical and topological requirements. It serves as an outer layer of the replacement, thus acquiring sufficient strength for holding the structure and to be handled. Meanwhile, it should mimic the native esophagus muscle to be flexible circumferentially to accommodate bolus. Dimension and mechanical properties customization of the tube is important because there is demand for implantation of esophagus TE construct across different ages, from the young children to the elderly. The temporary transplant should not differ too much from their own tissue to avoid tissue mismatch [26,27] and malfunction of the implant. At the same time, the tube should consist of anisotropic alignment in a specific direction, which is necessary for guiding unidirectional growth of muscle cells [28]. The alignment of muscle fibers is extremely important for peristalsis in the replaced segments [25].

Epithelium

Previous studies have found that the epithelium regeneration is of necessity to avoid stenosis and to facilitate the healing process of tubular esophagus implants [16]. The epithelium also serves as a protection layer to its underlying tissues. As opposed to the anisotropic muscle fibers, the epithelial cells grow in isotropic aggregates that collectively form the folded epithelium structure at esophageal lumen. The epithelium layer is not highly elastic, hence need to be unfolded for bolus transportation [29].

Due to the inherent diversity in structure of the esophagus, it is of interest to generate a multilayered, hybrid TE construct that mimics the heterogeneity in native esophagus.

1.3 Objectives

Based on the key challenges regarding esophageal TE as described in Section 1.2, the overall goal of this dissertation is to develop a technique for personalization of a tubular TE construct by emphasizing on the two important esophageal components, i.e. muscle and epithelium tissues. The inherent heterogeneity of the esophagus structure propels the interest to create a hybrid TE construct. In support of this goal, the main objectives of this dissertation are listed below:

- i) To develop customizable strategies for bioengineering of the structurally heterogeneous esophagus.
- ii) To bioengineer the anisotropic musculature with tunable strength and elasticity.
- iii) To bioprint the isotropic epithelium with high strength aiming for TE of folded mucosa.

1.4 Scope

This dissertation focuses on additive biofabrication design of customized TE esophageal construct based on the objectives listed in Section 1.3. The circumferential muscle layer of the esophagus is replicated by melt-drawing of elastic poly(L-lactide-co- ϵ -caprolactone) (PLC) into a tubular scaffold that is comprised of highly aligned microfibers in the circumferential direction. The interaction between the construct and the cells, especially for the formation of oriented muscle cells on the scaffolds, is systematically studied. Some aspects regarding scaffold customization, such as mechanical properties and scaffolds' diameter, are thoroughly considered.

The epithelium layer is 3D bioprinted in this dissertation as a preliminary study by using a new type of bioink consisted of isotropic poly(D,L-lactide-co-glycolide) (PLGA) microspheres. Fabrication of the bioink and 3D bioprinting strategy microspheres fabrication are illustrated in detail, respectively. Biocompatibility and mechanical properties of the bioprinted constructs are evaluated.

A hybrid construct is to be fabricated to demonstrate the viability of the proposed biofabrication concept.

1.5 Dissertation organization

In Chapter 1, a brief introduction to the research background and motivation for TE of esophagus is described. The objectives and scope of this dissertation are stated.

Chapter 2 highlights the importance of musculature and mucosa in esophageal TE. The concept and categorization of TE are described subsequently. Requirements and key challenges for esophageal TE are discussed. The concepts of additive, subtractive and formative TE fabrication processes are briefly introduced. Due to the key objective of customization of TE constructs, additive biofabrication is the main research focus in this dissertation. In the following sections, regeneration of the muscle to restore the tissue functions, such as the motility and peristalsis, in esophagus are discussed. The alignment and survival of the engineered muscle are the two most important concerns in the scaffold design. Vital fiber properties for cell and tissue alignment are described. Requirements for epithelium TE are then listed. To create the folded epithelium, bioprinting that combines the essence of 3D printing and TE represents the most

attractive option. Moreover, analysis on the commonly used bioinks is also included.

Chapter 3 begins with introductions of a melt-drawing method and the evaluation of biomaterials for melt-drawing process. Thereafter, PLC is melt-drawn to form elastic tubular scaffolds. The chapter focuses on (i) melt-drawing ability of the chosen elastic PLC and (ii) the possibility of forming oriented muscle cells on the unidirectional scaffolds. In addition, the dimensions and mechanical properties of esophagus vary across ages and genders. Hence, there is a need to customize these properties of the scaffolds, which is pinpointed in Chapter 4. An in-depth understanding of structural evolution during melt-drawing of PLC microfibrinous scaffold is presented. Additionally, tensile properties of the microfibers are studied to build the relationship between fabrication parameters and mechanical properties. These data are then used to compare with the properties of native esophagus.

Chapters 5 and 6 demonstrate 3D bioprinting of the epithelium layer of an esophagus. The novel idea presented is to seed epithelial cells in isotropic PLGA microspheres as bioink. Cells are expanded in stirred culture on the microspheres before printing. Chapter 5 reports the studies on the survivability of cells in the new bioink. Furthermore, to investigate the bio-printability of the bioink, Chapter 6 introduces a micropipette-based printing method that is to extrude the bioink layer by layer to form tubes. Strength of the bioink is also studied.

Chapter 7 summarizes the two important TE components that are presented, i.e. the outer melt-drawn PLC tubular scaffold and the inner bioprinted PLGA microsphere construct, which are supposed to replicate the circular muscle

layer and the interior epithelium, respectively. The distinctive features, e.g. strength and alignment, of the two key components are specified. Chapter 7 further concludes the main results obtained in this dissertation and points out the future work that needs to be followed up based on the significant findings of this dissertation.

Chapter 2. Literature review

2.1 Esophagus

The esophagus is part of the digestive system which extends across the three anatomical planes, i.e. the neck, the thorax, and the abdomen, of the human body. Hence, it can be categorized into the cervical (proximal), the thoracic and the abdominal (distal) regions [30]. In the human alimentary canal, the esophagus is ~250 mm long, connecting the lower end of the pharynx with the cardiac opening of the stomach [30]. Although the esophagus is part of the digestive system, it does not have any digestive, absorptive, metabolic, or endocrine functions. It mainly serves as a hollow and highly distensible muscular tube for the food bolus transportation from the mouth to the stomach via peristalsis. Its functions are supported by the upper and lower esophageal sphincters located at its proximal and distal ends [31]. The esophagus also acts as a barrier to protect the underlying tissues from abrasive bolus [32].

The organization of tissues within the esophageal wall from lumen outwards is described as the mucosa, the submucosa, the muscularis externa, and the adventitia [30] as shown in Figure 2.1. The mucosa layer lines the length of

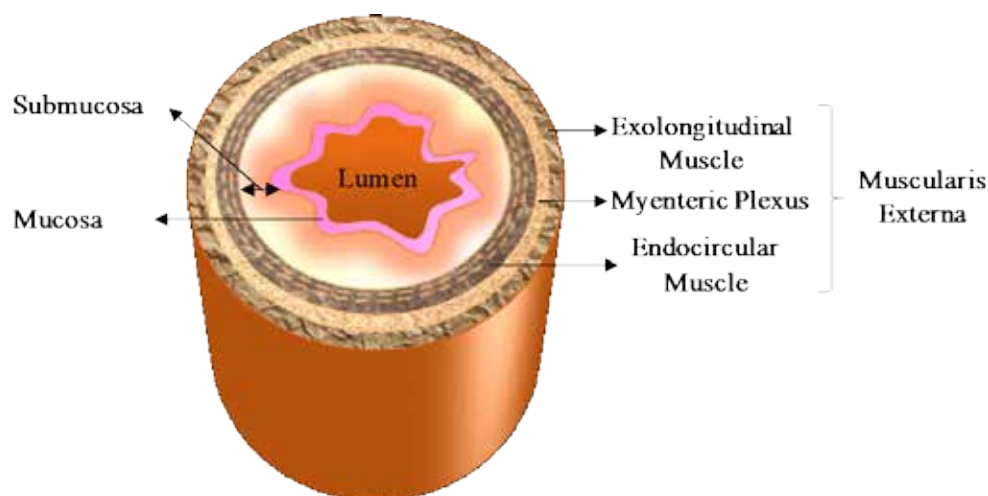


Figure 2.1 Cross-sectional view of an esophagus

the esophageal lumen. Stratified squamous non-keratinized epithelium with its basement membrane reposes in the inmost layer at the lumen in the human esophagus. Underneath it is a supporting layer of connective tissue called the lamina propria and a longitudinally oriented, thin layer of smooth muscle fiber called the muscularis mucosa.

The submucosa joins the mucosa to the muscularis externa. It is composed of loose connective tissue with blood vessels, lymphatic vessels, nerve fibers and minor salivary glands. Here, the secretions from the minor salivary glands can reach the epithelium surface via straight ducts [33]. Specific to the esophagus, the minor salivary glands produce secretion with high bicarbonate concentration to neutralize acid from stomach reflux [32]. These salivary glands also help to maintain a moist epithelium surface containing mucins, a variety of antimicrobial substances, and epidermal growth factor (EGF) [32].

The muscularis externa consists of the endocircular and exolongitudinal muscle layers, with a myenteric plexus between the two muscle layers, which facilitates peristaltic activity [30,34,35]. The circular muscle layer runs circumferentially around the tract and the longitudinal muscle layer runs parallel to the length. The muscularis externa is composed of striated muscles in the proximal portion, smooth muscles in the distal part, and smooth and striated muscles mixed in the middle of the esophagus [34]. The outermost layer of esophagus is the adventitia to join itself to the adjoining structures [34]. The adventitia is a thin layer composed of loose soft connective tissue [31].

2.1.1 Musculature and mucosa

Tubular organs vary substantially in sizes, shapes and structures. In fact, no two tubes are the same even within a given organism or tissue [36].

Nevertheless, they usually possess apical epithelial (or endothelial) surface lining the lumen. The apical surface faces the lumen or the external environment, whereas the basal surface faces surrounding tissues or basement membrane [36]. Epithelial cells contact neighboring cells via junctional structures i.e. adherens junctions and tight junctions in vertebrates. This structure serves to anchor the cells, provide structural support and barrier function to prevent the diffusion of membrane proteins and lipids between the different cell surfaces [37,38]. These tubes often comprise an outer musculature that either directly contact the epithelium or separated by connective tissues [38].

The musculature and mucosa's epithelium are the most important layers in the esophageal wall. The primary function of the esophagus is propulsive peristalsis of the swallowed bolus. This function is mainly mediated by esophageal musculature in the muscularis externa [6,32]. The peristalsis is initiated by swallowing and involves sequenced rhythmic contractions of the musculature, in concert with appropriately timed relaxation of the lower esophageal sphincter. The circular muscle contraction is well coordinated with the longitudinal muscle shortening during bolus propulsion [39].

The function of the epithelium in mucosa is the protection of the underlying tissue from mechanical, chemical, microbial toxins and enzymatic damage from food bolus as well as reflux from stomach [32,40]. The epithelium surface is always moistened by the glandular secretion to diminish the friction when food bolus passes through the lumen. Lipid-based permeability barriers in the outermost epithelial layers protect the underlying tissues against fluid loss [32]. The epithelium protects the underlying tissues by rapid epithelial homeostasis [41]. Cell loss from the epithelium surface is balanced by the cell

production at the basement membrane. The rapid clearance of surface cells serves as a protective mechanism whereby the colonization and the invasion of microorganisms which are adherent to the epithelium surface are limited [32]. The soft tissues of the human esophagus are covered by stratifying squamous non-keratinizing epithelium for flexibility to accommodate swallowing of boluses. The connective tissue of lining mucosa, i.e. lamina propria, is elastic and flexible in nature. It consists of loosely arranged collagen fibers and fibroblasts embedded in glycosaminoglycans (GAGs) matrix [42]. Under a relaxed state, the mucosa layer collapses into multiple folds, closing the lumen; while during passage of food bolus, the lumen opens up.

2.1.2 Variations among human esophagus

The human esophagus varies among individuals, including their geometrical features and mechanical properties.

Geometrical features

In humans, the esophagus is usually 180-250 mm long [39], extending from the upper to the lower esophageal sphincter. The length of the esophagus correlates with an individual's height [43]. The esophagus is approximately cylindrical in shape [31]. The diameters of the esophagus vary throughout the length. By using double-contrast esophagography, White *et al.* [44] showed the differences of normal diameter of the thoracic esophagus among 9 persons. The mean diameter was 20.2 ± 4.1 (range from 15 to 28) mm at the level of the aortic arch, 30.3 ± 5.6 (range from 24 to 42) mm at the level of the carina, and 28.7 ± 4.2 (range from 24 to 37) mm one vertebral body height above the gastroesophageal junction, with a mean overall thoracic esophageal diameter of 26.3 (range from 24 to 36) mm [44]. As study by Schraufnagel *et al.* [45]

illustrated the esophageal lumen diameter through measurement among 110 persons using computed tomography (CT). Greater than 60% of the esophageal segments contained no air. The average lumen of all segments of all subjects was 2.7 ± 2.3 mm. The average maximum for a given subject was 10.5 ± 5.0 mm. The greatest luminal dimensions occurred in the area between where the diaphragm first appears and where the esophagus enters the abdomen.

Bouma *et al.* [46] and Zuccaro *et al.* [47] measured the average tissue thickness of esophageal mucosa by using optical coherence tomography (OCT) as shown in Figure 2.2 (a). Five anatomic layers of the esophageal wall could be clearly distinguished, i.e. the squamous epithelium, lamina propria, muscularis mucosa, submucosa, and muscularis externa. Bouma *et al.* observed that the average epithelium thickness was ~ 270 nm. Zuccaro *et al.* described that the average esophageal epithelium was $\sim 182 \pm 11.7$ nm thick in the mid-esophagus, and $\sim 243 \pm 12.4$ nm thick in the distal esophagus [47]. The whole mucosa was measured to be ~ 582 nm thick. The thickness of submucosa and muscularis

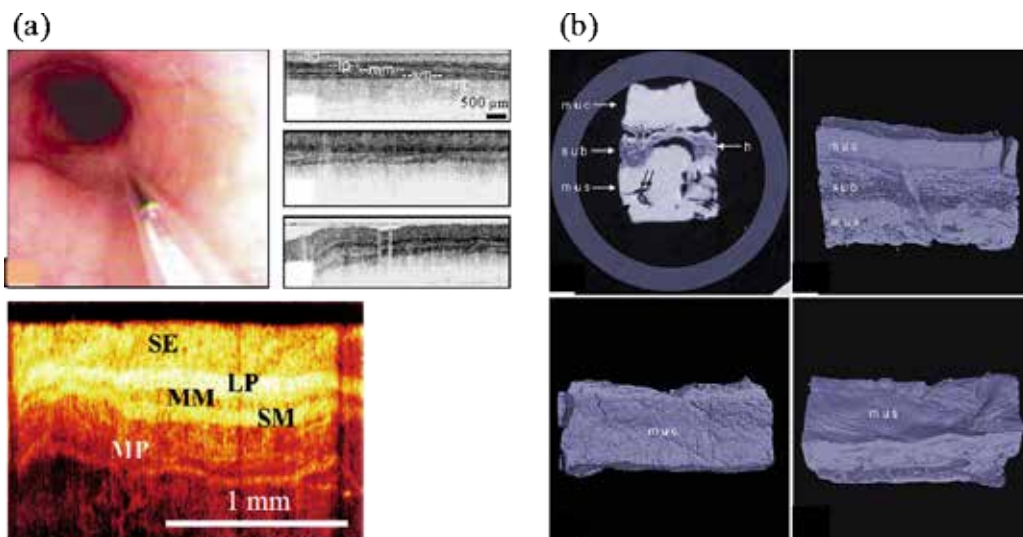


Figure 2.2 (a) OCT images of human esophagus showing epithelium (ep or SE), lamina propria (LP), muscularis mucosa (MM), submucosa (SM) and muscularis externa (MP) [46,47]. (b) Phase-contrast X-ray CT image illustrating 3D views of esophagus [48].

externa was ~ 130 mm and ~ 500 mm, respectively [46]. Nevertheless, it is noted that the layers of the esophageal wall are mainly composed of connective tissues and muscular fibers, which were compressed by $\sim 1/3 - 1/5$ of their overall thickness when measuring by OCT [47]. The thicknesses of the esophageal layers are shown in Table 1 as described by Bouma *et al.*, where he compared *in vivo* OCT with the *ex vivo* histology images.

Table 1. Comparison on measurements of architectural layer thickness in OCT and histology images of an *ex vivo* normal esophagus specimens [46]

Measurement	OCT mean (μm) \pm SD	Histology mean (μm) \pm SD
Epithelium thickness	269 ± 11.9	275 ± 13.7
Lumen - Lamina Propria	415 ± 29.6	408 ± 26.0
Lumen - Muscularis Mucosa	582 ± 29.9	581 ± 18.6
Lumen - Muscularis Externa	1032 ± 17.5	1013 ± 18.6

Using CT, Xia *et al.* [49] studied the esophageal wall thickness when contracting and dilating in normal circumstances. If visible air in the esophageal cavities could be found, then the esophagus was regarded as being in the status of dilatation. When contracting, the abdominal esophagus was the thickest and the thoracic was the least thick with average thicknesses of 5.68 (range from 5.28 to 6.09) mm and 4.05 (range from 3.71 to 4.21) mm, respectively. The cervical esophagus was the thickest and the thoracic part was the least thick with average thicknesses of 2.70 (range from 2.52 to 2.94) mm and 1.87 (range from 1.70 to 2.04) mm during dilatation, respectively. Cervical esophagus dilated least with a luminal diameter of 4.78 (range from 4.06 to 5.51) mm. An average thickness of esophagus was 4.70 ± 0.86 mm. Esophageal wall thickness was found to be

significantly larger in males with a thickness of 5.26 ± 0.92 mm as compared to females with a wall thickness of 4.34 ± 0.60 mm.

Literatures show that dimensions of the esophageal tissues differed among humans. Great variations have been found between the previous studies [44–47,49]. In addition, big standard deviations have been presented in each of the study. This could be an indication of the esophageal size variations among human. With the improving imaging techniques, the diameters and the thickness of the esophagus layers can be more precisely measured. One example would be the phase-contrast X-ray CT imaging technique which clearly depicted normal esophageal wall, including the mucous, submucosa and musculature [48] as previously shown in Figure 2.2 (b). These imaging techniques will be very useful in the dimension customization of esophageal TE constructs.

Mechanical properties

The esophagus possesses strong and tough mucosa layer to protect itself against propulsion of the abrasive food or fluid bolus. It must be highly extensible in the circumferential direction to accommodate bolus transportation from the pharynx into the stomach by sequenced peristalsis.

The esophagus is a highly elastic organ exhibiting anisotropic behavior [29,50]. Vanags *et al.* [29] reported that the human esophagus is stronger longitudinally than radially, with average ultimate strengths of 2.19 ± 0.06 and 1.41 ± 0.05 MPa, respectively. However, an opposite trend was observed for elasticity. The esophagus is more elastic circumferentially with an average elastic modulus of 1.44 ± 0.06 MPa, as compared to modulus of 2.30 ± 0.09 MPa in the longitudinal direction. It has lesser mean ultimate strain in the longitudinal direction, 70.0%, as compared to that in the circumferential direction, 82.5%.

Meanwhile, Egorov *et al.* [51] determined the ultimate longitudinal strength of the human esophagus to be 1.29 MPa, and the maximum elongation of 143.4%. Different parts of the esophagus have varying strengths, e.g. the cervical part has maximum ultimate tensile and strain when compared to the thoracic and the abdominal parts [29]. Modulus of the esophagus is compared with other tissues as shown in Figure 2.3 [52–55]. It is noted that the elasticity of muscle is ~ 10 kPa [52]. Meanwhile, the elasticity of full wall thickness tubular tissues lie in between 10^6 to 10^7 Pa range.

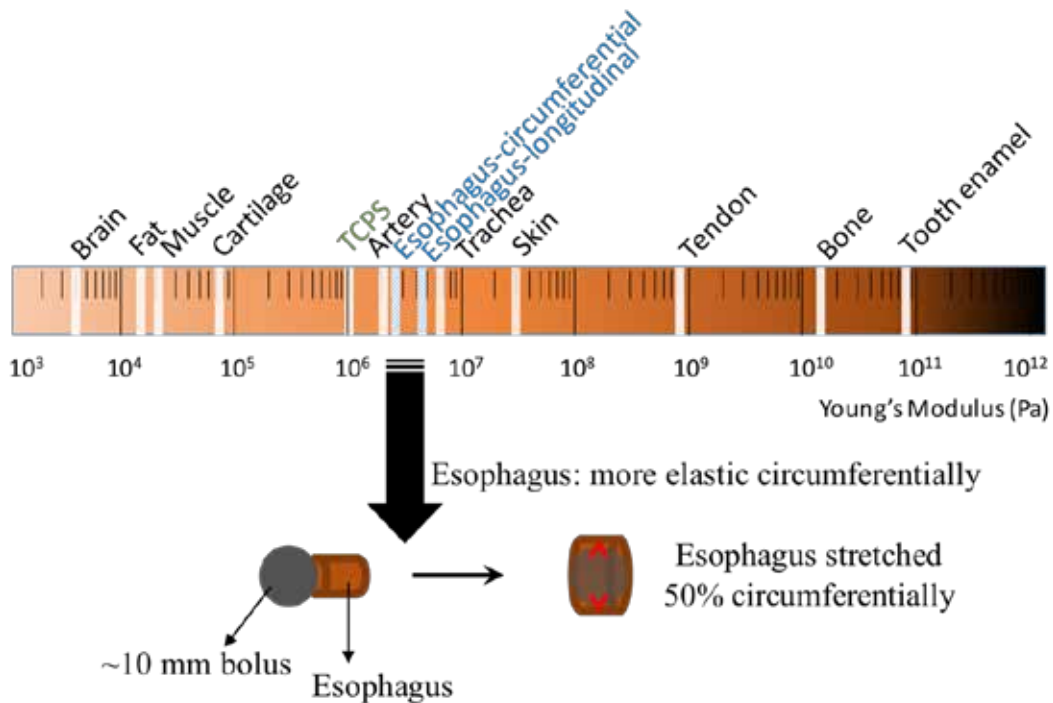


Figure 2.3 Modulus of esophagus in comparison with other tissues and tissue culture polystyrene (TCPS). Esophagus is more elastic in circumferential direction to accommodate normal food bolus of ~ 10 mm.

Vanags *et al.* [29] evaluated the esophageal stress, strain, ultimate strain deformation energy and the tangential modulus of elasticity of healthy human esophagi experimentally in 4 different age groups. A summary of their results is appended in Appendix A. Generally, esophageal stress and strain decrease with

age. Meanwhile the moduli vary among the age groups probably due to the different lifestyle for individuals.

The mucosa and the submucosa layer form numerous folds along the longitudinal direction, which results in an irregular outline of the lumen in the cross section. By pushing in the circumferential direction, these folds are unfolded with no damages [29]. The elastic fibers in smooth muscles and striated muscles provide elasticity to return to the normal state after stretching. The food bolus transportation through the esophagus is largely due to gravity, but also requires peristaltic contraction for its propulsion towards the stomach [35]. The esophagus could be stretched circumferentially by 50% under pressure in the range of 3–5 kPa that was exerted by a food bolus of the normal size of 10 mm [56] as shown earlier in Figure 2.3. The intraluminal pressure for rupture was determined to be 55 kPa [29]. When testing the stiffness of different layers of the tissue, it is the maximum in the mucosa–submucosa followed by the intact esophageal wall and then the muscle [57]. Gregerson *et al.* [58] found that there were significant compressive residual strains in the mucosa–submucosa layers and tensile residual strains in the muscular layers.

The mechanical strength of the tubular wall is largely derived from the extracellular matrix (ECM) components produced by cells, particularly collagen and elastin that exist in the tube wall. Collagens are fibrillar proteins and can give structural support to resident cells [59]. The collagens strengthen and organize the matrix. With the high tensile strength and stiffness imparted by collagen fibers, structural integrity of a tube can remain intact. Meanwhile, rubberlike elastin fibers contribute resilience to tissues [60,61], allowing them to stretch when needed and then recoil back to the original state. In the esophagus, collagen

type IV is secreted by the epithelial cells which forms the junction between cells and the basement membrane. Collagen type I and elastin are secreted by the fibroblasts and muscle cells [61].

2.2 Tissue engineering of tubular organs

“Tissue engineering” is a multidisciplinary field that uses biomaterials with or without the incorporation of cells to regenerate tissues as 'spare parts' [10,62]. The biomaterials served as temporary matrices or scaffolds to support tissue growth [63,64]. Cells are incorporated to stimulate the tissue growth [65]. TE constructs can be implanted in patients to induce the regeneration of tissues, aiming to replace or repair malfunctioning tissues or organs due to disease, trauma or ageing [66]. The structural complexity of the tissues induces enormous challenges to tissue engineering. Additionally, the functionalities of the tissues should be commenced by the TE constructs after implanted.

2.2.1 Requirements: Microenvironment and cell behavior

With decades of efforts and experiences in TE, it is summarized that the tissue-engineered scaffolds should possess: (i) biocompatibility; (ii) macro and micro tissue mimetic structures; (iii) sufficient mechanical properties; (iv) open, interconnected pores and high porosities with appropriate pore sizes; and (v) suitable surface area and surface chemistry [67] as shown in Figure 2.4.

First, the scaffold must be biocompatible. The materials chosen must be non-mutagenic, non-antigenic, non-carcinogenic, non-toxic, non-teratogenic and possess high cell compatibility [67]. The scaffold fabrication method must be carefully selected such that undesirable foreign matters (e.g. porogen, dirt, etc.) and solutions (e.g. organic solvent, detergent, etc.) would not remained in the scaffold. The degraded fractions and monomers of the scaffold should be

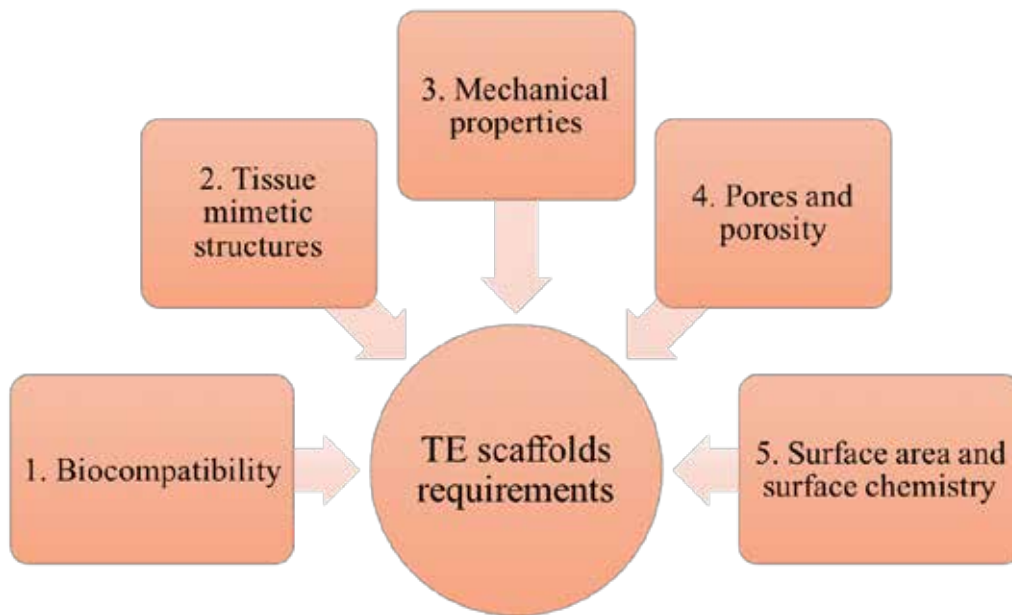


Figure 2.4 Requirements for tissue engineering scaffolds

biocompatible as well, such that they can be metabolized and discharged from the body.

Scaffolds should be made up of the biomaterials with 3D macrostructure that mimics the tissues or organs to be replaced [67,68]. In terms of TE of the tubular tissues, tubes of certain lengths, thicknesses and lumen diameters are required for different patients. For example, esophagus replacement for infant is shorter, thinner, with smaller lumen when compared to the adults. Hence, customization in the fabrication of scaffold is preferred to precisely replace the tissues of the patients. In addition, the microstructure of scaffold should be able to replicate the form of ECM in respective native tissue [69–71]. There are specific alignments of the ECM which affect the phenotype of each cell types that form the esophagus [11,72,73]. These complex cells and ECM orientations construct the proper functionalities and structural integrity of the esophagus. The temporary scaffold with micro- and macrostructural imitation would then guide

tissue regeneration where the healthy tissue will eventually take over the degrading scaffold [67].

The scaffold resembling the physiological functions of the native tissue should be fairly strong to prevent it from rupture or collapse [67]. Retention of adequate strength *in vivo* is especially critical for the tubular scaffold to accommodate stresses and loadings imposed onto it. This can avoid tube collapse that can cause stenosis or narrowing of tubes. Studies suggested that the elasticity of the scaffold ought to be well suited to the surrounding tissue in order to prevent modulus mismatch between them [74]. Other mechanical requirements to tubular tissue replacements include compliant, kink resistant and good suture retention strength. Elastic scaffold with similar compliance to the native tubular tissue would allow fluids or food boluses passing through it smoothly. Kink resistance of the scaffold can prevent it from bending after implantation. Suture-holding capacity of the scaffold is important as it should be sufficiently strong to retain surgical anastomosis. After implantation, degradation of the scaffold ought to be fine-tuned so that it possesses enough structural integrity before the new tissue replaces them [67].

Open, interconnected pores in scaffolds enable nutrients, oxygen and metabolic wastes transportation into, throughout and out of the construct for cell and tissue growth [75]. Scaffolds with high porosities and appropriate pore sizes are of necessities for cell infiltration. For thick tissue regeneration, these pores can enhance vascularization *in vivo*, i.e. formation of capillaries [76], which is critical for long-term tissue survival. Pore size is vital for guiding functional tissue growth. Tubular tissues usually consist of epithelium in the lumen and smooth muscle in the outermost layer. Although there are contradicting studies

that showed that large pore sizes ranging from 150 to 250 μm are good for growth and stratification of the epithelium [77,78], most of the studies have found that submicron pore sizes of 0.1-0.8 μm supports its stratification [79–81]. Meanwhile, the outer layer of the scaffold requires a large pore size ($>50 \mu\text{m}$) [82,83] for vascularization because there is abundance of vascular vessels found in the smooth muscle. In fact, a large pore size of $>400 \mu\text{m}$ is beneficial for the efficient growth of blood vessels [84].

Finally, the scaffold must have suitable surfaces and surface chemistry. A high scaffold surface area to volume ratio is needed for the high cell attachment to accelerate the tissue formation [85]. It also helps to speed up scaffold degradation [86]. Surface properties of the scaffold are important for cell attachment and proliferation [87]. It is vital in cell recruitment and healing at the tissue-scaffold interface *in vivo*. Surface modification is usually performed on the scaffold material if its surface property is not sufficiently satisfactory [88,89]. Some of the TE scaffolds require specific surface chemistry. In blood vessels regeneration, low thrombogenicity of the scaffold surface is usually required [90].

These five scaffold requirements are closely related to each other. Physiochemical properties, e.g. mechanical strength, degradation and pH stability, [91] of the scaffold directly determine the selection of biomaterials as well as processing, morphology and degradation kinetics of scaffold. Although high specific surface area is preferred in TE, the mechanical properties decrease with increasing specific surface area. On the other hand, specific surface area decreases with increasing pore size. Hence, there is no perfect solutions for all the requirements. However, there may exist optimal requirements for TE of a tissue. Based on experiences in regeneration of trachea [24], several criteria can

be summarized as follows: (i) suitable dimensions and shape; (ii) flexible circumferentially but rigid enough to maintain a lumen; (iii) with surface suitable for epithelium and muscle regeneration; and (iv) easy to handle and insert. Among others, these represent the qualities of an ideal esophageal scaffold. Due to its heterogeneity in structure throughout layers, it is almost impossible to regenerate an esophagus using one single TE approach. For example, in epithelium regeneration, pore size and surface continuity are of utmost importance for its stratification to multiple layers; while in smooth muscle regeneration, pore shape is essential to guide tissue growth in certain alignments.

2.2.2 Strategies: Additive, subtractive, and formative fabrication

There are various techniques in producing TE constructs. The techniques can be divided into three broad categories namely formative, subtractive, and additive fabrication as shown in Figure 2.5. The categorization is based on the three main classes of manufacturing [92]. Formative fabrication usually forms objects by casting or molding. Subtractive fabrication involves removal of materials during fabrication of a construct. Additive fabrication describes techniques that form constructs by adding materials, usually layer upon layer [92]. When cells are involved in the TE process, the design of cell incorporation in the TE construct will become very important. Based on observations, there are two different cell incorporation methods, i.e. “concurrent” and “asynchronous” modes. A concurrent method means that the living cells are involved during the TE construct fabrication. For instance, cell sheet stacking [93] and 3D bioprinting processes [94]. On the contrary, an asynchronous method refers to the conventional approach by post cell-seeding on the fabricated scaffolds. The

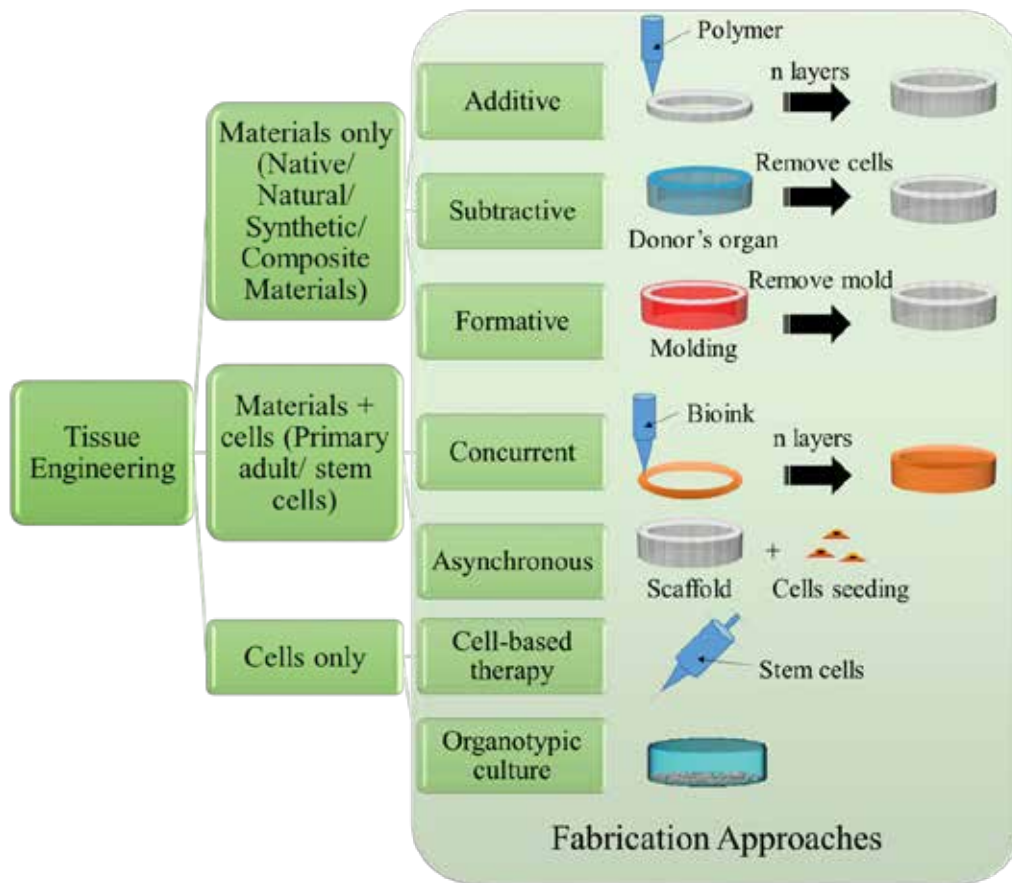


Figure 2.5 Illustration on the classification of tissue engineering approaches.

implementation of asynchronous method highly relies on the scaffold design particularly the pore size for sufficient cell infiltration. Furthermore, it is still challenging to involve multiple cell types within one TE construct. On the other hand, the concurrent method may require a stringent building environment for TE construction such that cells could remain viable throughout the entire process. In addition, there is another category of TE approach that merely employs living cells for regeneration of tissues or organs, in which cell-based therapy [95] and organotypic culture [96] are the two representative techniques. However, this category is beyond the scope of this dissertation work.

Materials that have been used in fabricating scaffolds are categorized in Figure 2.6. These materials have been extensively reviewed [97–99]. The selection of biomaterials usually depends on the biomechanical properties needed

to match to the implantation site as illustrated in Figure 2.7 [100] and the desired degradation time frame (if any).

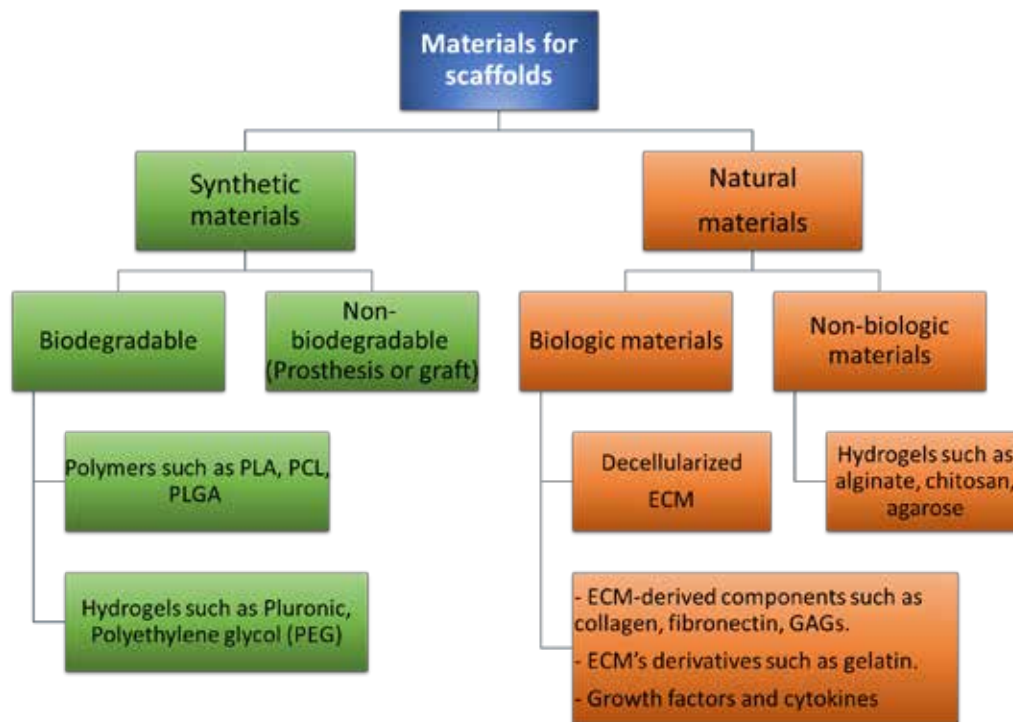


Figure 2.6 Classification of materials for engineering scaffolds

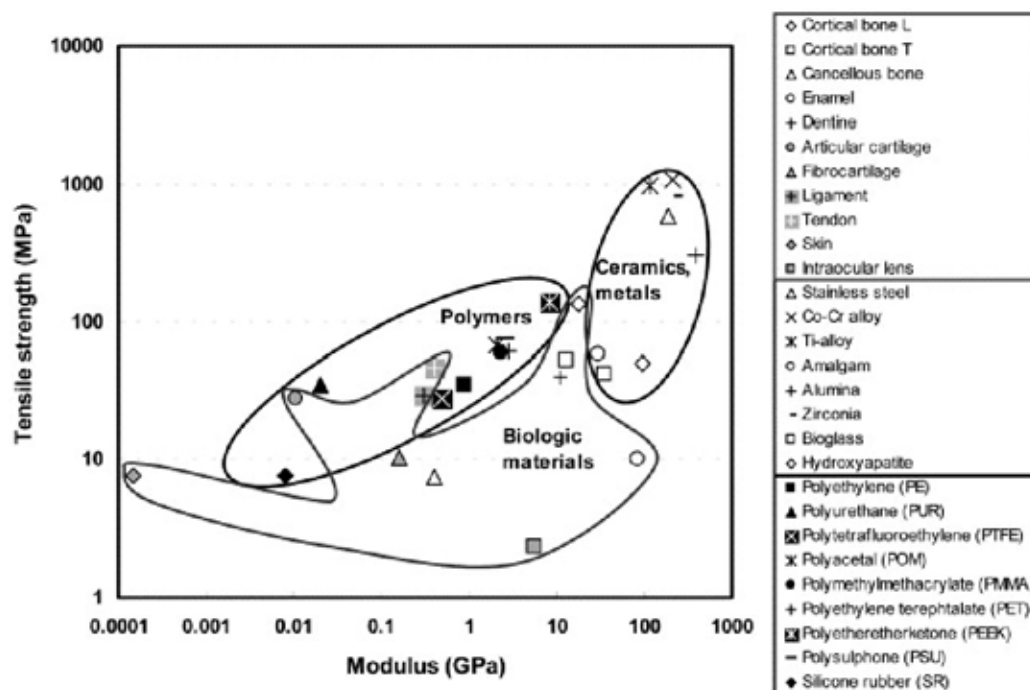


Figure 2.7 Graphical illustration of the material selection based on the modulus and tensile strength matching to the native tissue [100]

Here, only TE of tubular tissues are reviewed. Since tubular tissues are normally soft tissues, the TE methods described below are based on fabrication techniques using soft materials such as polymers (and hydrogels) and biologic materials.

Formative fabrication

Formative fabrication of TE constructs includes injection molding, compression molding [101], polymer precipitation [102,103], melt molding [104], solvent casting [105], gas foaming/high pressure processing (dispersion of a gaseous phase in a fluid polymer phase) [106], extrusion, hydrocarbon templating [107], and combinations of these techniques [77]. Molds or containers are utilized in these techniques to form macrostructure of scaffolds, usually in simple uniform geometries such as tubes. Gelatin, which is essentially denatured collagen, is frequently used to form TE tubes by casting or dipping [108–110]. In most cases, gelatin structure can be stabilized by chemical crosslinking [109,110]. The gelatin used to form constructs usually requires asynchronous cell seeding after scaffold formation as most of the chemicals involved such as aldehydes are not cell-compatible. A concurrent cell-material forming method was illustrated by Twal *et al.* [111]. They cast cell-laden gelatin microcarriers in agarose molds. Cellular microspheres adhere to one another by forming ECM to create 3D tubular constructs. Some other materials can also be used to form TE tubular scaffolds. A similar study reported the fabrication of tubular scaffold by dipping stainless steel rods into silk solutions [112]. It showed that sizes of the TE tubes could be varied by changing the rod dimensions. In their study, however, tubes with inner diameters larger than 2 mm were found to be occasionally

subject to cracking due to the silk drying around the stainless-steel rods after methanol treatment.

Subtractive fabrication

Subtractive fabrication includes removal of porogen or particulate (e.g. salt [102], sugar [113], wax, or ice [114]) [115], cells (i.e. decellularization) [16–18], solvent and even materials (e.g. laser drilling, etching) from the bulk. Porogens and particulates are employed in TE techniques (e.g., particulate leaching, hydrocarbon templating, etc.) to create porous scaffolds [113,115]. These porogens usually can be dissolved easily for pores formation. The pore sizes can be optimized by changing the porogen size [113]. On the other hand, solvents are usually required to dissolve the polymers for process-ability. When removing the solvents, pores will be created within the polymers [21]. Solvent evaporation or phase separation methods, e.g. thermally induced phase separation (TIPS), are also commonly used in creating scaffold porosity [116,117]. Porogens (e.g. ice) and solvents in the scaffolds can also be removed by lyophilizing or freeze drying [114], thus producing porous scaffolds. Laser machining which is used to produce macro-pores [118] or grooves [119] on scaffolds, usually for cell infiltration and alignment, is another effective subtractive fabrication approach.

Decellularization presents a unique subtractive fabrication process. Allogeneic or xenogeneic donor organs are obtained, followed by removing the cells to avoid adverse immune response. It gives an acellular naturally occurring 3D biologic scaffold material which provides the opportunity for direct connection to the patients' vasculature [120]. Decellularization is often applied to TE of tubular organs [121–123]. A successful example of transplantation of

decellularized cadaveric trachea, which was seeded with autologous pluripotent stem cells, was presented [124]. The scaffold maintained the morphological configuration of ECM, which leads to great success in trachea regeneration. Studies have shown that different decellularized matrices were used to regenerate esophagus [18,125]. The biologic esophageal scaffold is usually obtained from human skin (AlloDerm®) [126], porcine small intestine submucosa (SIS) [127] or porcine urinary bladder mucosa (UBM) [128]. The biologic matrices show promising results in supporting cell growth. However, unlike the trachea, it is still challenging currently to achieve a non-collapsible tubular biologic scaffold that can function temporarily for esophageal transplantation [7].

In subtractive fabrication, the removal processes must be cautiously carried out. Incomplete removal of porogens, cells, detergents, or solvents from the scaffolds, especially in thick constructs, will result in harmful residues that can have adverse effects on recipient upon implantation. TE methods that solely rely on subtractive fabrication can only belong to “asynchronous” TE approach, unless very mild subtractive process is used. Unavoidably, in most of the TE construct fabrication process, subtractive fabrication was involved to create interconnected macro- and micro- pores within the constructs. By incorporating subtractive method into the formative fabrication, dip TIPS involves dipping of a metallic template bar into a polymer solution. Polymer foams were produced via subsequent filling of a freezing mixture to induce the phase separation of the polymer solution and then freeze-extraction [117]. Like most of the formative fabrication methods, the dimensions of the tubes can be customized by using different sizes of mold. Another reported method involved the decellularization of SIS, followed by laser machining of micro-pores on the ECM. Then, cross-

linkable hyaluronan-based hydrogel was cast in the laser machined ECM [129] to produce a tubular scaffold.

Additive fabrication

Additive fabrication builds up objects by adding materials, which includes 3D printing [67,130,131], fibrous or textile technologies [132,133], membrane lamination [134], particle sintering [135] and cell sheet stacking [93]. As opposed to most of the conventional TE methods, additive fabrication can produce customized scaffolds. Due to these advantages, additive fabrication of tubular scaffolds will be the focus of this dissertation. 3D printing methods include but not limited to fused deposition modelling (FDM), selective laser sintering (SLS), stereolithography apparatus (SLA), and 3D bioprinting. These additive fabrication methods can maintain high levels of accurate control over their macro- (e.g., spatial form, mechanical strength, density, porosity) and microstructural (e.g., pore size, pore distribution, pore interconnectivity) properties [64,67]. The different 3D printing methods for tissue engineering and their advantages and disadvantages were discussed in the review papers [64,67,131].

Fibrous or textile technologies are very common in fabricating tubular scaffolds [26,136], particularly the electrospinning method [137–140]. It is evident that the tubular fibrous scaffold can be produced with controllable fiber alignment. Although the cell sheet technology presents a promising approach in fabricating vascularized tissues, the process is tedious and time-consuming due to the stacking or rolling of thin membrane layers. In esophageal TE, 2D cell sheet has been implanted and shown epithelization *in vivo* [141]. Nevertheless, tubular cell sheet fabrication for full-length and full-thickness esophageal TE

presents enormous challenge as they are too fragile and too weak to maintain the lumen. A similar example would be the cell-seeded polyglycolic acid (PGA) and poly(ϵ -caprolactone) (PCL) meshes that wrap around silicone tube for the elastic tube regeneration [142]. Thin layers of the cell-seeded meshes or membranes wrapping with great control over timing and skills are essential for tubular TE constructs.

To sum up the various TE materials studied for the esophageal TE, the strengths and weaknesses of these materials are summarized in Table 2. It was mentioned that the dimensions of esophagus vary among individuals. An ideal esophageal scaffold produced by an additive fabrication would serve as a customized organ substitute. This tailor-made scaffold could be based on the CT or magnetic resonance imaging (MRI) scan of the esophagus. FDM [143,144], fibrous or textile technologies [26,137], 3D bioprinting [145,146], and cell sheet stacking [93,147] have been utilized to generate tubular TE constructs. FDM and fibrous technologies represent the asynchronous cell incorporation TE method. They can produce anatomically-shaped acellular scaffolds followed by autologous cells or stem cells seeding before implantation. On the other hand, 3D bioprinting and cell sheet technologies belong to concurrent cell incorporation TE method.

Table 2. Various materials for esophageal tissue engineering

Scaffold type	Materials	Strength	Weakness
Non-absorbable (may couple with absorbable materials such as collagen [148] and AlloDerm [7])	PET, nylon, silicone [148,149], Dacron, self-expanding metal stents [7] Cells: Accelular	<ul style="list-style-type: none"> • Abundant materials • No product degradation and no cytotoxicity • Controlled off-the-shelf product • Reproducible product 	<ul style="list-style-type: none"> • Need stent (and removal) • No tissue regeneration in large defects • Stenosis after stent removed • Might provoke foreign body reaction
Bio-degradable synthetic materials	PGA-collagen [150], Vicryl mesh-collagen [151], PGA, PLA [152], PCL [153], PLC [20,116] Cells: Accelular or Epithelial and/or fibroblast and/or SMCs [77,154,155]	<ul style="list-style-type: none"> • Abundant biomaterials • Reproducible fabrication • Biocompatibility • Resorbable biomaterials • Wide variety of polymers • Possibility to control microarchitecture 	<ul style="list-style-type: none"> • Necessity of surface modification such as to cover polymer surface with coating of collagen • Lack control of degradation • No similarity component to the native tissue • Toxicity or acidity of products degradation • Scaffold architecture depending on the nature of fabrication • Control of variable types of fabrication
Biologic materials	Porcine's UBM, SIS [17], Human-derived AlloDerm [77] Cells: Accelular [156] or Stem cells especially BMSCs [18] or Epithelial and/or fibroblast and/or SMCs [16]	<ul style="list-style-type: none"> • Mimic the native tissue • Similar architectural environment as the native tissue • Mechanical properties similar to the native tissue • No immunogenicity if properly decellularized • Possibility of cells seeding with stem cells for controlled <i>in vitro</i> and <i>in vivo</i> differentiation • Industrial process (e.g. AlloDerm) 	<ul style="list-style-type: none"> • Possibility of cytotoxicity (chemical decellularization) • No standardized evaluation of immunogenicity • Lack of study for decellularized esophagus matrix for human transplantation • Heterologous matrix
<p>Legends: PET: Polyethylene terephthalate; PGA: Polyglycolide; PLA: Polylactide; PCL: Poly(ϵ-caprolactone); PLC: Poly(L-lactide-co-caprolactone); UBM: Urinary bladder matrix; SIS: Small intestinal submucosa; AlloDerm: Decellularized human dermis; SMCs: Smooth muscle cells; BMSCs: Bone marrow stem cells</p>			

There are specific phenotypes and alignments of each cell type that form the tubular tracts. In the esophagus, these complex cellular compositions construct its proper functionalities. Although the heterogeneity of the esophagus in terms of location, function, and tissue variation impedes the efforts in TE, substantial efforts have been made over the last decade to regenerate the tissue. TE esophageal scaffolds are used to mimic its vital function of peristalsis. While degradation of the scaffolds proceeds, it is envisioned that the newly formed tissue can restore the function of peristalsis, together with the other important functions e.g. the secretion of mucous by the esophageal mucosa which provides lubrication for the transportation of food bolus.

Most of the studies have focused on the regeneration of the smooth muscle [17,72,155] or the epithelial lining [14,77,153,157,158], or these both layers [159] of the esophagus. These were also applied for the other tubular tissues such as the rest of the gastrointestinal tract (GI tract) [6]. Taking these into account, the proposed strategy in this dissertation for esophagus TE shall be based on the approach of assembling these two heterogeneous components *in vitro*, which could be assimilated to construct a composite hybrid tissue for *in vivo* implantation.

2.3 Tissue engineering of musculature: Biomimetic fibers for cell alignment

Nakase *et al.* demonstrated the thoracic replacement of *in situ* tissue-engineered esophagus in a canine model [25] by using oral keratinocytes and fibroblast cultured on human amniotic membrane. These were attached to SMCs seeded on a PGA felt. However, an absence of peristalsis was observed in the

tissue engineered esophagus segment due to the lack of orientation of SMCs and the missing enteric nervous system.

In the esophagus, it is known that there are two different layers of muscle in the muscularis externa. Esophageal peristalsis primarily results from sequential contraction of circumferentially aligned muscle. Longitudinal muscle may also play a role [160] but is less critical when compared to the circumferential muscle. The muscle layers consist of SMCs or skeletal muscle cells together with ECM fibrils that have significant orientations to provide sufficient mechanical strength to withstand the pressure of food bolus and fluid.

Smooth and skeletal muscles are formed into highly organised and hierarchical tissues. Creating and maintaining cell morphology have been a challenge in TE of muscles [72,161,162]. Heterogeneity and phenotypic changes in SMCs are usually accompanied by morphological difference, i.e., elongated/spindle-like versus spread-out or epithelioid/rhomboid cell shapes [162]. Elongated SMCs retain its phenotype with expression of muscle-specific genes [163]. Similarly, when myoblasts grow in random swirling patterns, they are not conducive to the formation of efficient muscle contraction [164,165]. These muscle fibres must grow in parallel to one another with identical anisotropy. Among the additive fabrication methods, one of the most straightforward way to create elongated muscle cells and 3D cell alignment is via techniques that can form microfiber alignment. The reason is because it has long been known that the topography of a scaffold can affect these aspects of the cellular response. When placed on fibers of certain dimensions, many cell types align themselves in the direction of the fibers. This phenomenon is termed “contact guidance”. By contrast, a randomly distributed topography such as a

porous surface is unlikely to align cells in a desired direction. Additionally, when compared to grooved flat sheets, fibrous scaffolds can provide 3D cell alignment throughout the thickness of the constructs.

2.3.1 Fibrous scaffolds for cell alignment

Researchers have demonstrated that the fabricated scaffolds should consist of a high density of aligned muscle cells to regenerate functional muscular tissues [83,161,166]. Hence it is desired that scaffolds are designed to (i) support cell–cell interactions and (ii) guide cell alignment for mimicking the tissue structure.

Fabricating fibrous polymer scaffolds is one of the promising approaches for cell alignment as the fibers are geometrically similar and could duplicate the properties of these natural tissues. Meanwhile, aligned fibrous scaffolds can be designed to provide directional cues for cell migration and to enhance regeneration of oriented tissues [70,167,168]. Pre-alignment of the cells assists in the increase in muscle fiber formation and content [169]. After sufficient time for cell proliferation, the parallel fibers could also form high-density cell constructs, implying potential ability for muscle tissue regeneration.

In fibrous scaffold fabrication, the fiber diameter [170–172] and the fiber alignment [70,167,168] are the two most studied topics to achieve cell alignment among the others, such as the fiber surface roughness and texture [173], the fiber surface modification [168], the geometrical fiber spacing [132], and the scaffold mechanical strength [174]. In fact, all these design factors together with the engineering limits are equally important in TE applications.

Studies indicated that there was a fiber diameter range beyond which the cells would not be able to align to the fiber diameter. It was reported that the

human skeletal muscle fibers ranged from 5 to 100 μm in diameter [175], which could be an indication for the desired fiber diameter of TE muscular scaffolds. Charest *et al.* [176] reported that when culturing myoblasts on 5 to 75 μm grooves, significantly high cell alignment was observed on the grooves with widths of 5 to 25 μm . Neumann *et al.* further showed the high alignment of myoblasts cultured on fibers of 10 to 15 μm in diameter [132]. Hwang *et al.* demonstrated that when PLGA fiber diameter was greater than 80 μm , cells directionality did not exhibit preferential orientations [177]. On the other hand, when the fiber diameter fell below 0.97 μm , cells would react as if they were grown on flat surfaces [178]. Hence it can be concluded that when the fiber diameter fell in the range of \sim 1-80 μm , the integrin receptors could follow the edge of the fiber contour. Furthermore, small circumference of 1-80 μm fibers in diameter gave the cells little choice but align with the axis of the fiber [132,176]. Hence, due to the contact guidance provided by the fibers, fibers with the appropriate diameter can induce muscle cells to align along the fiber direction. When aligned on microfiber surfaces, SMCs demonstrated elongated morphology, significantly lower cell and nucleus shape indexes, less spreading, and a lower proliferation rate [162], which indicated the growth of normal SMCs phenotype. The substrate topology can guide muscle cells' orientation and control their shape, which is desirable for the reconstruction of functional esophagus.

Fiber alignment is another important feature that can influence cell response and tissue formation and, hence, determine the performance of fibrous scaffolds in TE. It is worth noting that aligned fibers is very useful for the tissue engineering of muscle tissues because of the similarity between the aligned topography of the TE fibers and the aligned topography of the fibers in the natural

ECM of these types of tissues. The elongated nature of muscle cell focal adhesions would favour their lengthwise formation on ridges. The attached actin filaments would then be oriented along the aligned fibers and grooves [179]. Aligned fibers can enhance cell infiltration into 3D scaffolds *in vitro* and *in vivo* [168]. This is because the oriented cells did not become confluent as quick as on the spun cast film. Cells cultured on randomly aligned fibers would be confluent on the bulk surface, which will prevent the subsequent cell infiltration into the scaffolds. Thus, cell proliferation was improved by fiber alignment. Fiber orientation was also shown to affect cell migration [178]. Xu *et al.* [180] found that SMCs attached, aligned and migrated along the axis of the aligned fibers and expressed spindle-like contractile phenotype; the distribution and organization of smooth muscle cytoskeleton proteins inside SMCs were parallel to the direction of the fibers; the adhesion and proliferation rate of SMCs on the aligned fibrous scaffold was significantly improved than on the plane polymer films [180]. These aligned scaffolds can influence the cells growth and morphology, and hence influence the gene expressions and increase the ECM secretion [70].

Highly anisotropic topographic features have been shown to induce many cell types to align and migrate along the direction of the anisotropy [181]. Fabrication of microfibers within ~1-80 μm with highly oriented fibers results in scaffolds with inherent anisotropy. A cell would be limited to lengthwise spreading and movement on the fiber [182]. The fiber surface is the only solid surface, where the cells can only grow directly on the fiber surface or on top of the cell layer. In addition, the space between fibers is essential for cell ingrowth and proliferation. Aligned microfibrinous scaffolds, which can provide sufficient

space in their layered structure, gave more room for cell ingrowth when comparing to submicron or nano-fibrous scaffolds [177].

In the medial layer of the arteries and the endomuscular layer of the GI tract, the SMCs and collagen fibrils have a circumferential orientation to provide the biomechanical strength necessary to withstand the high pressures existing in the circular motion. Both the structural integrity and physical activities of the tissues are dependent on the SMCs and fiber orientation. Hence, it is believed that with a scaffold topography that can imitate the native tissue, together with the induced alignment of SMCs, can lead to the great improvement of the tissue regeneration speed and the high probability to long-term success of implant.

2.3.2 Fibrous scaffold fabrication techniques

It is common to fabricate scaffolds based on fibers for the TE purposes. These fibers are then combined to form 3D patterned tissue constructs, with purpose in creating cell alignment and mimicking native ECM. Aligned microfibers within a range of ~1-80 μm [177,178] have been shown to provide 3D cell alignment while submicron and nanofibers are increasingly being used to imitate the ECM of native tissues [183]. Fiber diameter along with the technique to construct itself are the most important design concerns TE to geometrically and spatially replicate native tissues. Different scales of fibers are required for different applications, depending on the tissue's geometrical and mechanical properties. The fiber diameter and the scaffold fabrication technique also affect the spatial arrangement of the fibers and hence the macro-scale mechanical properties and tissue fusion. Besides, both the individual fiber diameter and the topological constraints (the gap between the fibers) have effects on the cellular level as it can influence the individual response of cells. Therefore, the effects of

various fibers fabrication techniques and their processing parameters on fiber diameters have attracted considerable attention.

TE fibrous scaffolds can be made of (i) natural biomaterials e.g. collagen [184,185], alginate [186] and peptides [187]; or (ii) synthetic biomaterials e.g. polylactides (PLA) [188,189], PCL [190], and PGA [133]; or (iii) their composites [191], which are of benefit for creating tissue constructs. The materials were categorized based on three types of fiber fabrication, namely the thermal-based, solution-based, and self-assembly techniques as illustrated in Figure 2.8.

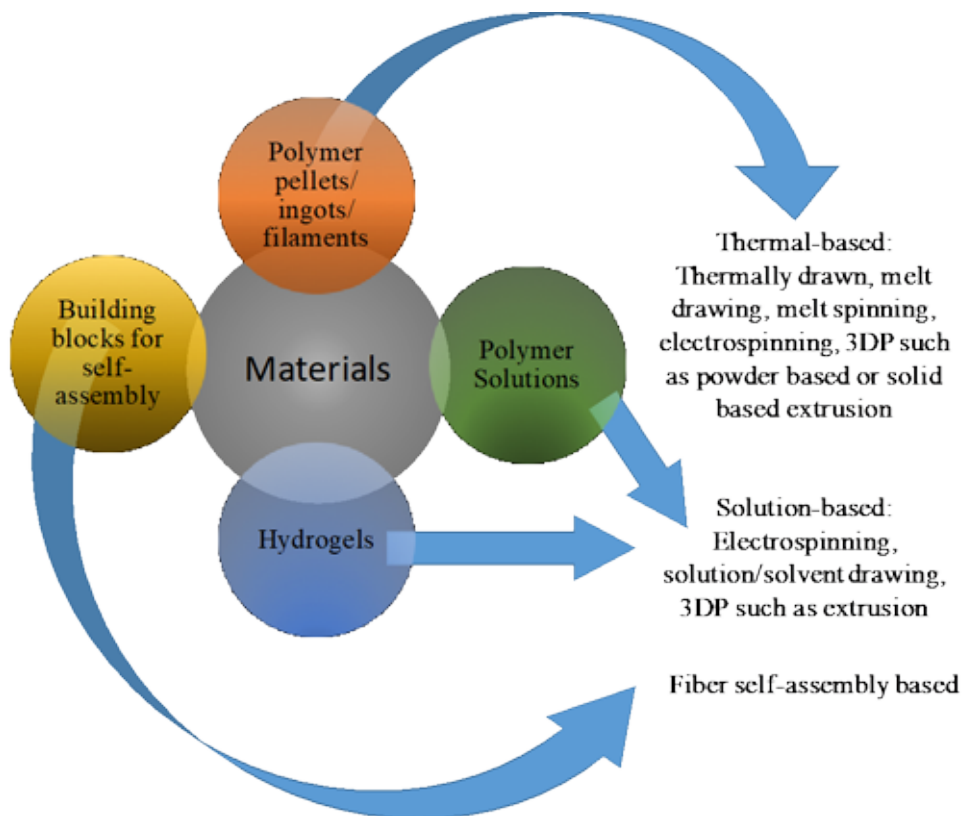


Figure 2.8. Classification of different fibrous scaffold fabrication techniques based on the form of raw materials

These fibers can be fabricated using either the bottom-up or the top-down approaches. The bottom-up approaches utilize monomers or short peptides to build up the fibrous polymers [187], while the top-down approaches employ

polymers, either in melt or solution forms, to form the fibers. Various approaches like fiber drawing [192], template synthesis [193], fiber-bonding [133], self-assembly [187,194], melt-blowing [195], melt spinning [188,189], centrifugal spinning [196], microfluidic spinning [177,186] and electrospinning [76,197] have been successfully used for bioengineering of fibers. Most of these approaches can form fibers layer by layer and hence can be exploited to form 3D constructs using the additive fabrication method. In some cases, cells and/or bioactive components can be added between the layers of the fibers and/or within the fibers [192] for TE applications. These fiber fabrication technologies provide the methods to make various forms of 3D scaffolds.

2.4 Tissue engineering of mucosa: Biomimetic scaffolds for epithelium stratification

2.4.1 Esophageal mucosa tissue engineering

The stratified squamous epithelium lining of the esophageal mucosa serves as a barrier or a protective layer to the underlying tissues. Studies have found that the epithelial component in esophageal reconstruction is necessary to avoid stenosis and to facilitate the healing process [198,199]. Hence, regeneration of the epithelium has been highlighted in esophageal TE. Epithelial cells are located within a specialized ECM of the basement membrane [200]. Basement membrane of the esophagus mainly consists of type IV collagen and laminin [73]. It appears like a multiple nano- and submicron- scale “Velcro” that holds the epithelial cells in place [201], where the cell borders are demarcated. Cells are stratified into ~20 layers [154] towards the luminal surface, forming mosaic patterns at the lumen [202]. Epithelium is avascular with a thickness of ~270 μm thick [46]. It exists near vascularized connective tissue i.e. lamina

propria which contains an abundance of ECM and a diverse population of stromal cells, e.g. fibroblasts. Epithelium and connective tissue are functionally interdependent units [200]. The lamina propria together with the underneath thin muscularis mucosa are ~300 μm thick [46]. These two layers together support the epithelium.

The submucosa is ~ 130 μm thick [46] in the esophagus. The mucosa and submucosa layers are inseparable physically, but are not strongly bonded to the muscularis extern. The mucosa and submucosa are folded at its luminal surfaces along the circumferential direction as shown in Figure 2.9 during contraction of the muscle *in vivo*. They are also folded when there is no active muscle contraction or external loading [203]. The folding is due to circumferential buckling [204] and is commonly referred to as the “mucosal folding”. Mucosal folding plays important physiological roles. It is a common phenomenon observed in several tubular organs, such as in airways [204], blood vessels [205], Eustachian tubes and GI tracts [206].

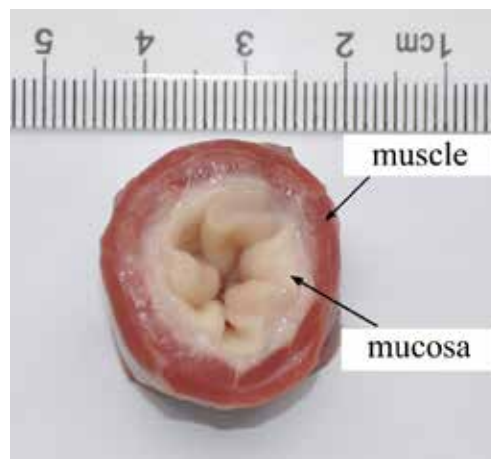


Figure 2.9 Bovine esophagus showing the mucosal folding [206]

The regeneration of esophageal epithelium is always focused on the biomimetic TE of basement membrane for the population of epithelial cells

followed by stratification of the epithelium [153,158]. Flat polymer sheets or membranes have always been the focus in basement membrane regeneration. The flat sheet should be cell impermeable but nutrients permeable. It was found that tissue-engineered basement membrane containing pores in the diameter range of 0.1–0.8 mm supported superior epithelium stratification and protein deposition. On the contrary, tissues on the non-porous surface or surfaces with pores of larger than 1.0 mm had low level of stratification [207]. However, there is also contradicting study showing that the larger pore sizes of 150–250 mm as compared to 38–75 mm result in increased stratification and improved construct morphology with better connectivity between regions of cells [77]. In their study, Beckstead *et al.* showed that AlloDerm, the decellularized human skin showed superior morphology compared to the synthetic scaffolds. The synthetic polymeric scaffolds showed some stratification but still lacked a continuous epithelial lining [77].

Decellularized biologic scaffolds which represent subtractive fabrication were studied for the epithelium stratification. Esophageal epithelial cells that were seeded on the scaffold stratified into three, four layers inside the decellularized esophageal matrix [16]. Epithelial cells were also seeded on collagen sheets [208,209] and Alloderm [77] for their growth and stratification. To study the interaction between esophageal epithelial cell and scaffolds, salt-leached and gas-foamed esophageal scaffolds were fabricated to observe epithelium morphology, continuity and stratification [77]. The scaffolds showed regions of stratification and correct epithelial microstructure.

Among the additively fabricated TE constructs, electrospinning has been widely utilized for esophageal epithelium TE due to their morphology and size-

scale similarities with the native basement membrane [14,21]. These scaffolds were found to be beneficial for epithelium stratification. Oral mucosa cell sheet patch was successfully stratified *in vitro* for esophageal mucosa regeneration [141]. Oral epithelium was chosen over esophageal epithelium owing to the ease of cell extraction.

It is difficult to fulfill properties and dimensions customization of scaffolds with subtractive fabrication. To date, all the reported additively fabricated esophageal epithelium TE constructs were in the form of flat sheets. In practice, it has many technical difficulties to create a tubular epithelium construct. Moreover, the epithelium as well as the lamina propria, muscularis mucosa and submucosa are folded in the esophagus. These features are far too intricate to be replicated simply with folding flat sheets.

2.4.2 3D bioprinting methods

Tubular TE constructs can be fabricated using various methods but mucosal folding is not easy to be replicated. Furthermore, esophageal epithelial cells are to be seeded on the luminal surface of the scaffolds. The luminal dimension of human esophagus is very small as stated in Section 2.1.2 [45]. Seeding of epithelial cells in the folded tubular lumen is exceptionally challenging. Problems such as low seeding densities, limited cell adhesion, and incomplete cell coverage on the scaffold can be foreseen. However, 3D bioprinting may provide a viable solution to these problems. Mucosal folding could be reconstructed from the CT images. In addition, as cells are embedded in bioinks, cell seeding is not needed after the construct is built. A schematic drawing to compare between the conventional 2D membrane culture of epithelium and the new 3D bioprinting approach is illustrated in Figure 2.10. It

is challenging to roll the flat sheet of cells into a tubular form without damaging the cellular construct or harming the cells in it. Meanwhile, folded mucosa could not be achieved yet using the conventional methods. It is possible that 3D bioprinting may be able to regenerate the 3D folded epithelium.

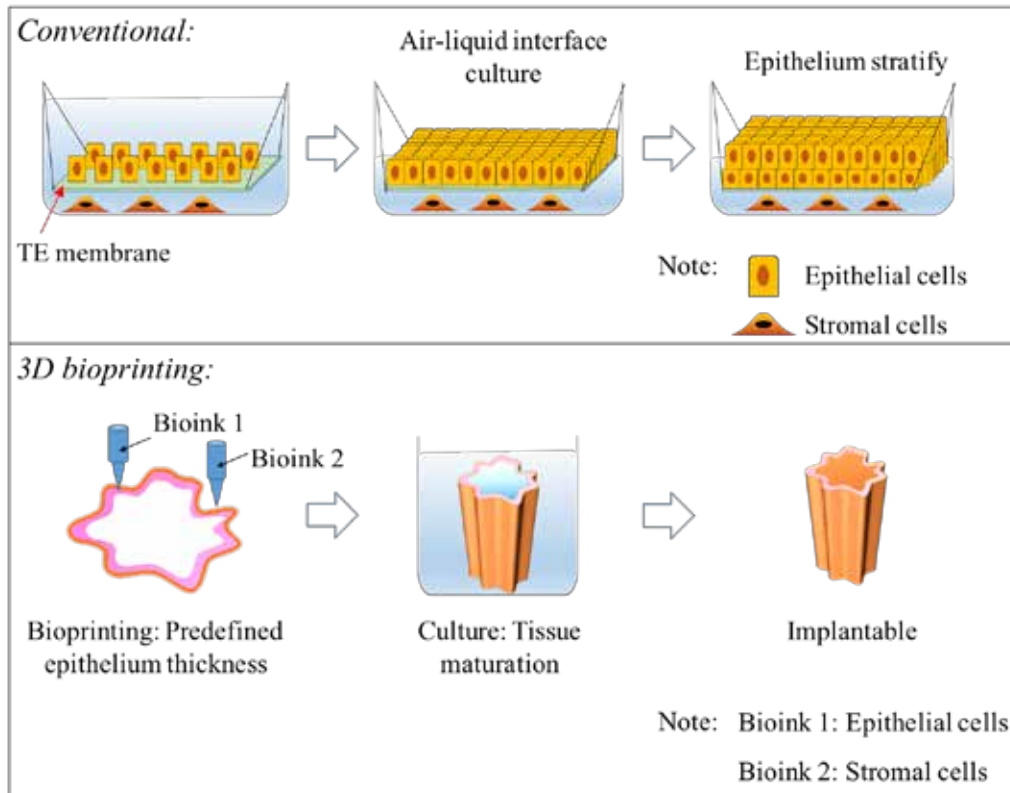


Figure 2.10. Schematic illustration of the conventional TE of flat membrane and the new 3D bioprinting approach for epithelium regeneration

3D bioprinting is a relatively new field that combines the knowledge of TE and 3D printing [94]. It is the layer-by-layer spatial patterning of living cells together with biologics and/or biomaterials with a prescribed organization, forming a 3D living cellular construct [94]. It is a highly challenging process as living cells must be delivered in each bioprinted layer without drastically affecting the phenotype and viability of cells. At the same time, the biological constructs should be self-supported without collapsing. 3D bioprinting has been used to create the air-blood barrier as a lung epithelium model [210]. The air-

blood tissue barrier analogue was comprised of endothelial cells, basement membrane and epithelial cell layers, which could be used as a 3D lung model for drug testing. Nevertheless, this model was still based on a flat sheet that was not desired for 3D tubular organ TE.

One main advantage of 3D bioprinting is the high cell density distributed within the construct. Moreover, there is a high degree of freedom in designing the spatial distribution of different types of cells. There are generally three different types of bioprinting methods, namely extrusion-based, inkjet-based and laser-assisted based [94]. Among these techniques, the extrusion-based 3D bioprinting is widely studied because it enables the precise fabrication of complex structures; facilitates the patterning of multiple types of cells; and allows high cell density printing. Extrusion-based 3D bioprinting usually utilizes bioinks of the cell-laden hydrogels or the high cell density tissue spheroids or tissue strands.

The cell-laden hydrogel constructs are generally too weak to be handled unless strong cross-linking agents are utilized but these are usually not favorable for cell printing process. There are two general types of hydrogels used in bioprinting as reported by literatures. One is a thick hydrogel that possesses shear thinning properties for smooth extrusion [211]; another one is a less viscous hydrogel that relies on cross-linking [212] to strengthen the hydrogel construct upon printing. It is difficult to load cells with high density for the first method, while the latter needs special design of the hydrogel such as an addition of methacrylate functional group for ultraviolet (UV) crosslinking [213]. However, environmental stresses e.g. UV irradiation may induce deoxyribonucleic acid

(DNA) damage to cells if the process is not well-controlled, which can result in apoptotic cell death [214].

Tissue spheroids or tissue strands can be fused together as building blocks, allowing the high initial cell density, without using any scaffolds. An example of scaffold-free bioprinted construct is the vascular tubular tissue created by Itoh *et al.* [146]. Briefly, they “skewered” 500 spheroids ($\sim 2.5 \times 10^4$ cells per spheroid) into a 9x9 needle-array according to a 3D CAD model. Prior to perfusion culture, the needle-array was removed after 4 days of static culture. The printer utilizes needles as the skewer to aggregate the spheroids into a 3D shape.

One distinct advantage of the bioprinting strategy using scaffold-free spheroids is that it could expedite tissue organization. However, the scaffold-free bioprinting process requires rapid tissue maturation so that any shrinkage of the construct is minimized, and the shape, tissue composition and integrity are well-controlled. Furthermore, a very high initial cell number is needed for the fabrication of scaffold-free tissue spheroids/strands for tissues bioprinting. The printing of small vascular tubular tissue of 1.5 mm in diameter and 7 mm in length aforementioned needs an initial cell number of $\sim 1.25 \times 10^7$ [146]. Scaling up tissue constructs will require a tremendous number of cells that must be extracted from the patient; otherwise the primary cells should be greatly expanded *in vitro* in laboratory, which is unrealistic currently as each type of cell has its passage limitation [215].

It was initially thought that the solid scaffold-based TE methods and the solid scaffold-free bioprinting approaches are difficult to be integrated [216]. However, bioprinting approaches utilizing solid scaffolds as support are recently presented by Kang *et al.* [217] and Jung *et al.* [218]. 3D printing of solid PCL

scaffolds was accomplished simultaneously with the cell-laden hydrogels. Stacking of the bioprinted constructs becomes feasible when they incorporated 3D printing of scaffolds into bioprinting. The printed construct also become stronger with the PCL scaffolds. However, thermoplastic polymer was melted at elevated temperatures (e.g. PCL at ≥ 60 °C) and then deposited onto the previous layer containing cell-laden hydrogel, which may induce adverse hyperthermia effects to some cells [219]. PCL represents the only choice in the scaffold printing because it has a lowest melting point of 60 °C among the commonly used biopolymers. PCL degrades over a long period of ≥ 2 years [220] and the cell number per unit volume of the bioprinted construct is comparatively low in this case.

2.4.3 Cell sources for 3D bioprinting

The ability to extract, isolate and expand esophageal epithelial cells is a prerequisite for cell-seeded scaffolds. However, it is obviously very challenging to obtain a huge amount of healthy esophageal epithelium from the patient. Without using xenogeneic animal-derived feeder cell layer, cultivation of epithelial is arduous [141]. Contamination of fibroblastic cells are a main concern in culturing and passaging epithelial cells [22]. The esophageal epithelial cells are cuboidal in morphology and connected to each other by tight junction in nature [200]. Once the change in their morphology and phenotype occurs during passage, the cells are already being contaminated. Depending on the cell origin and culturing techniques, primary esophageal epithelial cells could be passaged up to 3-12 passages [16,22,221].

The difficulty in culturing primary epithelial cells has shifted the research focus to TE using stem cells. Embryonic stem cells have been investigated in the

stomach tissue engineering. In one report, *in vitro* 3D gastric tissue was developed, starting with embryonic stem cells and involving a multistep differentiation process. The generated stomach tissue exhibited a differentiated epithelium that demonstrated the capacity to secrete pepsinogen and gastric acid [222].

MSCs are another type of attractive cell source which can be easily derived from bone marrow or adipose tissue. There are now several reports reporting that bone marrow MSCs can repopulate gastrointestinal epithelial cells and mesenchymal lineages in animals and human [18,41,223]. In one of the studies, decellularized rat esophagus graft was seeded with autologous MSCs and implanted to replace 15 mm of resected esophagus. Results showed that the cell-seeded scaffold promoted re-epithelialization, revascularization, and muscular regeneration as shown in Figure 2.11 [18]. As similar study was found in canine model [223] whereby MSCs seeded on decellularized scaffold successfully regenerated the muscular layer and mature epithelium. Patency was maintained in both cases as epithelium and muscle tissues were regenerated.

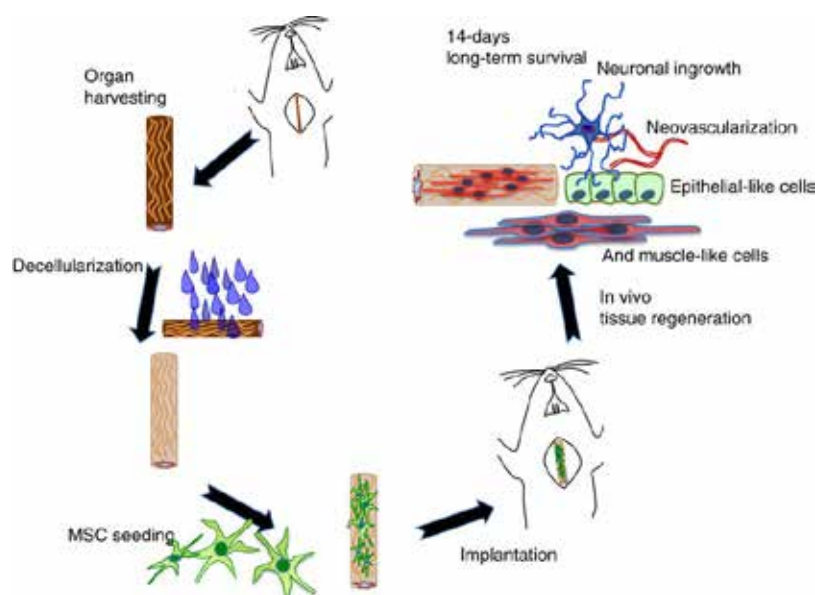


Figure 2.11. Schematic illustration of the use of MSC to seed on decellularized donor esophagus [18]

A porcine-derived urinary bladder matrix was sutured in the full-thickness mucosal defect under the muscle in a mouse model [224]. After 8 weeks, the bone-marrow-derived cells populated within the construct have repaired with the matrix, which showed complete regeneration of the epithelium. These bone-marrow-derived cells are thought to participate in the re-modelling process. Nevertheless, the mechanism is yet to be understood and the precise identity of the recruited cells at the site of injury also needs to be properly established. The implants showed no signs of leakage or stricture. Krause *et al.* [225] found the bone-marrow-derived epithelial cells in the GI tract after transplantation of a single hematopoietic bone marrow stem cell in the mouse. Hence, there exists the possibility of regeneration of a failing organ by transplanting an individual's own bone marrow stem cells to colonize and repopulate the diseased tissue, thus avoiding the allograft reaction [41].

2.5 Summary

Based on the reviewed literatures, the TE construct for esophageal bioengineering should consist of multiple layers to mimic the inherent diversity in structure of native esophagus.

To aid the regeneration of smooth and striated muscles in the outer layer, a highly-aligned scaffold that provides a template for cell orientation could be used to encourage organization of smooth muscle or myoblasts. Elongated muscle cells could retain their phenotype. The microfibers that are to be fabricated should be within a range of ~1-80 μm [177,178] with highly oriented fibers. This results in scaffolds with inherent anisotropy and assists in contact guided cell alignment. In addition, the microfibers must be aligned to form 3D tubes. Mechanical properties of the tubular scaffolds are of significance for

esophageal TE. They should be elastic circumferentially to allow propulsion of food bolus and keep a lumen while contracted. However, most of the reported esophageal TE methods created flat sheets, which were then folded up to form a tube. These constructs need considerable design effort at the joining area to prevent failure such as interfacial failures. Dimensions of esophagus together with its mechanical and physiological properties vary with age, gender and lifestyle. Hence, dimensions and mechanical properties of the tubular scaffolds should be properly considered in attempts to engineer the esophagus. Elastic scaffolds were reported for esophageal TE but have not reported to be able to tune their elasticity. An engineering method that has great flexibility and versatility would be great in regenerating tubular scaffolds with different dimensions and properties.

The squamous non-keratinized epithelium lining at the esophageal lumen shields the underlying tissue from abrasive action of the food bolus movement, as well as protects it against the ingress of a range of potentially harmful environmental agents such as microbial toxins, enzymes, refluxing stomach acid, antigens and carcinogens from food and beverages [32]. The epithelium layer also protects the underlying tissues against fluid loss. When food bolus passes through the esophagus, the mucosa folds are unfolded by pushing in the circumferential direction with no damages [29]. Thus, the epithelium is one of the most important layers to be regenerated in TE. Epithelial cells should be involved in the mucosa regeneration so that the TE construct will be functional without stenosis upon implantation [153,154,209]. Due to the difficulties in cells seeding in folded lumen, 3D bioprinting could be a viable and convenient solution in TE of folded epithelium.

Chapter 3. Bioengineering of esophageal musculature:

Fabrication of elastic, aligned microfibrinous scaffold

3.1 Introduction: Techniques and biomaterials evaluation

After evaluating all the fiber fabrication techniques, it was decided that techniques utilizing potential harmful subtractive fabrication techniques were not considered to create the scaffolds. For example, porogens and toxic organic solvents removal should be avoided in the fabrication process. Fabrication techniques that could precisely control fiber diameters were preferred over those techniques that produced random and uncontrollable fibers with a wide range of diameters. For example, electrospinning that would produce fibers that are highly sensitive to environmental control thereby often producing fibers with broad diameter distributions [226] would not be considered for uniform or aligned fiber fabrication. Concerning the advantages and disadvantages, a melt-drawing method which required only bench-top equipment and was less sensitive to external environment was exploited.

Melt-drawing method was realized using a table-top device built in-house previously. Rounded filament could be fabricated with low variability due to slow fiber drawing speeds. Floor space required is minimized when compared to other big machines such as conventional melt-spinning machines. Melt-drawn fibers can be used to fabricate polymeric tubular scaffolds via a layer-by-layer manner based on the concept of additive fabrication. This technique offers several advantages over the other TE methods. One of the main advantages is its capability to produce highly aligned fibers, which shows high potential to provide the 3D alignment of cells. Customization of scaffolds' size and shape could also

be achieved. Another distinct benefit of using this technique is that no undesirable toxic solvents or chemicals are used, which eliminates the risk of incomplete solvent extraction from the scaffolds. Tubular scaffolds can be formed in a single step without subsequent knitting or porogen removal. Its additive fabrication nature also results in minimal waste produced during the fabrication. It is a green scaffold fabrication technique and at the same time cost-effective.

The esophagus performs function of peristalsis. Thus, the engineered esophagus should be able to temporarily function in propulsive bolus transportation. This propulsive component is dependent on the elasticity of scaffold to enable the return of tissue engineered esophagus to its normal shape once a bolus has passed through. Among the commercially available biomaterials, copolymers of poly(L-lactide) (PLLA) and poly(ϵ -caprolactone) (PCL), i.e. PLC, have been used widely in the TE of elastic tissues. The properties of PLC copolymers, such as their biodegradation rate, mechanical behavior and thermal properties, are considerably influenced by the composition, distribution, and block sequence lengths of both L-lactide (LA) and ϵ -caprolactone (CL) monomers. For example, PLC can vary from elastomeric to glassy thermoplastic, depending on the tunable composition and chain microstructure [227]. When tuned suitably, PLC combines the advantage of the soft PCL together with the strong and hydrophilic PLLA, thus exhibiting rubber-like elasticity and shape memory properties [228]. Since most of the tubular organs including esophagus exhibit certain elasticity for fluid and/or food bolus flow, elastic PLC is thought to be a suitable material for esophageal TE. The melt-drawing fabrication process

together with the PLC biomaterials chosen can achieve the required mechanical properties of scaffolds.

This chapter describes the exploration of whether elastic PLC can be formed into tubular scaffolds by using the melt-drawing method described in this section. Due to the viscoelasticity and the stickiness of PLC, intact tubular scaffolds are supposed to form without any subsequent post-processing such as knitting. The *in vitro* biocompatibility will be systematically studied to further verify if this PLC scaffold is favorable to cell growth and alignment. The fabrication process will not involve any additional materials hence it would be biocompatible. As no additional locking mechanisms and extra gluing materials exerted in other directions, it is hypothesized that the melt-drawn microfibers would have the capacity to guide cell alignment along the fiber direction.

3.2 Materials and methods

3.2.1 Materials and sample preparations

Pristine PLC pellets with LA to CL with 70 to 30 molar ratios (Corbion Purac, PURASORB® PLC 7015) is chosen in this work for the fabrication of tubular scaffolds. PLC is a statistical copolymer with an inherent viscosity midpoint of 1.5 dl/g. The pellets were used without further treatment or purification. PLC with a high LA ratio displaying high deformation at break and high stiffness, while the copolymer with a high CL ratio possessed an elastomeric thermoplastic behavior. PLC with LA:CL ratio of 70:30 was chosen as it is sufficiently elastic while maintaining its high yield strength.

There were four types of samples tested in this work, namely the pristine PLC, the moisturized PLC, the PLC flat sheet and the melt-drawn PLC fibrous scaffold. Pristine PLC pellets were kept in -20 °C freezer for storage. They were

freeze dried before use. To test the moisture absorption properties of the polymer, the pellets were conditioned at humidity in a refrigerator at 4 °C (below T_g of PLC) for 3 days. Briefly, PLC pellets were first put in a petri dish, and covered using perforated aluminum foil. The petri dish was then placed inside a covered container (Tupperware) filled with some water, whereby water could not flow into the petri dish. After 3 days, these moisturized samples were taken out to room temperature for testing. To produce PLC flat sheets, the pristine PLC pellets were hot pressed using heated lab press (Carver, Model 3856) before testing. The PLC was heated at 120 °C and pressed to form thin sheets of 1 mm thick. To produce PLC fibrous scaffolds, PLC was melt-drawn which will be described in Section 3.2.3.

3.2.2 Thermal and rheological analysis

The thermal stability of the pristine and moisturized PLC pellets was tested on a thermogravimetric analyzer (TGA, TA Instruments, Q500). The thermogram was recorded from 25 °C to ~600 °C at a heating rate of 5 °C/min under an inert nitrogen atmosphere. The thermal behavior of the pristine PLC pellets was tested on a differential scanning calorimeter (DSC, TA Instruments, Q200). Samples of 15-20 mg were cooled down to -10 °C and heated to 150 °C at 5 °C/min under nitrogen purge. This was used to determine the glass transition temperature (T_g) and the melting temperature (T_m) of the pristine PLC. TA Instruments Universal Analysis 2000 software package was used to identify T_g and T_m .

Melt rheological characterization was performed on a rheometer (TA Instruments, TA DHR-2) with dynamic oscillatory shear measurements. The PLC pellets were hot pressed. Viscosities of the PLC melt at different

temperatures were monitored using rheometer. Dynamic frequency sweep tests at 110, 120, 130, 140, and 150 °C were conducted with a parallel plate fixture of 25 mm in diameter at 2.0% strain and angular frequency from 0.1 to 100 rad/s. Zero-shear viscosity, η_0 at low shear rates was plotted against the tested temperatures.

3.2.3 Melt-drawing process

Melt-drawing capability

A customized table-top microfiber melt-drawing device was employed to fabricate PLC fibers as shown in Figure 3.1. Motor 1 rotates the mandrel in certain rotation speed for continuous fiber collection. Motor 2 utilizes motion conversion system to transform rotary motion to transverse motion of the melt-holder. A cylindrical mandrel with a diameter of 30 mm was used in this work.

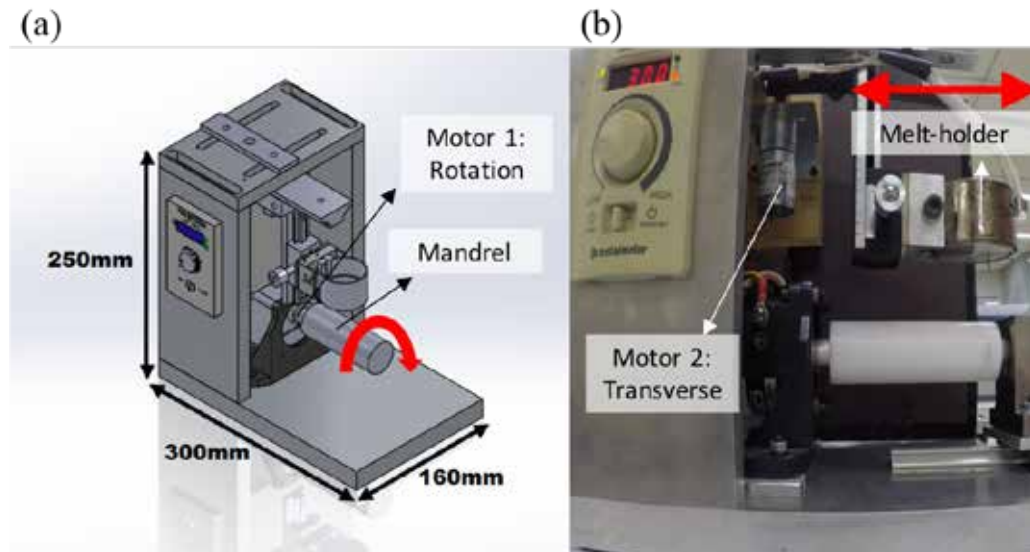


Figure 3.1. (a) Illustration of the melt-drawing device (b) Fiber drawing using the device.

The mandrel rotational speeds of 150, 300, 600, 1200 and 2400 rotations per minute (RPM) were selected. These mandrel rotation speeds can be converted

to the linear velocities (i.e. melt-drawing speeds, v) of 0.24, 0.47, 0.94, 1.88 and 3.77 m/s respectively by using formula of:

$$v=r' w \quad (1)$$

where r is radius of the mandrel, and w is the angular speed which can be calculated by:

$$w=2\pi' \text{ RPM}/60 \quad (2)$$

It is noted that the minimum sustainable rotational speed of the motor is 150 RPM. The maximum achievable rotational speed is 2400 RPM. To determine the processing window, PLC was melted at different temperatures and then drawn at various melt-drawing speeds. A lower melt-drawing temperature would be preferred as heating the polymer at high temperature for a long period will cause thermal degradation. Consequently, a suitable temperature that enables the polymer to be drawn out at the pre-determined melt-drawing speed ranges will be finalized. The fiber was drawn for 2 min to ascertain the fiber drawing sustainability.

Microfibrous scaffold fabrication

The melt-drawing process involves melting the PLC in a melt holder at 150 ± 5 °C, and then continuous pulling a single microfiber from the melt. It was first manually initiated with a needle inserted into the melt through the orifice at the bottom of melt holder, where the microfiber was pulled down from the melt pool. The drawn single microfiber was wound onto a rotating cylindrical mandrel, and the microfiber was then constantly collected on the rotating cylindrical mandrel as illustrated in Figure 3.2.

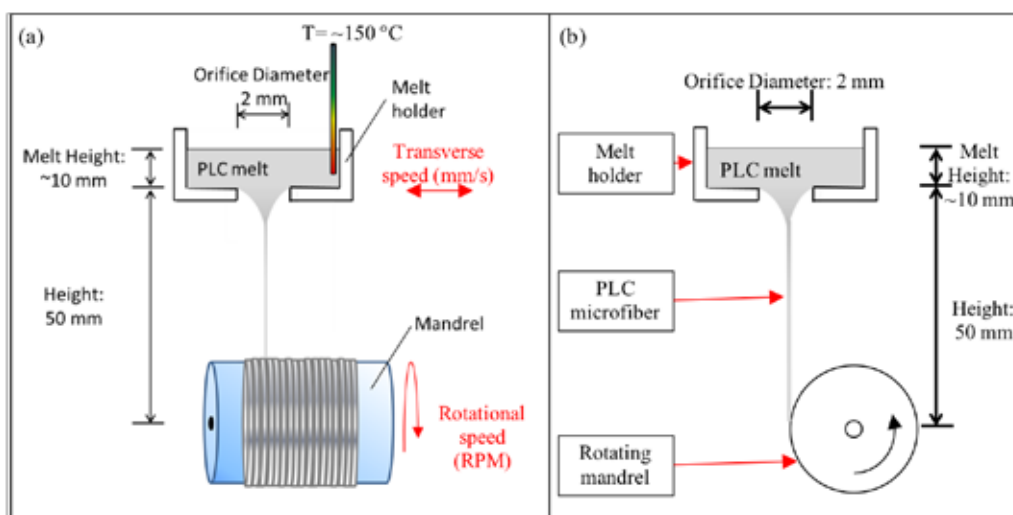


Figure 3.2. Schematic illustration of (a) front view, and (b) side view of the melt-drawing process

The mass flow rate of PLC in the melt-drawing process was ~ 0.2 g/min when using a melt-holder orifice diameter, d of 2 mm. PLC fibers were drawn at melt-drawing speeds of 0.24, 0.47, 0.94, 1.88 and 3.77 m/s respectively. The samples produced by the previously mentioned speeds were termed $V_{0.24}$, $V_{0.47}$, $V_{0.94}$, $V_{1.88}$ and $V_{3.77}$, respectively. A tubular scaffold formed when melt holder moved transversely along the length of 20 mm and distributed the microfibers on the mandrel layer by layer for 10 layers. The transverse speed was fixed at $v_t = 0.7$ mm/s. The fabricated tubular scaffold was then removed from the mandrel.

3.2.4 Gel permeation chromatography

The molecular weight distribution of the pristine PLC and the melt-drawn PLC were studied to investigate the effects of melt-drawing on the molecules of the polymer. The number-average molecular weights (M_n), weight-average molecular weights (M_w) and the polydispersity indices (PDI) of the pristine PLC and the melt-drawn PLC were measured at room temperature using gel permeation chromatography (GPC; Waters E2695 Alliance system with Waters 2414 RI detector). The standard polymers used for calibration of molecular

weights were Polystyrene (PS) ReadyCal Standards 4 mL Kit (WAT058930) with molecular weights of PS ranging from 560 to 2,500,000 Da. Chloroform was used as the effluent.

3.2.5 Scanning electron microscopy

The surface morphology of the microfibrous scaffolds was examined using a scanning electron microscope (SEM; JEOL JSM-5600LV; 10 kV). The average microfiber diameter was computed from the SEM images using the ImageJ software.

3.2.6 Scaffold density

The Archimedes method was used to compute the PLC density based on the Archimedes Principle. Weights of the pristine PLC and the melt-drawn PLC were measured in both air and ethanol at room temperature. Since the ethanol's density is known at room temperature, the PLC samples' densities can be computed.

3.2.7 Cell culture and cell seeding

Cell culture

L929 murine fibroblasts were used in a preliminary biocompatibility study. The cells were cultured in the cell culture media of high glucose Dulbecco's modified Eagle's medium (DMEM; Gibco) supplemented with 10% fetal bovine serum (FBS; Sigma–Aldrich). Murine myoblasts C2C12, which is primordial muscle cells with the potential to develop into a muscle fiber, were used to demonstrate the ability of myoblasts to grow and align on the scaffolds. The cells were cultured in high glucose DMEM supplemented with 10% FBS.

The cells were cultured separately in a humidified incubator (37 °C/ 5% CO₂) until sufficient confluence.

Human mesenchymal stem cells (hMSCs) from a 26-year-old female donor and cell culture medium were both obtained from Lonza. The hMSCs expressed CD 105/+, CD166/+, CD 44/+, CD 90/+, CD 73/+, CD 14/–, CD34/–, CD19/– and CD45/–. Information of the surface antigens were obtained via flow cytometry analysis provided in the company's data sheet. The hMSCs were expanded and cultured in mesenchymal stem cell basal medium (Lonza) according to the vendor's instructions. All the cells were maintained at 37 °C in a humidified atmosphere of 5% CO₂. Culture medium was changed every 2–3 days.

Cell seeding on scaffolds

Scaffold samples were sterilized by immersing in a 70% ethanol solution, followed by washing several times in a phosphate buffer solution (PBS). They were then soaked in the culture medium overnight for protein adsorption. The cells were detached from the culture flask and counted under optical microscope using hemocytometer and then seeded at a required cell density.

Cell proliferation on scaffolds

The initial cell proliferation on scaffold surface was determined by the RealTime-Glo™ MT Cell Viability Assay (Promega), which measured cell viability in real-time. The MT cell viability substrate in the assay is cell permeable, which gets reduced inside metabolically active cells. The reduced substrate exits the cell and is rapidly used by the NanoLuc® Luciferase enzyme of the assay to produce a luminescent signal. Only metabolically active cells can

reduce the MT cell viability substrate, and the luminescent signal is proportional to the quantity of viable cells in culture.

In this study, 5×10^3 cells/10 μ L of cells were seeded onto each flat 4 \times 4 mm² scaffolds in a white 96-well plate. Cells seeded TCPS served as positive controls. After incubation (37 °C/ 5% CO₂) for 1 h, 90 μ L of culture media was added into each well. 100 μ L of 2 \times RealTime-Glo Reagent was then added to each well and the culture was further incubated for up to 2 days. The number of viable cells was determined in the culture by measuring the luminescence at several time-points up to 48 h using a microplate reader (Ultra Evolution, Tecan).

Longer term cell proliferation up to one week was determined by the MTS (3-(4,5-dimethylthiazol-2-yl)-5-(3-carboxymethoxyphenyl)-2-(4-sulfophenyl)-2H-tetrazolium) colorimetric assay (CellTiter 96® AQueous One Solution), which is based on the conversion of a tetrazolium salt into a colored formazan product by viable cells at 37 °C. Cells were seeded onto flat 4 \times 4 mm² scaffolds at a density of 5×10^4 cells per sample. TCPS was served as a positive control. At 1 day, 3 days and 7 days, the constructs were rinsed twice with PBS and incubated in 200 μ L of MTS assay solution for 4 hours. Thereafter, the absorbance of the supernatants was measured at 492 nm using a microplate reader (Ultra Evolution, Tecan).

Cell adhesion and alignment on scaffolds

L929, C2C12 and hMSCs were cultured and seeded onto the scaffolds. Cell adhesion, spreading and alignment of cells on the scaffolds were studied. Cells were seeded on flat 10 \times 10 mm² microfibrous scaffolds at a density of 1×10^5 cells/scaffold. C2C12 cells were differentiated to skeletal muscle cells by changing its cell culture medium to high glucose DMEM with 2% horse serum

(Gibco) after 1 day of culture. The constructs were maintained in a humidified incubator (37 °C/ 5% CO₂) and the cell growth was monitored daily using an inverted optical microscope (OM; Zeiss Axio Vert.A1). The cell adhesion and alignment on the scaffolds was imaged using SEM after 3 and 6 days of culture [230]. Before imaging, cellular constructs were rinsed with PBS and fixed with 3% glutaraldehyde overnight at 4 °C. Following PBS rinses, the samples were dehydrated through a series of graded alcohol solutions, and then dried using a critical point dryer (BAL-TEC CPD 030). The constructs were gold coated and observed under the SEM.

Cell viability on scaffolds

The viability of the cells seeded on the scaffolds was imaged using the live/dead cell viability kit (Sigma-Aldrich) after 3 and 6 days of *in vitro* culture. Calcein-AM, acetoxymethyl ester of calcein, is highly lipophilic and cell membrane permeable. The calcein generated from Calcein-AM by esterase in a viable cell emits strong green fluorescence. Meanwhile, the nuclei staining dye propidium iodide (PI) cannot pass through a viable cell membrane. It reaches the nucleus by passing through disordered areas of dead cell membrane, and intercalates with the DNA double helix of the cell to emit red fluorescence [231].

L929 and C2C12 cells were seeded on 10×10 mm² scaffolds at a density of 1×10^5 cells/50 µL per scaffold in a 24-well plate. Cells seeded TCPS served as a positive control. After incubation in an incubator for 1 h, 950 µL of cell culture medium was added to each well. The medium was changed every two days. For C2C12 cells, they were differentiated to skeletal muscle cells by changing its cell culture medium to high glucose DMEM with 2% horse serum (Gibco) after 1 day of culture. The cell seeded constructs were maintained in an

incubator and harvested after 3 and 6 days. The cellular constructs were rinsed twice with PBS and incubated in a PBS solution containing 5 $\mu\text{mol/l}$ PI and 2 $\mu\text{mol/l}$ calcein AM for 15 min at 37 °C before examining using an inverted fluorescent microscope (Zeiss Axio Vert.A1). The percentage of live cells (reported as the cell viability) was computed from the fluorescence readings using the ZEN microscope software.

Immunocytochemistry analysis

C2C12 cells were cultured for 7 days to observe cell infiltration. Cells were seeded on flat 5×5 mm² microfibrous scaffolds at cell density of 1×10^4 cells per sample. Cells were seeded only on 1 side of the scaffold. C2C12 cells were differentiated to skeletal muscle cells by changing its cell culture medium to high glucose DMEM with 2% horse serum after 1 day of culture. The medium was changed every 2 to 3 days. At 7th day, the scaffolds were harvested, washed thrice with PBS. The cells were fixed with 4% paraformaldehyde for 40 min at room temperature. These cells were then permeabilized with 0.1% Triton X-100 in PBS for 15 min at room temperature and blocked with 5% bovine serum albumin (BSA) in PBS. F-actin was stained with fluorescein phalloidin (Thermo Fisher Scientific) and nuclei were stained with 4'-6-Diamidino-2-phenylindole (DAPI) respectively. Fluorescence images were visualized and imaged with confocal microscope of Zeiss LSM 710.

For the hMSCs cell seeding experiments, hMSCs were cultured in the mesenchymal stem cell basal medium (Lonza) without using soluble differentiation factors. hMSCs (passage 5) were seeded on flat 10×10 mm² microfibrous scaffolds following the same cell seeding protocol. Cells were

seeded at a density of 2×10^5 cells/scaffold. Culture medium was changed every 2–3 days.

The hMSCs positive (CD44) and negative (CD31) markers, smooth muscle actin and cell nucleus were immuno-stained with staining kits (Thermo Fisher Scientific) according to the manufacturer's instructions. After 5 days of culture, cells were fixed with 4% paraformaldehyde for 15 min at room temperature. These cells were then permeabilized with 0.1% Triton X-100 in PBS for 10 min at room temperature and blocked with 5% BSA in PBS before the subcellular components were immuno-labeled. CD44, CD31 and cell nucleus were counter stained with rabbit monoclonal anti CD44 (2 $\mu\text{g/mL}$) counterstained with Cy3 goat anti rabbit IgG, mouse monoclonal anti CD31 (1:50) counterstained with AlexaFluor 488 donkey anti mouse IgG and DAPI respectively. Smooth muscle actin (SMA) and cell nucleus were counter stained with rabbit monoclonal anti SMA (3 $\mu\text{g/mL}$) counterstained with Cy3 goat anti rabbit IgG, and DAPI respectively. Fluorescence images were visualized and imaged with Zeiss Axio Vert.A1. microscope.

3.2.8 Statistical analysis

All data were expressed as means \pm standard deviation (SD). Statistical differences were evaluated with one-way ANOVA analysis coupled with the Tukey ' s test. Differences were statistically significant when $p < 0.05$ and greatly significant when $p < 0.001$.

3.3 Results

3.3.1 Tubular microfibrinous scaffold formation

Tubular scaffolds were formed in one step due to the high viscoelasticity and stickiness of the PLC at room temperature. Polymer fibers are merged together during melt-drawing on the tubular mandrels, thus forming tubular scaffolds. As a comparison, PLGA (Purac PDLG5010) and PCL (Purac PC12) can be melt-drawn, but forming loose fibers instead of an intact tube as shown in Figure 3.3. In addition, PLC scaffolds are elastic circumferentially as illustrated in Figure 3.4.

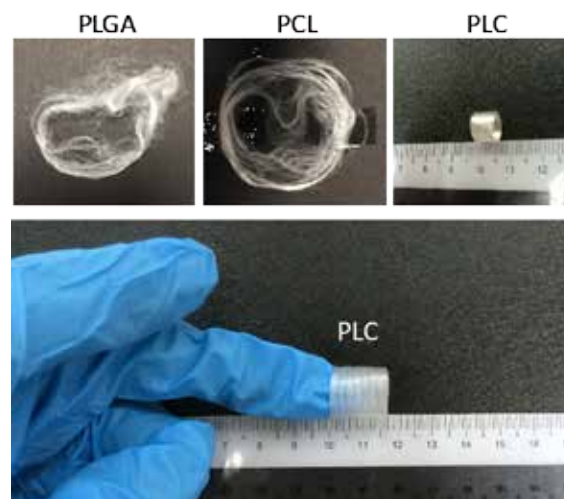


Figure 3.3. Melt-drawn PLGA, PCL and PLC. PLGA and PCL was melt-drawn into loose fibers but the PLC remained as an intact tube.

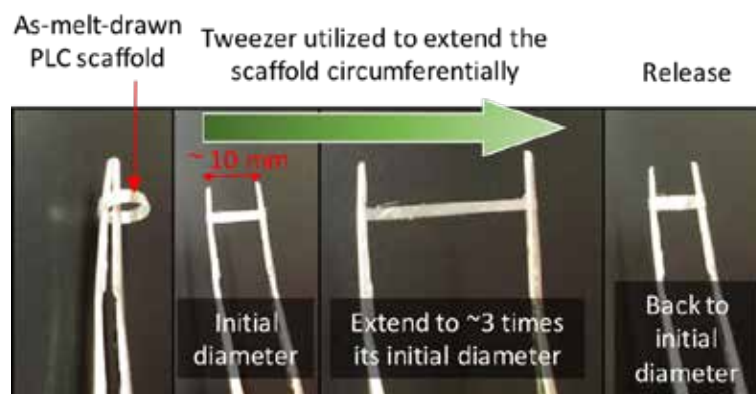


Figure 3.4. Illustration of circumferential extensibility of a melt-drawn PLC scaffold

3.3.2 Thermal and rheological properties

The thermal decomposition study of PLC pellets is shown in Figure 3.5. The onset of thermal degradation was at $\sim 296^\circ\text{C}$. Moisturized PLC showed water absorption or hygroscopic properties. Storage of the materials in dry or frozen condition was of importance to protect the polymer from moisture before processing. As illustrated in Figure 3.6, T_g of the PLC was from 10.2 to 17.3°C . There were two T_m determined for PLC, i.e. one is at 52°C and another one at 109°C .

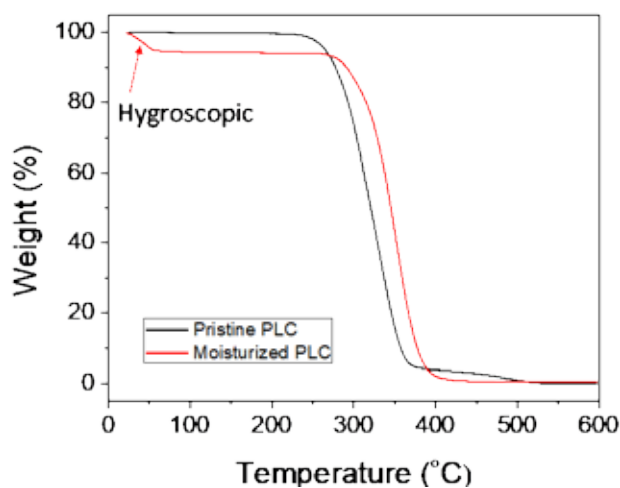


Figure 3.5. TGA results with heating rate of $5^\circ\text{C}/\text{min}$ showing thermal degradation temperature of PLC.

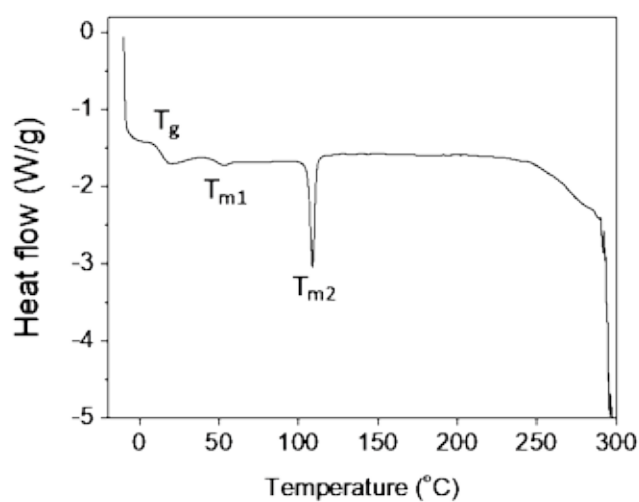


Figure 3.6. DSC results with heating rate of $5^\circ\text{C}/\text{min}$ showing thermal properties of PLC.

Figure 3.7 illustrates the frequency dependencies of storage modulus (G'), loss modulus (G''), and complex viscosity (η^*) for PLC at 150 °C. The rheological results of the PLC melts at various temperatures are illustrated in Appendix B. The relationship of zero-shear viscosities of PLC melt at different temperatures are shown in the inset of Figure 3.7. PLC melted at 110 °C with a viscosity of 9889 Pa.s. It would start to flow when the temperature reached 130 °C where the viscosity decreases to ≤ 2000 Pa.s.

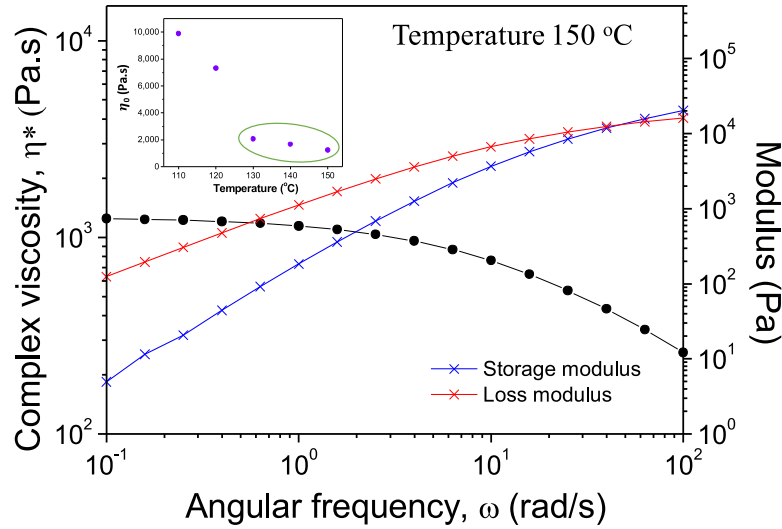


Figure 3.7. Dynamic frequency sweep test of PLC at 150 °C. Inset illustrates the zero-shear viscosities at different temperatures.

3.3.3 Melt-drawn tubular microfibrinous scaffolds

Melt-drawing process window

Figure 3.8 illustrates the melt-drawing ability of PLC at different temperatures and melt-drawing speeds. Here the melt-drawing temperature of 150 °C was chosen for the best drawing capacity of PLC, while having the least possibility to degrade the polymer during processing. PLC exhibits viscosity of 1245 Pa.s at 150 °C. PLC maintains its polymeric properties and was not thermally degraded after the melt-drawing process. M_n , M_w , and PDI of the as-

received PLC measured by GPC were 13121, 54855 and 4.18, respectively. M_n , M_w , and PDI of melt-drawn PLC ($V_{3.77}$) were 15588, 59560 and 3.82, respectively. The GPC reports are shown in Appendix C. The results indicated that the PLC was not thermally degraded after the melt-drawing process, thus it is expected to retain its original materials properties.

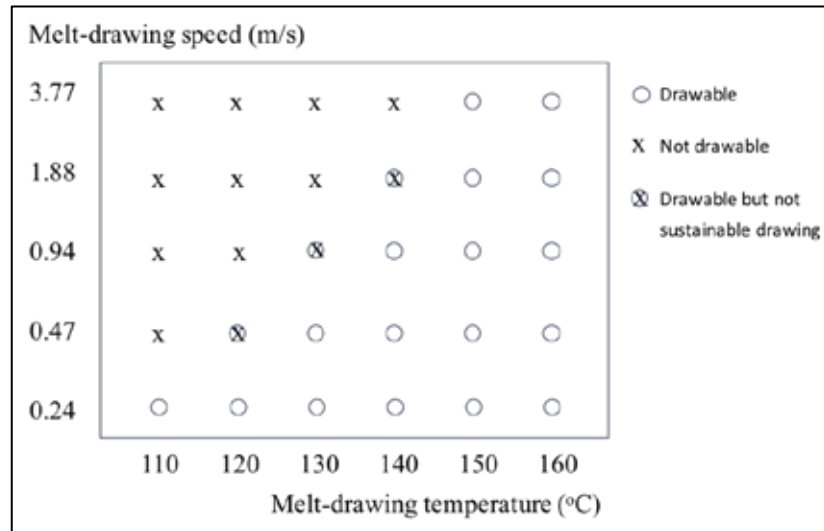


Figure 3.8. Melt-drawing ability of PLC at different temperatures and melt-drawing speeds. Note: “Drawable but not sustainable drawing” means that the fibers can be drawn, but sometimes the fibers break during fabrication.

Scaffolds fabricated and fiber diameters

A representative scaffold fabricated is shown in Figure 3.9, with a diameter of 30 mm and length of 20 mm. Diameter of 30 mm was chosen because it likens to the dimensions of a native esophageal diameters of an adult.

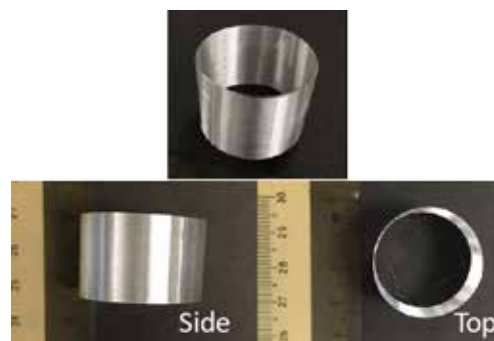


Figure 3.9. Representative tubular scaffold fabricated by melt-drawing. This scaffold has diameter of 30 mm, width of 20 mm and thickness of 130 μ m.

Melt-drawing speed was computed from the mandrel rotation speeds and the mandrel diameters. Figure 3.10 shows the surface morphology and the fiber

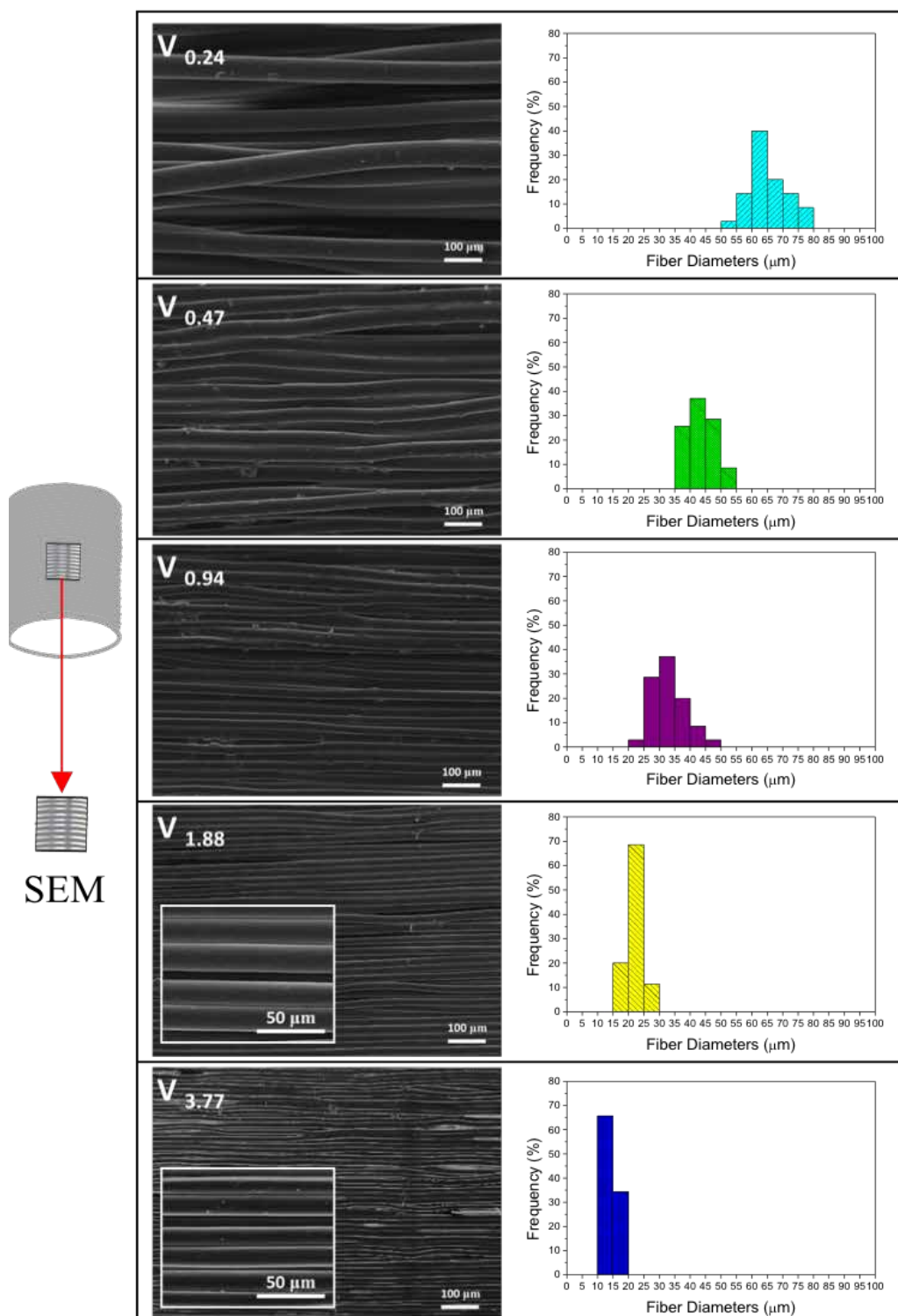


Figure 3.10. SEM micrographs and fiber diameter distribution of melt-drawn scaffolds V_{0.24}, V_{0.47}, V_{0.94}, V_{1.88}, and V_{3.77}. Inset illustrates the sample taken from the tubular scaffolds for SEM.

diameter distribution of the five scaffold samples with different melt-drawing speeds as labelled. The presented SEM figures were taken at the mid-section of the scaffold, the position is as shown in the inset. The highly-aligned microfibers are clearly seen in all five samples and the fiber diameter markedly decreases corresponding to the increasing melt-drawing speeds.

The fiber diameters of the sample $V_{0.24}$, $V_{0.47}$, $V_{0.94}$, $V_{1.88}$ and $V_{3.77}$ were determined to be 65.7 ± 6.2 , 43.5 ± 4.1 , 32.6 ± 5.0 , 21.5 ± 1.8 , and 13.9 ± 1.7 nm, respectively. In addition, the fiber diameter becomes more uniform with increasing melt-drawing speeds. The density of pristine PLC is 1.215 g/cm^3 when computed using the Archimedes method. Meanwhile the density percentage of the samples $V_{0.24}$, $V_{0.47}$, $V_{0.94}$, $V_{1.88}$ and $V_{3.77}$ were determined to be 91.7%, 91.0%, 90.7%, 86.2%, 84.4%, respectively.

3.3.4 Biocompatibility and cell alignment

Proliferation of L929 on scaffolds were observed using OM every day during the experiment. Figure 3.11 (a) illustrates the OM observations of L929 on the PLC scaffold of $V_{0.94}$ at day 1, 3 and 6. Cell number is clearly seen to increase with the day of culture. Cells growth and distribution is good on the scaffold surface. The proliferation ($n=3$) of L929 was evaluated and the results are presented in Figure 3.11 (b) and (c). Note that the error bars in Figure 3.11 (b) represent the SD for $n= 3$, * $P < 0.05$ and *** $P < 0.001$ by ANOVA followed by Tukey ' s tests when comparing between $V_{0.47}$ and $V_{3.77}$. Inset in Figure 3.11 (c) shows the low water contact angle of $\sim 66^\circ$ on the scaffold, which indicates good hydrophilicity for cell growth.

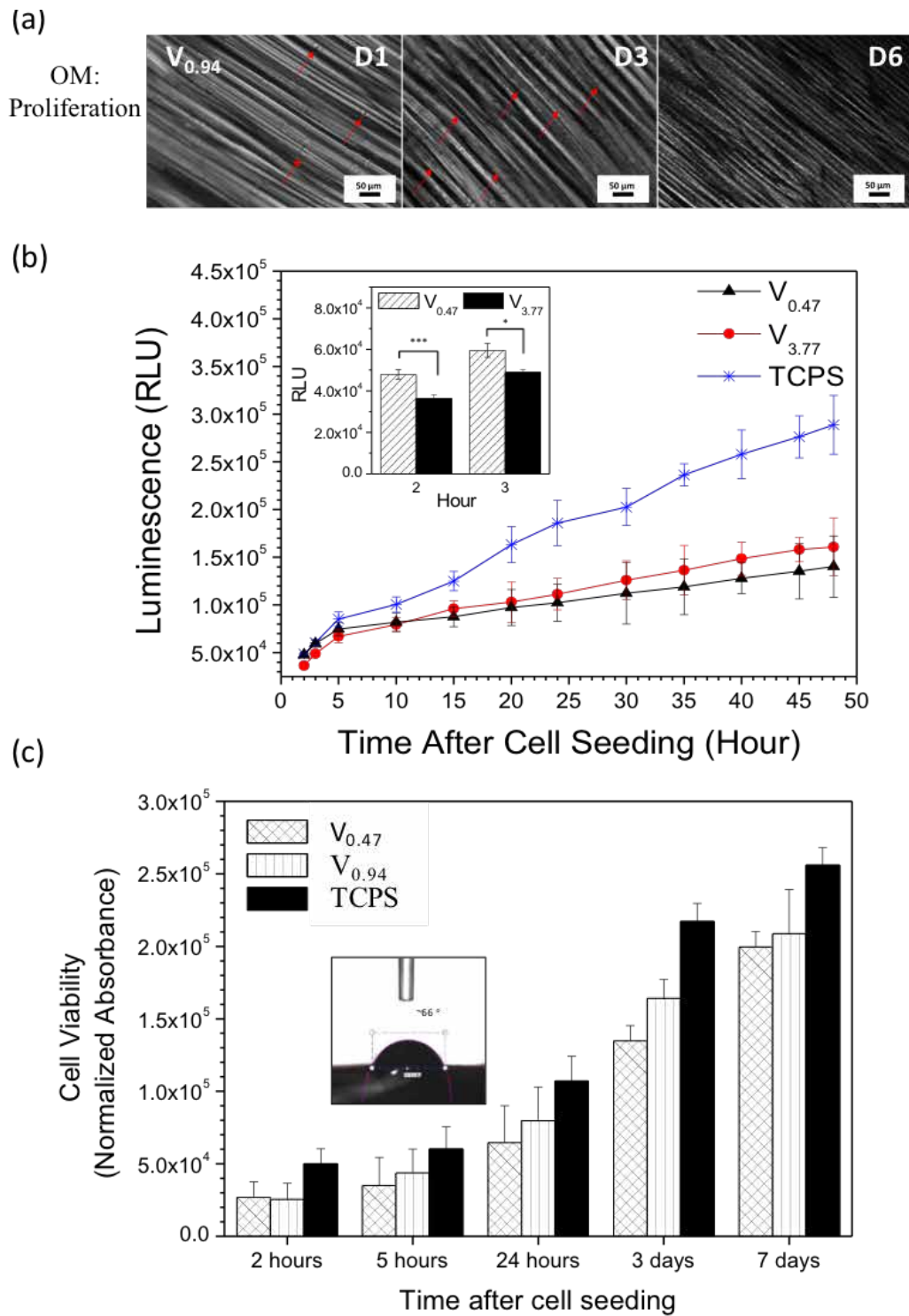


Figure 3.11. (a) OM images of L929 cell growth and distribution on $V_{0.94}$ scaffold for day 1, 3 and 6. (b) Real-time cell proliferation of L929 on the scaffolds $V_{0.47}$ and $V_{3.77}$. (c) Cell proliferation on the scaffolds $V_{0.47}$ and $V_{0.94}$ comparing to TCPS. Inset: water contact angle of PLC scaffold.

L929 was found to attach on the PLC scaffolds. Cell proliferation can be observed continuously on the scaffolds for up to 48 h. Initial cell attachment was significantly better for $V_{0.47}$ samples, whereas its subsequent cell proliferation became marginally slower when compared to those of $V_{3.77}$. A longer-term proliferation on the scaffold was studied by using MTS assay. L929 cells were proliferating well with time on the samples. After 7 days, the cell number had become quadruple compared to the initial cell seeding number on the melt-drawn PLC scaffolds.

The viabilities of L929 cells on the PLC scaffolds (and controls of TCPS and PLC flat sheets) were evaluated after 6 days' culture. Figure 3.12 shows the fluorescence images of L929 cultured on these substrates. Live cells which were

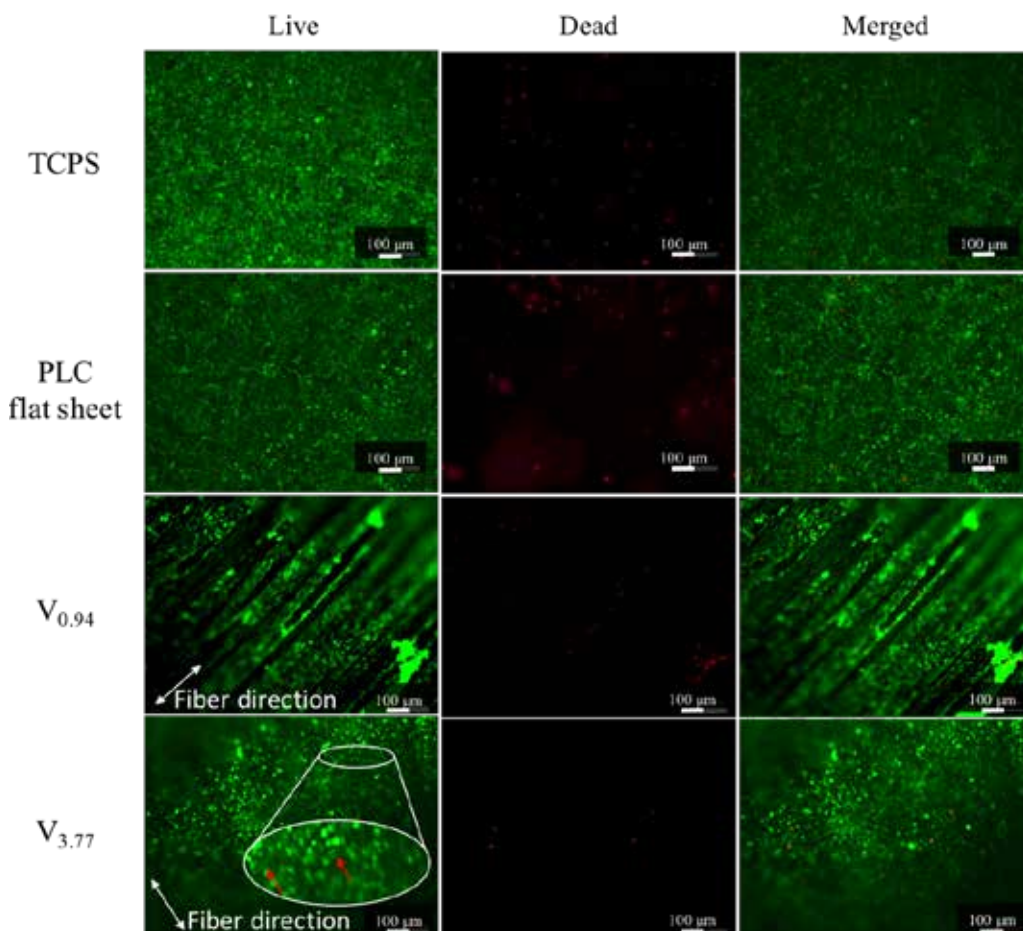


Figure 3.12. Live/dead staining of L929 after 6 days of culture on TCPS, PLC flat sheet, $V_{0.94}$, and $V_{3.77}$ scaffolds.

stained green, appeared to adhere well on the scaffold surfaces. Nuclei of the dead cells, stained red, were barely found on both scaffold surfaces. All the scaffolds exhibited cell viability of $> 90\%$. SEM (Figure 3.13 and Appendix D) shows clearly that L929 adhered well to the scaffold surfaces with a normal elongated spread morphology. All the samples showed cell alignment, but $V_{0.94}$ illustrates the best cell alignment among the samples. Arrows in Figure 3.13 highlighted the alignment of L929 on the sample $V_{0.94}$. Cells elongate by following the alignment of the microfibers.

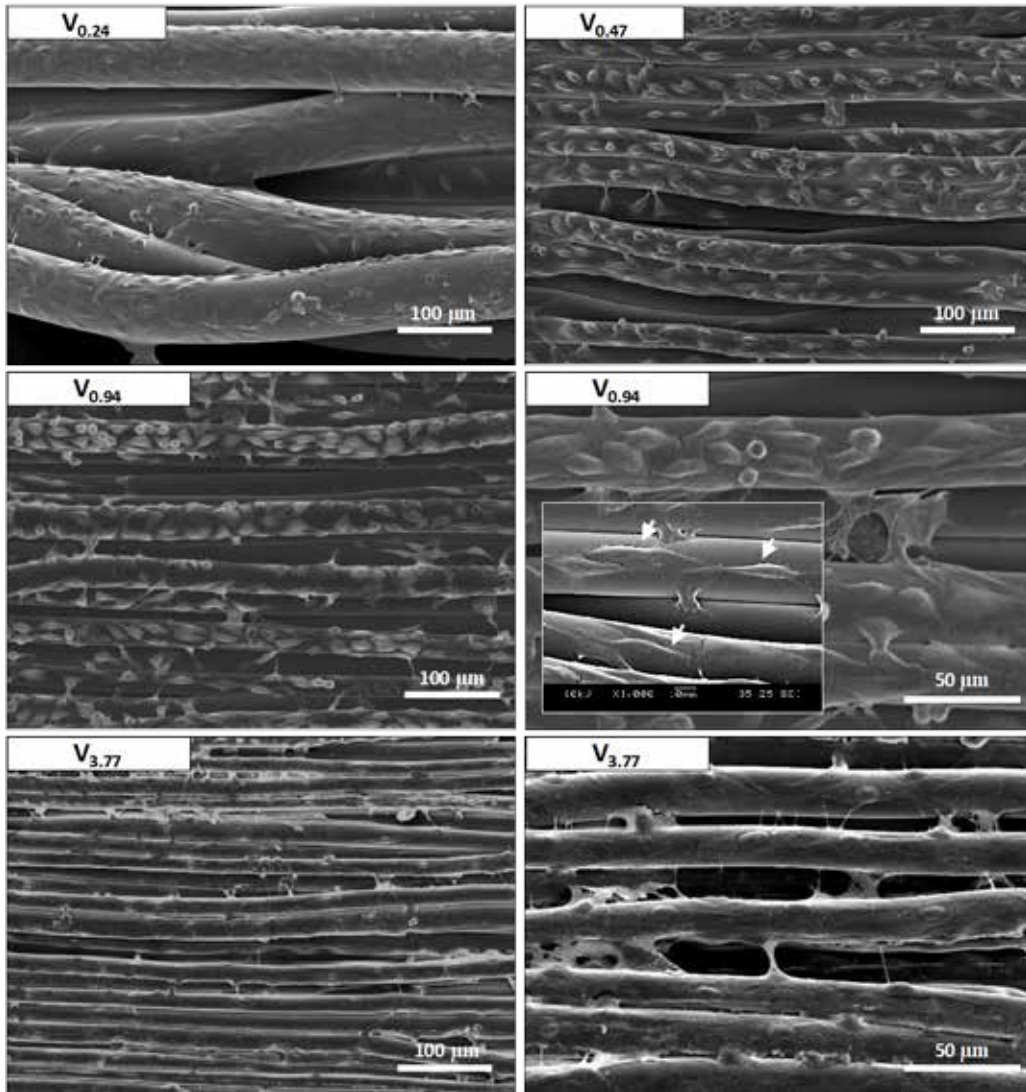


Figure 3.13. SEM images showing the L929 cell adhesion on the scaffolds with the different melt-drawing speeds after 6 days of culture.

Myoblasts C2C12 (see Figure 3.14) was highly aligned on $V_{0.94}$. Arrows indicating cell alignment on the fibers. F-actin fibers were stretched along the length of the fibers in the scaffolds. Nuclei of C2C12 were obviously elongated following the fiber direction too. Thus, the fiber diameter and fiber alignment

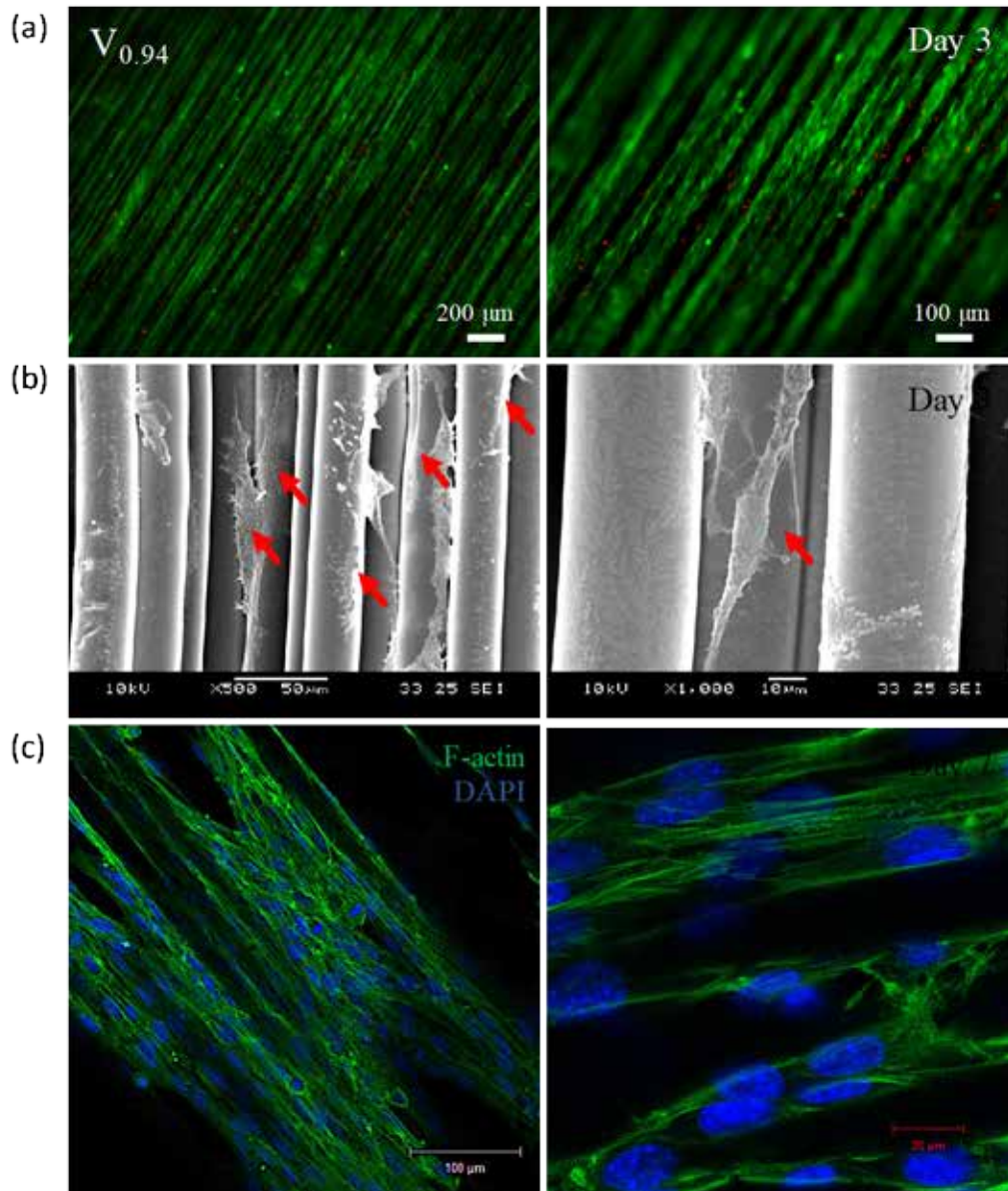


Figure 3.14. (a) Live(green)/dead(red) staining and (b) SEM images of myoblasts C2C12 cultured on $V_{0.94}$ for 3 days. (c) Confocal microscope images showing F-actin and DAPI nucleus staining of C2C12 cultured on $V_{0.94}$ for 7 days.

were shown to have significantly contribute to cell alignment. Cells were found to infiltrate into at least 3 layers of the scaffolds after 7 days of culture as shown in Figure 3.15. The infiltrated cells showed significant cell alignment as well.

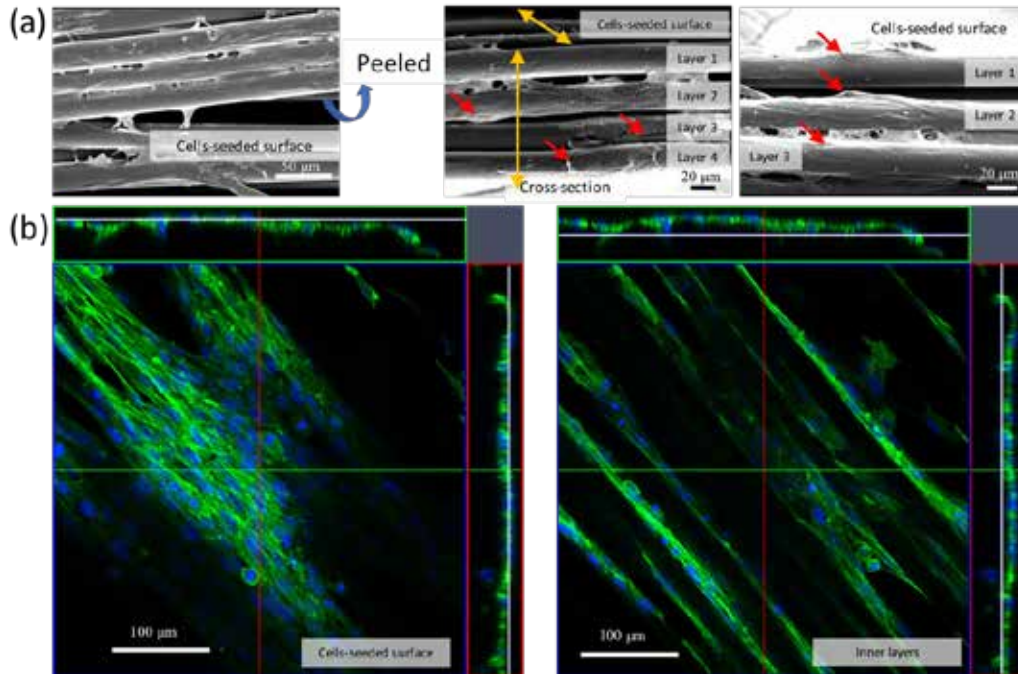


Figure 3.15. (a) SEM images and (b) confocal microscopy showing C2C12 cells infiltration into $V_{0.94}$ scaffolds after culturing for 7 days. Note: confocal microscope images showing F-actin (green) and DAPI (blue) nucleus staining.

Similarly, hMSCs attached well on the microfibrinous scaffolds are shown in Figure 3.16. The cells were aligned along the fiber direction. After culturing hMSCs on the melt-drawn scaffolds for 5 days, the cells were immuno-stained for the myogenic protein, smooth muscle actin (SM actin). SM actin expressed in the cells indicative of differentiation along the SMC lineage. As opposed to the TCPS control, positive marker CD44 of MSCs was not found on the scaffolds.

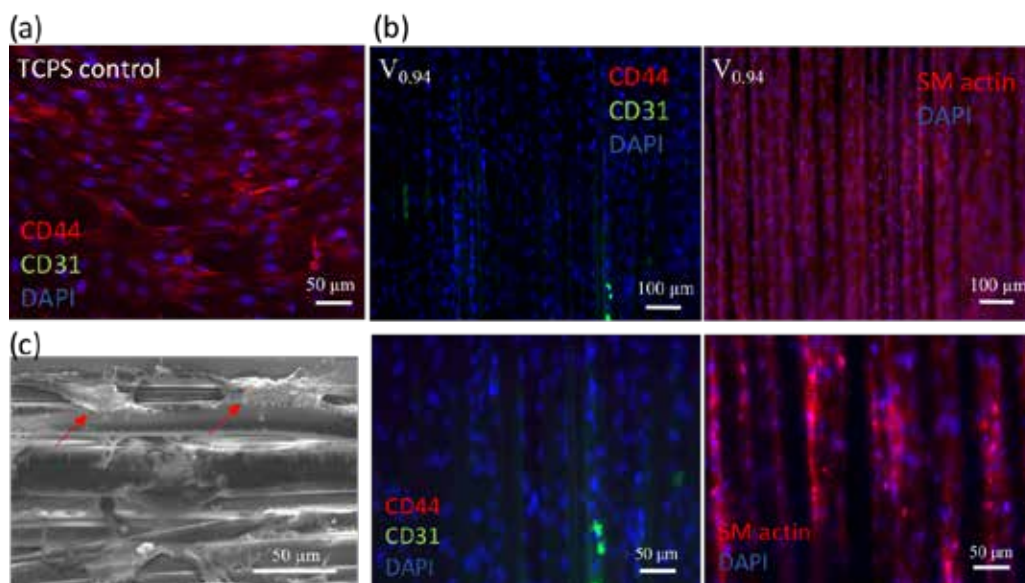


Figure 3.16. Immuno-staining of hMSCs cultured on (a) TCPS control and (b) microfibers. (c) SEM image of the hMSCs on the microfibers.

3.4 Discussion

As T_g of the PLC was from 10.2 to 17.3 °C, it is elastic at the ambient room and body temperatures. It is noted that PLC is a hygroscopic material. The moisturized samples can absorb moisture to as high as $7.44 \pm 0.02\%$ of their weight. The moisturized PLC were not immersed in water nor placed in an ambient room temperature. Water immersion and/or conditioning at temperature above T_g will accelerate the water absorption. PLC should be stored dry to avoid water absorption, which will cause properties of materials to degrade [232, 233]. If PLC contains moisture, melting the polymer will further accelerate its degradation. Moisture on the materials will also cause difficulty in processing because bubbles can be formed in the melt. Fiber drawing process might be disrupted intermittently.

The onset of PLC thermal degradation was at ~ 296 °C. The melt-drawing temperature of the PLC should be kept as low as possible to prevent long term thermal degradation. Two T_m of PLC was found at 52 °C and 109 °C. To melt the

polymer completely, a minimum temperature needed is 109 °C. However, the viscosity of PLC at 109 °C is not sufficiently low for fiber drawing. The study of rheological properties of polymer melts is important in determining the materials' processability. It was found that the polymer needed to be heated up to above 130 °C for better flowability. Further processing window determination shows that 150 °C is the most suitable temperature to produce fibers from the full range of melt-drawing speeds.

Microfibers fabricated from the PLC polymer melt were found to be good matrices for TE applications [226,234] as organic solvents or toxic chemicals have not been used in the fabrication. The polymer melt-based microfibers fabrication process is also better in controlling the distribution uniformity of fibers diameter and the architecture of scaffolds when compared to the solution-based methods. For example, a broad fiber diameter distribution was reported in the polymer solution electrospinning process [235,236], probably due to the fast phase separation of polymer and the uncontrollable evaporation of volatile solvents during fabrication [226].

By using melt-drawing, a uniform diameter distribution has been achieved for all the fabricated PLC microfibrous scaffolds. To model the fiber diameter with the processing parameters, a mathematical model was modified from the developed empirical model [229] for the melt-drawing process. By applying conservation of mass, the mass flow rate of the materials is:

$$\rho \frac{\pi}{4} d^2 v_0 = \rho \frac{\pi}{4} D^2 v, \quad (3)$$

where ρ is density of melt-drawn materials, d is the orifice diameter, v_0 is velocity when the polymer melt exits the orifice plane, D is the theoretical final fiber diameter, and v is the melt-drawing speed. By simplifying the stress tensor

into a vector with a magnitude and a downward direction, the conservation of energy can simply be represented as:

$$-\sigma + \rho gh = \frac{1}{2} \rho v_0^2, \quad (4)$$

where σ is the shear stress, g is gravitational constant, and h is melt height. Polymer melt is assumed to behave like a Newtonian fluid [229], where its viscosity is assumed to be constant with the shear rate. By conforming Trouton's ratio of 3 [229], the Newton's law of viscosity can be expressed as:

$$\sigma = 3\eta \frac{dv}{dx}, \quad (5)$$

where η is shear viscosity and dv/dx is velocity gradient of shear flow. Combining and solving Equation (3-5), the final fiber diameter [229] can be shown as:

$$D = \left(\frac{\sqrt{2gh}}{v} \tanh \left(\frac{\rho d}{12\eta} \sqrt{2gh} \right) \right)^{\frac{1}{2}} d. \quad (6)$$

Simple Arrhenius equation was used to relate temperature with the shear viscosity; and the flow activation energy, E_a is related to T_g [237], as the melt temperature falls in the Arrhenius region [238]:

$$\eta = A \exp \left(\frac{E_a}{RT} \right), \quad (7)$$

$$E_a = \frac{R T_g (T_g + 150)^2}{0.164 (0.23 T_g + 150)^2}, \quad (8)$$

where T is melt temperature, A is materials constant, and R is the gas constant. By combining Equation (6-8), the final fiber diameter can be mathematically expressed as:

$$D = \left[\frac{\sqrt{2gh}}{v} \tanh \left(\frac{\rho d \sqrt{2gh}}{12A} \exp \left(\frac{-T_g (T_g + 150)^2}{0.164 T (0.23 T_g + 150)^2} \right) \right) \right]^{\frac{1}{2}} d \quad (9)$$

In this work, $h = 50$ mm, $r = 1.215$ g/cm³, $d = 2$ mm, $T = 423.2$ K and $T_g = 286.9$ K respectively. v represents the different melt-drawing speeds and A was calculated from Equation (7) and (8) to be 5.607×10^{-5} Pa·s when $h = 1245$ Pa·s at 150 °C. The theoretical results of the fiber diameter were calculated and shown in Figure 3.17 (a). Note that the error bars represent the SD for $n = 35$ and *** $P < 0.001$ by ANOVA followed by Tukey's tests when compared with the melt-drawing speeds. Both the experimental and the theoretical fiber diameters decrease significantly with melt-drawing speeds. It is noted that the theoretical D slightly underestimated but fit relatively well to the experimental results. D is also found to be a linear function of the $\sqrt{1/v}$ as illustrated in Figure 3.17 (b), which fits with the empirical model developed. It demonstrates that the PLC fiber diameter can be tailored effectively by manipulating the melt-drawing speeds.

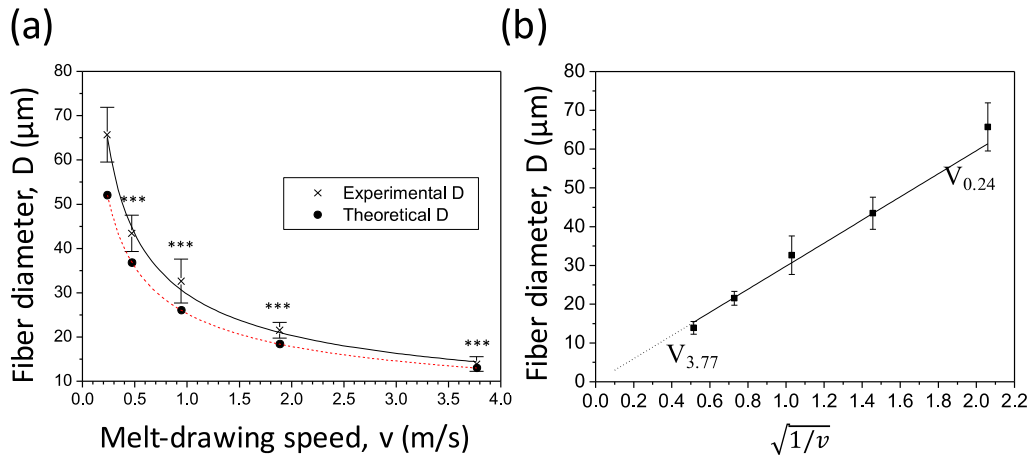


Figure 3.17. Effect of melt-drawing speeds on the fiber diameters from theoretical and experimental results; and (b) linear relationship of fiber diameters with melt-drawing speeds obtained from experiments.

Microfibers could be fabricated according to the desired fiber diameter with superb reproducibility and uniform fiber distribution. Microfibers of 13.9 ± 1.7 μm can be produced by the melt-drawing speed of 3.77 m/s in $V_{3.77}$. Owing to the limitation of the current experimental set up, the highest rotation speed that

can be achieved is 2400 RPM, which is equivalent to a melt-drawing speed of 3.77 m/s. Theoretically, even finer PLC fibers could be achieved via a higher melt-drawing speed. Nonetheless, to produce very fine fibers, e.g. nanofibers, these would be increased difficulty as fiber breakage would often occur during the melt-drawing at a very high speed.

Biocompatibility tests were first done on L929. Note that there was no surface modification conducted on the materials surface. It was shown that PLC is biocompatible on the flat PLC surface. Cells were $\geq 90\%$ viable on the melt-drawn fibers, irrespective to the fiber diameter. SEM micrographs showed that there are some filament-like focal adhesions structures that extended from these cells and attached to the microfibers. These structures are expected to be the adhesion sites between the cultured cells and the ECM. Good biocompatibility can be due to the high hydrophilicity of PLC. When looking at the cell proliferation, cells were attached more on the larger fiber diameter initially for up to 3 hours. Subsequent observations showed that cells proliferated marginally faster on fine fibers due to high specific surface area, i.e. cells have more surface to grow onto.

The scaffolds' fiber size decreases and the scaffolds' porosity increases with the increasing melt-drawing speed. It might be desirable to fabricate fibers with the highest melt-drawing speeds. It was thought that cell alignment will be higher on the finer fibers. Results show that cells were found to align on all the fibers. However, some L929 cells were observed to grow across the fibers (perpendicular to the fiber) on $V_{3.77}$ after 6 days of culture. It was observed that the best cell alignment was found on $V_{0.94}$ fibers. Hence, myoblasts C2C12 and hMSCs were cultured only on $V_{0.94}$ to illustrate their cell distribution and

alignment. It was also shown that the skeletal myoblasts C2C12 adhered well to the scaffold surfaces and distributed throughout the scaffold surface. The cells were observed to have normal elongated spread morphology. The elongation followed the alignment of the microfibers. Similarly, Agrawal *et al.* [161] had shown that human smooth muscle cells aligned on the melt-drawn PCL fibers. Cells could infiltrate into the scaffolds and still followed the fiber alignment. Hence, the scaffold could provide 3D guided muscle cell growth.

hMSCs differentiated to smooth muscle lineage on the microfibrinous scaffolds in the absence of soluble induction factors, showing cellular shape modulation may encourage the differentiation of stem cells. Although soluble factors, e.g., transforming growth factor $\beta 1$ (TGF- $\beta 1$) could induce MSC differentiation towards the SMC lineage, there were studies illustrating the potential to control stem cell fate via cell shape modulation [239,240]. Tay *et al.* [240] showed that enforced cell shape distortion resulted in physical impetus, by which the mechanical deformation was then translated into biochemical response. Here, cells were shown to be enforced to elongate following fiber direction, which could be the reason why the hMSCs differentiate to SMC lineage.

3.5 Summary

The tubular microfibrinous PLC scaffold presented in this work was successfully fabricated by the simple but efficient method based on a similar premise of additive fabrication. Tubular esophageal scaffolds with fiber diameters ranging from $13.9 \pm 1.7 \mu\text{m}$ to $65.7 \pm 6.2 \mu\text{m}$ were created from the highly elastic PLC via a melt-drawing method at varying speeds. They were highly aligned with uniform diameter distributions. When melt-drawn at 150 °C, the fiber diameter can be altered by adjusting the melt-drawing speeds,

conforming to the mathematical model developed. Fiber diameter was found to be proportional to $(1/\sqrt{v})$.

L929 cells could attach and proliferate on the scaffolds very well. The cells seeded on the scaffolds showed normal morphology with >90% cell viability after 6 days of culture. All the melt-drawn scaffolds illustrated great potential in producing 3D guided cell alignment. Best cell alignment was found on $V_{0.94}$. It was shown that fibroblasts L929, skeletal myoblasts C2C12 and hMSCs aligned well on the parallel $V_{0.94}$ microfibrinous scaffolds. hMSCs differentiated to smooth muscle lineage after 5 days of culture without the use of soluble induction factors, showing that cellular shape modulation may differentiate the MSCs. Cell infiltration was demonstrated by showing C2C12 cells infiltrated into the scaffolds after culturing for 7 days. PLC scaffolds for TE of oriented smooth and skeletal muscles demonstrated the effective use of polymer technology in meeting the requirements of the tissue-engineered constructs to match the native myoarchitecture. These results demonstrated that the PLC fibrous scaffold has good potential for creating cell alignment in esophageal tissue engineering applications.

Chapter 4. Bioengineering of esophageal musculature:

Customization of tubular scaffolds

4.1 Introduction: Mechanical properties and dimensions

Melt-drawing is used to produce elastic PLC microfibers from polymer melt. The fibers are then drawn on a rotating mandrel to steer the fiber orientation. The fiber drawing process generates fiber elongation, which decreases the fiber diameter while enhancing its strength. PLC is a semicrystalline polymer, thus the scaffolds' mechanical properties and biodegradation will highly dependent on the fibers' diameters and crystallinity. Meanwhile, the dimension and microstructure of melt-drawn PLC must be controllable in terms of different processing parameters, particularly the melt-drawing speed. To verify this hypothesis, the aim of this work is to fabricate the PLC microfibers by melt-drawing and then systematically study the influences of melt-drawing speeds on their crystallinity and thermal properties. The mechanisms underlying the change in the crystalline structure of the PLC will be examined in detail before and after melt-drawing, to better understand the structural evolution during the fabrication of this microfibrinous scaffold. Additionally, the tensile properties of the microfibers will be studied to determine the relationship between the drawing speeds and the mechanical properties.

4.2 Materials and methods

4.2.1 Crystallinity analysis

To study the crystallinity in melt-drawn PLC, PLC microfibrinous scaffolds were drawn at melt-drawing speeds of 0.24, 0.47, 0.94, 1.88 and 3.77 m/s as

described in Section 3.2.3. PLC flat sheets were hot pressed as described in Section 3.2.1.

Fourier transform infrared (FTIR)

FTIR spectroscopy was used to determine the chemical functionalities of PLC and analyze any structural changes that might have occur due to the melt-drawing process. The chemical functionalities of the samples were determined by an attenuated total reflectance (ATR) cell on the FTIR spectrophotometer (Thermo Scientific™ Nicolet™ 6700) over the range between 4000 and 500 cm^{-1} at 4 cm^{-1} resolutions, averaging 32 scans. All spectra were recorded at room temperature. PLC flat sheets were fabricated as control.

X-ray diffraction (XRD)

XRD technique was used to identify the crystalline structures of the pristine PLC and the melt-drawn PLC. Samples were examined using a Philips PW-1830 x-ray diffractometer with Cu K α radiation ($\lambda = 0.15418 \text{ nm}$) over the $2\theta = 10\text{-}35^\circ$ with a step size of 0.02° . Incident beam was parallel to the fiber direction of the melt-drawn samples, while the pristine PLC pellets were randomly placed over the sample holder. The diffraction peaks (in 2θ) were analyzed using the HighScore software from PANalytical. Crystallite sizes were computed from the full width at half maximum (FWHM) and Bragg angle (θ) according to the Scherrer's formula [241].

Differential scanning calorimeter (DSC)

The thermal behavior of the pristine PLC pellets and the melt-drawn fibers were tested on a DSC (TA Instruments, Q200). Samples of 15-20 mg were cooled down to -10°C and heated to 150°C at $5^\circ\text{C}/\text{min}$ under nitrogen purge. This was used to determine the T_g , the T_m , the enthalpy of fusion (ΔH_f), and

estimate the degree of crystallinity (X_c) of the pristine PLC and the melt-drawn samples. TA Instruments Universal Analysis 2000 software package was used to identify T_g , T_m and measure ΔH_f .

4.2.2 Tensile testing for PLC rings

Tensile tests were performed to determine stiffness, ultimate tensile strengths (UTS) and elongation of melt-drawn PLC samples in the radial direction by using a modified ASTM D1414 rubber O-ring tensile strength testing. PLC microfibrous rings were drawn with a mandrel size of 30 mm diameter and at melt-drawing speeds of 0.24, 0.94 and 3.77 m/s, without moving the melt-holder transversely as shown in Figure 4.1. It is highly challenging to fabricate samples with the exact same cross-sectional area. Thus, two groups of ring samples were fabricated by fixing (a) total time used to fabricate the samples and (b) number of rotations or number of layers. The first group of samples were fabricated by melt-drawing for 1 min which hereinafter named as $A_{0.24}$, $A_{0.94}$, and $A_{3.77}$ corresponding to their respective drawing speeds. The samples $A_{0.24}$, $A_{0.94}$, and $A_{3.77}$ have almost the same weight at 0.2 g. The other set of ring samples were fabricated by melt-drawing for 2400 rotations or 2400 layers which are

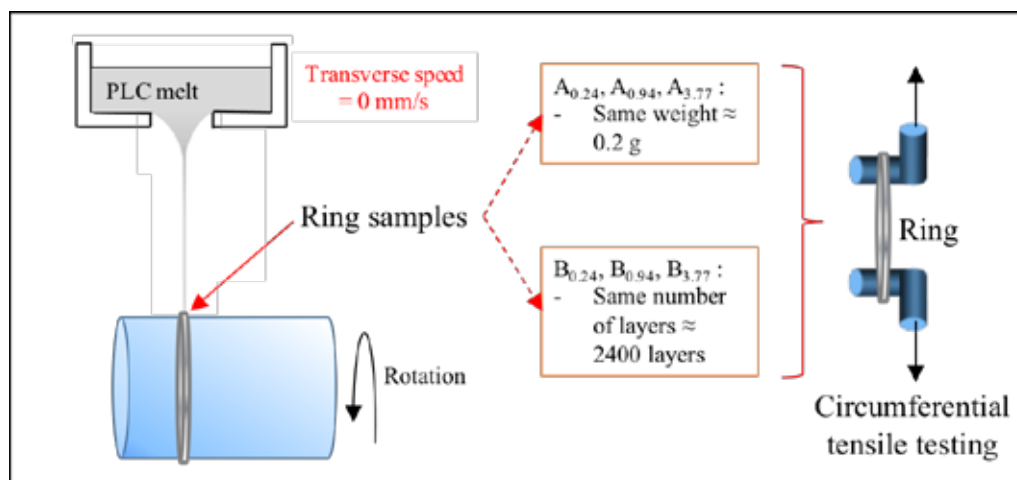


Figure 4.1. Illustration of fabrication process of various ring samples for circumferential tensile testing.

labeled B_{0.24}, B_{0.94}, and B_{3.77}, again corresponding to their respective drawing speeds. The second set of samples B_{0.24}, B_{0.94}, and B_{3.77} were fabricated with total melt-drawing times of 16 min, 4 min, and 1 min, respectively.

As-fabricated

The melt-drawn ring samples were stored in a dry box prior to the tensile tests. Tensile tests were carried out with an Instron Universal Testing Machine (Model 5569). The samples (n=3) were mounted between two metallic arms as described by Shazly T. *et al.* [242]. The samples were subjected to monotonic uniaxial extension by applying a displacement at 20 mm/min. The UTS tangent modulus at 40% elongation, and elongation at break were computed from the tensile stress–strain curves. Tangent modulus at the 40% elongation was computed as it is closely related to the esophageal properties *in vivo* [29].

Moisturized PLC rings

To investigate the effect of moisture absorption on the tensile properties, samples of A_{0.24}, A_{0.94}, A_{3.77} were conditioned indirectly at humidity in a refrigerator at 4 °C before tensile tests, as described in Section 3.2.1. After 3 days, these moisturized samples were taken out and incubated to room temperature before tensile tests.

Cyclic tensile testing

Cyclic tensile testing was conducted to mimic the esophagus condition *in vivo*. The purpose of the test is to verify if the circumference of the scaffold could return to its original dimensions after a bolus of normal size pass through the construct with a normal strain of 50% [56]. A_{0.24}, A_{0.94}, A_{3.77} were immersed in PBS at 37 °C for 24 h prior to cyclic tensile testing. The samples were tap dried and subjected to cyclic uniaxial extension by applying displacement at 5 mm/min

up to 50% elongation for 10 cycles. The initial and final ring diameters were measured using a Vernier caliper.

4.2.3 Planar tensile testing

Tubular scaffolds were fabricated using a melt-drawing speed of 0.94 m/s as described in Section 3.2.3. Briefly, a tubular scaffold formed when melt holder moved transversely along the length of 20 mm and distributed the microfibers on the mandrel layer by layer. Planar tensile tests were performed on rectangular strips of 20 mm (length) x 5 mm (width) to determine the tensile properties of samples at two directions, namely the circumferential and the longitudinal directions, as shown in Figure 4.2. The average Young's modulus, UTS and maximum elongation of the samples were computed from the stress-strain curves.

Three different types of tubular scaffolds were fabricated: the first and second types of samples were fabricated using transverse speed, $v_t = 0.7$ mm/s for 10 layers (time: 285 s) and 20 layers (time: 571 s), respectively; the third type of samples were fabricated using $v_{t1} = 0.7$ mm/s for 5 layers (time: 142 s), followed by $v_{t2} = 4.0$ mm/s for 30 layers (time: 150 s) (total time: 292 s). Note that transverse speeds of 0.7 mm/s and 4.0 mm/s were the minimum and maximum limits of the melt-drawing set-up, respectively. The first, second, and third types of samples were named "10L_0.7 mm/s", "20L_0.7 mm/s", and "5L_0.7 mm/s + 30L_4.0 mm/s", respectively.

The first two sets of samples were fabricated using the slowest transverse speed (0.7 mm/s) of the set-up, which was shown to create highly aligned fibers in circumferential direction in Section 3.3.3. The samples were thought to be strong circumferentially but weak longitudinally. By varying the sample

thickness between 10L_0.7 mm/s and 20L_0.7 mm/s, their tensile properties were examined.

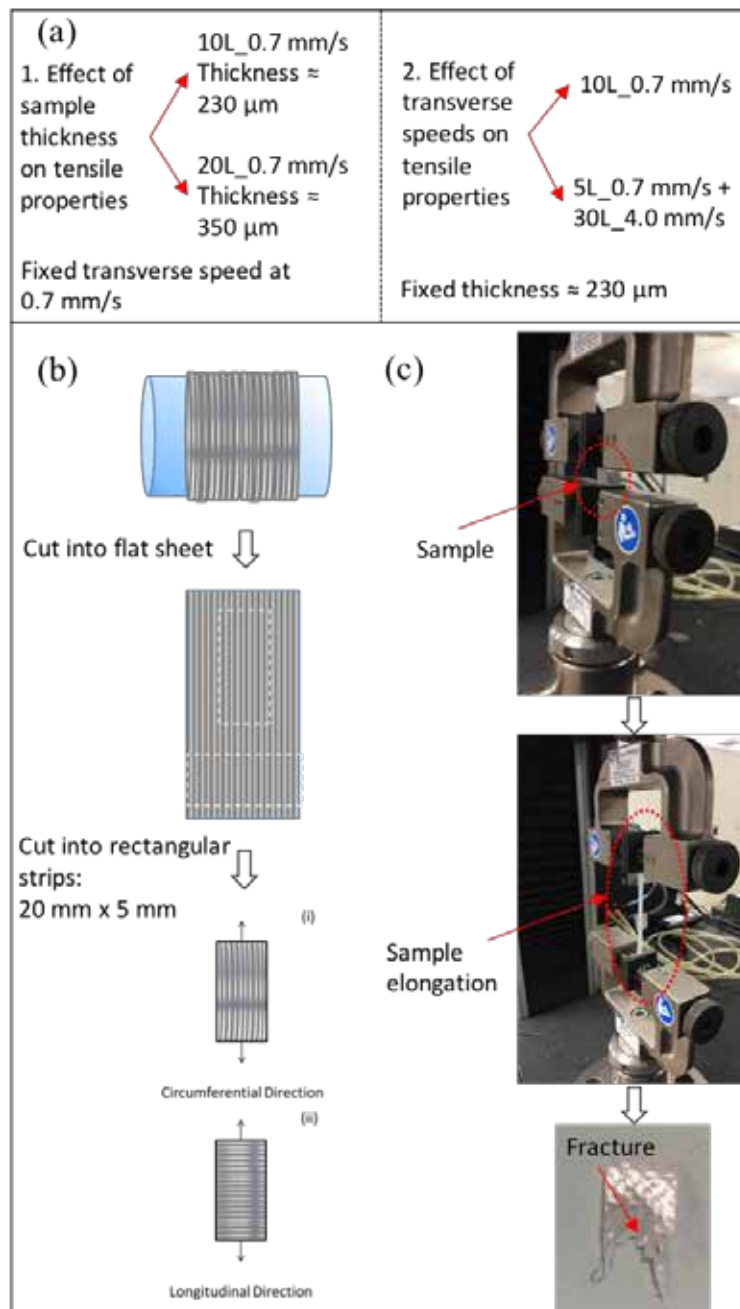


Figure 4.2. (a) Classification of three different types of samples fabricated for planar tensile testing. (b) Illustration of samples preparation for circumferential and longitudinal samples for planar tensile testing (c) Planar tensile testing process for flat scaffold samples.

Meanwhile, the third set of samples were fabricated using the slowest transverse speed (0.7 mm/s) on the lumen side, followed by the fastest transverse speed (4.0 mm/s) on the outer side of the tube. It was postulated that the highly-

aligned fibers will be formed in the lumen, and the crisscross fibers could be formed on the tubes' external surface. This structure might improve the tensile properties of the scaffold in longitudinal direction. By controlling the sample thickness of 5L_0.7 mm/s + 30L_4.0 mm/s to be similar to the 10L_0.7 mm/s, tensile properties were compared between the samples.

4.2.4 Scaffold fabrication with varying dimensions

PLC scaffolds with different diameters were fabricated using different mandrel sizes. To vary the scaffold thickness, PLC were melt-drawn for different number of layers. Meanwhile, the fiber sizes can be varied by using different melt-drawing speeds as discussed in Section 3.3.3. Spacing between fiber and the fiber orientation may be customized by changing the transverse speed of the melt-holder.

4.2.5 Statistical Analysis

All data are expressed as means \pm SD. Statistical differences were evaluated by one-way ANOVA analysis coupled with the Tukey's test. Differences were statistically significant when $p \leq 0.05$ and greatly significant when $p \leq 0.001$.

4.3 Results

4.3.1 Crystalline structure and crystallinity

Fourier transform infrared (FTIR)

The FTIR spectra recorded from the flat PLC sheet and the melt-drawn PLC samples are compared in Figure 4.3.

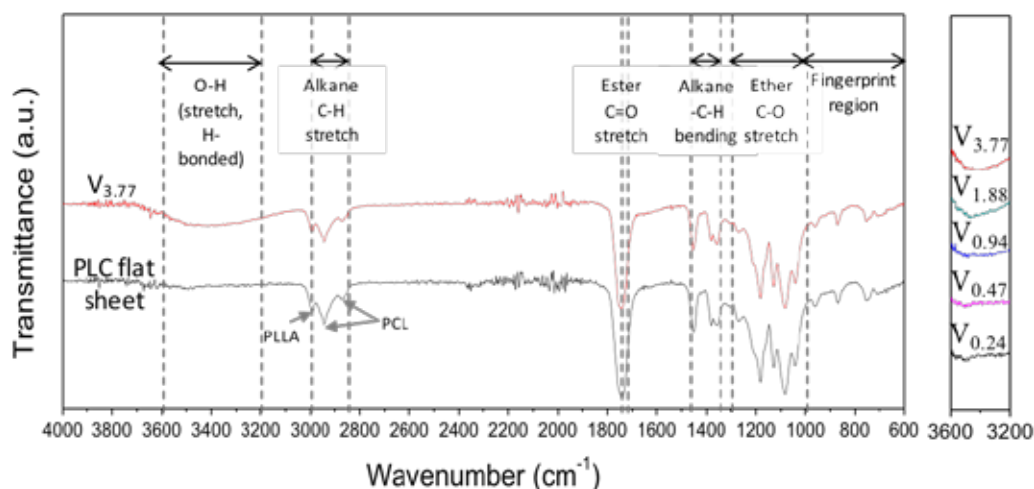
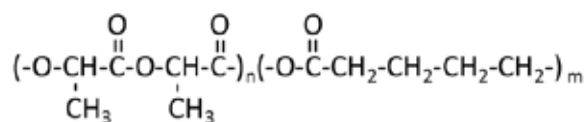


Figure 4.3. FTIR spectra of PLC flat sheet and melt-drawn PLC samples.

The spectra of the semicrystalline PLC exhibit the absorption bands of linear aliphatic polyester, which is consistent with its structure as follows:



Both spectra revealed the characteristic ester absorbance peaks at 1743 cm^{-1} for the stretching vibration of the C=O bonds. The three absorbance peaks occurred at 1084, 1128, and 1181 cm^{-1} due to the stretching of the C–O–C bonds. Strong and broad absorbance from 3200 to 3600 cm^{-1} were attributed to the stretching vibration of the –OH bonds. The absorbance peaks corresponding to the C–H and the CH₃ of LA units appeared at 2993 and 1045 cm^{-1} , respectively. The absorbance peaks found at 2873 and 2944 cm^{-1} were due to the stretching of the C–H bonds in CL units. It was observed that the broad absorbance valley at 3200 – 3600 cm^{-1} occurs, due to the stretching vibration of –OH bond, and increased in the intensity when melt-drawing speed increased. The results suggested that it was more prone to form hydrophilic bonds on the fiber surfaces with the decreasing fiber diameters.

X-ray diffraction (XRD)

Figure 4.4 shows the XRD patterns are shown in between 10 and 35° in 2 θ of the pristine and the melt-drawn samples. It was found that all the samples exhibited diffraction peaks that corresponding to and consistent with the orthorhombic α -form of LA crystal structure, with unit cell dimensions of $a = 1.05$ nm, $b = 0.61$ nm, and $c = 2.88$ nm that were suggested by Kobayashi *et al.* [243]. The α -LA peaks were indexed in Figure 4.4. Moreover, there were another two diffraction peaks indexed β that were in good agreement with another orthorhombic crystal structure, reported as the β -form of LA crystal [244]. Its unit cell dimensions were $a = 1.03$ nm, $b = 1.82$ nm, and $c = 0.90$ nm.

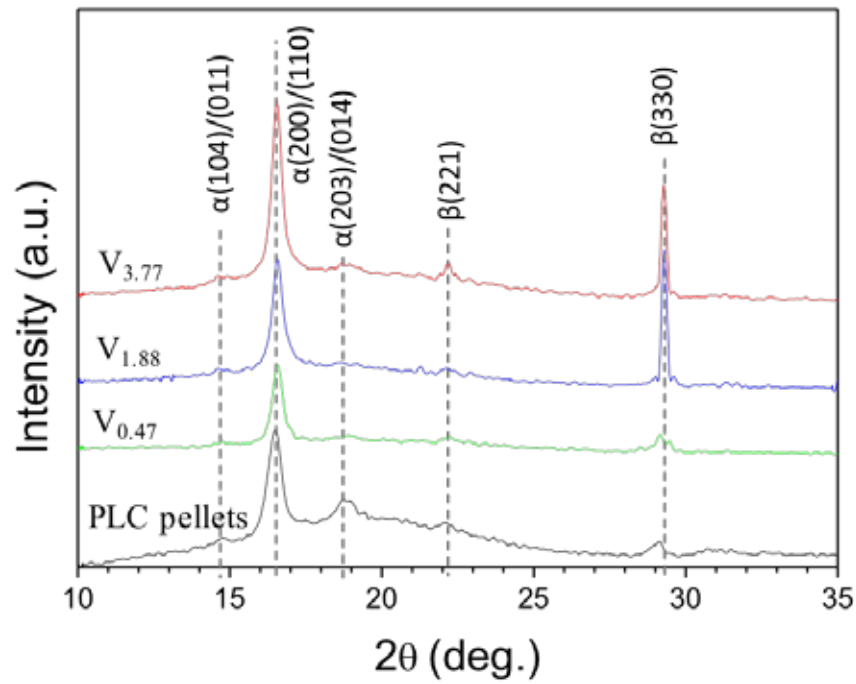


Figure 4.4. XRD patterns for pristine PLC pellets and melt-drawn PLC

Differential scanning calorimeter (DSC)

Figure 4.5 presents DSC thermograms of the pristine PLC pellets and the melt-drawn PLC fibers. The T_g of the pristine PLC was observed to be in the range of 10.2 - 17.3 °C, whereas the T_g of the PLC microfibers was found to

decrease from 16.5 - 22.4 °C ($V_{0.24}$) to 8.6 - 16.8 °C ($V_{3.77}$) as the melt-drawing speed increases. It was noted that all the thermograms exhibited two melting peaks. These melting peaks were found in between T_m of PCL ($T_m = -60$ °C [245]) and PLLA ($T_m = 175$ -178 °C [245]). The lower melting peak ($T_{m,\beta}$) was attributed to the melting of β -form crystals of LA (β -LA), and the higher peak ($T_{m,\alpha}$) was owing to the melting of α -form crystals of LA (α -LA), as it was reported that the α -LA is more stable than the β -LA [244]. The pristine PLC pellet showed a small peak of $T_{m,\beta}$ at ~52 °C in addition to the main peak $T_{m,\alpha}$ at ~109 °C. With increasing melt-drawing speeds, $T_{m,\beta}$ was observed to shift to a higher temperature and $T_{m,\alpha}$ shifted to a lower temperature.

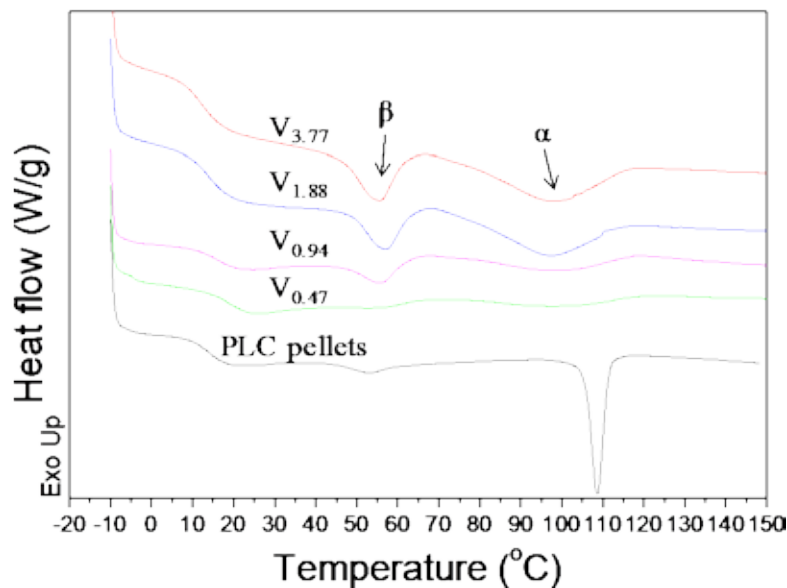


Figure 4.5. DSC thermograms of the pristine PLC pellets and the melt-drawn PLC samples

4.3.2 Tensile properties of PLC rings

The tensile stress-strain curves of the melt drawn PLC rings are presented in Figure 4.6. All the samples showed the typical stress-strain curves of rubbery materials. It is clearly seen from Figure 4.6 that the $A_{0.24}$, $A_{0.94}$, and $A_{3.77}$ (A series) samples have obvious yield points in the tensile stress-strain curves but $B_{0.24}$,

B_{0.94}, and B_{3.77} (B series) samples do not have. Young's moduli of these B series samples were significantly lower than that of the A series samples.

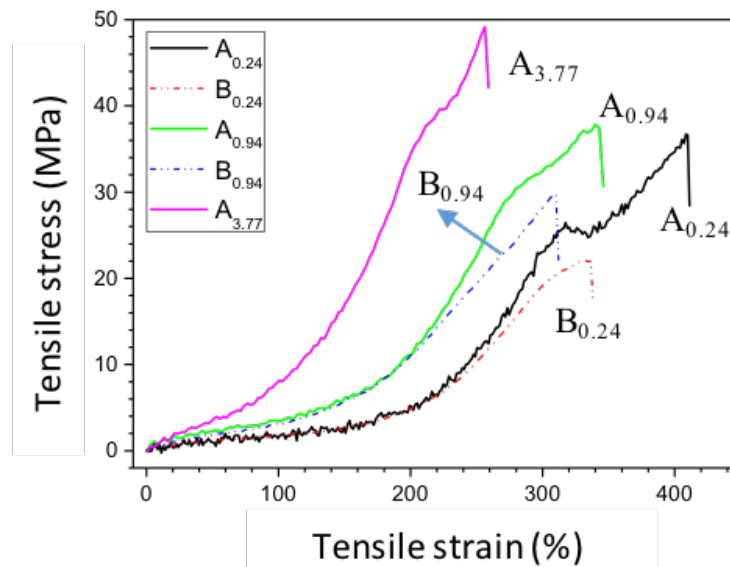


Figure 4.6. Engineering stress–engineering strain curves for PLC rings with varying melt-drawing speeds. Note: A_{3.77} and B_{3.77} refer to the same set of samples.

Moisturized samples were compared to the dry samples as illustrated in Figure 4.7. PLC is highly hygroscopic, so this high moisture content would affect

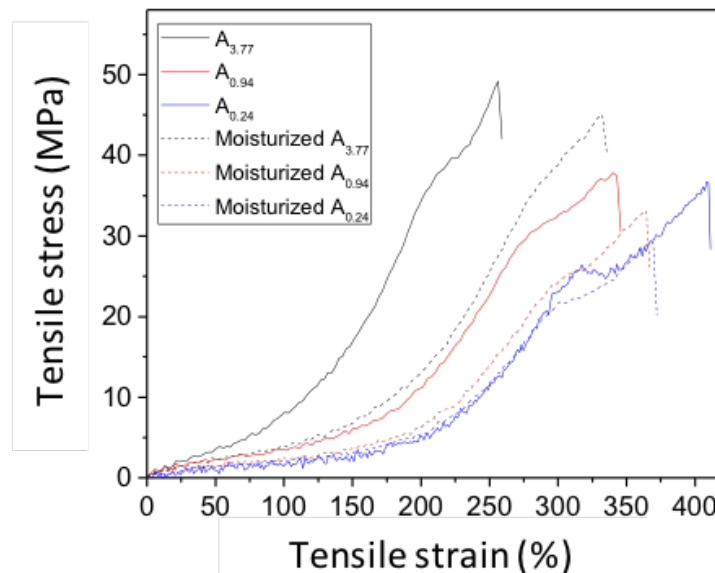


Figure 4.7. Engineering stress–engineering strain curves for dry and moisturized PLC rings with varying melt-drawing speeds.

samples' moduli. The tangent modulus at the 40% elongation of A_{0.94} and A_{3.77} showed a significant decrease after moisturized. Nevertheless, nearly all the moisturized samples had no significant difference in their UTS and elongation at break when compared to the dry samples.

The UTS, tangent modulus at the 40% elongation, and elongation at break of the samples were shown in Figure 4.8. It is noted that A_{3.77} and B_{3.77} refer to the same set of samples. The error bars represent the SD for n= 3, and *P = 0.05 and *** P = 0.001 by ANOVA followed by Tukey ' s tests when comparing within samples with the same melt-drawing speed. It was illustrated that there was a significant drop in UTS and maximum elongation when comparing between the dry samples A_{0.24} and B_{0.24}. The lower tensile properties of B series samples might be due to the formation of more structural defects or undesirable structures during fabrication, such as fiber misalignment and poor fusion of fibers.

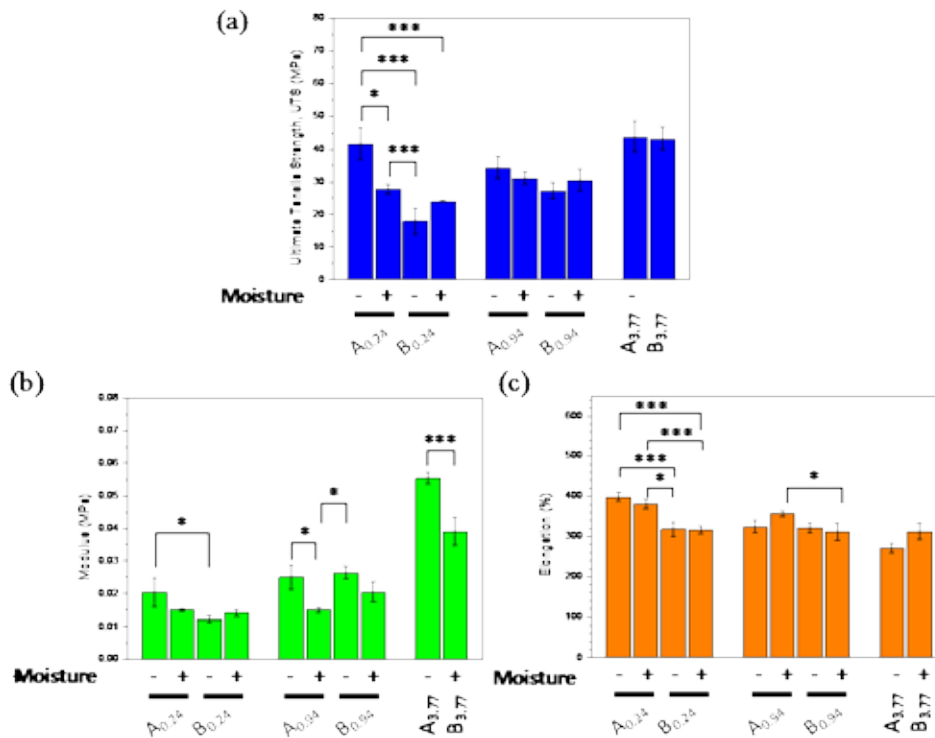


Figure 4.8. Histograms showing the comparison of (a) UTS, (b) tangent modulus at 40% elongation, and (c) elongation properties of the PLC rings (dry and moisturized) with varying melt-drawing speeds.

The cyclic tensile test results are shown in Figure 4.9. The $A_{0.94}$ and $A_{3.77}$ showed no obvious differences in their recovery at each cycle. Also, $A_{0.24}$ recovered very slowly. After 10 cycles, all the tested samples recovered to their original diameters.

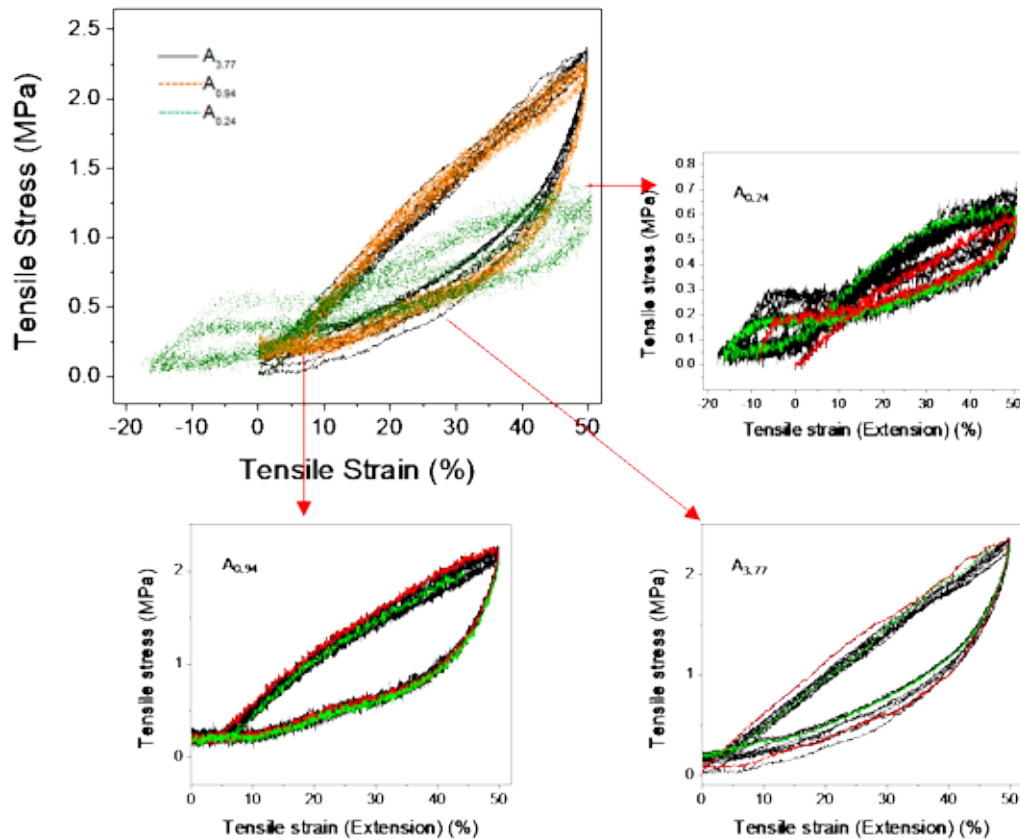


Figure 4.9. Cyclic tensile engineering stress–engineering strain curves for PLC rings with varying melt-drawing speeds. The results were shown separately, where each red line shows the first cycle and each green line shows the 10th cycle.

4.3.3 Scaffolds' planar tensile properties

2D flat sheet samples cut from tubular scaffolds were shown in Figure 4.10 (a). Samples 10L_0.7 mm/s and 20L_0.7 mm/s show highly aligned fibers, while 5L_0.7 mm/s+30L_4.0 mm/s samples show aligned fibers in the luminal side but slightly wavy pattern in the outer tubular surface. Due to the insufficient transverse speed provided by the current melt-drawing set-up, the highest

transverse speed achievable (4.0 mm/s) is still low to form an obvious crisscross fiber structure.

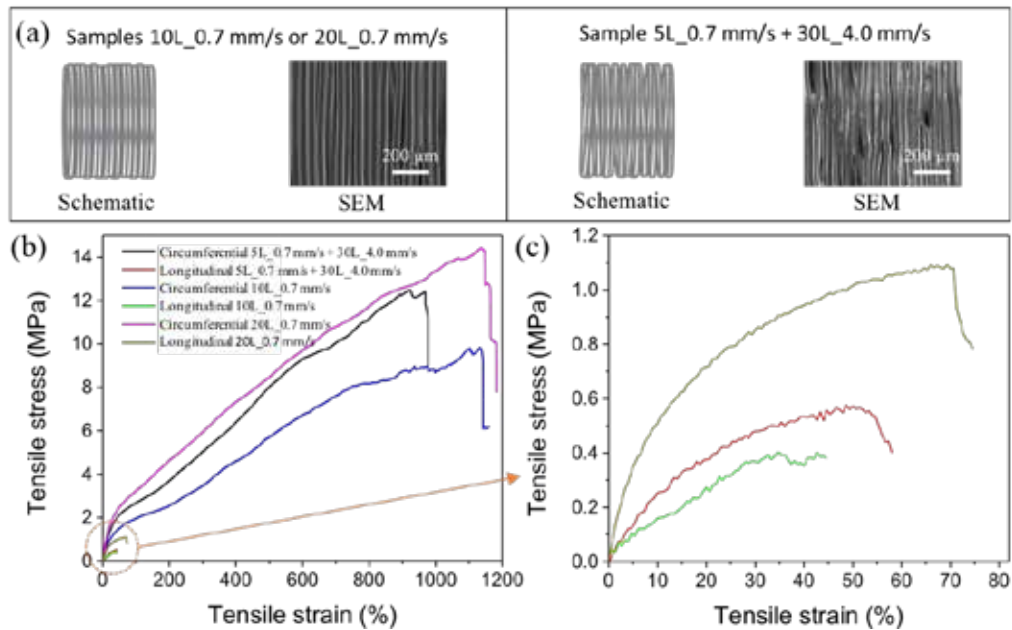


Figure 4.10. (a) Schematic illustrations and SEM images illustrating the fiber arrangement of different samples. Planar tensile stress-strain results of the 10L_0.7 mm/s, 20L_0.7 mm/s and 5L_0.7 mm/s+30L_4.0 mm/s samples in (b) circumferential and (c) longitudinal directions.

The three types of samples, i.e. 10L_0.7 mm/s, 20L_0.7 mm/s, and 5L_0.7 mm/s+30L_4.0 mm/s were tensile tested in two directions i.e. circumferential and longitudinal direction. The planar tensile test results are shown in Figure 4.10 (b) and tabulated in Table 3. It was observed that the tensile properties increased with the thickness of the scaffolds. However, the 20L_0.7 mm/s samples of (average sample thickness: 0.378 mm) was too thick when compared to the endomuscular layer (~0.250 mm) of the esophagus [46]. 10L_0.7 mm/s (average sample thickness: 0.224 mm) and 5L_0.7 mm/s+30L_4.0 mm/s (average sample thickness: 0.245 mm) showed comparable thickness to the native esophageal endomuscular layer [46]. By fabricating the samples in a combination of slowest and fastest transverse speeds (5L_0.7

mm/s+30L_4.0 mm/s), tensile properties were improved when compared to the samples fabricated by a transverse speed of 0.7 mm/s (10L_0.7 mm/s).

Table 3. Tensile properties of the fabricated scaffolds as compared to the native esophagus.

	Native esophagus	10L_0.7 mm/s	20L_0.7 mm/s	5L_0.7 mm/s+ 30L_4.0 mm/s
UTS Circumferential (Mpa)	1.41 ± 0.05	8.94 ± 0.03	14.09 ± 0.32	12.50 ± 0.26
UTS Longitudinal (Mpa)	2.19 ± 0.06	0.39 ± 0.03	1.09 ± 0.03	0.56 ± 0.01
Modulus Circumferential (Mpa)	1.44 ± 0.06	1.24 ± 0.24	1.75 ± 0.06	1.45 ± 0.12
Modulus Longitudinal (Mpa)	2.30 ± 0.09	1.11 ± 0.01	4.24 ± 0.11	2.24 ± 0.02
Max Elongation Circumferential (%)	83	1140	1140	910
Max Elongation Longitudinal (%)	70	35	70	55

4.3.4 Customization of scaffold dimensions

Topographical control of the scaffold is one of the advantage of this fabrication technique. Figure 4.11 shows the PLC tubular scaffolds with different

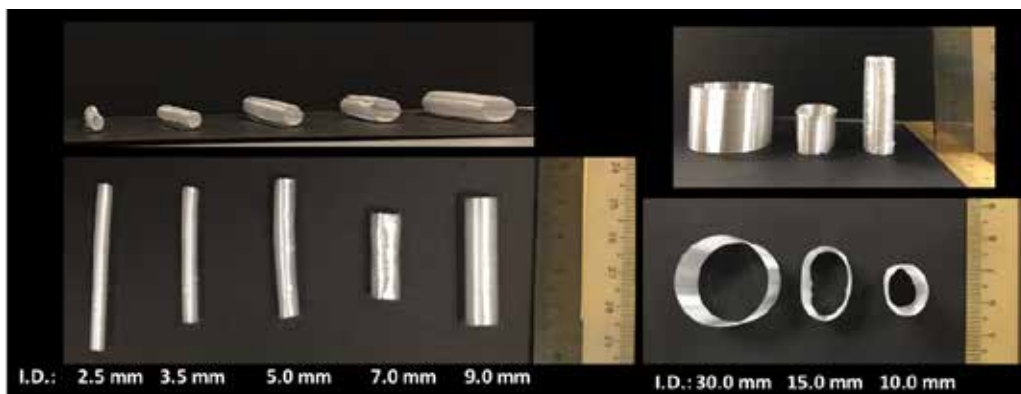


Figure 4.11. Pictures of scaffolds fabricated with different inner diameters (ranging from 2.5 mm to 30 mm) and different lengths (ranging from 12 mm to 45 mm).

dimensions, i.e. diameter and length. These mandrels were designed on a computer aided design (CAD) system using SOLIDWORKS and then 3D printed. The 3D printer used in this study was the PolyJet (Objet Eden350V; Stratasys). The wall thickness of the scaffold can also be varied according to the number of layers of the PLC melt-drawn onto the surface of the mandrel. For example, the V_{0.94} samples fabricated with 10 layers and 20 layers would have wall thicknesses of 224 μm and 378 μm , respectively. These demonstrated the possibility to produce a size-customizable scaffold for a specific patient.

4.4 Discussion

Semicrystalline polymers have regular repeating units which allow the polymer chains to fold into 3D regular structures that are called crystallites [245]. In general, high crystallinity would lead to a high tensile strength and modulus (stiffness). Consequently, it is imperative to study the evolution of crystallinity for PLC during the melt-drawing process. FTIR absorbance peaks at 2944, 2873, 1382, and 960 cm^{-1} in all the tested samples and these correspond to the amorphous segments of CL [246]. There was no crystalline CL absorbance peak, suggesting that CL only contributes to the amorphous portion in this copolymer.

CL crystal was not detected by XRD in the pristine PLC, as its two distinct diffraction peaks at 21.5° and 23.8° were not found. Moreover, CL units were also not crystallized after the melt-drawing process based on the XRD results. These findings are in good agreement with the FTIR results. A possible reason why CL is not crystallized is because the percentage of CL in this random copolymer is low. This is an important finding as CL crystals take a long time (up to 3 years) to degrade [220,247], which is not desirable in the TE applications.

LA crystals have been extensively investigated previously by other researchers. Literatures reported that fibrous PLLA typically contained two crystal structures, namely the α - and the β -form. In general, the α form structure is believed to grow upon melting or during cold crystallization [248]. When the semicrystalline PLLA comprised of α -form crystals was drawn uniaxial near the T_m , some of the α -LA would be transformed into the oriented β -form structure [244]. In this study, fiber was directly drawn from amorphous PLC melt, which was different from conventional multistep melt spinning with subsequent solid fiber drawing. The XRD patterns of the pristine PLC pellets indicated that there were some β -LA crystals in addition to the predominant α -LA crystals. It is known that the polymer pellets are usually manufactured via a hot-extrusion process with some extend of drawing. That may lead to the formation of some of the β -form crystals in the pristine PLC. The main peaks for α -LA crystals [249,250] were indexed in the XRD results. It was worth noting that all the distinct peaks of β -LA crystals [244] were indexed in the results while the most characteristic $\beta(200)$ peak was not labelled. As the crystallography spacing (d) of $\beta(200)$ was slightly smaller than that of $\alpha(200)$ and/or $\alpha(110)$ [244], it would have marginally larger 2θ ($\sim 17^\circ$) in the XRD pattern. This explained why the $\alpha(200)/(110)$ peak was asymmetrical as the weak $\beta(200)$ peak was located at the higher 2θ . After melt-drawing, the samples exhibited similar XRD patterns to those of the pristine PLC. Nevertheless, intensities of $\alpha(110)$ and $\beta(330)$ peaks were increased notably after melt-drawing. It indicated that (110) was the preferred crystallographic plane in the melt-drawn samples. In addition, the intensities of $\alpha(110)$ and $\beta(330)$ peaks were found to be increasingly stronger in the samples fabricated with higher melt-drawing speeds. Apparently, more

texture (or preferred crystallographic orientation) occurred with the increase in melt-drawing speed.

The T_g observed in the DSC curves should be associated with the hybrid amorphous LA/CL phase. In samples with low melt-drawing speeds ($V_{0.24}$ - $V_{0.94}$), the T_g shifted to a higher temperature as compared to that of the pristine PLC. It is attributed to the incorporation of more LA units in the amorphous LA/CL phase because LA has a higher T_g compare to that of CL. Therefore, samples of $V_{0.24}$ - $V_{0.94}$ should contain more amorphous structures than the pristine PLC. Moreover, T_g of melt-drawn PLC was found to drop down with increasing melt-drawing speeds. The LA content of the LA/CL hybrid phase reduced along with the increase in melt-drawing speed. This was because of the incorporation of LA units to the LA crystals. It can be deduced that crystallinity of the melt-drawn PLC increases with the decrease in the fiber diameter. $T_{m,\alpha}$ of the melt-drawn PLC microfibers was observed to decrease with the increasing melt-drawing speed. This was likely due to the gradual disintegration of the α -crystals. By contrast, the increase of the $T_{m,\beta}$ with the increasing melt-drawing speed might be due to the increase in the β -LA crystallite size. The crystallite size that computed from the $\beta(330)$ peaks in XRD patterns was found to increase with the increasing melt-drawing speed. The β -LA crystallite size of the pristine PLC pellets was 37.6 nm, while it increased up to 44.7 nm in the $V_{3.77}$ sample. The α crystallite size could not be directly computed from the $\alpha(110)$ peak using the same methodology because there were several peaks observed that were overlapping with each other.

The percentage of crystallinity (X_c) of the melt-drawn PLC microfibers was investigated from the DSC thermograms based on the following equation [248]:

$$x_c (\%) = 100\% \times \left(\frac{\Delta H_f}{\Delta H_f^\circ} \right), \quad (10)$$

where ΔH_f is the enthalpy of fusion of sample, and ΔH_f° is the enthalpy of fusion of 100% crystal. As shown beforehand by FTIR and XRD that only the LA units in the PLC will be crystallized, the X_c can be calculated by the deduced equation [251,252]:

$$x_c (\text{Total}) (\%) = \frac{100\% \times \left(\frac{\Delta H_{f,\beta}}{\Delta H_{f,\beta}^\circ} + \frac{\Delta H_{f,\alpha}}{\Delta H_{f,\alpha}^\circ} \right)}{LA^*}, \quad (11)$$

where $\Delta H_{f,\beta}$ and $\Delta H_{f,\alpha}$ are the enthalpy of fusion at $T_{m,\beta}$ and $T_{m,\alpha}$, respectively; $\Delta H_{f,\beta}^\circ$ and $\Delta H_{f,\alpha}^\circ$ are the enthalpy of fusion of 100% β - and α -LA crystals, respectively; and LA^* is the molar mass fraction of LA in the copolymer. LA^* used in this calculation was 0.78. The most commonly used value for $\Delta H_{f,\alpha}^\circ$ is 93 J/g that was estimated by Fischer *et al.* [251]; and $\Delta H_{f,\beta}^\circ$ was calculated by Sawai *et al.* to be 124 J/g [252]. These two values were used in the calculation.

Figure 4.12 shows the crystallinity variation with different melt-drawing speeds, including the variation of crystallinity of α -LA ($X_{c,\alpha}$) and crystallinity of β -LA ($X_{c,\beta}$) with melt-drawing speeds. Note that *** $P < 0.001$ by ANOVA followed by Tukey's tests when comparing $X_{c (\text{Total})}$ with the melt drawing speeds. The cast PLC was defined as the one with a melt-drawing speed of zero in the results. $\Delta H_{f,\beta}$ and $\Delta H_{f,\alpha}$ were not detected in the cast PLC probably due to the inability of LA to form crystals during melt-casting.

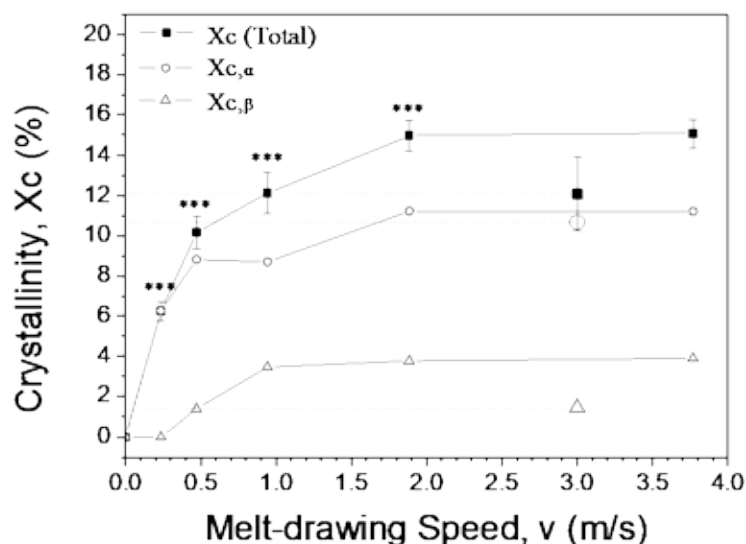


Figure 4.12. Relationship between crystallinity (predicted from DSC) and melt-drawing speed. Crystallinity of the pristine PLC pellets is included (with horizontal dotted lines) for comparison.

A higher total crystallinity was clearly observed in the samples with a higher melt-drawing speed, which could be expected from the decrease of T_g . It suggested that the microfibers having a certain alignment of polymer chains would lead to obvious crystallization during melt-drawing. This was consistent with the XRD results showing that there was a preferred crystallization orientation exists. The crystallinity of both α -LA and β -LA was increased with the increase in melt-drawing speed, but remained almost constant at higher melt-drawing speeds. It was noted that $V_{1.88}$ and $V_{3.77}$ had a very close $X_{c,\alpha}$ to that of the pristine PLC. Crystallinity of the α -LA almost remained constant except the one at the very low melt-drawing speed, but their texture became increasingly pronounced after melt-drawing. Meanwhile, $X_{c,\beta}$ of the $V_{0.94}$, $V_{1.88}$ and $V_{3.77}$ are twice larger than that of the pristine PLC. Thus, it can be inferred that those LA in the hybrid amorphous LA/CL structures will be crystallized to form β -LA in the (110) plane after melt-drawing.

Based on the close observations, it was proposed that the crystallization of such an oriented melt would lead to a specific morphology known as fibrillar morphology [253]. The fibrillary morphology of the PLC microfibers in this work can be illustrated in Figure 4.13. The crystalline and amorphous regions were stacked in each microfibril. The LA crystallites in adjacent microfibrils were aligned parallel to each other. The interfibrillar region was comprised of extended but uncrystallized chains. The air-cooled PLC displays LA/CL amorphous structure. There were only α -LA crystallites formed when melt-drawing at a low melt-drawing speed, while both α - and β -LA crystallites formed at high melt-drawing speeds.

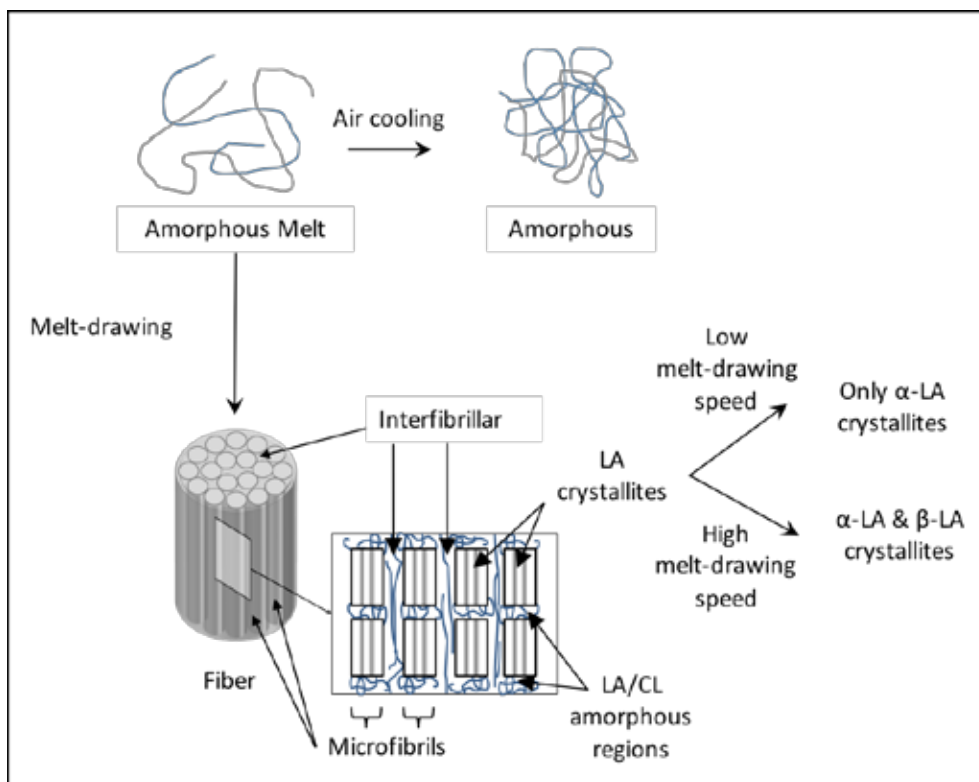


Figure 4.13. Schematic illustration of the structural evolution of PLC after melt-drawing and air cooling.

As illustrated in all the tensile stress-strain curves, the deformation behavior of the highly elastic PLC ring was like typical rubbery materials. PLC was originally not stretched and its polymer chains were entangled. When it

started to deform, the slippage of polymeric chains occurred with an initial short period of softening, followed by a long shear hardening. The softening of PLC at the very beginning was probably due to the existence of sliding distance in space [254]. The polymer chains were slowly aligned with the progress of deformation until the yield point by which the material started to deform permanently. Beyond the yield point, the hardening of the PLC at the high deformation level was due to the inextensibility where there was a sharp upturn before the fracture [255]. It was observed that the samples fabricated with lower melt-drawing speeds, especially those samples with a melt-drawing speed of 0.24 m/s, illustrated obvious serrated tensile stress-strain curves. This might be due to the structural heterogeneity in the PLC copolymer that consisted of both amorphous and crystalline components. This phenomenon became less pronounced due to a larger percentage of crystallinity in the samples at higher melt-drawing speeds.

Esophagus is an organ that is always subjected to varying stresses and strains especially in the circumferential direction. Mechanical properties of the TE scaffold are extremely important to its performance as a temporary construct when implanted *in vivo*. The mechanical properties of the scaffold, on the other hand, are closely linked to the crystallinity of the semicrystalline polymers. The tensile properties of PLC are plotted against the crystallinity of the samples in Figure 4.14. Note that *P = 0.05 and *** P = 0.001 by ANOVA followed by Tukey ' s tests when comparing the tensile properties of each set of samples with their crystallinity. Trends were clearly seen that most of the Young's moduli and UTS of PLC rings increased significantly with the increase in the crystallinity. Crystalline structures significantly enhanced the stiffness and strength of the PLC ring. PLC had a T_g below body temperature and room temperature, hence the

ductility of PLC scaffolds could be estimated at room temperature when they were implanted. Ductility for most of the samples decreased with the crystallinity % of PLC in this work. The T_g of PLC was shown to drop down with the increasing melt-drawing speeds, which caused a significant drop in ductility with the increasing crystallinity.

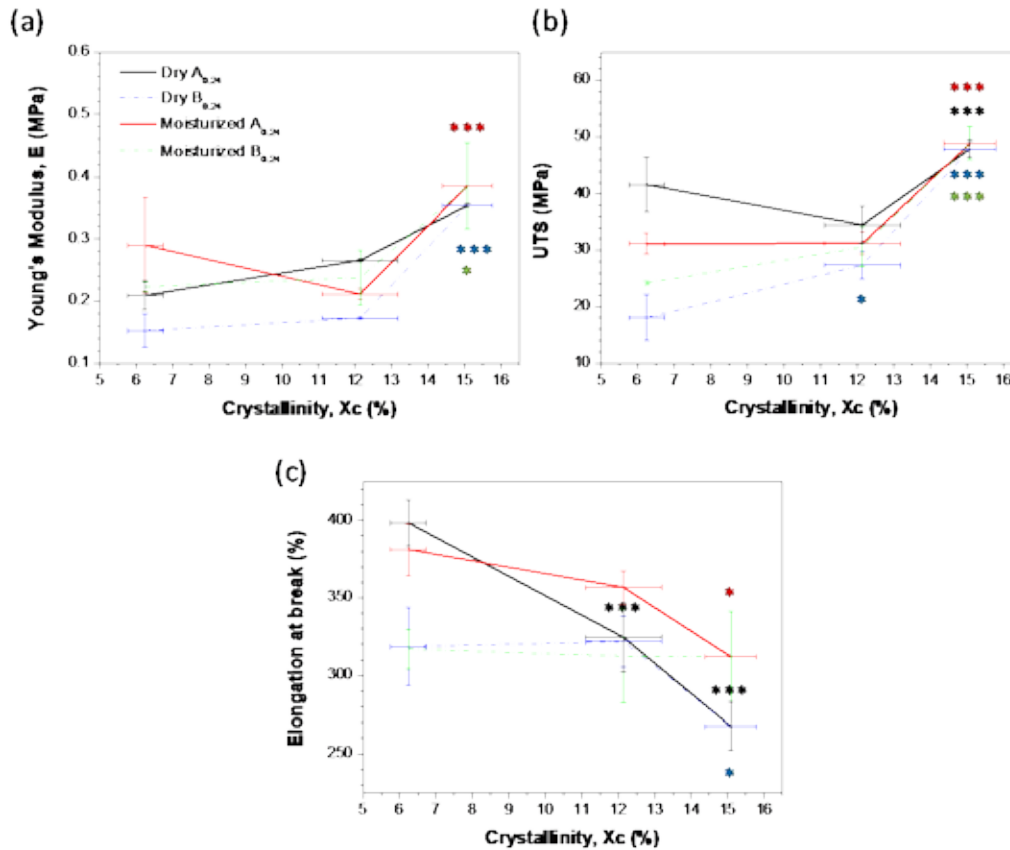


Figure 4.14. Relationship between (a) Young's modulus, (b) UTS, and (c) maximum elongation with samples' crystallinity.

The high moisture content in the hygroscopic polymers could often lead to negative effects on their mechanical properties [233]. The presence of water could act as a plasticizer and lower the T_g [245], which would affect the mechanical properties and the degradation rate [256]. In this work, the moisturized samples, however, showed no significant difference in their UTS and Young's modulus when compared to those of the dry samples. Ductility of the

PLC rings were consistent regardless of the moisture content although a lower T_g was observed in the moisturized samples. Nonetheless, the tangent modulus at the 40% elongation of $A_{0.94}$ and $A_{3.77}$ showed a significant decrease after being moisturized. This could be explained by the polymer plasticizing effect due to the moisture inside the polymer networks. At a low elongation, the PLC fibers would be deformed easily when it is moisturized.

The moisturized samples did not show significant reduction in tensile properties, which means that the PLC scaffold could be suitable to be implanted *in vivo* as the lumen of the esophagus would always be moistened by the secreted mucus. The scaffolds illustrated tangent modulus at the 40% elongation of 10-60 kPa and Young's modulus ranging from 200 to 350 kPa. According to Han *et al.* [257], MSCs cultured on a substrate with elasticity of around 1–500 kPa may express SMC markers because the elasticity of native muscles is ~10 kPa [52]. Without the soluble factors, MSCs differentiated towards the SMC lineage in Section 3.3.4. The matrix elasticity [52,239,257] might also be the reason for SMC differentiation in addition to the fiber alignment according to the previously described cell shape modulation theory [240]. Furthermore, all the rings returned to their original diameter lengths upon stretching for 50% strain for 10 cycles. The stretched $V_{0.94}$ and $V_{3.77}$ rings returned rapidly to their original length after released in all the cycles. These showed that they could be very useful as temporary esophageal prostheses.

Planar tensile test results in the two directions for human esophagus were reported and described in Section 2.1.2. In short, the average UTS were 2.19 ± 0.06 and 1.41 ± 0.05 MPa for longitudinal and circumferential esophageal samples, respectively [29]. Human esophagus illustrated an elastic modulus of

1.44 \pm 0.06 MPa, as compared to the modulus of 2.30 \pm 0.09 MPa in the longitudinal direction [29]. Here, in the planar tensile test results, the average UTS in the circumferential direction was \sim 10 MPa, which is obviously stronger than that of the esophagus. However, the UTS in longitudinal direction ranged from 0.4-1.0 MPa, which is comparatively weaker than the esophageal. Most of the samples failed through delamination in the longitudinal direction. Thin samples, i.e. 10L_0.7 mm/s and 5L_0.7 mm/s + 30L_4.0 mm/s, had thicknesses similar to the native esophageal endomuscular layer [46]. Slight improvement in the UTS was observed in the longitudinal direction of \sim 170 kPa when comparing 5L_0.7 mm/s+30L_4.0 mm/s samples to 10L_0.7 mm/s samples. Tensile properties in the longitudinal direction was improved by using a combination of different transverse speeds in the fabrication strategy. It was noted that the maximum transverse speed achievable by the current melt-drawing machine was 4.0 mm/s. Efforts need to be made to increase the melt-holder transverse speed such that obvious crisscross-patterned fibers can be made to further increase the scaffolds' tensile strength in the longitudinal direction. Meanwhile, the modulus of all the samples in circumferential direction were very close to those of the native esophagus. The modulus of 5L_0.7 mm/s+30L_4.0 mm/s sample in the longitudinal direction was comparable to that of the native esophagus.

PLC degrades in 12 to 24 months according to the manufacturer (Corbion Purac). The slow degradation rate allows the PLC scaffold to maintain its mechanical strength before tissue remodeling *in vivo*, which would eventually lead to a formation of normal tissue capable of self-support. On the other hand, CL do not form crystallites in the PLC. The degradation time of the copolymer of PLC is not as long as its homopolymers, i.e. PLLC and PCL, due to the

decrease in crystallinity and increase in water penetration [258]. Nevertheless, animal study is needed for a clearer indication of the scaffolds' behavior and degradation *in vivo*. Studies by Jeong *et al.* [258,259] showed that PLC 50:50 did not provoke foreign body reaction after *in vivo* transplantation in mice for up to 8 weeks. Tissue remodeled with smooth muscles growth and vascularization were observed. After 15 weeks of transplantation, the PLC scaffold's weight decreased to 81% of its original value in their studies.

Topographical control of the scaffold is one of the advantage of this fabrication technique, i.e. the scaffold can be customized to achieve the required properties of a scaffold. To demonstrate the general applicability of this technique towards tubular tissue TE, tubes were manufactured in a range from 2.5 mm to 30 mm inner diameters. The melt-drawing technique allows tubes to be formed with different diameters and lengths quickly and easily. Infants, for example, have much smaller esophageal diameter [260]. When a patient in need of a scaffold with a certain diameter, it can be manufactured with the same inner diameter. Definable wall thickness, which is controlled by number of layers of drawing, based on different portion of the esophagus can also be achieved. This kind of versatility positions these tubular scaffolds as a potentially viable new method of creating TE constructs.

4.5 Summary

The crystallinity, thermal and mechanical properties of the PLC fibers were investigated. The PLC experimented on was found to be semicrystalline. CL units formed amorphous chains in the PLC copolymer. On the contrary, LA units were crystallized, giving rise to a mixture of α - and β -form crystals. The crystallinity increased up to ~15 % with increasing melt-drawing speeds due to

strain-induced crystallization. There was a preferential crystallographic plane of (110) in the melt-drawn PLC fibers. An increase in β -LA crystallite size was noticed when its crystallinity was increased. A schematic illustration of the structural evolution of PLC after melt-drawing was provided based on extensive observation (see Figure 4.13).

The modulus and the strength were increased while the ductility was decreased with an increase in crystallinity of the PLC samples. Moisture would not degrade their overall tensile properties but affect their tangent modulus at low strains. The planar tensile test results showed that the tubular scaffolds exhibited similar tensile properties to those of the esophagus in circumferential direction. However, the longitudinal strength of the scaffold was still insufficient to replicate the native esophagus.

In terms of the ability to control properties of the scaffolds, combined with their relative ease of fabrication compared to other techniques, it is suggested that these tubular scaffolds can be an attractive candidate for tubular tissues TE applications. Furthermore, the melt-drawing method is shown to be a promising technique for microfiber fabrication with its simplicity and customizability. Tubular scaffolds with various dimensions, such as inner diameter, length and thickness, were successfully fabricated. The fiber diameters and tensile properties were tunable by varying melt-drawing speeds. These tailorable topographies and tensile properties showed that the additive-based scaffold fabrication technique was customizable in micro- and macro-scale for different tubular tissues. The merits of these scaffolds in TE were also exhibited by the findings that cells seeded onto the scaffolds *in vitro* showed excellent cell proliferation, distribution and alignment. To sum up, these results strongly

suggested that the melt-drawn PLC scaffolds would be a suitable substrate for TE of circular muscle layer in esophagus.

Chapter 5. Bioengineering of esophageal mucosa: A new bioink for 3D bioprinting

5.1 Introduction: A new bioink

In native esophagus, the epithelium is separated from the underlying lamina propria by a layer of basement membrane. The esophageal epithelial regeneration technique proposed aims to mimic the submicron and nano-scaled structure of the basement membrane [14,21] so that (i) epithelial cells can grow uniformly on the tissue engineered membrane; (ii) epithelial cells grow on the membrane, separated from the underlying stromal cells, but still allow the cells communication; (iii) protein can be deposited on the membrane; and (iv) the epithelium will be able to stratify into multiple layers [73]. It was acknowledged that there were fiber diameter limitations using the melt-drawing method. The melt-drawn fibers were in tens of micron but the basement membrane consists of submicron and nano-scaled structures [261]. Figure 5.1 illustrates the epithelial cells cultured on the fibrous scaffolds, where the arrows highlight the cells attached on the scaffold surface. Red arrow shows the cells grew into the scaffold, which is not desirable.

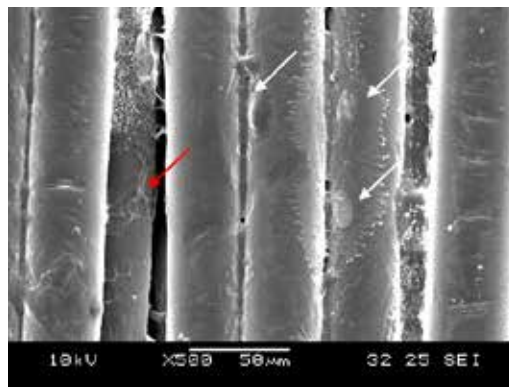


Figure 5.1. SEM image of human buccal epithelial cell TR146 cultured on V_{0.94} scaffold.



It was found that while the epithelial cells were able to attach onto the fibers, the scaffolds were also cell-permeable. This did not meet the requirement of epithelium TE as the scaffold should be impermeable to epithelial cells. The melt-drawn fibers are not able to mimic the basement membrane and support the epithelium stratification. In addition, the melt-drawing technique described was not able to produce tubes that could mimic mucosa folding. Alternatives are designed in this work to reproduce these critical structures. To create the patient personalized structures, additive fabrication is still the most feasible option. Among all the additive fabrication techniques, 3D bioprinting represents the most viable method to create these structures. Epithelium and fibroblasts will be delivered in different desired layers which could eliminate potential difficulties in cell seeding.

The commonly utilized bioinks in bioprinting, i.e. the cell-laden hydrogels and tissue spheroids or tissue strands, were reviewed. Hydrogels are generally too weak unless using a suitable strong cross-linking method which might induce DNA damage [214]. There are also difficulties in loading high cell density in hydrogels. On the other hand, it is a challenge to form and process tissue spheroids. The fabrication of scaffold-free tissue spheroids or strands which requires a large number of autologous cells from patient is difficult to realize in order to print large organs such as the esophagus [215].

Considering what is feasible for 3D bioprinting currently, in this work, a new bioink using cell-laden microscaffold is presented. The reasons behind the choice of selecting biodegradable cell microcarriers in bioinks are listed in Table 4 when comparing it to the use of the tissue spheroids. Polymer microcarriers, especially microspheres, are commonly utilized as injectable biomaterials for

clinically relevant applications, such as therapy for Parkinson's disease [262] and venous leg ulcers [263]. Most of the normal mammalian cells need substrates to adhere and proliferate [264]. These include the anchorage-dependent epithelium and fibroblasts. Here the porous microspheres provide high specific surface areas so that they allow the cells to attach, infiltrate and grow before an extrusion-based printing. The cells seeded on the microspheres will be expanded in stirred or perfused culture, and form cell-laden microspheres (CLMs) without further passaging.

Table 4. Comparison between the tissue spheroids and the cell-laden microspheres in their usage in 3D bioprinting.

	Tissue spheroid	Cell-laden microscaffolds
Components	<ul style="list-style-type: none"> • Tissue formed from cells. • Some rely on hydrogels/ natural ECM for the formation 	<ul style="list-style-type: none"> • Polymer microscaffolds/microcarriers with cells seeded
Illustration		
Utilization in 3D Bio/organ Printing	Tissue fusion (self-assembly)	Serve as mini scaffolds. Cell/tissue growth together with degradation of synthetic polymer. Tissue will eventually replace the original shape of 3D printed polymer/cell construct.
Advantages and disadvantages in 3D bioprinting	<p>Advantages:</p> <ul style="list-style-type: none"> • No/less additional materials involved • Slower cells fusion (during tissue spheroid formation) but faster tissue fusion after 3D printed • Lower throughput <p>Disadvantages:</p> <ul style="list-style-type: none"> • Requires a very high initial cell number • Most of the spheroids formation are not automated and rely on careful manual work • Difficult to obtain spheroids with narrow size distribution • Not all the cells can be self-aggregated • Extensive and uncontrollable shrinkage after tissue fusion 	<p>Advantages:</p> <ul style="list-style-type: none"> • Controllable fabrication of cell carriers with higher throughput by using widely recognized synthetic biomaterials • All types of cells can be cultured on the carriers • More controllable tissue/organ formation with less shrinkage • Requires lower initial cell number • Easily encapsulate necessary elements/nutrients inside microsphere for controlled release during tissue formation <p>Disadvantages:</p> <ul style="list-style-type: none"> • Mini scaffolds (additional materials) are needed • More steps are required to fabricate the microspheres • Slower tissue/organ formation

PLGA was chosen as a suitable material for fabricating the biodegradable porous microspheres. This is because its safety in clinically relevant applications has been well established [265] and it can be processed into highly porous microspheres with a controllable size range [102]. A highly porous microsphere is favourable for packing a high density of cells into the scaffold and achieving desired degradation after printing as compared to a full solid scaffold. Biomaterials with a controllable degradation time frame is also preferred as the scaffold materials.

Cells are aggregated in the porous microspheres and each of the microsphere represents a basic unit in the bioink. By exploiting this property, epithelium regeneration is enhanced as epithelium aggregate could improve cell-cell interactions [266] and this is beneficial for epithelium TE. These CLMs together with thin hydrogel encapsulation would act as the bioink for the 3D bioprinting of the epithelium. Fibroblasts would also be bioprinted, joining the mucosa layer to the melt-drawn PLC scaffold for regeneration of connective tissue.

The hydrogel encapsulation would lubricate the CLMs and then glue the microtissues together after printing upon gelation. Here, agarose hydrogel with low gelling temperature (less than 37 °C) was chosen for these purposes. The use of agarose hydrogel is not uncommon in TE scaffolds fabrication [267]. It has also been used in bioprinting but are usually printed as molds [145], due to its superb thermal properties, extrudability, and non-stickiness. Agarose exhibits pronounced hysteresis between the gelling and the melting [268], gels at below 18-42 °C and re-melts at above 60-90 °C. This property makes it to be very suitable to be bioprinted. Its gelling and melting temperatures depend on its end

groups. When submerged in water, agarose hydrogel has pore sizes of 0.3–0.4 mm when measured by atomic-force microscopy (AFM) [269], which will be very useful for epithelium regeneration and stratification. Despite its advantages, agarose is a polysaccharide and it lacks the arginyl-glycyl-aspartic acid (RGD) for cell attachment and proliferation. A study has shown that fibronectin, collagen I, and collagen IV can enhance the esophageal epithelial attachment [77]. Hence, type I collagen would be added here as a favoured adhesive substrate to make the agarose-collagen blend hydrogel (AC blend hydrogel) for better cell-affinity. The addition of type I collagen in the hydrogel could also improve its cell adhesion during culture.

5.2 Materials and methods

5.2.1 Materials

The materials used in this Chapter are the amorphous PLGA (PURASORB® PDLG 5010, Corbion, Netherland) with DL-lactide and glycolide in a 50/50 molar ratio, poly(vinyl alcohol) (PVA; Mowiol® 8-88; Sigma–Aldrich, St. Louis, MO, USA), agarose type IX-A with ultra-low gelling temperature (A2576; Sigma–Aldrich), collagen type I (3.34 mg/ml rat tail collagen, Corning®, USA), double-distilled water (ddH₂O, PURELAB Option-Q), PBS (P5368; Sigma–Aldrich), dichloromethane (DCM, AppliChem GmbH, Germany), sodium hydroxide (NaOH; 35274 FLUKA; Sigma–Aldrich), absolute ethanol (EtOH; Merck, Germany), high glucose DMEM medium (Gibco, UK), FBS (Gibco, UK) and 1 v/v% antibiotic/antimycotic solution (Gibco, UK).

5.2.2 Porous microsphere fabrication

Porous PLGA microspheres were fabricated via a modified double emulsion method. 5 mL of PLGA solution with 20 wt/v% of PLGA dissolved in DCM was prepared. The salt solution was prepared separately by mixing 1 mL of 10× PBS into 4 mL of 0.3 wt/v% PVA solution (PVA sln). Both the solutions were previously prepared in a ddH₂O. PVA sln was vacuum filtered using a membrane with 0.4 μm pore size prior to the experiments. The salt solution was carefully poured onto the PLGA solution whereby the two-layered solution were left to sit for 2 min prior to emulsification.

Emulsification was initiated by homogenizing the solution at 10,000 rpm for 2 min using a homogenizer (Wiggenhauser Homogenizer D-500). The primary water in oil (w/o) emulsion was then quickly poured into a magnetically stirred 200 mL of PVA sln at 1000 rpm. The resultant water-in-oil-in-water (w/o/w) double emulsion was left stirring overnight to allow microspheres hardening and DCM evaporation. The microspheres were harvested and followed by three ddH₂O wash and vacuum filtration. The microspheres were sieved by using sieves with nominal aperture of 88 and 149 μm.

Subsequently, the pores of the microspheres were further enlarged by treating the microspheres with ethanolic sodium hydroxide (EtOH–NaOH) with 0.25 M NaOH: 70 v/v% EtOH in a ratio of 3:7. Both the solutions were diluted with ddH₂O to the desired concentrations prior to mixing. Briefly, one portion of microspheres was suspended in ten portions of EtOH–NaOH solution with magnetically stirring at 1000 rpm for 5 min. The microspheres were vacuum filtered, followed by three ddH₂O rinse. After final vacuum filtration, the microspheres were dried in a freeze-drier (ScanVac CoolSafe Freeze Drying,

LaboGene™, Denmark) for ~24 hrs and then kept in a fridge at 4 °C till further usage.

5.2.3 Hydrogel preparation

The AC blend hydrogel to glue the microspheres was made of agarose and collagen mixed into high glucose DMEM medium. Stock agarose solutions were prepared by dissolving 3 wt/v% agarose Type IX-A in high glucose DMEM and autoclaving the mixture for 15 minutes at 100 °C. The solution was then brought to 37 °C in a water bath. Stock collagen solutions were prepared on ice immediately prior to use by neutralizing collagen type I solution with dropping 1 M NaOH to bring the pH to 7.4. AC blend hydrogels were prepared by mixing agarose and collagen stock solutions with additional warm high glucose DMEM at 37 °C in appropriate volumes to create the blend hydrogel with 1.5 mg/ml collagen and 1.5 wt/v% agarose concentrations. The solution was mixed thoroughly and was incubated at 37 °C prior to testing.

5.2.4 Characterization techniques

The microspheres were observed under an inverted microscope (Zeiss Axio Vert. A1). The surface morphology of microspheres was viewed under a SEM at an accelerating voltage of 5 kV. A cross-section of microspheres was captured under SEM after fracturing the microspheres. The sizes of microspheres, microsphere pores and CLMs were measured using the Image J software. Note that any pore size smaller than 1 μ m was not measurable but it was known that they vastly exist in the microspheres.

1.5 wt/v% agarose, 1.5 mg/ml collagen and the AC blend hydrogel with 1.5 mg/ml collagen and 1.5 wt/v% agarose concentrations were prepared as previously described in Section 5.2.3. The hydrogels were first casted on ice,

followed by incubation at 37 °C for 24 hrs, and then freeze-dried prior to SEM imaging. The hydrogels were imaged at an accelerating voltage of 5 kV.

The T_g of the PLGA was determined by DSC (TA Instruments, Q200). Hydrolytic degradation of the microspheres was studied in PBS at 37 °C. 10 mg of PLGA microspheres were placed in 1 ml of PBS using 1 mL centrifuge tube, and incubated in a 37 °C oven. Three tubes were centrifuged to remove the supernatant from the microsphere pellet every week during experiment, dried under freeze-drier and then weighed and observed under SEM.

5.2.5 Biocompatibility testing

Cell culture

L929 mouse fibroblasts were cultured to assess the biocompatibility of the bioink in a preliminary study. L929 cells were cultured in high glucose DMEM medium supplemented with 10 v/v% FBS and 1 v/v% antibiotic/antimycotic solution as explained in Section 3.2.7.

Cell seeding on microspheres

Prior to cell seeding on microspheres, 0.3 g of microspheres were sterilized by immersing them in 70 v/v% EtOH at 4 °C for 5 hrs. The microspheres were then washed with cold PBS before being suspended in 10 mL of warm (37 °C) cell culture media in a 125-mL siliconized Techne biological stirrer flask (Bibby Scientific Limited, UK). A total cell number of 2.5×10^7 was suspended into the biological stirrer. Warm (37 °C) cell culture medium was added into the biological stirrer to make a total solution volume of 40 mL. The culture was stirred intermittently for 2 min every 30 min at the speed of 30 RPM for initial cell attachment and growth. After 6 hrs, the total volume of the culture was increased to 125 mL with pre-warm (37 °C) culture medium and a continuous

stirring of 60 RPM commenced and continued for the next 20 hrs prior to preparation of the bioink.

Bioink preparation

The AC blend hydrogel and the support material gelatin hydrogel were kept in a water bath at 37 °C. The CLMs were centrifuged and the first supernatant (medium) was removed. The AC blend hydrogel was quickly added to the CLMs and gently pipetted prior to centrifugation and followed by a second supernatant (hydrogel) removal. This would form thin coating of AC blend hydrogel around the CLMs.

Cell viability on bioink

Cell viability of L929 on the microspheres and hydrogels were assessed using live/dead assay (Molecular Probes, USA) after 7 and 14 days of culture as described in Section 3.2.7. Fluorescence microscopy (Zeiss Axio Vert. A1) was used to evaluate the live/dead staining of cells in the samples. The quantification of live cells was computed from the fluorescence readings using the ZEN microscope software. In preparation for SEM observations, the CLMs were rinsed with PBS and fixed with 2.5% glutaraldehyde in ddH₂O overnight at 4 °C. Following PBS rinses, the samples were dehydrated through a series of graded alcohol solutions, and then air-dried. Cellular constructs were gold-coated and observed under the SEM.

5.3 Results and discussion

5.3.1 Porous microspheres

The PLGA microspheres were fabricated as shown in Figure 5.2. The fabrication process was first optimized to create spherical shaped PLGA with

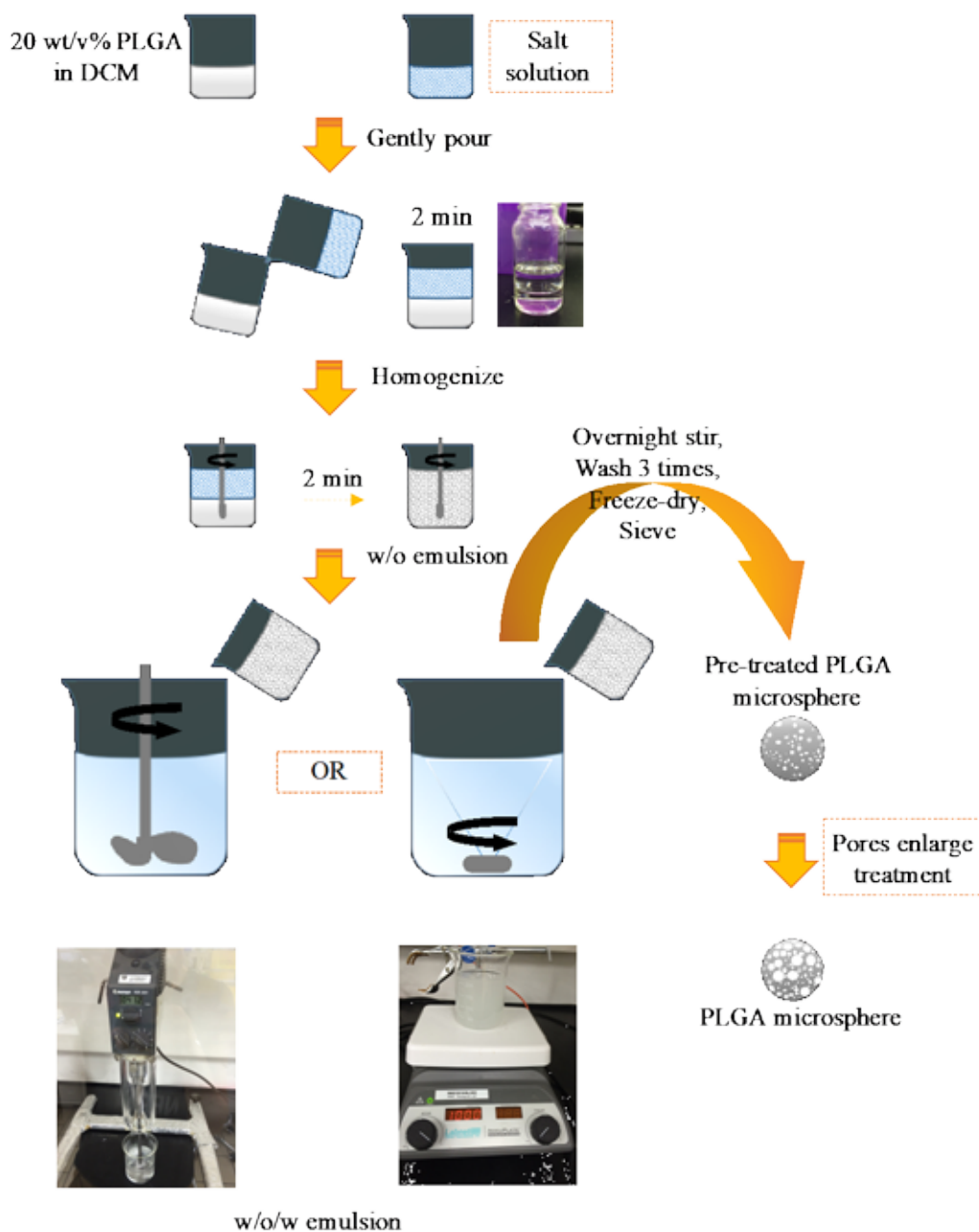


Figure 5.2. Schematic and pictorial illustration on the fabrication of porous PLGA microspheres

observable pores. It was planned that the sizes of the PLGA microspheres would fall in the range of ~ 80 μm as would be explained later in this Section. First, the salt solution was optimized to produce a well emulsified solution upon homogenization. The salt solution was initially pure PBS as suggested by literature [102]. However, clumping of the PLGA solution was observed during homogenization. Thereafter, the salt solution was prepared by adding PVA soln

into the PBS. The homogenization process was improved and a homogenized cloudy emulsion was produced.

This primary w/o emulsion was then pour into a stirring PVA sln to produce the w/o/w emulsion process. The stirring commenced by a propeller stirrer (Heidolph Mechanical Overhead Stirrers RZR 2021) as shown in Figure 5.3. Due to the large size distribution of the microspheres fabricated, a magnetic stirrer was then chosen to stir the emulsion. The size distribution was then improved. PBS was used to create pores in microspheres. The salt solution was optimized to produce spherical microspheres with pores. After substantial optimization, a salt solution of 1 mL PBS (10x) mixed with 4 mL PVA sln was found to be the best, producing spherical microspheres that fall into a range of 10 to 200 μm . Pores can be observed as shown in Figure 5.4. Cross-section of the microspheres was observed. Hollow microspheres and solid microspheres with multiple pores throughout the internal structure were observed. The microspheres were sieved into size range of 90 to 150 μm for a narrower size distribution.

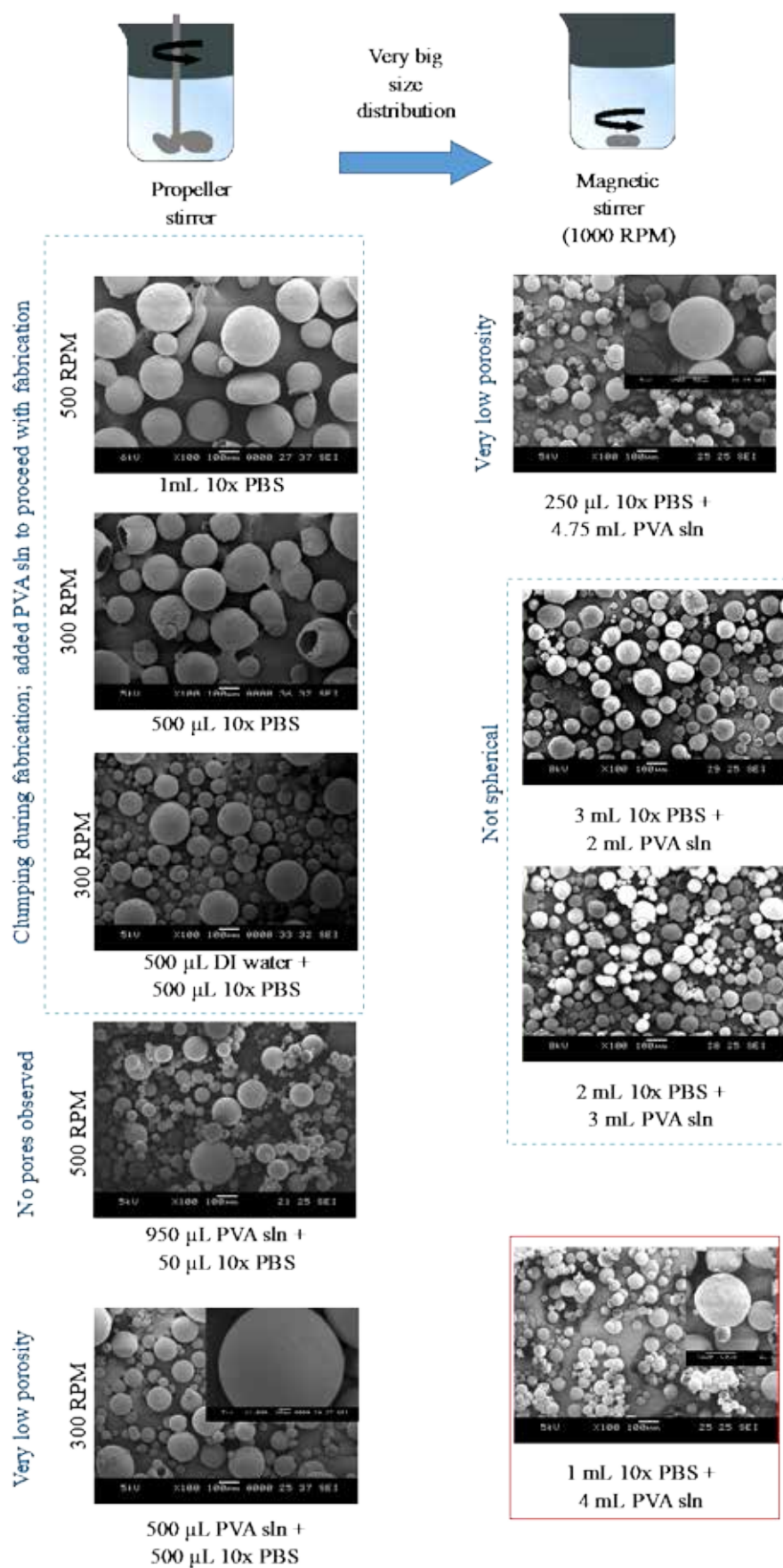


Figure 5.3. SEM images of PLGA microspheres fabricated by different parameters. The optimized parameter is indicated in the red box.

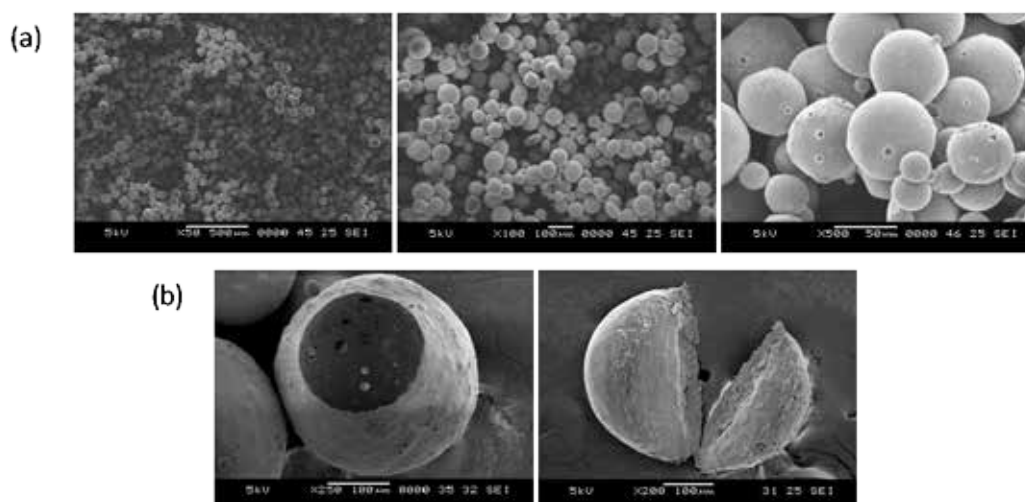


Figure 5.4. SEM images of (a) the optimized pre-treated microspheres and (b) their cross-sections

An EtOH-NaOH treatment was used to enlarge the pores in the microspheres as illustrated in Figure 5.5. A shaker (Orbit™ 1000 Multipurpose Digital Shaker) was initially utilized to “etch” the surface of the microspheres in the EtOH-NaOH solution [102]. However, clumping of the microspheres was

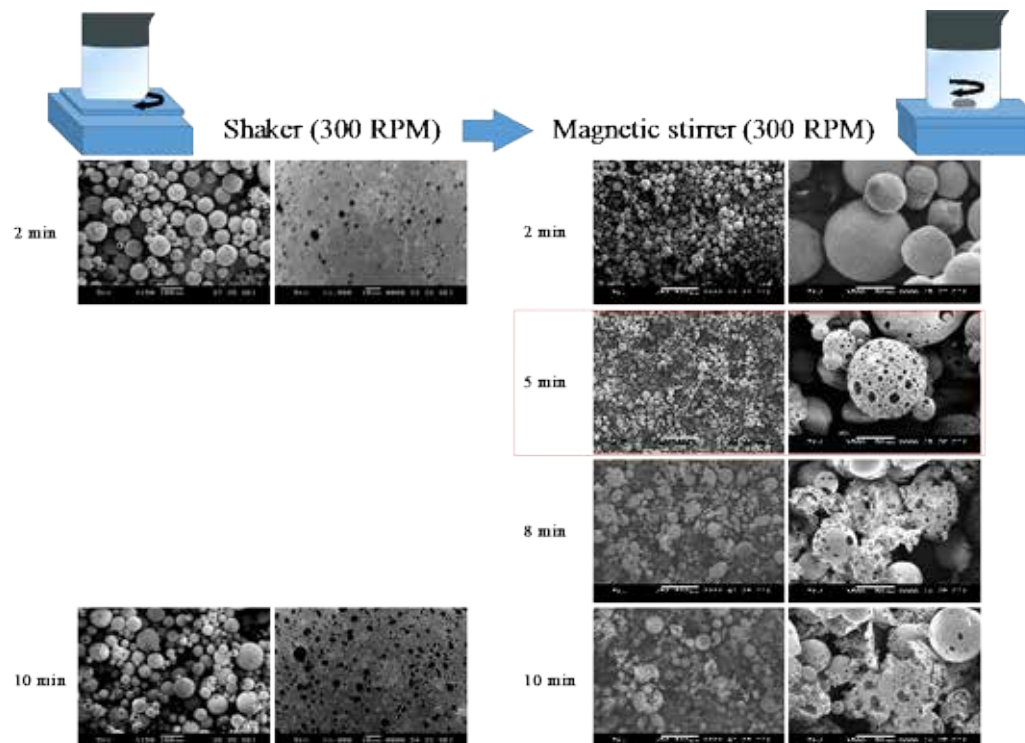


Figure 5.5. SEM images of the EtOH-NaOH treated microspheres by using different parameters. The optimized parameter is indicated in red box.

observed with naked eyes during fabrication. After freeze-drying the microspheres, it was observed that many of the microspheres were not treated due to the clumping when shaking. A magnetic stirrer was again chosen to “etch” the microspheres as it could create a more homogenous stirring. “Etching” time of 5 min was identified as the optimum for enlarging the pore size of the microspheres without compromising their structural integrity.

The microspheres fabricated ranged from 60 to 130 μm . They possessed an extremely high porosity with an average pore size of 7.3 μm (ranging from 1.0 to 20.9 μm). Calculations were performed excluding multiple submicron pores concurrently observed on the microspheres. Microspheres were fractured and their cross-sections were shown in Figure 5.6.

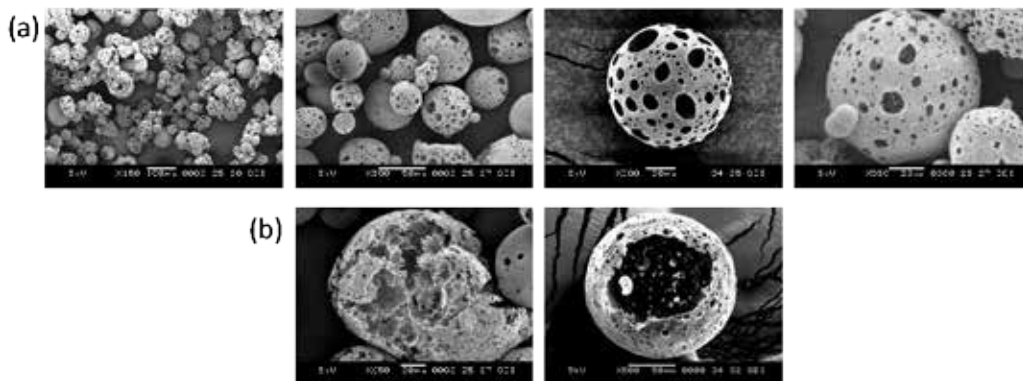


Figure 5.6. SEM images of (a) the optimized EtOH-NaOH treated microspheres and (b) their cross-sections

The microspheres size range was selected with the reasons as illustrated and explained in Figure 5.7. The chosen pre-treated microspheres size range (before EtOH-NaOH treatment: sieved to $\sim 90\text{-}150\ \mu\text{m}$) was ideal for this study as pores' enlargement using EtOH-NaOH was limited by the microsphere size, especially when microsphere sizes were small. It is known that most of the mammalian cells have a diameter of $\sim 10\ \mu\text{m}$ when rounded up after detachment. Cell infiltration would be impossible if the pores on the microspheres were too

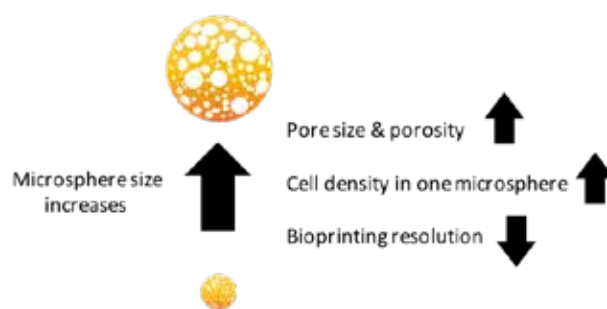


Figure 5.7. Schematic showing the relationship between the microsphere size selection and its effect on the 3D bioprinting

small, which would reduce the cell density per microsphere. The optimized pore size range was found to be $\sim 0.1\text{-}20\text{ }\mu\text{m}$. Further pore enlargement treatment caused microsphere fragments to form which were previously shown in Figure 5.5. Submicron pores would assist in nutrient exchange while the macropores would allow cells to infiltrate. The submicron pores are also beneficial for epithelium stratification [207]. After enlargement of pores, the microspheres size became smaller ($60\text{-}130\text{ }\mu\text{m}$) due to the “etching effect” of EtOH-NaOH. Obviously, a higher printing resolution could be realized by using smaller microspheres. Hence the adopted microspheres size range was determined as a trade-off between printing resolution and cell density.

Scaffolds fabricated from biomaterials with a controllable degradation time frame are preferred. PLGA microspheres could degrade within 12 weeks hydrolytically *in vitro* at $37\text{ }^{\circ}\text{C}$ as illustrated in Figure 5.8. Microspheres aggregated and the forms of microspheres were lost (not spherical anymore) after 7 weeks. 99% of weight loss occurs after 12 weeks. Also, a highly porous microscaffold is favorable compared to a solid scaffold to pack high density of cells into the scaffold and achieve expedite degradation after printing. As amorphous PLGA had a T_g much higher than $37\text{ }^{\circ}\text{C}$ as shown in Figure 5.9, the

microspheres could remain non-cohesive [102] for smooth printing without clogging.

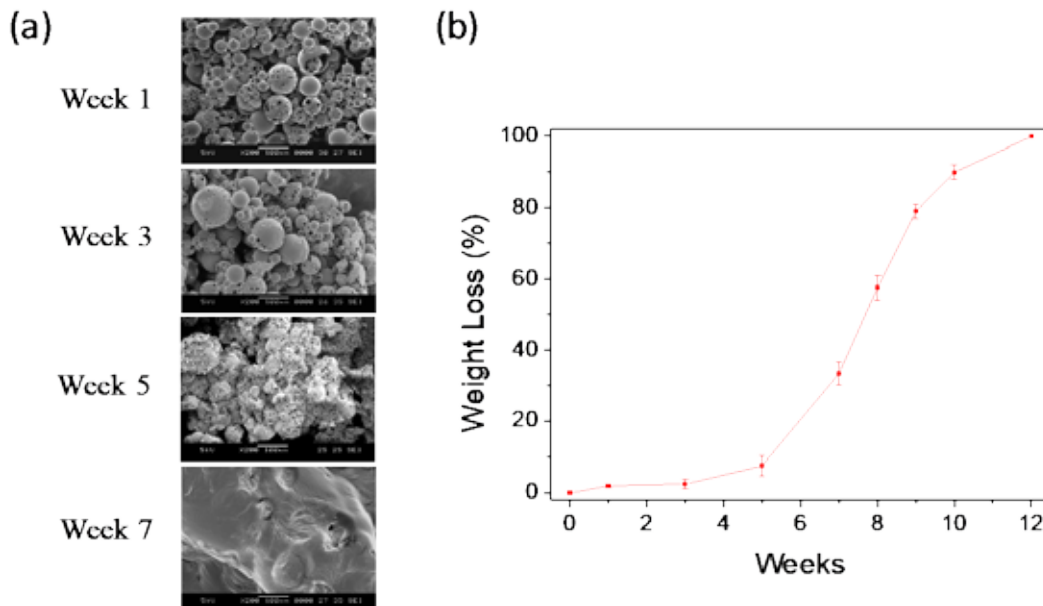


Figure 5.8. (a) SEM images of PLGA microspheres after 1, 3, 5, and 7 week(s) of hydrolytic degradation in PBS at 37 °C. (b) Graph showing the weight loss of microspheres (n=3) with the weeks of hydrolytic degradation.

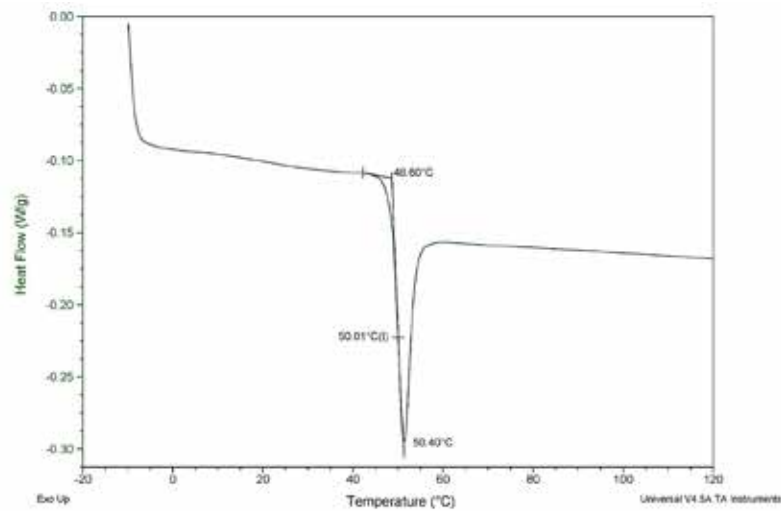


Figure 5.9. DSC results showing T_g of amorphous PLGA at ~50 °C.

The PLGA scaffolds provided 2D surfaces with pseudo-3D environments for the anchorage-dependent epithelial and fibroblasts cells to adhere and proliferate. By using cell-laden microscaffolds in bioprinting of a 3D construct, a lower initial cell density is achievable as compared to that required by

conventional cell-laden hydrogels or tissue spheroids/strands. For example, when using highly porous microspheres, initial density of $\sim 2.7 \times 10^4$ cells/mm³ would be sufficient. By contrast, cell-laden hydrogel printing would require a cell density of $\sim 1.7 \times 10^5$ cells/mm³ while tissue spheroids printing would entail $\sim 1.8 \times 10^6$ cells/mm³ (as calculated in Appendix E). With the readily available biomaterials and the mature technology in fabrication of the microcaffolds, microcaffold-based bioprinting becomes simple to implement. Size distribution of the microcaffolds can be well controlled by varying the appropriate fabrication parameters. Furthermore, the polymeric microcaffolds were found to be stable over a relatively long period after fabrication if properly stored. With the support of these biodegradable microcaffolds, printed constructs can undergo a slower and more controllable process of tissue maturation as compared to the scaffold-free constructs.

5.3.2 Thermoresponsive AC blend hydrogel

Lubricating AC blend hydrogel [270, 271] was used as a thin encapsulating material enveloping the microspheres for ease of printing. At below ~ 20 °C, the AC blend hydrogel should work as an adhesive that assembles the microspheres into a pre-defined shape. Ice was placed under the build platform to expedite adhesion. The AC blend hydrogel was selected among other hydrogels because it had good extrudability; enabled immediate gelation upon cooling; and allowed formation of collagen fiber networks within the printed construct during culture at 37 °C. Collagen fibrils were formed in the AC blend hydrogel as shown in Figure 5.10 after incubation at 37 °C for 24 hrs. Arrows in Figure 5.10 (a) show the whitish opaque collagen as opposed to the transparent agarose. Collagen fibrils (arrows in Figure 5.10 (b)) can be observed under SEM

in collagen and AC blend hydrogel, but not in the agarose. Moreover, AC blend hydrogel provided fine microstructure which can replicate the ECM of epithelium. Although could not be viewed under SEM, it was shown that agarose hydrogel in water has pore size of 0.3–0.4 mm when measured by AFM [269]. This biomimicry structure would be very useful for epithelium regeneration.

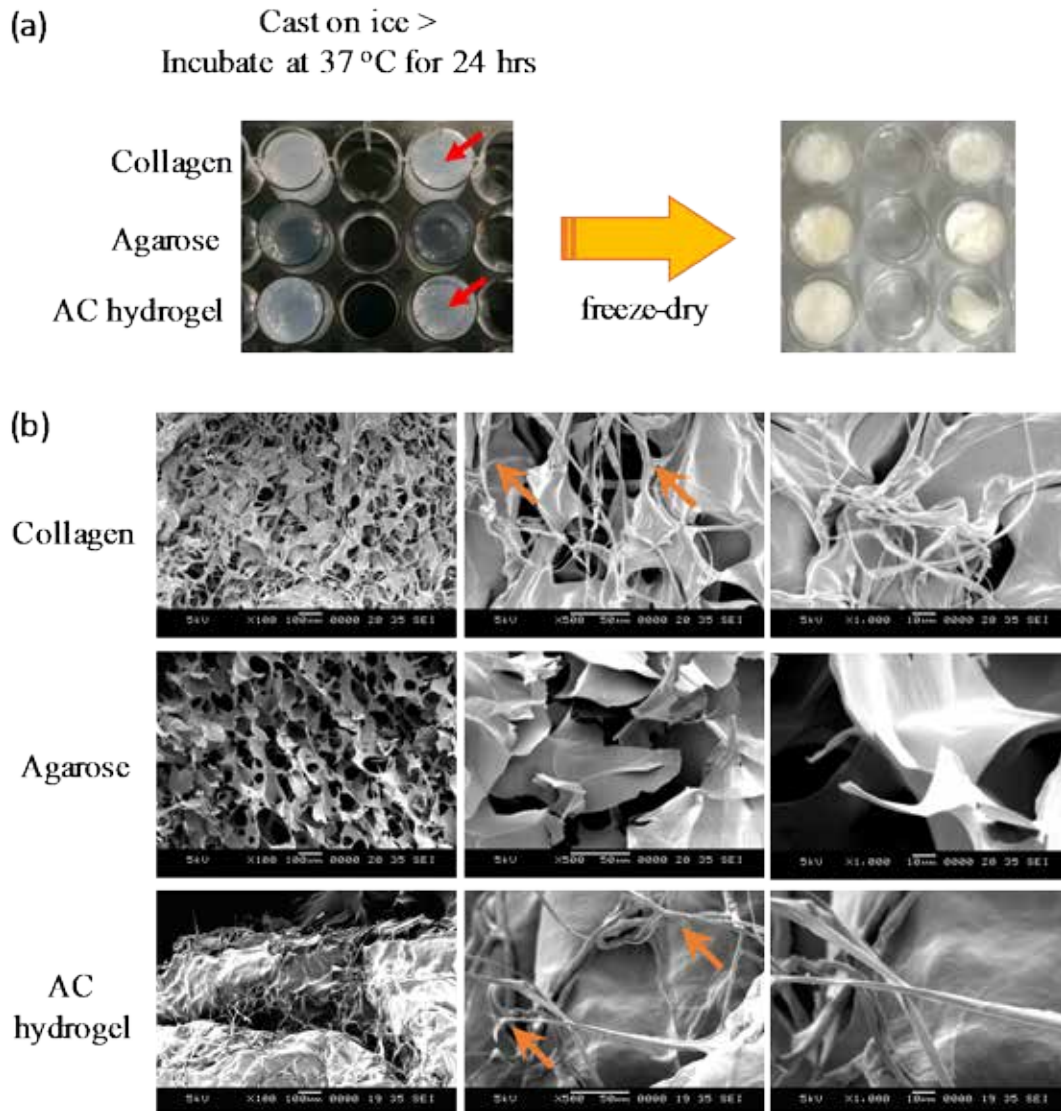


Figure 5.10. (a) Pictures showing the incubated and freeze-dried 1.5 mg/ml collagen, 1.5 wt/v% agarose, and AC blend hydrogels prior to SEM imaging. (b) SEM images showing the microarchitecture of the hydrogels.

A variety of AC blend hydrogels with different combinations had been tested to achieve optimal printing resolution, dispensing uniformity, solidifying

time, and stacking ability while not sacrificing its cell viability and spreading. By increasing the agarose hydrogel concentration, the blend hydrogels possessed high extrudability, but they solidified too fast on ice which lead to serious delamination between layers upon printing. In addition, when the agarose content was higher, the cells were clumped in the AC blend hydrogel as shown in Figure 5.11 in a similar way to the pure agarose. Note that the images shown in Figure 5.11 were taken from the top surface of the hydrogel to avoid imaging of cells attached to the TCPS. AC blend hydrogel with low concentrations of collagen lacked RGD for cell attachment e.g. cells colonization (dotted arrows) occurred. Although most of the cells became elongated (arrows) after 3 days of culture, they remained in colonies (dashed circles). On the other hand, cells attained normal morphology (arrows) in the optimized AC concentration.

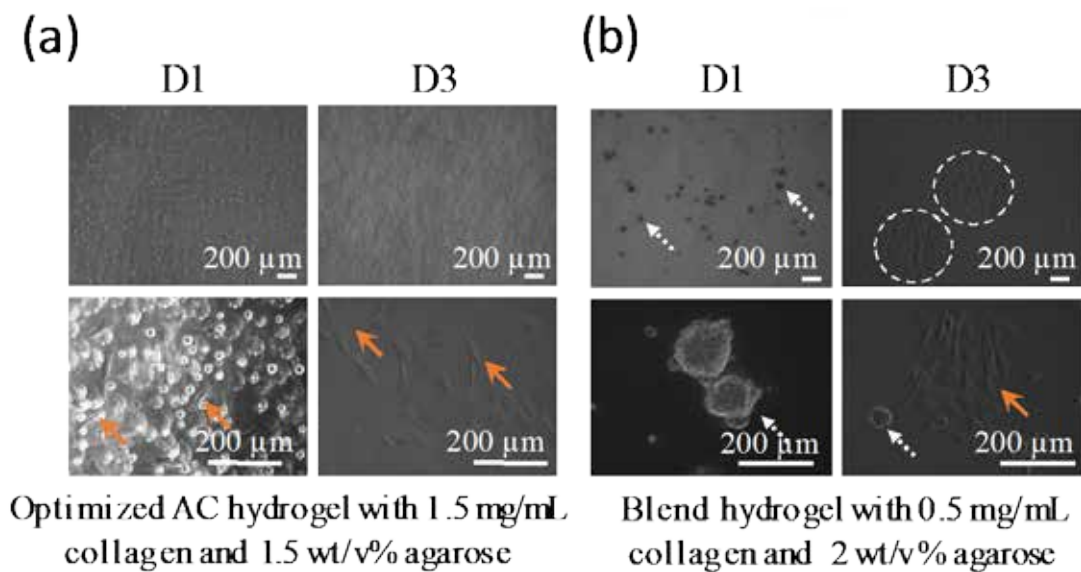


Figure 5.11. OM images of C2C12 cast in AC blend hydrogels with (a) 1.5 mg/ml collagen and 1.5 wt/v% agarose and (b) 0.5 mg/mL collagen and 2 wt/v% agarose, after 1 and 3 day(s) of culture.

Meanwhile AC blend hydrogels with lower concentrations of agarose (1.5 wt/v%) were not favoured in the printing process as gelation of the hydrogel

in each layer were slow. Additionally, by increasing the collagen concentration, the blend hydrogels solidified before printing at 37 °C as collagen fibrils were forming rapidly. Also, the higher the collagen concentration, the more the construct shrunk after printing. Figure 5.12 shows that pure collagen had shrunk by more than two times after culturing for 10 days. Moreover, the shrinkage was not controllable whereby the size and shape changed considerably. On the other hand, the AC blend hydrogel maintained its shape and dimensions after culturing correspondingly for 10 days.

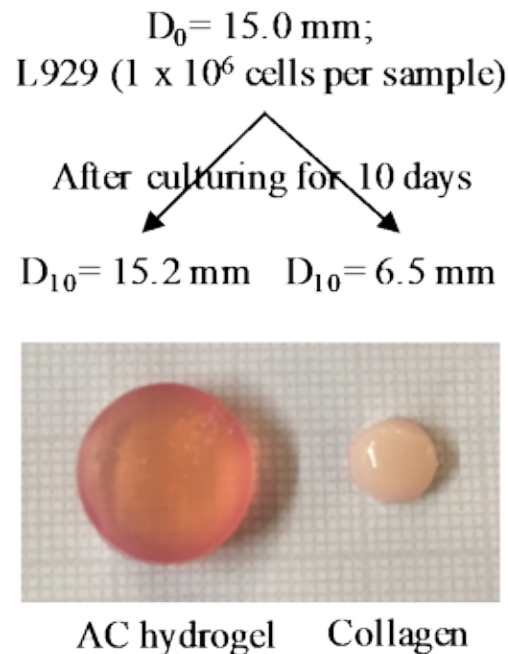


Figure 5.12. L929 cells cultured on cylindrical AC blend hydrogel and collagen with initial diameter (D_0) of 15.0 mm. D_{10} is the final diameter of the cells-hydrogel constructs.

5.3.3 Cell attachment and viability

To understand cell attachment and proliferation in the PLGA microspheres, mouse fibroblasts L929 cells were seeded onto the microspheres using stirred culture. Cells attached well on the microspheres as shown in Figure 5.13. The highly porous PLGA microspheres had good cell affinity as expected and thus high cell density CLMs were produced. The CLMs sizes ranged from

60 to 150 μm . Of note is that size of CLMs became bigger when compared to the PLGA microspheres as shown in Figure 5.13 because of the slight swelling of PLGA microspheres after submerging in cell culture media at 37 °C [106]. Cells seeded on the microspheres also contribute to the larger size of the CLMs when compared to those before seeding.

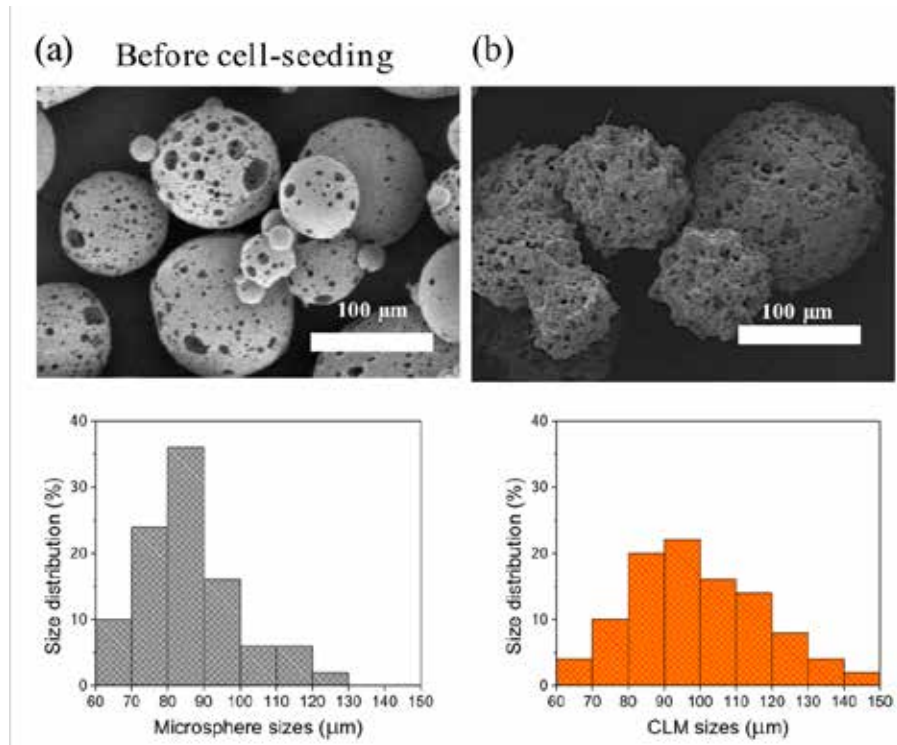


Figure 5.13. SEM images showing (a) the PLGA microspheres and (b) the CLMs. The size distribution histograms of the microspheres and the CLMs are shown below the respective SEM images.

The cell viabilities of L929 on the microspheres and hydrogels were accessed through live/dead assay on day 7 (Figure 5.14) and day 14 (Figure 5.15) of culture. First set of fluorescence images on the left are the live (green)/dead (red) images of the cellular construct captured by the fluorescence microscope. The graphs in the middle show the 2.5D reconstruction of the fluorescence images for a clearer visualization of the positions of live and dead cells. The right images are the zoomed-in live (green)/dead (red) images. Both the fabricated PLGA porous microspheres and the AC blend hydrogel were highly

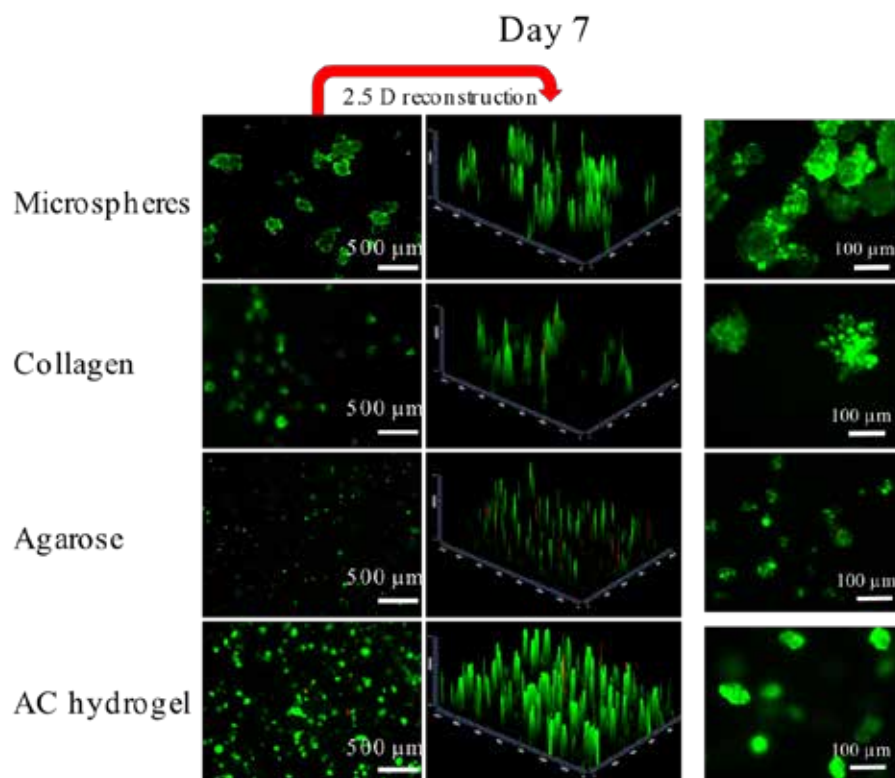


Figure 5.14. Day 7 L929 cell viabilities on PLGA microspheres, 1.5 mg/mL collagen, 1.5 wt/v% agarose and AC blend hydrogel.

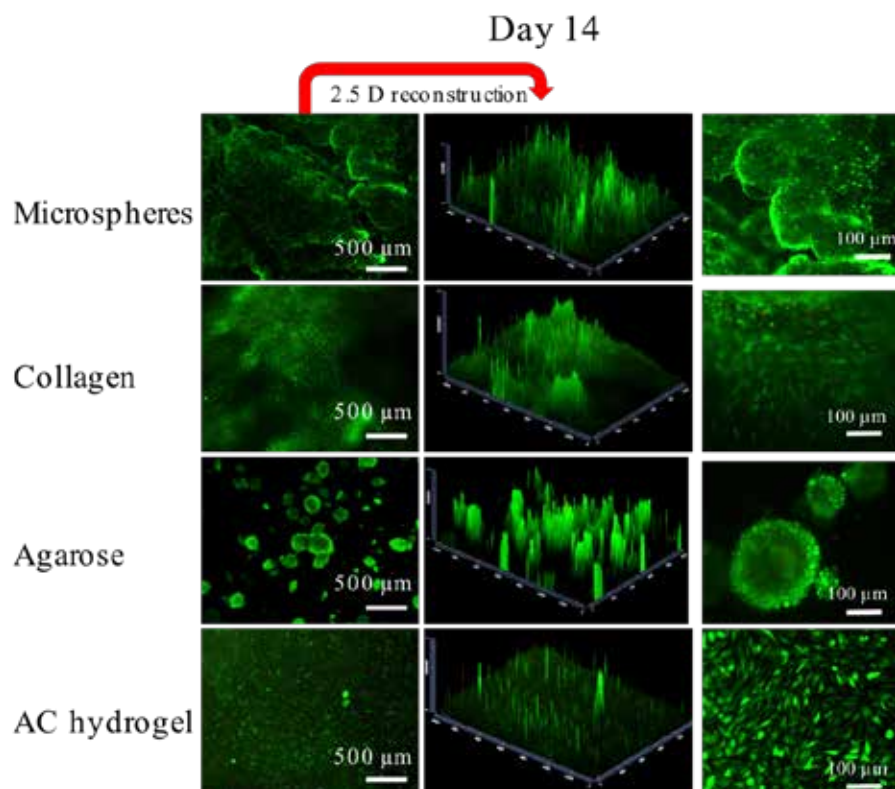


Figure 5.15. Day 14 L929 cell viabilities on PLGA microspheres, 1.5 mg/mL collagen, 1.5 wt/v% agarose and AC blend hydrogel.

biocompatible, showing more than 90% viable cells after 1 and 2 week(s) of culture. Cells were spread out in the AC blend hydrogels after 14 days of culture, in a similar fashion to those on the collagen. By contrast, in agarose hydrogels, cells were rounded and formed into large cell aggregates. The results showed that cell spreading was promoted using the AC blend hydrogel as compared to the agarose.

5.4 Summary

A new bioink constituting of cell-laden PLGA porous microspheres with thin encapsulation of AC blend hydrogel was presented. Optimizations of the microspheres and AC blend hydrogel fabrication were presented. The L929 cells were shown to attach and proliferate in the microspheres and AC blend hydrogel. The use of cell-laden microscaffolds instead of the conventional scaffold-free cell-laden hydrogels and tissue spheroids or strands as the building block in bioprinting can potentially solve the problem of cell source shortage. The porous microspheres provide high specific surface areas so that they allow the cells to attach, infiltrate and expanded in stirred culture, and form CLMs. By using CLMs in bioprinting of a 3D construct, a lower initial cell number is achievable as compared to that required by conventional cell-laden hydrogels and tissue spheroids or strands.

Chapter 6. Bioengineering of esophageal mucosa: A 3D bioprinting strategy

6.1 Introduction: A novel 3D bioprinting method

Extrusion-based technology enables the precise fabrication of complex structures and facilitates the patterning of multiple types of cells. Instead of applying the commonly used extrusion approaches, a micropipette-based extrusion method is proposed for finer control, as illustrated in Figure 6.1, for 3D printing of tightly packed CLMs. Cells are indicated in orange in the figure.

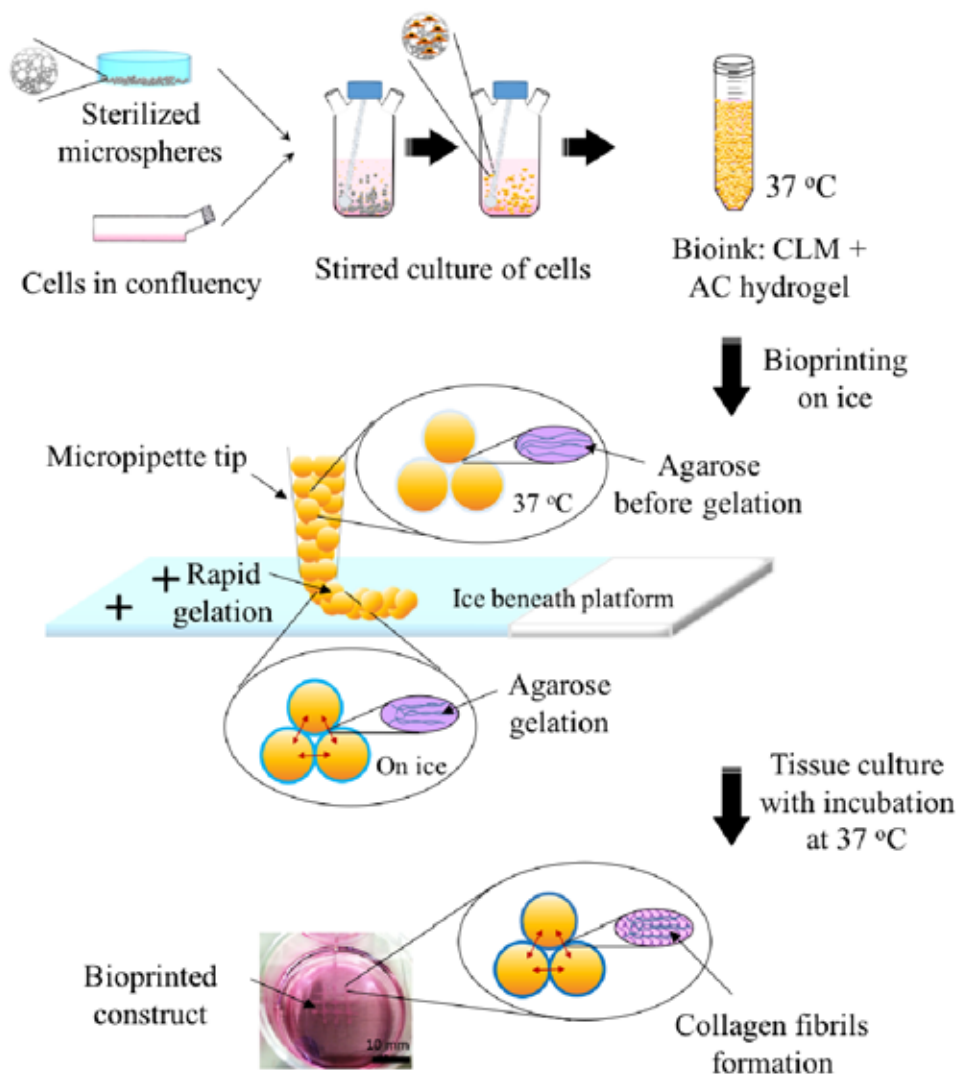


Figure 6.1. Schematic illustration of the bioprinting process.

The cells are seeded onto the porous PLGA microspheres. After stirred culturing, cells infiltrate and proliferate into the microspheres, producing CLMs. The bioink, i.e. CLMs encapsulated in thin AC blend hydrogel, will be made by adding the hydrogel into the CLMs, followed by pipetting, centrifuging and removal of supernatant. The packing of the microspheres per unit volume of the bioink is estimated to be ~74% [272], assuming a densest packing of monodispersed microspheres. The bioink is prepared before bioprinting on a chilled platform, where agarose gelation occurs. Collagen fibrils are formed after culturing the construct at 37 °C.

The proposed bioprinter design for CLMs printing is shown in Figure 6.2. The system consists of four major units: (i) a 3-axis robotic controlled dispensing system using micropipette tips, (ii) a printing preparation stage with boxes of

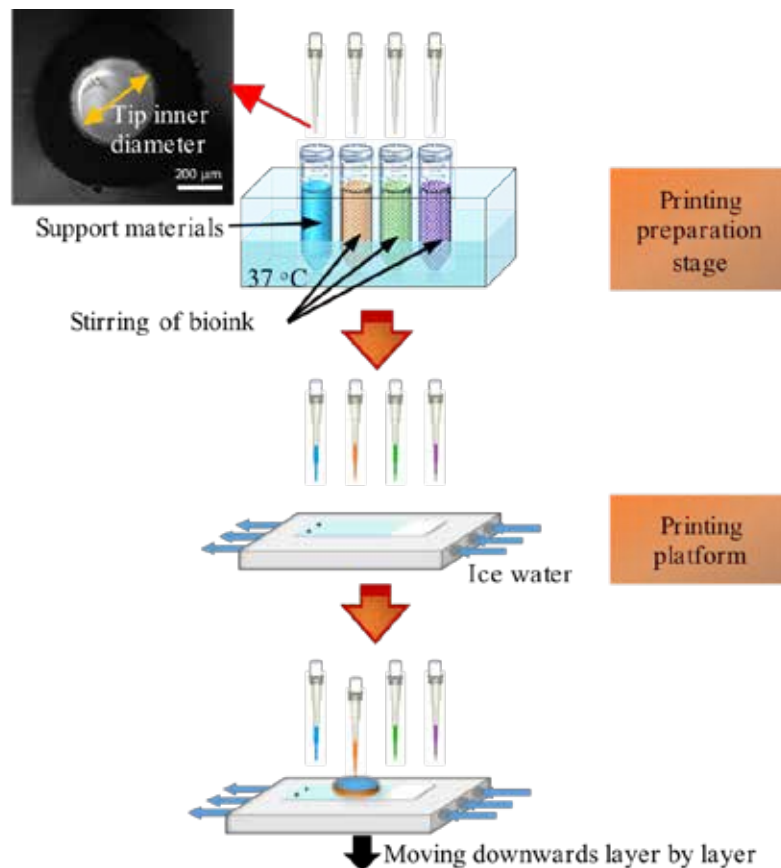


Figure 6.2. Schematic of an automated bioprinting system. Inset shows the OM image of the micropipette tip.

new micropipettes and bioinks under stirring and temperature control (37 °C), (iii) an ice-water-chilled printing platform, and (iv) a closed chamber with humidifier, UV lamp, and trash container.

Before printing, the chamber could be sterilized with an UV lamp. Bioink with different cell types would be prepared in separate centrifuge tubes and then loaded into a printer, with gentle stirring and precise temperature control. This design would prevent CLMs from fusing before the start of the bioprinting process. Each micropipette tip could draw up bioink from the respective centrifuge tube concurrently for printing of a few layers. Printing was conducted on the chilled platform where the hydrogel will glue the microspheres into designed shapes layer by layer. Used tips would be removed into the trash container after layers of printing and new tips would be fetched onto the dispensing system before drawing the bioinks for subsequent printing. It was noted that clogging of tips during printing and the resultant waste of bioink were the main limitations for extrusion-based bioprinting. However, clogged tips could be replaced in an automated way when using micropipette-based extrusion printing. In fact, there had been some other commercial machines that feature automated pipetting systems, which could be implemented into a bioprinter. Although it might induce wastage of bioinks when removing the clogged tips, this bioprinter could print large 3D tissues consecutively in a humidified closed chamber with the reduced risks of contamination.

6.2 Materials and methods

6.2.1 Bioprinting process

Printing of constructs was accomplished using a simple, hand-held printing process using micropipettes (size of 1-10 μL). An ice platform was

prepared to bind the microspheres together. Prior to printing, all the equipment was sterilized by rinsing with 70% EtOH followed by 1 hour of UV bath. Superfrost plus microscope slides (Thermo Scientific, USA) or 12-well plates were put onto the ice platform and the bioink was withdrawn into the micropipette. The bioink was then extruded into the desired shape on the glass slides and the 2.5D construct was formed immediately. A 3D construct was built after a layer-by-layer printing. To build a tall, complex construct, gelatin hydrogel was utilized as a support material, whereby it is laid down layer by layer to support the biological structure.

6.2.2 Mechanical evaluation

Compressive testing

Three types of acellular samples were prepared, i.e. AC blend hydrogel, cast samples with PLGA microspheres that were loosely packed in AC blend hydrogel (loosely packed samples; ~20 v/v%), and bioink (tightly packed PLGA microspheres in AC blend hydrogel samples). The disc samples were cast on ice, followed by incubation in an 37 °C oven for 3 days before testing. The samples were submerged in high glucose DMEM medium (Gibco, UK) supplemented with 10 v/v% FBS (Gibco, UK) and 1 v/v% antibiotic/antimycotic solution (Gibco, UK) during incubation to mimic the cell culture condition.

The uniaxial compressive stress–strain measurements were performed on the disc samples using the Instron 5566 universal testing machine with a load cell of 100 N and a crosshead speed of 1 mm/min. The cylindrical AC blend hydrogel, loosely packed PLGA microspheres (~20% v/v) in AC blend hydrogel and tightly packed PLGA microspheres in AC blend hydrogel samples (each n=3) were 13–15 mm in diameter and ~4 mm in thickness. The compressive stress (σ) was

computed by $s = \text{Load}/\pi r^2$, where r is the initial unloaded radius; the compressive strain (ϵ) was defined as the change in the thickness relative to the thickness of the freestanding specimen.

Tensile testing

The uniaxial tensile stress–strain measurements were performed on dumb bell-shaped samples of acellular bioink. The samples were casted on a polydimethylsiloxane (PDMS) mold.

To simulate the aggregated PLGA microspheres due to surface hydrolysis after submerging in water at 37 °C as illustrated in Figure 5.8 (a) and Figure 5.15, ethanol was sprayed on the dumb bell-shaped samples to speed up PLGA aggregation. Tensile tests were carried out with an Instron Universal Testing Machine (Model 5566) with a load cell of 100 N. The samples were clamped and subjected to monotonic uniaxial extension by applying displacement at 0.1 mm/min. The UTS, Young’s modulus, and elongation at break were computed from the tensile stress–strain curves.

6.2.3 Cell culture

The cells seeding and bioink preparation steps were described in Section 5.2.5. Cells were maintained in a humidified tissue-culture incubator at 37 °C and with 5% CO₂. The bioinks (CLMs coated with AC) were kept in a water bath at 37 °C prior to printing. Printing of the cellular constructs were conducted under sterile conditions.

Mouse fibroblasts L929 and human epithelial TR146 cells were cultured, seeded and printed. These two cells were chosen to demonstrate that fibroblasts and epithelial cells can be bioprinted to regenerate the esophagus mucosa and submucosa. TR146 was cultured and expanded in HAMS F12 media

supplemented with 2mM Glutamine (Biological Industries, Israel), 10 v/v% FBS (Gibco, UK) and 1 v/v% antibiotic/antimycotic solution (Gibco, UK). L929 cells were labelled with green fluorescent cell linker (PKH67GL; Sigma–Aldrich, St. Louis, MO, USA) and TR146 cells were labelled with red fluorescent cell linker (PKH26GL; Sigma–Aldrich, St. Louis, MO, USA) before cell seeding on microspheres.

To check the myoblasts and SMCs alignment after bioprinting, C2C12 and rat smooth muscle cells A10 cell line were seeded on the microspheres and bioprinted. C2C12 was cultured and expanded as described in Section 3.2.7. A10 was cultured in a high glucose DMEM medium (Gibco, UK) supplemented with 20 v/v% FBS (Gibco, UK) and 1 v/v% antibiotic/antimycotic solution (Gibco, UK). C2C12 and A10 were labelled with red fluorescent cell linker PKH26GL before cell seeding on microspheres.

After printing, all the cellular constructs were maintained at 37 °C in a humidified incubator and the medium was changed every 2–3 days. Constructs were observed daily. Viable cells remained fluoresce under fluorescence microscope.

Additionally, to illustrate that stem cells can be bioprinted and maintained their stem cells lineage after printing, hMSCs (passage 5) were seeded on the microspheres, printed and cultured in mesenchymal stem cell basal medium (Lonza) without using soluble differentiation factors. hMSCs were cultured prior to seeding on the microspheres as described in Section 3.2.7. After 24 hours of culture of the bioprinted hMSCs, the culture medium was changed to the StemPro osteogenesis differentiation kit (A1007201, Gibco). hMSCs were differentiated

into osteoblasts to demonstrate its multipotent lineage. Culture medium was changed every 2–3 days up to 5 weeks.

Cell viability and proliferation

Cell viability of L929 on the bioprinted constructs were accessed using live/dead assay (Molecular Probes, USA) after 2, 7 and 14 days of culture. The viability of the cells within the printed 3D constructs were studied using CellTiter-Glo® 3D (Promega, USA). The cells seeded microspheres served as a control. Briefly, pre-mixed assay solution was added to each well of the constructs with vigorous mixing before incubation at room temperature for 25 min. 100 µl of each resulting solution (n=3) was pipetted into a white 96-well plate. Luminescence intensity was measured using a microplate reader (Ultra Evolution, Tecan).

Cell proliferation of the 3D printed constructs was determined by the RealTime-Glo™ MT Cell Viability Assay (Promega, USA), which measures cell viability in real-time. Similarly, the cells seeded microspheres served as a control. Briefly, after mixing the 2× assay solution with cell culture medium at 1:1 volume ratio, it was added to each construct in a white 96-well plate which was incubated at humidified tissue-culture incubator at 37 °C and with 5% CO₂ for up to 72 hrs. The viable cells were determined in culture by measuring the intensity of luminescence signals at several time points from 1 hour up to 72 hours after culture using the microplate reader.

Immunocytochemistry studies

For hMSCs immunostaining, constructs were fixed with 4% paraformaldehyde for 15 min at room temperature. These cells were then permeabilized with 0.1% Triton X-100 in PBS for 10 min at room temperature

and blocked with 5% BSA in PBS before the subcellular components were immuno-labeled. CD44, CD31 and cell nuclei were counterstained with rabbit monoclonal anti CD44 (2 mg/mL) counterstained with Cy3 goat anti rabbit IgG, mouse monoclonal anti CD31 (1:50) counterstained with AlexaFluor 488 donkey anti mouse IgG and NucBlue respectively. All images were acquired with the fluorescent microscope Zeiss Axio Vert.A1.

After culturing the hMSCs bioprinted construct in osteo-differentiation media for 2 weeks, alkaline phosphatase detection kit (ALP; Sigma) was used to detect the ALP activity within the cells. Control in this study was the hMSCs bioprinted constructs that were cultured in normal MSC media (Lonza) without differentiation. Briefly, 20 ml of cell lysate (n=3) was collected from the constructs and pipetted into black 96-well plates. Samples were incubated at 65 °C for 15 minutes then cooled to room temperature. Assay solutions were added and mixed according to the manufacturer's instructions. Fluorescence set at 360 nm excitation and 440 nm emission was measured by the microplate reader.

Calcified nodules on the constructs were further demonstrated by using Alizarin red S solution (ARS; Sigma) staining after 5 weeks of culture in osteo-differentiation media. ARS is an anthraquinone dye that has been widely used to evaluate extracellular calcium deposits in cell culture. 2 wt/v% of ARS solution was prepared using ddH₂O, where the pH was confirmed to be ~4.2. The solution was freshly prepared in the dark and vacuum filtered. The control was the 2D culture of MSCs on TCPS which were differentiated to osteoblasts using the same method described above. The constructs were washed with Dulbecco's phosphate-buffered saline (DPBS; Gibco) and formalin fixed for 30 min. ARS solution was added to the fixed constructs and incubated at room temperature in

the dark for 45 minutes. The solution was then removed and washed four times with ddH₂O. DPBS was added to the construct before imaging.

6.3 Results

6.3.1 Bioprinted constructs

The extrusion-based printing was achieved manually in this work as a proof of concept. However, it is obvious that complex 3D biological constructs can be similarly bioprinted using an automated printer. 3D printing of a tube with a mean diameter of 15.0 mm and height of ~5.5 mm was carried out using the micropipette extrusion method as shown in Figure 6.3.

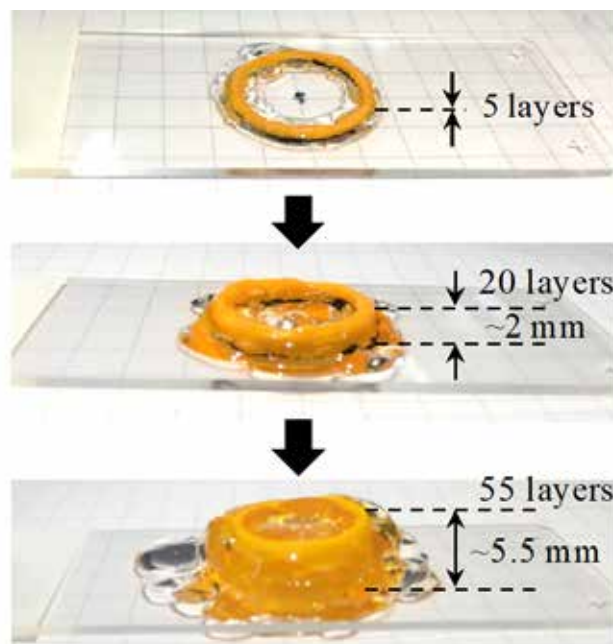


Figure 6.3. Pictures demonstrating a 3D printed tubular construct with gelatin (transparent) as support. Construct was printed on superfrost plus microscope slides with a dimension of 25 mm×75 mm.

Orange-coloured food dye was added to AC blend hydrogel for illustration purpose. Extrusion of the bioink can be performed effectively, with a fast gelation upon printing onto the cold build platform. High concentration of gelatin hydrogel (transparent) was used as a support material. It gels at temperatures lower than 37 °C, forming a firm support to the construct. The

gelatin support liquefied during subsequent culture at 37 °C, which was removed together with medium. More bioprinted constructs are illustrated in Appendix F. As shown in Figure 6.4, tightly packed PLGA microspheres can be printed using the micropipette extrusion method, with a printing resolution of ~500 nm.

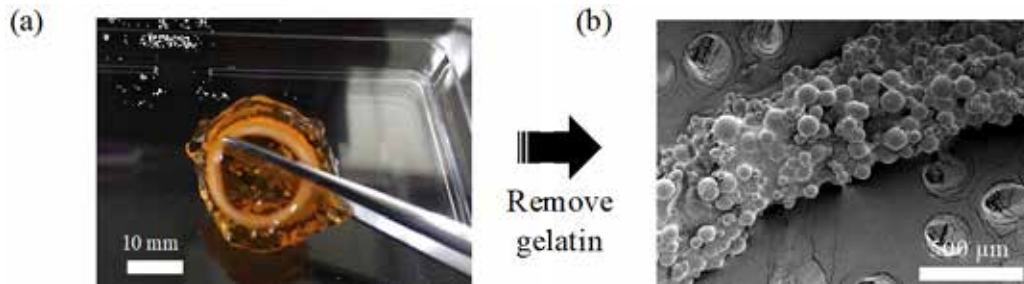


Figure 6.4. (a) Picture of a 3D printed tubular construct with gelatin (transparent) as support. (b) SEM image illustrates the microarchitecture of the printed construct.

6.3.2 Mechanical properties

To demonstrate the advantage of the bioprinted construct in terms of its mechanical properties, compression tests of the cast AC blend hydrogel, loosely packed samples and bioink (acellular PLGA microspheres tightly packed in AC blend hydrogel; ~74%) were conducted. Figure 6.5 shows the corresponding compressive stress–compressive strain curves of the samples.

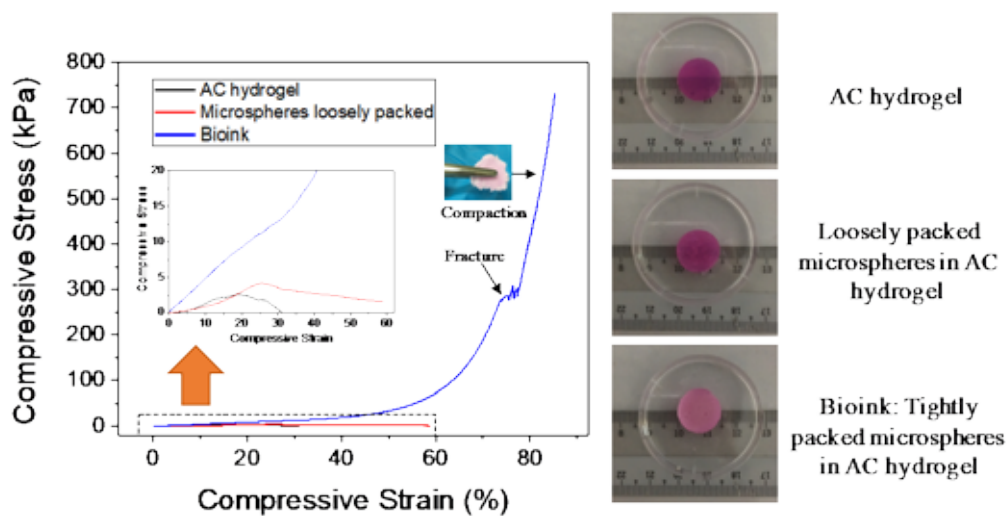


Figure 6.5. Compressive stress–compressive strain curves for the AC blend hydrogel, the loosely packed samples, and the bioink. Pictures on the right show the representative samples used for compression tests.

The AC blend hydrogels fractured under low deformation as expected. It failed at an average stress of 2.7 kPa and strain of ~30 %. The loosely packed samples were fractured at a higher average stress of 4.4 kPa and strain of ~60 %. Meanwhile, the cast bioink broke at a much higher stress of 270.6 kPa and at a high strain of ~75 % compared to the other types of samples. These samples continued to compact after fracture as shown in the inset in Figure 6.5. The average compressive moduli of the AC blend hydrogel, the loosely packed samples and the bioink were computed to be 22.5 kPa, 29.1 kPa and 47.6 kPa, respectively. Tensile testing results of the bioink showed that its UTS is ~25 kPa, its elastic modulus is ~136 kPa, the maximum elongation is ~35% as shown in Figure 6.6. From the SEM figures in Figure 6.6 (c), the fracture surface showed intergranular fracture, whereby the fracture started from the weakest boundary between the microspheres.

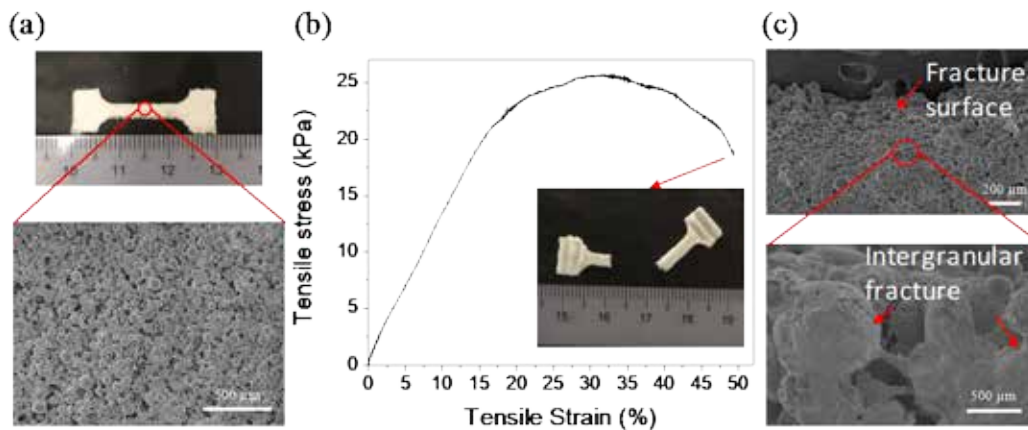


Figure 6.6. (a) Picture showing the representative sample used for tensile tests. SEM image illustrates the surface of the sample. (b) Tensile stress-strain curves for the bioink, the inset shows a picture of a fractured sample. (c) SEM images showing fracture surface of the samples.

6.3.3 Cell viability and proliferation

L929 was tagged with green fluorescence as shown in Figure 6.7.

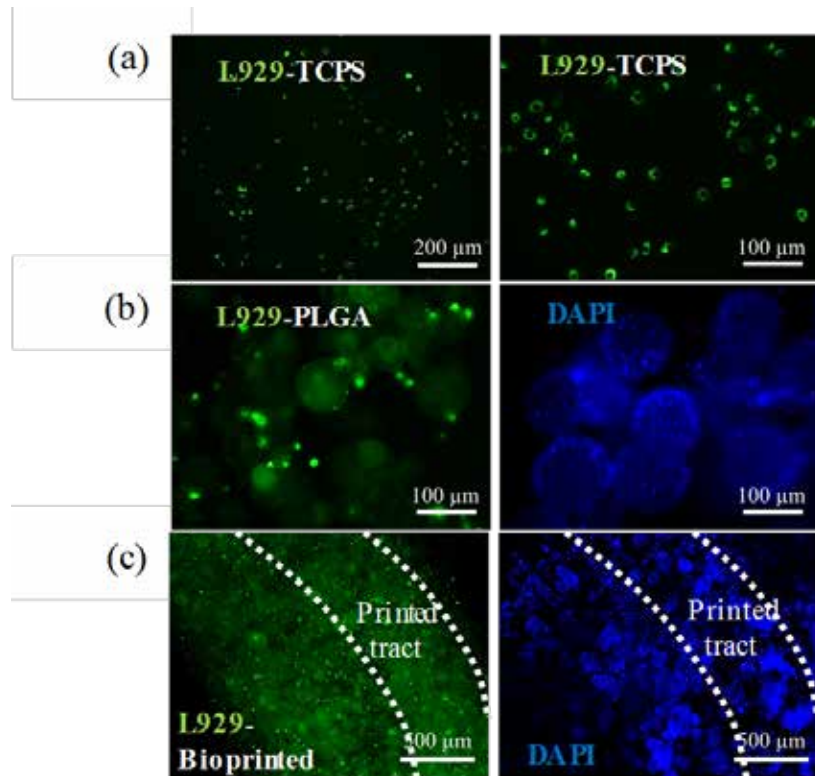


Figure 6.7. Fluorescence images of L929 cells labelled by green fluorescent cell linker PKH67GL cultured on (a) TCPS, (b) PLGA microspheres, and (c) printed construct.

L929 seeded on the microspheres and bioprinted L929 constructs are shown in Figure 6.7 (b) and (c). The green fluorescence on the cells showed that they were viable. SEM images in Figure 6.8 shows that there were many cells in the construct. Obvious cells are indicated by arrows. Dashed arrow shows the thin

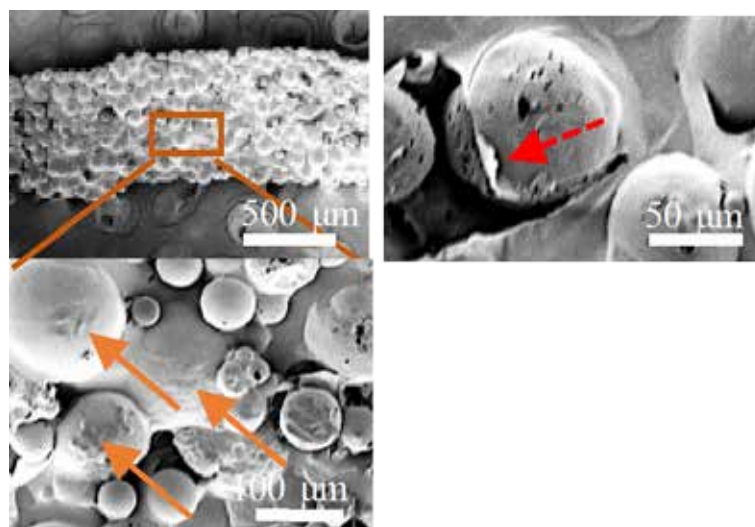


Figure 6.8. SEM images of the printed construct using L929 cells.

AC blend hydrogel coating, which was peeled off due to dehydration steps prior to SEM.

Observation of as-bioprinted ring constructs using different types of cells are shown in Figure 6.9 and Figure 6.10. L929 cells were labelled by green fluorescent cell linker PKH67GL, and A10, T146 and C2C12 cells were labelled with red fluorescent cell linker PKH26GL. The ring-shaped fluorescence images in Figure 6.9 were combined from multiple images of each samples captured under fluorescence microscope. Patterning different types of cells into 3D rings was possible with the current 3D bioprinting method. Concurrent printing of two different cell types can be achieved in each layer as illustrated in Figure 6.10. The multi-cell type bioprinting is useful for printing complex biological tissues or organs.

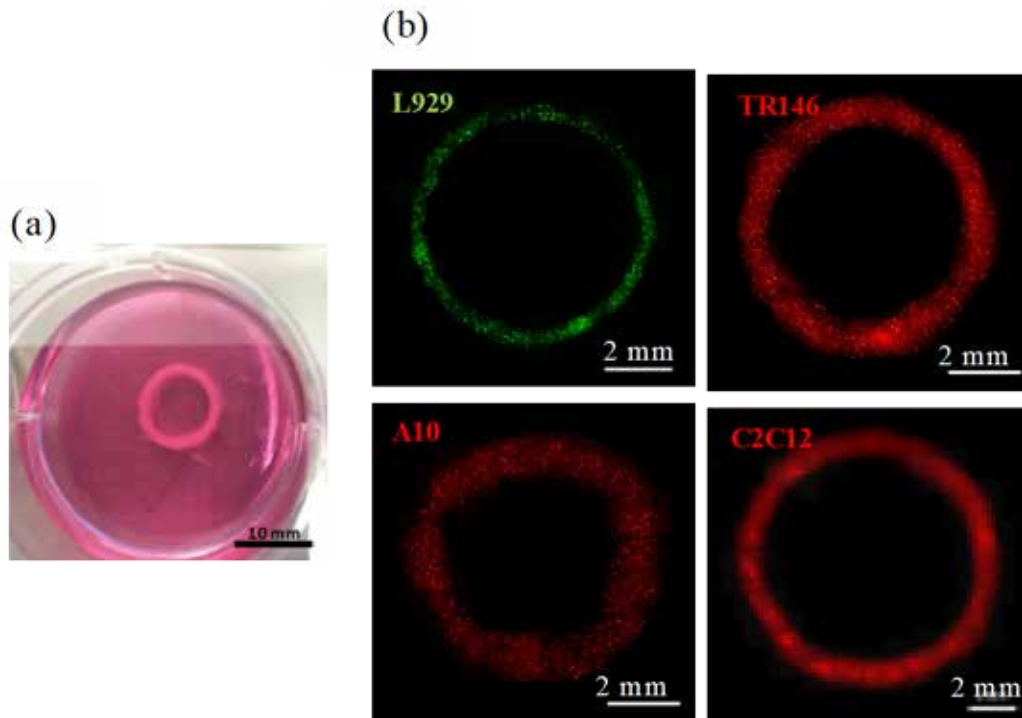


Figure 6.9. (a) Photograph of a bioprinted ring using C2C12. (b) Fluorescence images of printed ring constructs with L929, A10, TR146 and C2C12 cells.

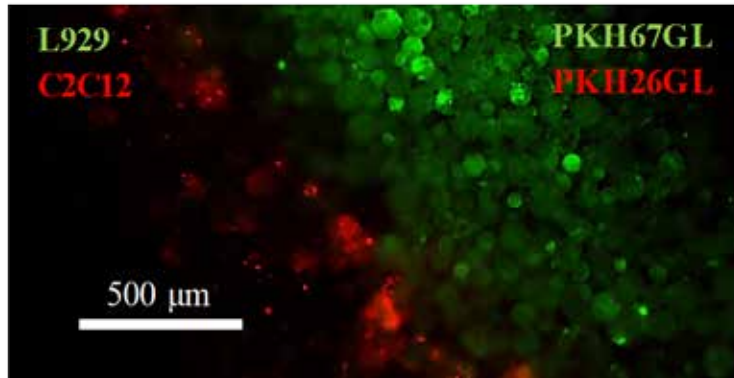


Figure 6.10. Fluorescence image reveal patterning of L929 cells (green) together with C2C12 cells (red) side-by-side achieved by printing.

To determine cell viability after extrusion, the survival of L929 from 1 to 72 hour(s) was firstly assessed as shown in Figure 6.11 (a). The printed cells were found to survive well after printing. The number of cells was continuously increased over 72 hours. For a longer-term study of printed cellular construct, the

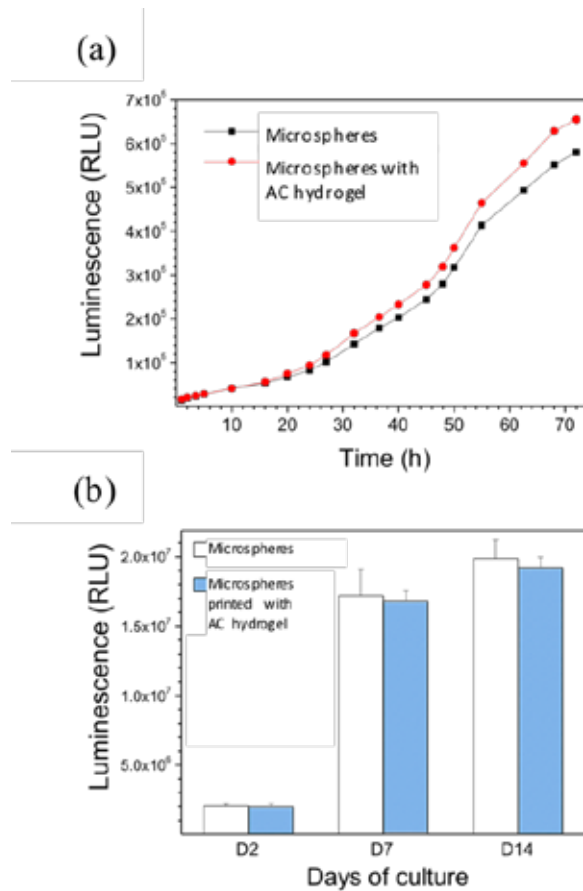


Figure 6.11. (a) Real time cell viability and proliferation of printed 3D constructs. (b) 3D cell viability within the printed construct on the day 2, 7, and 14 of culture after printing shows the cell growth over 14 days.

cell viability was accessed after culturing the bioprinted constructs for 2, 7 and 14 days. The printed cells continued to proliferate for 14 days after printing, with no significant difference (n=3) when compared to the control wells as illustrated in Figure 6.11 (b). Fluorescence images on the left in Figure 6.12 show the live (green)/dead (red) images of the construct captured by a fluorescence microscope; graphs on the right show the 2.5D reconstruction of the fluorescence images. Imaging by live/dead cell assays showed $\geq 90\%$ L929 cell viability for 2, 7 and 14 days after extrusion.

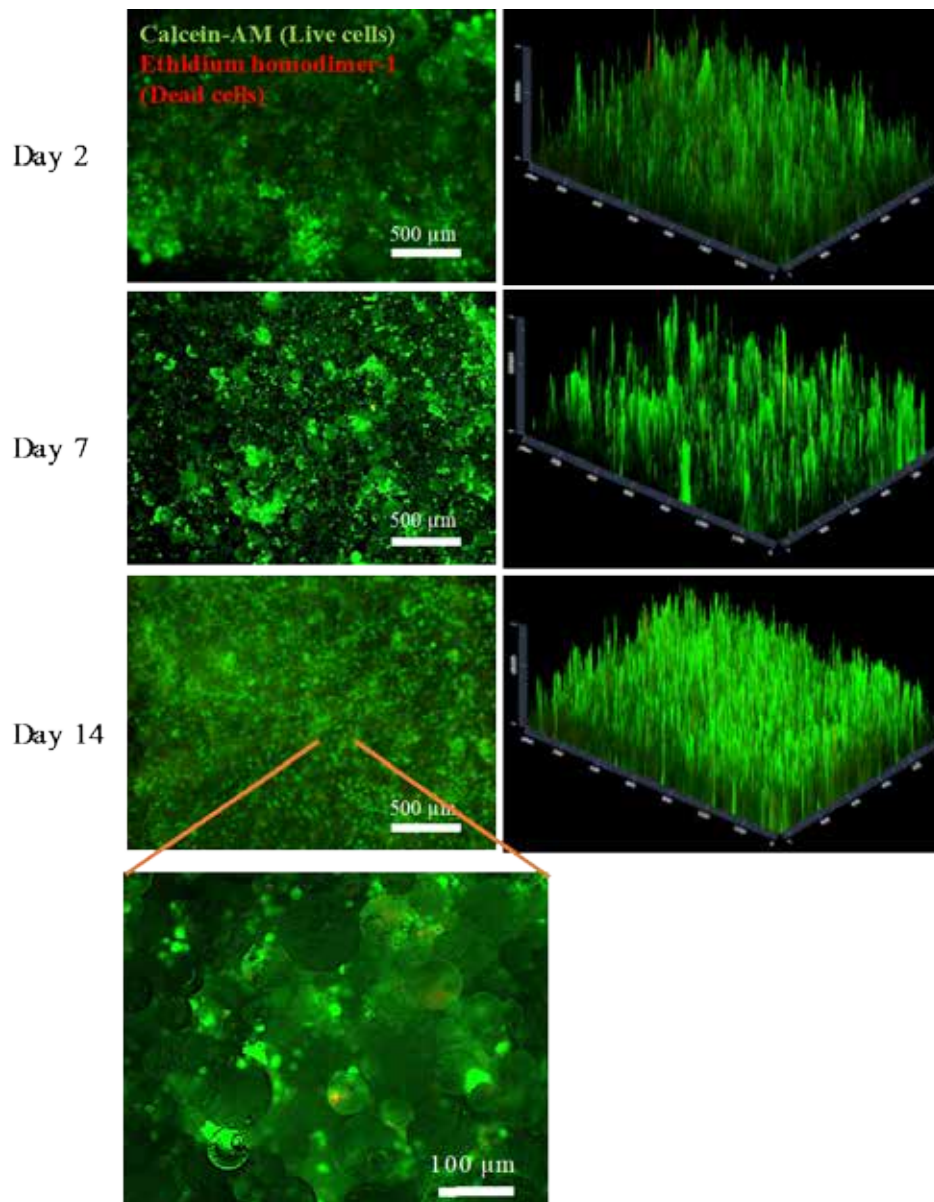


Figure 6.12. L929 cell viability on day 2, 7 and 14 of culture after printing.

Human epithelial TR146 cells from buccal mucosa were cell-seeded on the microspheres as shown in Figure 6.13. The cells maintained their morphology on the microspheres as shown in Figure 6.13 (a). The TR146 CLMs were printed and cultured for 2 weeks. TR146 with red fluorescent cell linker was shown to be printable and stayed viable after printing and culturing as shown in Figure 6.13 (b). Cells can be seen under SEM, but the epithelial cells were relatively flat so could not be identified easily. These results indicated that the printed construct maintained cell viability during the bioprinting process and provided a favourable microenvironment for cell growth.

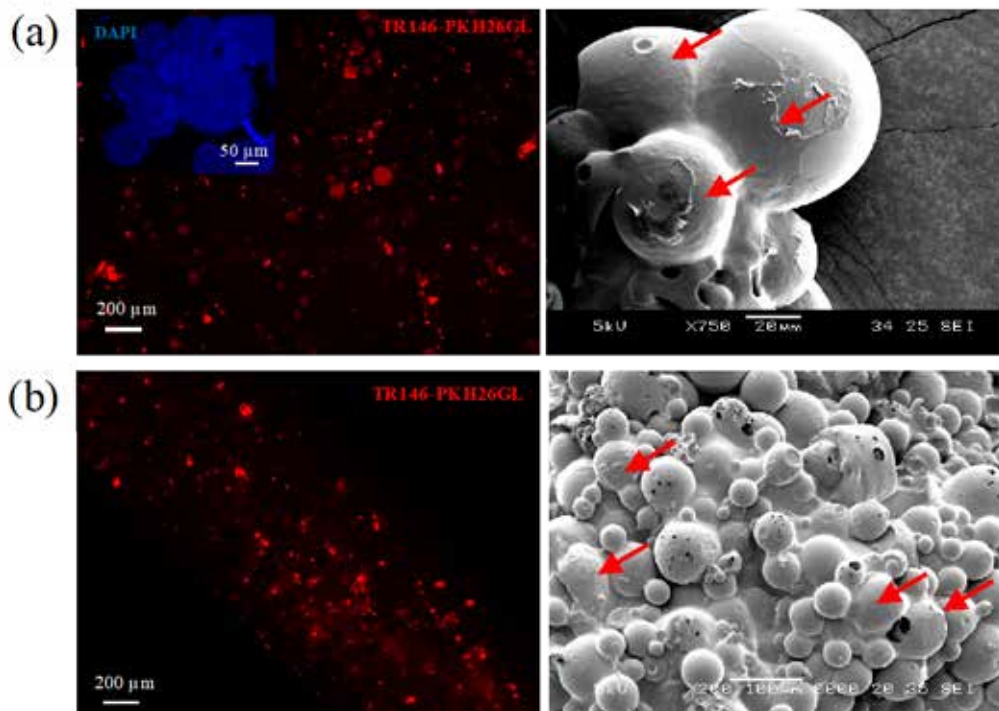


Figure 6.13. Fluorescence microscopy and SEM pictures of (a) TR146 epithelial cultured on microspheres and (b) bioprinted TR146 CLMs and cultured for 2 weeks. Cells are indicated by the arrows.

Myoblasts C2C12 and smooth muscle A10 were cell seeded on the microspheres separately. The C2C12 and A10 CLMs were printed separately into rings. C2C12 and its CLMs are shown in Figure 6.14 (a). After 3 days of culture,

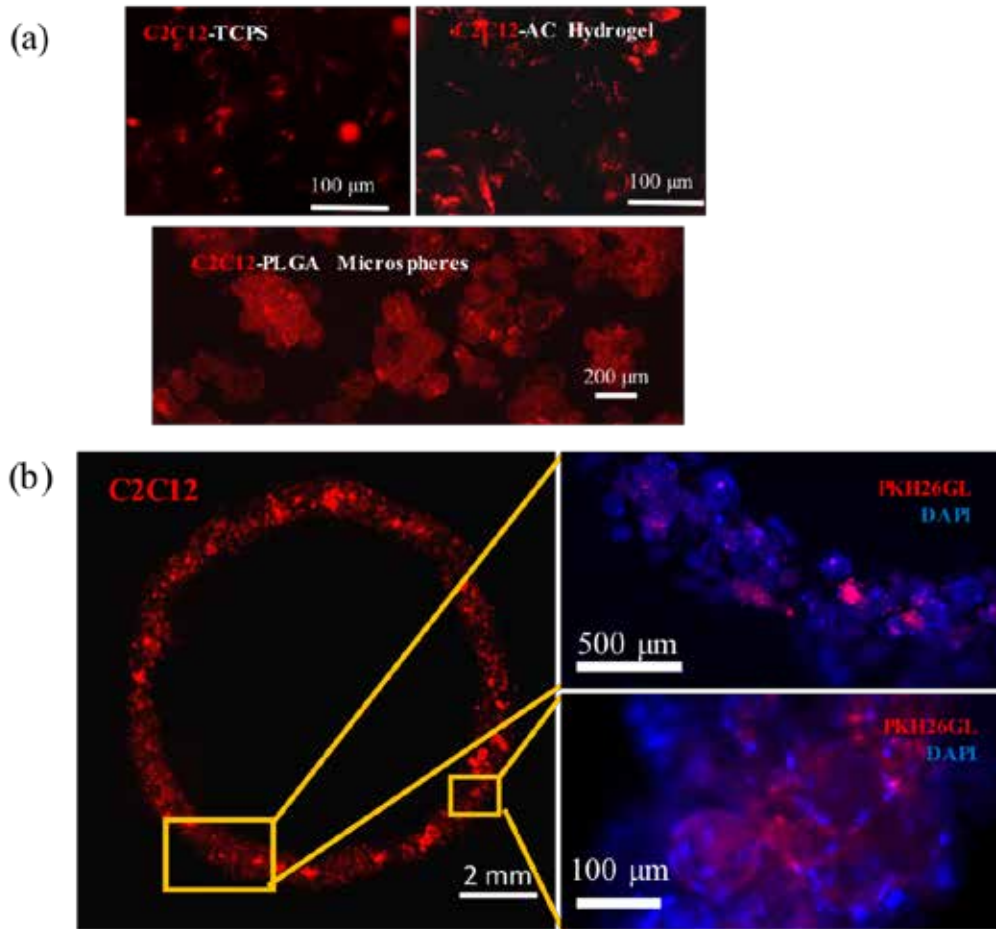


Figure 6.14. Fluorescence microscopic images of C2C12 tagged with red fluorescence (a) cultured on TCPS, AC blend hydrogel and PLGA microspheres (b) bioprinted into ring.

the bioprinted C2C12 construct were stained with DAPI as illustrated in Figure 6.14 (b). Note that the ring-shaped fluorescence image was combined from multiple images of the same sample captured under fluorescence microscope. DAPI staining of nucleus clearly indicated that cells were not aligned in these constructs. Smooth muscle A10 cells cultured on microspheres are shown in Figure 6.15 (a). Cells were shown to grow on the microspheres in an isotropic manner. After 3 days of culturing the bioprinted construct, the cells still showed no alignment as opposed to the control TCPS as illustrated in Figure 6.15 (b, c). SEM figures of bioprinted construct as illustrated in Figure 6.15 (d) also showed similar isotropic A10 cell growth.

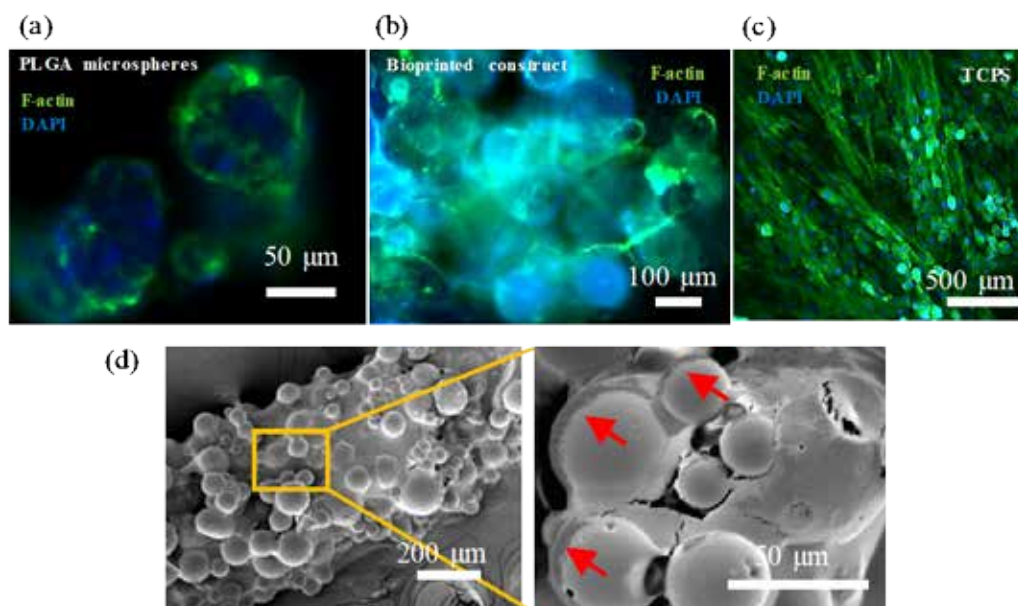


Figure 6.15. (a-c) Fluorescence microscopic images of A10 smooth muscle cells that were cultured on PLGA microspheres, bioprinted construct and TCPS. (d) SEM microscopic images of A10 bioprinted into ring. Cells were indicated by the arrows.

hMSCs were seeded onto the PLGA microspheres as shown in live (green)/dead (red) image in Figure 6.16. The normal elongated morphology of hMSCs was observed on the microspheres, similar to the TCPS control. Also, the hMSCs have high cell viability ($\geq 90\%$) on the PLGA microspheres. The CLMs were then bioprinted. The constructs were stained with CD44 (positive marker for hMSCs) and CD31 (negative marker for hMSCs) to show the hMSCs lineage

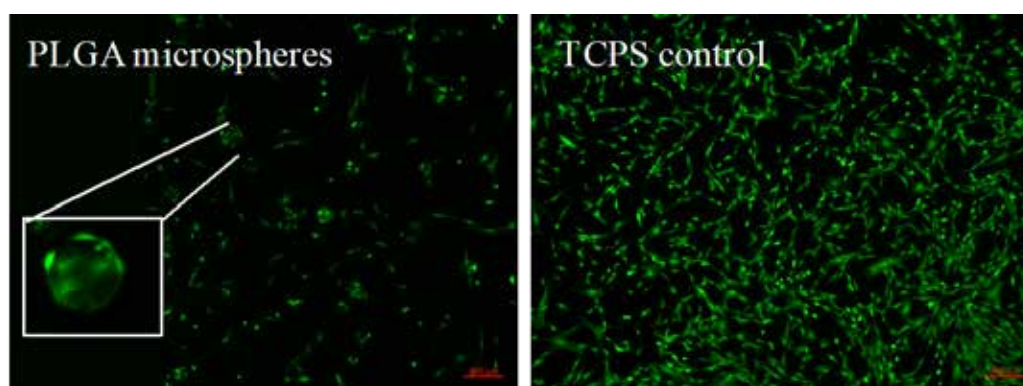


Figure 6.16. Live/dead imaging of hMSCs cultured on PLGA microspheres and TCPS (control).

as shown in Figure 6.17. After 2 weeks of culture, the osteo-differentiated construct showed a significantly higher (doubled) ALP activity when compared to the control, which was an indication of successful differentiation of hMSCs into osteoblasts. After 5 weeks of culture, the osteo-differentiated constructs stained with ARS showed red color (as seen in Figure 6.17) which indicated the calcium deposition by the mature osteoblasts.

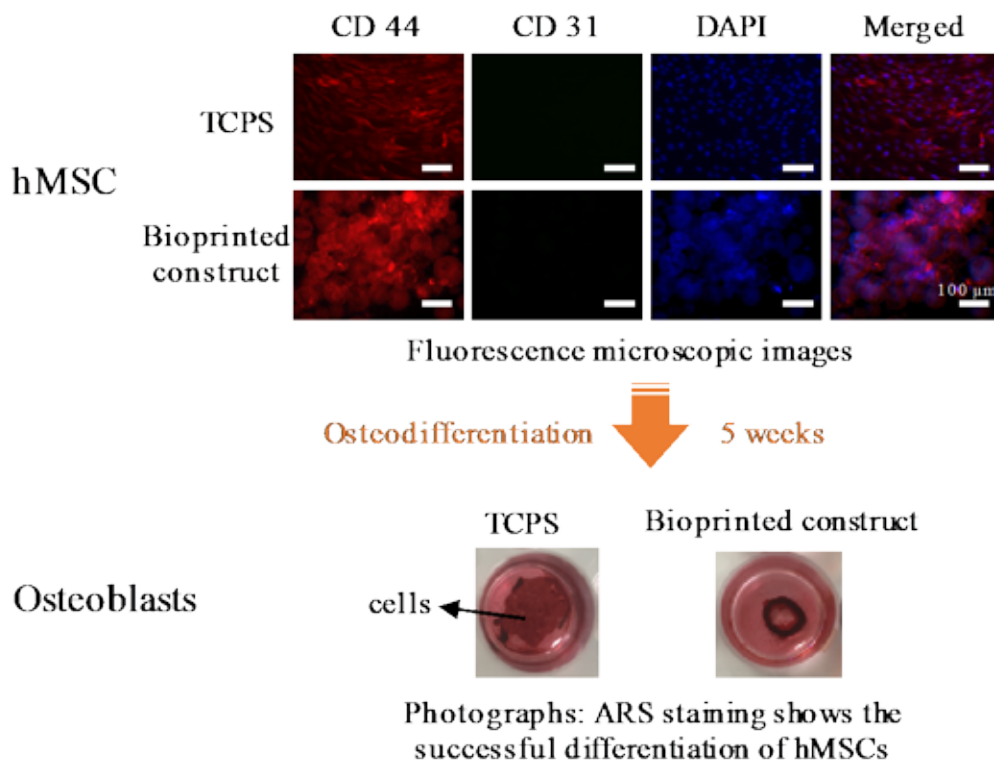


Figure 6.17. Fluorescence microscopic images showing Cy3 labeled CD44 (red), AlexaFluor 488 labeled CD31 (green), and DAPI nuclear staining (blue) for the hMSCs on control (TCPS) and bioprinted construct. Photographs of the ARS stained (red) osteo-differentiated cells on the TCPS and the bioprinted constructs.

6.4 Discussion

The micropipette extrusion-based bioprinting method explored in this Chapter using cell-laden microscaffold-based bioinks had shown good printability. This method exhibited good extrudability; enabled immediate gelation upon extrusion onto cold platform; and allowed formation of collagen

fiber networks within the printed construct during subsequent culture at 37 °C. High concentration gelatin was chosen as a support material due to its attribute as a biocompatible hydrogel gelling at low temperatures. It has been commonly used as support material in bioprinting [273] as it melts at culture temperature of 37 °C, allowing easy removal of the temporary support material once the bioprinted construct can self-support itself.

The current bioprinting strategies include extrusion-based, microvalve-based, laser-based, and inkjet-based printing. Microneedle, tapered tip, or nozzle based syringe extrusion methods were widely applied in the reported extrusion-based bioprinting approaches. It was found that the micropipette-based extrusion method was a good approach to print tightly packed PLGA microspheres. The tightly packed microspheres encapsulated in thin AC blend hydrogel samples could sustain a much higher stress and strain than both the AC blend hydrogel and the loosely packed samples. The mechanical strength of the bioink was dramatically improved by more than 100 times when compared to that of the AC blend hydrogel. Also, when the microspheres were loosely packed in AC blend hydrogel, the mechanical strength of the construct was increased only by 1.5 times compared to that of the AC blend hydrogel. The compressive moduli of the tightly packed microspheres samples were superior compared to the AC blend hydrogel. The improvement in mechanical properties was attributed to the packing of the strong polymer microspheres.

After the cellular constructs were cultured for two weeks, the PLGA microspheres started to self-aggregate, which might have further improved the strength of the construct. The tensile strength of the simulated construct with acellular PLGA aggregation was conducted. It was noted that the AC blend

hydrogel and loosely packed samples were not able to be clamped for tensile testing. The bioink was measured to have tensile UTS of ~25 kPa. The fracture initiated and propagated along the weakest intergranular boundary of the sample as was predicted.

This 3D bioprinting approach, when compared to pure hydrogel bioprinting, allowed for a better stacking ability for the fabrication of 3D constructs. With cushioning or shielding effect from the microspheres, there would be less shear stress-induced cell damage during extrusion-based printing process. The printed construct has been shown to provide a suitable 3D environment for different types of cells to grow on. By observing the results from live/dead assay, prediction of the cell growth patterns in bioprinted constructs is shown in Figure 6.18. Cells were initially seeded on the microspheres, forming thin spikes of green signals in the 2.5D reconstruction graph. After 7 days of culture, the cells continued proliferating within the CLMs; and started migrating out to the AC blend hydrogel. Homogeneous green signals from the live/dead graph after 14 days of culture indicated that cells were populating the whole bioprinted construct. Microspheres started to merge with each other at the

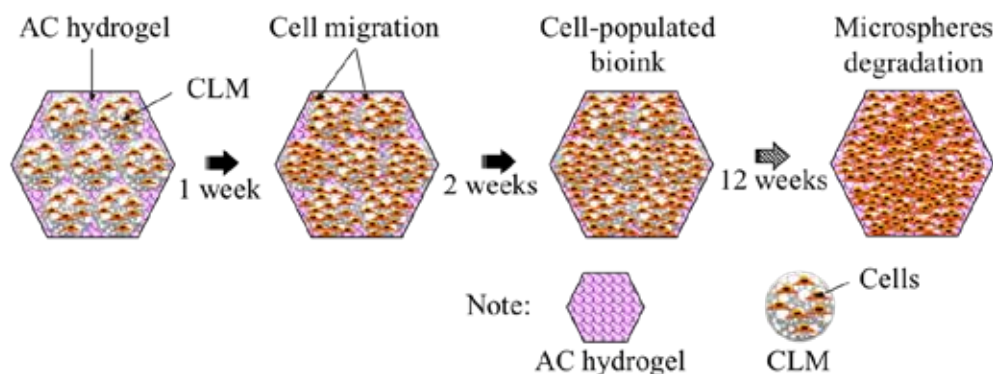


Figure 6.18. Schematic illustration of prediction of the cell growth patterns in bioprinted constructs

time point. Microspheres were supposed to degrade after 12 weeks of culture based on the PLGA hydrolytic degradation results.

The main purpose of bioprinting in this dissertation was to deliver the epithelial cells at the esophageal lumen; and the fibroblasts to create connective tissue adjoining epithelium to muscle layer. Folded structure with different diameters can be printed using the proposed approach. Fibroblasts and epithelial cells were shown to be viable after printing, and they continue to proliferate with time. As discussed in Section 2.4, it is challenging in extracting and culturing of primary epithelial cells without fibroblasts contamination. Hence, current research has been shifted to stem cells, especially the MSCs in esophageal TE [18,223]. Bone-marrow MSCs repopulated both GI epithelial cells and mesenchymal lineages in humans [225]. Here, the ability to deliver and pattern MSCs using the bioprinting approach was demonstrated. If the MSCs can maintain their stem cell lineage, then the bioprinted construct might be able to reconstruct the esophageal epithelium when implanted. Preliminary results showed that hMSCs can be printed without changing its lineage upon printing.

PLGA microspheres were used in this work, but other injectable microscaffolds could also serve the same purpose in this context. The scaffolds provided 2D surfaces with pseudo-3D environment for the anchorage-dependent epithelial and fibroblasts cells to adhere and proliferate. By using microscaffolds in 3D bioprinting, well-established surface treatment on scaffolds could be applied to enhance cell affinity. Bioactive factors could be added into the scaffolds and thus effectively control the stem cell fate. Levato *et al.* [274] used a collagen-functionalized solid microcarrier-based approach to print bi-layered osteochondral models for the bone compartment. They showed that the

microcarriers facilitated cell adhesion and supported bone cells differentiation by mesenchymal stem cells. The incorporation of proteins and drugs such as growth factors, antibody, and cell adhesion peptides into the microscaffolds could be realized for a sustainable release system in the printed construct. Poldervaart *et al.* [275,276] printed bone morphogenetic protein 2 (BMP-2) and vascular endothelial growth factor (VEGF) loaded gelatin microparticles for bone regeneration. A graded concentration of these molecules could also be accomplished in this printing. In addition, the microscaffolds could be functionalized, for example by encapsulation of magnets for *in vivo* imaging [277] of the implanted organ.

After culturing the bioprinted mouse myoblasts C2C12 and rat smooth muscle A10 cells, the cells were growing in the bioink with no preferential directional growth. C2C12 nuclei showed random distribution within the bioink. The A10 cells could be observed under SEM after 3 days of culture with no alignment. The F-actin architecture observed from the printed A10 construct was random as opposed to that of the TCPS control. This could be attributed to the random distribution of the highly isotropic microspheres. These results suggested that bioprinted CLMs could not provide anisotropic alignment for the TE of esophageal muscle layers.

The optimized AC blend hydrogel could be remained unsolidified at 37 °C for up to ~1 hr. Upon printing on ice, the hydrogel would solidify but still could sustain bonding between layers. Nonetheless, collagen displayed significant batch-by-batch variation [278]. The optimization process might need to be re-iterated when using a new batch of the collagen. In addition, there was currently no known mechanism for degradation of agarose. Although it was

suspected that the cells infiltration into the agarose may occur via discontinuities within the agarose hydrogel which might have occurred during the mechanical deformation of the hydrogel [279], the exact mechanism of clearance of agarose in the mammalian tissue environment was still unclear. Collagen and PLGA microspheres degradation might have caused large defects in agarose hydrogel which might accelerate agarose degradation *in vivo*.

In this study, the ability of bioprinting CLMs by using the micropipette extrusion-based method was demonstrated. Tight packing of microspheres was achieved. However, both resolution and speed of the extrusion-based printing method were still not in the desired range for large tissue printing. Exact and intricate printing has yet to be achieved. Indirect printing of the construct, e.g. printing of sacrificial moulds before extrusion of the bioink, could improve the printing resolution due to dimensional constriction whilst within the limitation of the microsphere sizes. It was also suggested that 3D bioprinting of microscaffolds was not restricted to extrusion-mode. For instance, CLMs could be tightly packed in photocurable hydrogels, followed by photo-curing layer by layer for highly efficient printing of tissue constructs. The current bioprinted construct is still weak when compared to the native tissue, mainly due to the weak AC blend hydrogel.

6.5 Summary

In summary, a hybrid 3D bioprinting approach using porous microscaffolds and micropipette extrusion-based printing method was presented. The bioink was constituted with cell-laden PLGA porous microspheres and thin encapsulation of AC blend hydrogel. The mechanical strength of the construct was greatly improved by more than 100 times when compared to the AC blend

hydrogel. Highly porous microspheres enabled anchorage-dependent epithelial cells, fibroblasts and hMSCs to adhere and proliferate in stirred culture before printing. Also, AC blend hydrogel allowed a smooth delivery of CLMs, with immediate gelation of construct upon printing on the cold build platform. Cells were successfully printed and they maintained high viability after printing. The cells also continued to proliferate with culture time. The bioprinted construct possessed high biocompatibility, with cell viability of more than 90% after culturing for 2, 7, and 14 days. hMSCs maintained its stem cells lineage after printing. Nevertheless, it was noted that alignment of myoblasts and SMCs could not be achieved by bioprinting of isotropic CLMs. A potential alternative in TE of epithelium was made possible by combining the advantages of the conventional solid scaffolds with the new 3D bioprinting technology.

Chapter 7. Overall summary, conclusions and future work

7.1 Summary

To achieve the TE of inherent structural heterogeneity in the esophageal tissues, this dissertation presented a hybrid biofabrication strategy to mimic the musculature and the mucosa of the esophagus.

The highly anisotropic endomuscular layer of musculature was constructed by the tubular microfibrinous PLC scaffold fabricated by the melt-drawing method. The scaffold, i.e. the exterior of the TE construct, was found to be sufficiently strong and elastic circumferentially. Tubular scaffolds with various dimensions, such as diameter, length and thickness, were successfully fabricated. The fibers were observed to be highly aligned and have a uniform fiber diameter distribution. The fiber diameters ranging from $13.9 \pm 1.7 \text{ }\mu\text{m}$ to $65.7 \pm 6.2 \text{ }\mu\text{m}$ was obtained by varying the melt-drawing speeds, which was found to be in good agreement with the developed mathematical model. The cells seeded onto the scaffolds *in vitro* showed appropriate cell proliferation, distribution, and infiltration. Myoblasts and hMSCs were highly aligned on the melt-drawn samples along the direction of the fiber alignment, which illustrated that the scaffold could support 3D-guided cells growth. hMSCs were differentiated into SMC lineage, showing that cellular shape modulation and scaffold elasticity adaptation could induce myogenic differentiation of stem cells. PLC scaffolds for TE of oriented smooth and skeletal muscles could meet the needs to the native myoarchitecture. The crystallinity of PLC was increased up to ~15 % with increasing melt-drawing speeds due to strain-induced

crystallization. Modulus and strength were increased while ductility decreased with an increase in crystallinity. Tensile properties of the scaffolds are comparable with the reported native human esophagus. The capability to control properties of the scaffolds, combined with their relative ease of manufacture compared to other TE techniques suggest that melt-drawn PLC tubular scaffold is an attractive candidate for TE of esophageal musculature.

The epithelium of mucosa was 3D bioprinted, which provided a platform for biofabrication of the folded mucosa. A novel bioink constituted with cell-laden PLGA porous microspheres with thin encapsulation of AC blend hydrogel was presented. The use of the cell-laden microscaffolds instead of the conventional cell-laden hydrogels and tissue spheroids as the building block in bioprinting could potentially solve the problem of cell source shortage. Highly porous microspheres enabled anchorage-dependent epithelial cells, fibroblasts and hMSCs to adhere and proliferate in the stirred culture before bioprinting. Also, AC blend hydrogel allowed a good printability of CLMs, with immediate gelation of construct upon printing on a chilled build platform. AC blend hydrogel also provided fine microstructure that could mimic the ECM of epithelium. Printing of tightly packed microspheres was demonstrated by using the micropipette extrusion-based 3D bioprinting approach. The mechanical strength of the cast bioink with tightly packed microspheres was greatly improved by more than 100 times when compared to that of the AC blend hydrogel. By utilizing the 3D bioprinting approach, all four different types of cells were successfully printed with high viability. The cells continued to proliferate within the bioprinted construct up to 14 days. The hMSCs maintained

its stem cell lineage after bioprinting, which could serve as an alternative to epithelial cells in the epithelium *in vivo* regeneration.

In vitro performances of individual components of a hybrid construct were successfully illustrated for TE of esophageal muscles and epithelium TE. The hybrid melt-drawn PLC exterior and bioprinted mucosa and submucosa are shown in Figure 7.1, offering the benefit of macro- and microstructural biomimicry for esophageal TE.

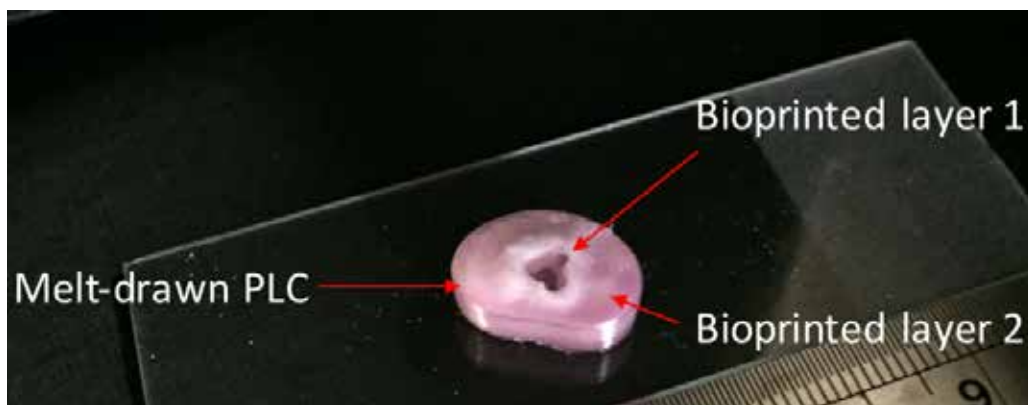


Figure 7.1. A prototype combining melt-drawn PLC fibrous scaffold with the bioprinted PLGA microspheres. The bioprinted layers 1 and 2 are to mimic the folded epithelium and the underlying connective tissues, respectively.

The melt-drawn PLC and bioprinted PLGA microspheres components have distinctive features. Melt-drawn PLC tubular scaffold exhibited high anisotropy but bioprinted PLGA microsphere construct was nearly isotropic. The melt-drawn PLC complemented the strength and elasticity of the construct. On the other hand, the bioprinted construct could complement the ability to control structural integrity and form the epithelium. Bioprinting of connective tissues could adjoin the inner bioprinted epithelium layer and the outer cell-seeded PLC scaffold layer. Overall, this hybrid bioengineered TE construct provided a new insight into the customization of critical properties of esophageal scaffolds.

7.2 Conclusions

The goal of this dissertation was to develop personalization of esophageal TE construct, focusing on the two main components, i.e. the muscle and the epithelium tissues. Towards this end, customizable strategies to create a hybrid TE construct for bioengineering of the structurally heterogeneous esophagus were successfully developed. For bioengineering of the anisotropic musculature with tunable strength and elasticity, semicrystalline PLC could be melt-drawn at different melt-drawing speeds. The capability to customize the scaffolds' dimensions was clearly demonstrated. To regenerate the folded mucosa, isotropic epithelial cells-seeded PLGA microspheres were bioprinted. The bioink showed high strength and good stacking ability when compared to pure hydrogels.

The fabrication of PLC scaffolds demonstrated the asynchronous cell incorporation method, while the bioprinting of cell-laden PLGA microspheres affirmed the concurrent cell incorporation TE method. The hybrid bioengineering of muscle cell-seeded exterior of tubular scaffold and 3D bioprinting of interior folded mucosa in the lumen had demonstrated their potential application prospect in esophageal TE.

The hybrid biofabricated construct met all the necessary requirements for esophageal TE, i.e. (i) achieving suitable dimensions and shape; (ii) being flexible circumferentially; (iii) possessing a surface suitable for epithelium and muscle regeneration; and (iv) being strong enough for holding the structure and to be handled by practitioner. The construct was shown to be biocompatible with certain degree of both macro- and micro-structural tissue mimicry. Moreover, it possessed open, interconnected pores, with satisfactory pore sizes for cell infiltration and cell growth.

7.3 Future work

As most of the mammals' major organs, including the lung, trachea, kidney, GI tract, genitourinary system and vasculature, are composed primarily of tubes, the hybrid TE construct could be particularly useful when applied to these tubular organs TE. One example would be TE of arterial tissues. Biomechanical properties of arterial tissues have been determined to follow a "J" curve in the pressure–diameter plot, i.e. large inflation in the low-pressure regions, gradually reduced inflation in physiological pressure regions and then a little inflation in the high-pressure regions [280]. An arterial tissue TE construct requires compliance matching with the native arteries. The difference in mechanical properties between a TE construct and a native artery may induce hemodynamically flow disturbance. Stress concentrates near the anastomosed site, thereby enhancing thrombus formation and neointimal hyperplasia [280]. The melt-drawing technique was adapted to draw PLC on a dip-coated PLC tube to fabricate a compliant arterial tissue TE construct [281]. The fabricated tube simulated well with the a "J" curve of a native artery, when compared to a dip-coated PLC tube. Moreover, the fabricated tube was highly kink resistant. Further improvement can be made by bioprinting of a layer of endothelium in the lumen of the tube, enhancing endothelium regeneration in the construct.

The resection of native colon had caused significant morbidities, which include the changes in water and sodium absorption, the production of short chain fatty acids, and the lack of storage capacity [282]. Vacanti *et al.* [282] fabricated TE colon based on PGA and PLA polymers. The polymer tubes were internally loaded with organoid units, which were isolated from the sigmoid colon, by micropipette. The TE conduits had significant absorptive capacity when

implanted, but there was no direct measurement of motility. Hecker *et al.* [283] bioengineered fibrin-based tissue construct with smooth muscle alignment, which was shown to maintain aspects of colonic physiology such as motility. The combination of these two approaches can be akin to the proposed method in this dissertation. The PLC microfibers fabricated by melt-drawing and mimicking native smooth muscle alignment might improve the motility of the TE construct. The adoption of bioprinting of mucosal folds may also assist in the intestinal epithelium regeneration, hence has a high potential to improve the functionality of the colonic TE construct.

Based on the results achieved in this dissertation, future work can be carried out to improve the performance of the techniques described in this dissertation in the following three directions: (1) to enhance the melt-drawing processability for a wide variety of tubular scaffolds; (2) to increase the porosity of melt-drawn tubular scaffolds; and (3) to improve the microscaffold-based bioprinting technique.

To produce PLC scaffolds with more precise control and a larger variety in process parameters, a new melt-drawing machine is being developed in progress as shown in Figure 7.2. The new machine can be adjusted for a great variety of sizes of mandrels, thus widening the range of diameters and lengths of the tubular scaffolds to be fabricated. An increase in the machine length could allow to fabricate longer scaffolds for large-gap esophageal replacement. The mandrel's rotational speed could be further increased compared to the current set up, and this would enable the machine to fabricate even finer fibers. There will be also a larger range of transverse movement speeds for melt-holder in the new machine. Furthermore, cross fibers could be created with the new design to

improve the tubular scaffold's strength in longitudinal direction. The new set up has two melt-holders that can increase the efficiency in scaffold fabrication. More importantly, multi-material scaffold design will become possible. In the future, the machine will have more automated control such that control of transverse motion and fiber layering will be more precise. Compiling all the technical improvements, this new machine will be able to create tubular scaffolds with better control in both structure and topology.

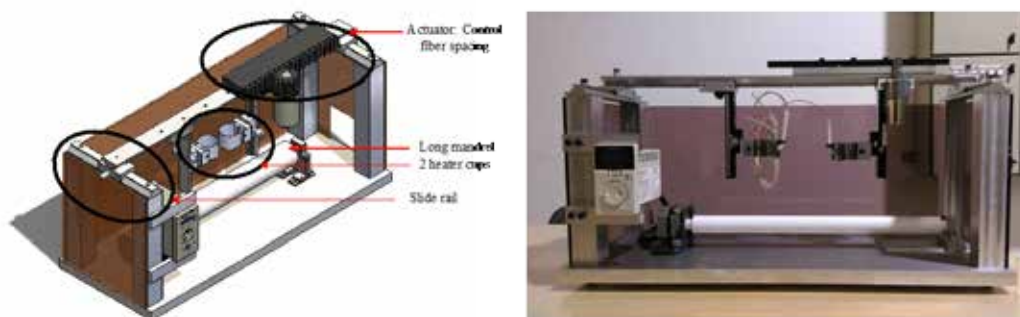


Figure 7.2. Rendered design (left) and picture (right) of the melt-drawing machine being newly designed.

The melt-drawn PLC scaffolds fabricated have interconnected pores due to the single fiber drawing process, but their main drawback is their low porosities. Hence, it is important to increase the porosities of the scaffolds so that cell infiltration and vascularization, which are the factors critical for *in vivo* applications, can be much enhanced. The new scaffolds comprised of melt-drawn fluffy PCL fibers concurrently with PLC to form tubes as illustrated in Figure 7.3 have high porosities. Further improvements on these scaffolds will be made, especially on the parameter optimization such as controlling the ratio of PLC and PCL to improve the scaffold's porosity, strength, and alignment.

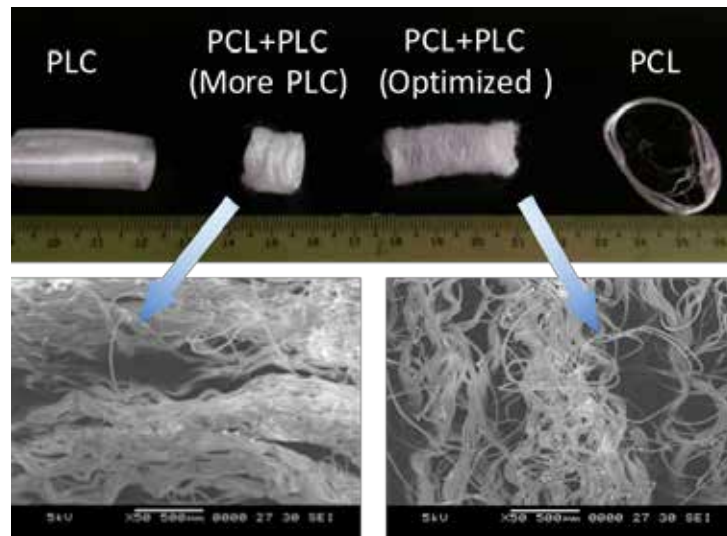


Figure 7.3. Illustrations and SEM images showing melt-drawn PLC (left), PCL (right) and hybrid co-melt-drawing of PLC and PCL

For the 3D bioprinting part, future work will be focusing on improvement in the fabrication process through automation to establish procedures for 3D printing of reproducible and complicated constructs. To further explore the possibility of the microscaffolds-based bioprinting approach, concerns regarding innervation and vascularization of TE construct should be addressed. These delicate and complex features, which would be difficult to be achieved using melt-drawing method, can be realized using CLMs bioprinting.

Thin nerve fibers and numerous ganglia provide the innervation of the esophagus [34]. The ganglia that lie between the longitudinal and the circular layers of the muscularis externa form the myenteric plexus, which regulates contraction of the muscle layers. Meanwhile, the ganglia that lie in the submucosa form the Meissner's plexus, which regulates secretion and the peristaltic contractions of the muscularis mucosa [34]. Previous reported TE methods relied on neural stem cells therapy to re-innervate the muscles [6,284,285]. These stem cells migrate, proliferate and differentiate *in vivo* after their transplantation into animal models. It is strongly suggested here that the

bioengineering of nervous components could be made possible by utilizing CLMs bioprinting. The microspheres can be seeded with neural stem cells before bioprinting. However, there is a need to reduce the size and size distribution of microspheres to achieve the replication of the nerve fibers (micron-scale). These CLMs should be printed side-by-side for a controlled nerve tissue maturation such that signal transmission could be made possible. Here, alginate beads with uniform size distribution (but with large diameters of ~ 1 mm) were fabricated and printed for illustration purposes, as shown in Figure 7.4. Note that it is challenging to fabricate micron-scale beads with uniform size distribution, and that it is also technically difficult to print them side-by-side. More efforts are needed in order to achieve the esophageal innervation using CLMs bioprinting.

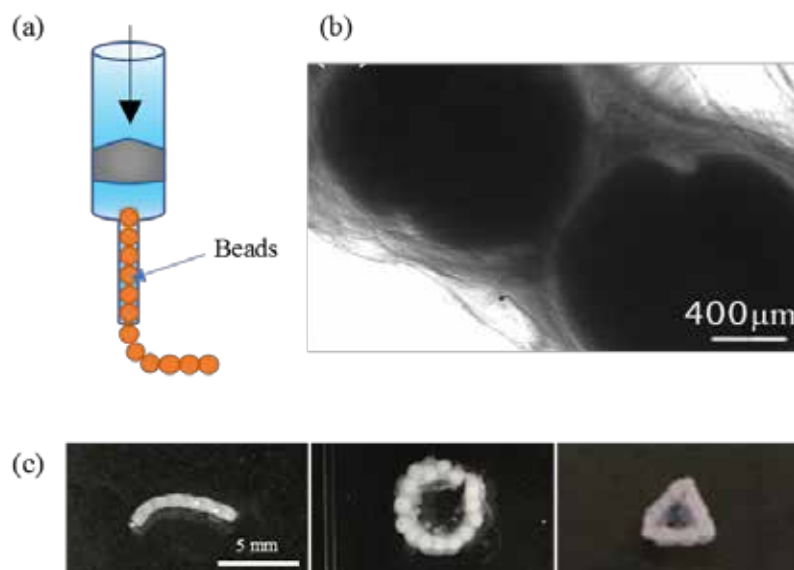


Figure 7.4. (a) Illustration of beads printing for the bioprinting of nervous CLMs in the future. (b) OM and (c) pictures of the printed beads.

Vascularization of the esophagus is also important since substantial thicknesses of the organ are to be engineered. Similar approach as discussed in the last paragraph could be applied to bioengineer the vascular system of the esophagus. The bioprinting strategies could be extended to utilize new material

combinations, producing different forms of microscaffolds, and developing novel printing methods to assemble the CLMs. Growth factors encapsulation, especially EGFs and vascular endothelial growth factors (VEGFs), can be incorporated in the microscaffolds to improve epithelium growth and vascularization.

The study on tissue interface bonding between the melt-drawn tubular scaffold and the bioprinted layers would be required. Combining the improved techniques in fabricating each layer, the implantable TE construct could be realized.

References

- [1] Chian KS, Leong MF, Kono K. Regenerative medicine for oesophageal reconstruction after cancer treatment. *Lancet Oncol* 2015;16:84–92.
- [2] Esophagus Cancer. *Am Cancer Soc* 2016:1–59. <http://www.cancer.org/cancer/esophaguscancer/detailedguide/esophagus-cancer-key-statistics>.
- [3] Kujawski K, Stasiak M, Rysz J. The evaluation of esophageal stenting complications in palliative treatment of dysphagia related to esophageal cancer. *Med Sci Monit* 2012;18:323-9.
- [4] Tai P, Yu E. Esophageal cancer management controversies: Radiation oncology point of view. *World J Gastrointest Oncol* 2014;6:263–74.
- [5] Hindy P, Hong J, Lam-Tsai Y, Gress F. A comprehensive review of esophageal stents. *Gastroenterol Hepatol* 2012;8:526–34.
- [6] Bitar KN, Zakhem E. Bioengineering the gut: future prospects of regenerative medicine. *Nat Rev Gastroenterol Hepatol* 2016;13:543–56.
- [7] Dua KS, Hogan WJ, Aadam AA, Gasparri M. In-vivo oesophageal regeneration in a human being by use of a non-biological scaffold and extracellular matrix. *Lancet* 2016;388:55–61.
- [8] Taylor AL, Watson CJE, Bradley JA. Immunosuppressive agents in solid organ transplantation: Mechanisms of action and therapeutic efficacy. *Crit Rev Oncol Hematol* 2005;56:23–46.
- [9] Lyons AS, Robert Beck A, Lester LJ. Esophageal replacement with prosthesis: Preliminary report of experimental studies. Vol. 2. Academic Press; 1962.
- [10] Langer R, Vacanti JP. Tissue engineering. *Science* 1993;260:920–6.
- [11] Tan JY, Chua CK, Leong KF, Chian KS, Leong WS, Tan LP. Esophageal tissue engineering: An in-depth review on scaffold design. *Biotechnol Bioeng* 2012;109:1–15.
- [12] Macchiarini P, Jungebluth P, Go T, Asnaghi MA, Rees LE, Cogan TA, *et al.* Clinical transplantation of a tissue-engineered airway. *Lancet*

2008;372:2023–30.

- [13] Badylak SF, Weiss DJ, Caplan A, Macchiarini P. Engineered whole organs and complex tissues. *Lancet* 2012;379:943–52.
- [14] Zhu Y, Leong MF, Ong WF, Chan-Park MB, Chian KS. Esophageal epithelium regeneration on fibronectin grafted poly (L-lactide-co-caprolactone)(PLLC) nanofiber scaffold. *Biomaterials* 2007;28:861–8.
- [15] Gong C, Hou L, Zhu Y, Lv J, Liu Y, Luo L. In vitro constitution of esophageal muscle tissue with endocyclic and exolongitudinal patterns. *ACS Appl Mater Interfaces* 2013;5:6549–55.
- [16] Ozeki M, Narita Y, Kagami H, Ohmiya N, Itoh A, Hirooka Y, *et al.* Evaluation of decellularized esophagus as a scaffold for cultured esophageal epithelial cells. *J Biomed Mater Res Part A* 2006;79A:771–8.
- [17] Badylak SF, Vorp DA, Spievack AR, Simmons-Byrd A, Hanke J, Freytes DO, *et al.* Esophageal reconstruction with ECM and muscle tissue in a dog model. *J Surg Res* 2005;128:87–97.
- [18] Sjöqvist S, Jungebluth P, Ling Lim M, Haag JC, Gustafsson Y, Lemon G, *et al.* Experimental orthotopic transplantation of a tissue-engineered oesophagus in rats. *Nat Commun* 2014;5.
- [19] Saxena AK, Faraj KA, Damen WF, van Kuppevelt TH, Weijnen R, Ainoedhofer H, *et al.* Comparison of collagen scaffold tubes for possible esophagus organ tissue engineering applications: In-situ omental implantation study in an ovine model. *Eur Surg* 2010;42:309–13.
- [20] Diemer P, Markoew S, Le DQS, Qvist N. Poly- ϵ -caprolactone mesh as a scaffold for *in vivo* tissue engineering in rabbit esophagus. *Dis Esophagus* 2014;28:240–5.
- [21] Leong MF, Chian KS, Mhaisalkar PS, Ong WF, Ratner BD. Effect of electrospun poly (D, L-lactide) fibrous scaffold with nanoporous surface on attachment of porcine esophageal epithelial cells and protein adsorption. *J Biomed Mater Res Part A* 2009;89:1040–8.
- [22] Mhaisalkar P, Kerm Sin C. Long-term culture of porcine esophageal epithelial cells without use of feeder layers. *Cell Biol Int* 2007;31:433–7.

- [23] Macheiner T, Kuess A, Dye J, Saxena AK. A novel method for isolation of epithelial cells from ovine esophagus for tissue engineering. *Biomed Mater Eng* 2014;24:1457–68.
- [24] Góra A, Pliszka D, Mukherjee S, Ramakrishna S. Tubular tissues and organs of human body—challenges in regenerative medicine. *J Nanosci Nanotechnol* 2016;16:19-39.
- [25] Nakase Y, Nakamura T, Kin S, Nakashima S, Yoshikawa T, Kuriu Y, *et al.* Intrathoracic esophageal replacement by in situ tissue-engineered esophagus. *J Thorac Cardiovasc Surg* 2008;136:850–9.
- [26] Chung S, Ingle NP, Montero GA, Kim SH, King MW. Bioresorbable elastomeric vascular tissue engineering scaffolds via melt spinning and electrospinning. *Acta Biomater* 2010;6:1958–67.
- [27] Wu S, Liu X, Yeung KWK, Liu C, Yang X. Biomimetic porous scaffolds for bone tissue engineering. *Mater Sci Eng R Reports* 2014;80:1–36.
- [28] Lim TC, Chian KS, Leong KF. Cryogenic prototyping of chitosan scaffolds with controlled micro and macro architecture and their effect on *in vivo* neo-vascularization and cellular infiltration. *J Biomed Mater Res Part A* 2010;94A:1303–11.
- [29] Vanags I, Petersons A, Ose V, Ozolanta I, Kasyanov V, Laizans J, *et al.* Biomechanical properties of oesophagus wall under loading. *J Biomech* 2003;36:1387–90.
- [30] Standring S, Ellis H, Healy JC, Jhonson D, Williams A, Collins P. Gray’s anatomy: the anatomical basis of clinical practice. *Am J Neuroradiol* 2005;26:2703.
- [31] Mir M, Ali MN, Ansari U, Sami J. Structure and motility of the esophagus from a mechanical perspective. *Esophagus* 2016;13:8–16.
- [32] Squier CA, Kremer MJ. Biology of oral mucosa and esophagus. *JNCI Monogr* 2001;2001:7–15.
- [33] Al Yassin TM, Toner PG. Fine structure of squamous epithelium and submucosal glands of human oesophagus. *J Anat* 1977;123:705.

- [34] Kuo B, Urma D. Esophagus - anatomy and development. GI Motil Online, 2006.
- [35] Mashimo H, Goyal RK. Physiology of esophageal motility. GI Motil Online, 2006.
- [36] Hogan BLM, Kolodziej PA. Organogenesis: molecular mechanisms of tubulogenesis. Nat Rev Genet 2002;3:513–23.
- [37] Chung S, Andrew DJ. The formation of epithelial tubes. J Cell Sci 2008;121.
- [38] Andrew DJ, Ewald AJ. Morphogenesis of epithelial tubes: Insights into tube formation, elongation, and elaboration. Dev Biol 2010;341:34–55.
- [39] Kou W, Bhalla APS, Griffith BE, Pandolfino JE, Kahrilas PJ, Patankar NA. A fully resolved active musculo-mechanical model for esophageal transport. J Comput Phys 2015;298:446–65.
- [40] Orlando RC. Esophageal mucosal defense mechanisms. GI Motil Online, 2006.
- [41] Preston S, Wright NA, Direkze N, Brittan M. Stem cells in the gastrointestinal tract. Princ. Tissue Eng., 2014, p. 901–33.
- [42] Lowe JS, James S, Anderson PG, Preceded by: Stevens A. Stevens & Lowe's human histology.
- [43] Song TJ, Kim YH, Ryu HS, Hyun JH. Correlation of esophageal lengths with measurable external parameters. Korean J Intern Med 1991;6:16–20.
- [44] White SB, Levine MS, Rubesin SE, Spencer GS, Katzka DA, Laufer I. The small-caliber esophagus: Radiographic sign of idiopathic eosinophilic esophagitis. Radiology 2010;256:127–34.
- [45] Schraufnagel DE, Michel JC, Sheppard TJ, Saffold PC, Kondos GT. CT of the normal esophagus to define the normal air column and its extent and distribution. Am J Roentgenol 2008;191:748–52.
- [46] Bouma BE, Tearney GJ, Compton CC, Nishioka NS. High-resolution imaging of the human esophagus and stomach *in vivo* using optical coherence tomography. Gastrointest Endosc 2000;51:467–74.

- [47] Zuccaro G, Gladkova N, Vargo J, Feldchtein F, Zagaynova E, Conwell D, *et al.* Optical coherence tomography of the esophagus and proximal stomach in health and disease. *Am J Gastroenterol* 2001;96:2633-9.
- [48] Zhang J, Tian D, Lin R, Zhou G, Peng G, Su M, *et al.* Phase-contrast X-ray CT imaging of esophagus and esophageal carcinoma. *Sci Rep* 2014;4:74–108.
- [49] Xia F, Mao J, Ding J, Yang H. Observation of normal appearance and wall thickness of esophagus on CT images. *Eur J Radiol* 2009;72:406–11.
- [50] Natali AN, Carniel EL, Gregersen H. Biomechanical behaviour of oesophageal tissues: material and structural configuration, experimental data and constitutive analysis. *Med Eng Phys* 2009;31:1056–62.
- [51] Egorov VI, Schastlivtsev I V, Prut E V, Baranov AO, Turusov RA. Mechanical properties of the human gastrointestinal tract. *J Biomech* 2002;35:1417–25.
- [52] Gilbert PM, Havenstrite KL, Magnusson KEG, Sacco A, Leonardi NA, Kraft P, *et al.* Substrate elasticity regulates skeletal muscle stem cell self-renewal in culture. *Science* 2010;329:1078–81.
- [53] Rus D, Tolley MT. Design, fabrication and control of soft robots. *Nature* 2015;521:467–75.
- [54] Trabelsi O, del Palomar AP, López-villalobos JL, Ginel A, Doblaré M. Experimental characterization and constitutive modeling of the mechanical behavior of the human trachea. *Med Eng Phys* 2010;32:76–82.
- [55] Chen Q, Liang S, Thouas GA. Elastomeric biomaterials for tissue engineering. *Prog Polym Sci* 2013;38:584–671.
- [56] Gregersen H. Biomechanics of the gastrointestinal tract: new perspectives in motility research and diagnostics. Springer; 2003.
- [57] Sokolis DP. Strain-energy function and three-dimensional stress distribution in esophageal biomechanics. *J Biomech* 2010;43:2753–64.
- [58] Gregersen H, Lee TC, Chien S, Skalak R, Fung YC. Strain distribution in the layered wall of the esophagus. *J Biomech Eng* 1999;121:442.

- [59] van der Rest M, Garrone R. Collagen family of proteins. *FASEB J* 1991;5:2814–23.
- [60] Daamen WF, Veerkamp JH, van Hest JCM, van Kuppevelt TH. Elastin as a biomaterial for tissue engineering. *Biomaterials* 2007;28:4378–98.
- [61] Alberts B, Johnson A, Lewis J, Raff M, Roberts K, Walter P. *Molecular Biology of the Cell*, 4th edition. 4th ed. New York: Garland Science; 2002.
- [62] Bianco P, Robey PG. Stem cells in tissue engineering. *Nature* 2001;414:118–21.
- [63] Yang S, Leong KF, Du Z, Chua CK. The design of scaffolds for use in tissue engineering. Part I. Traditional factors. *Tissue Eng* 2001;7:679–89.
- [64] Yang S, Leong KF, Du Z, Chua CK. The design of scaffolds for use in tissue engineering. Part II. Rapid prototyping techniques. *Tissue Eng* 2002;8:1–11.
- [65] Hollister SJ. Porous scaffold design for tissue engineering. *Nat Mater* 2005;4:518–24.
- [66] Leong KF, Chua CK, Sudarmadji N, Yeong WY. Engineering functionally graded tissue engineering scaffolds. *J Mech Behav Biomed Mater* 2008;1:140–52.
- [67] Leong KF, Cheah CM, Chua CK. Solid freeform fabrication of three-dimensional scaffolds for engineering replacement tissues and organs. *Biomaterials* 2003;24:2363–78.
- [68] Sachlos E, Czernuszka JT. Making tissue engineering scaffolds work. Review: the application of solid freeform fabrication technology to the production of tissue engineering scaffolds. *Eur Cell Mater* 2003;5:29-39-40.
- [69] Davidenko N, Gibb T, Schuster C, Best SM, Campbell JJ, Watson CJ, *et al.* Biomimetic collagen scaffolds with anisotropic pore architecture. *Acta Biomater* 2012;8:667–76.
- [70] Lee CH, Shin HJ, Cho IH, Kang YM, Kim IA, Park KD, *et al.* Nanofiber alignment and direction of mechanical strain affect the ECM production

of human ACL fibroblast. *Biomaterials* 2005;26:1261–70.

- [71] Phu D, Wray LS, Warren R V, Haskell RC, Orwin EJ. Effect of substrate composition and alignment on corneal cell phenotype. *Tissue Eng Part A* 2011;17:799–807.
- [72] Ritchie AC, Wijaya S, Ong WF, Zhong SP, Chian KS. Dependence of alignment direction on magnitude of strain in esophageal smooth muscle cells. *Biotechnol Bioeng* 2009;102:1703–11.
- [73] Shen Q, Shi P, Gao M, Yu X, Liu Y, Luo L, *et al.* Progress on materials and scaffold fabrications applied to esophageal tissue engineering. *Mater Sci Eng C* 2013;33:1860–6.
- [74] Yang J, Motlagh D, Webb AR, Ameer GA. Novel biphasic elastomeric scaffold for small-diameter blood vessel tissue engineering. *Tissue Eng* 2005;11:1876–86.
- [75] Hutmacher DW. Scaffold design and fabrication technologies for engineering tissues—state of the art and future perspectives. *J Biomater Sci Polym Ed* 2001;12:107–24.
- [76] Leong MF, Rasheed MZ, Lim TC, Chian KS. In vitro cell infiltration and *in vivo* cell infiltration and vascularization in a fibrous, highly porous poly (D, L-lactide) scaffold fabricated by cryogenic electrospinning technique. *J Biomed Mater Res Part A* 2009;91:231–40.
- [77] Beckstead BL, Pan S, Bhrany AD, Bratt-Leal AM, Ratner BD, Giachelli CM. Esophageal epithelial cell interaction with synthetic and natural scaffolds for tissue engineering. *Biomaterials* 2005;26:6217–28.
- [78] Saxena AK, Baumgart H, Komann C, Ainoedhofer H, Soltysiak P, Kofler K, *et al.* Esophagus tissue engineering: in situ generation of rudimentary tubular vascularized esophageal conduit using the ovine model. *J Pediatr Surg* 2010;45:859–64.
- [79] Evans MDM, Dalton BA, Steele JG. Persistent adhesion of epithelial tissue is sensitive to polymer topography. *J Biomed Mater Res* 1999;46:485–93.
- [80] Takeuchi S. Wound healing in the cornea of the chick embryo: III. The

influence of pore size of millipore filters on the migration of isolated epithelial sheets in culture. *Dev Biol* 1976;51:49–62.

- [81] Evans MDM, Taylor S, Dalton BA, Lohmann D. Polymer design for corneal epithelial tissue adhesion: Pore density. *J Biomed Mater Res* 2003;64A:357–64.
- [82] Chiu YC, Cheng MH, Engel H, Kao SW, Larson JC, Gupta S, *et al.* The role of pore size on vascularization and tissue remodeling in PEG hydrogels. *Biomaterials* 2011;32:6045–51.
- [83] Levenberg S, Rouwkema J, Macdonald M, Garfein ES, Kohane DS, Darland DC, *et al.* Engineering vascularized skeletal muscle tissue. *Nat Biotechnol* 2005;23:879–84.
- [84] Feng B, Jinkang Z, Zhen W, Jianxi L, Jiang C, Jian L, *et al.* The effect of pore size on tissue ingrowth and neovascularization in porous bioceramics of controlled architecture *in vivo*. *Biomed Mater* 2011;6:15007.
- [85] Murphy CM, Haugh MG, O'Brien FJ. The effect of mean pore size on cell attachment, proliferation and migration in collagen–glycosaminoglycan scaffolds for bone tissue engineering. *Biomaterials* 2010;31:461–6.
- [86] Chen VJ, Ma PX. The effect of surface area on the degradation rate of nano-fibrous poly(l-lactic acid) foams. *Biomaterials* 2006;27:3708–15.
- [87] Castner DG, Ratner BD. Biomedical surface science: foundations to frontiers. *Surf Sci* 2002;500:28–60.
- [88] Desmet T, Morent R, Geyter N De, Leys C, Schacht E, Dubruel P. Nonthermal Plasma Technology as a Versatile Strategy for Polymeric Biomaterials Surface Modification: A Review. *Biomacromolecules* 2009;10:2351–78.
- [89] Jiao YP, Cui FZ. Surface modification of polyester biomaterials for tissue engineering. *Biomed Mater* 2007;2:R24–37.
- [90] Baguneid MS, Seifalian AM, Salacinski HJ, Murray D, Hamilton G, Walker MG. Tissue engineering of blood vessels. *Br J Surg* 2006;93:282–90.

- [91] Wu C, Zhang Y, Zhou Y, Fan W, Xiao Y. A comparative study of mesoporous glass/silk and non-mesoporous glass/silk scaffolds: Physiochemistry and *in vivo* osteogenesis. *Acta Biomater* 2011;7:2229–36.
- [92] Chua CK, Leong KF. 3D Printing and additive manufacturing: principles and applications of rapid prototyping. 4th ed. Singapore: World Scientific; 2014.
- [93] Kubo H, Shimizu T, Yamato M, Fujimoto T, Okano T. Creation of myocardial tubes using cardiomyocyte sheets and an *in vitro* cell sheet-wrapping device. *Biomaterials* 2007;28:3508–16.
- [94] Murphy S V, Atala A. 3D bioprinting of tissues and organs. *Nat Biotechnol* 2014;32:773–85.
- [95] Zuk PA, Zhu M, Mizuno H, Huang J, Futrell JW, Katz AJ, *et al.* Multilineage Cells from Human Adipose Tissue: Implications for Cell-Based Therapies. *Tissue Eng* 2001;7:211–28.
- [96] Layer PG, Robitzki A, Rothermel A, Willbold E. Of layers and spheres: the reaggregate approach in tissue engineering. *Trends Neurosci* 2002;25:131–4.
- [97] Drury JL, Mooney DJ. Hydrogels for tissue engineering: scaffold design variables and applications. *Biomaterials* 2003;24:4337–51.
- [98] Jagur-Grodzinski J. Polymers for tissue engineering, medical devices, and regenerative medicine. Concise general review of recent studies. *Polym Adv Technol* 2006;17:395–418.
- [99] Gunatillake PA, Adhikari R. Biodegradable synthetic polymers for tissue engineering. *Eur Cell Mater* 2003;5:1–16.
- [100] Mano JF, Sousa RA, Boesel LF, Neves NM, Reis RL. Bioinert, biodegradable and injectable polymeric matrix composites for hard tissue replacement: state of the art and recent developments. *Compos Sci Technol* 2004;64:789–817.
- [101] Hou Q, Grijpma DW, Feijen J. Porous polymeric structures for tissue engineering prepared by a coagulation, compression moulding and salt

- leaching technique. *Biomaterials* 2003;24:1937–47.
- [102] Qutachi O, Vetsch JR, Gill D, Cox H, Scurr DJ, Hofmann S, *et al.* Injectable and porous PLGA microspheres that form highly porous scaffolds at body temperature. *Acta Biomater* 2014;10:5090–8.
- [103] Bible E, Chau DYS, Alexander MR, Price J, Shakesheff KM, Modo M. Attachment of stem cells to scaffold particles for intra-cerebral transplantation. *Nat Protoc* 2009;4:1440–53.
- [104] Oh SH, Kang SG, Kim ES, Cho SH, Lee JH. Fabrication and characterization of hydrophilic poly(lactic-co-glycolic acid)/poly(vinyl alcohol) blend cell scaffolds by melt-molding particulate-leaching method. *Biomaterials* 2003;24:4011–21.
- [105] Vaquette C, Frochot C, Rahouadj R, Muller S, Wang X. Mechanical and biological characterization of a porous poly-L-lactic acid-co- ϵ -caprolactone scaffold for tissue engineering. *Soft Mater* 2008;6:25–33.
- [106] Yoon JJ, Park TG. Degradation behaviors of biodegradable macroporous scaffolds prepared by gas foaming of effervescent salts. *J Biomed Mater Res* 2001;55:401–8.
- [107] Shastri VP, Martin I, Langer R. Macroporous polymer foams by hydrocarbon templating. *Proc Natl Acad Sci* 2000;97:1970–5.
- [108] Zhu J, Yang F, He F, Tian X, Tang S, Chen X. A tubular gelatin scaffold capable of the time-dependent controlled release of epidermal growth factor and mitomycin C. *Colloids Surfaces B Biointerfaces* 2015;135:416–24.
- [109] Chen YS, Chang JY, Cheng CY, Tsai FJ, Yao CH, Liu BS. An *in vivo* evaluation of a biodegradable genipin-cross-linked gelatin peripheral nerve guide conduit material. *Biomaterials* 2005;26:3911–8.
- [110] Chang JY, Lin JH, Yao CH, Chen JH, Lai TY, Chen YS. In vivo evaluation of a biodegradable EDC/NHS-cross-linked gelatin peripheral nerve guide conduit material. *Macromol Biosci* 2007;7:500–7.
- [111] Twal WO, Klatt SC, Harikrishnan K, Gerges E, Cooley MA, Trusk TC, *et al.* Cellularized microcarriers as adhesive building blocks for fabrication

- of tubular tissue constructs. *Ann Biomed Eng* 2014;42:1470–81.
- [112] Lovett M, Cannizzaro C, Daheron L, Messmer B, Vunjak-Novakovic G, Kaplan DL. Silk fibroin microtubes for blood vessel engineering. *Biomaterials* 2007;28:5271–9.
 - [113] Lee M, Wu BM, Dunn JCY. Effect of scaffold architecture and pore size on smooth muscle cell growth. *J Biomed Mater Res Part A* 2008;87A:1010–6.
 - [114] Pham CB, Leong KF, Lim TC, Chian KS. Rapid freeze prototyping technique in bio-plotters for tissue scaffold fabrication. *Rapid Prototyp J* 2008;14:246–53.
 - [115] Draghi L, Resta S, Pirozzolo MG, Tanzi MC. Microspheres leaching for scaffold porosity control. *J Mater Sci Mater Med* 2005;16:1093–7.
 - [116] Hou L, Jin J, Lv J, Chen L, Zhu Y, Liu X. Constitution and *in vivo* test of micro-porous tubular scaffold for esophageal tissue engineering. *J Biomater Appl* 2015;30:568–78.
 - [117] Kasoju N, Kubies D, Kumorek MM, Kříž J, Fábryová E, Machová L, *et al.* Dip TIPS as a facile and versatile method for fabrication of polymer foams with controlled shape, size and pore architecture for bioengineering applications. *PLoS One* 2014;9:e108792.
 - [118] Walthers CM, Nazemi AK, Patel SL, Wu BM, Dunn JCY. The effect of scaffold macroporosity on angiogenesis and cell survival in tissue-engineered smooth muscle. *Biomaterials* 2014;35:5129–37.
 - [119] Yeong WY, Yu H, Lim KP, Ng KLG, Boey YCF, Subbu VS, *et al.* Multiscale topological guidance for cell alignment via direct laser writing on biodegradable polymer. *Tissue Eng Part C Methods* 2010;16:1011–21.
 - [120] Badylak SF, Taylor D, Uygun K. Whole-organ tissue engineering: decellularization and recellularization of three-dimensional matrix scaffolds. *Annu Rev Biomed Eng* 2011;13:27–53.
 - [121] Baiguera S, Del Gaudio C, Jaus MO, Polizzi L, Gonfiotti A, Comin CE, *et al.* Long-term changes to *in vitro* preserved bioengineered human trachea and their implications for decellularized tissues. *Biomaterials*

2012;33:3662–72.

- [122] Oliveira AC, Garzón I, Ionescu AM, Carriel V, Cardona J de la C, González-Andrades M, *et al.* Evaluation of small intestine grafts decellularization methods for corneal tissue engineering. PLoS One 2013;8:e66538.
- [123] Quint C, Kondo Y, Manson RJ, Lawson JH, Dardik A, Niklason LE. Decellularized tissue-engineered blood vessel as an arterial conduit. Proc Natl Acad Sci 2011;108:9214–9.
- [124] Elliott MJ, De Coppi P, Speggin S, Roebuck D, Butler CR, Samuel E, *et al.* Stem-cell-based, tissue engineered tracheal replacement in a child: a 2-year follow-up study. Lancet 2012;380:994–1000.
- [125] Keane TJ, Londono R, Carey RM, Carruthers CA, Reing JE, Dearth CL, *et al.* Preparation and characterization of a biologic scaffold from esophageal mucosa. Biomaterials 2013;34:6729–37.
- [126] Isch JA, Engum SA, Ruble CA, Davis MM, Grosfeld JL. Patch esophagoplasty using AlloDerm as a tissue scaffold. J Pediatr Surg 2001;36:266–8.
- [127] Badylak SF, Hoppo T, Nieponice A, Gilbert TW, Davison JM, Jobe BA. Esophageal preservation in five male patients after endoscopic inner-layer circumferential resection in the setting of superficial cancer: a regenerative medicine approach with a biologic scaffold. Tissue Eng Part A 2011;17:1643–50.
- [128] Nieponice A, Ciotola FF, Nachman F, Jobe BA, Hoppo T, Londono R, *et al.* Patch Esophagoplasty: Esophageal reconstruction using biologic scaffolds. Ann Thorac Surg 2014;97:283–8.
- [129] Kasyanov VA, Hodde J, Hiles MC, Eisenberg C, Eisenberg L, De Castro LEF, *et al.* Rapid biofabrication of tubular tissue constructs by centrifugal casting in a decellularized natural scaffold with laser-machined micropores. J Mater Sci Mater Med 2009;20:329–37.
- [130] Yeong WY, Sudarmadji N, Yu HY, Chua CK, Leong KF, Venkatraman SS, *et al.* Porous polycaprolactone scaffold for cardiac tissue engineering

- fabricated by selective laser sintering. *Acta Biomater* 2010;6:2028–34.
- [131] Yeong WY, Chua CK, Leong KF, Chandrasekaran M. Rapid prototyping in tissue engineering: challenges and potential. *Trends Biotechnol* 2004;22:643–52.
 - [132] Neumann T, Hauschka SD, Sanders JE. Tissue engineering of skeletal muscle using polymer fiber arrays. *Tissue Eng* 2003;9:995–1003.
 - [133] Mikos AG, Bao Y, Cima LG, Ingber DE, Vacanti JP, Langer R. Preparation of poly(glycolic acid) bonded fiber structures for cell attachment and transplantation. *J Biomed Mater Res* 1993;27:183–9.
 - [134] Mikos AG, Sarakinos G, Vacanti JP, Langer RS, Linda G. Cima. Biocompatible polymer membranes and methods of preparation of three dimensional membrane structures, US 5514378 A, 1993.
 - [135] Rahman CV, Kuhn G, White LJ, Kirby GTS, Varghese OP, McLaren JS, *et al.* PLGA/PEG-hydrogel composite scaffolds with controllable mechanical properties. *J Biomed Mater Res Part B Appl Biomater* 2013;101B:648–55.
 - [136] Smith MJ, McClure MJ, Sell SA, Barnes CP, Walpoth BH, Simpson DG, *et al.* Suture-reinforced electrospun polydioxanone–elastin small-diameter tubes for use in vascular tissue engineering: A feasibility study. *Acta Biomater* 2008;4:58–66.
 - [137] Panseri S, Cunha C, Lowery J, Del Carro U, Taraballi F, Amadio S, *et al.* Electrospun micro- and nanofiber tubes for functional nervous regeneration in sciatic nerve transections. *BMC Biotechnol* 2008;8:39.
 - [138] Wang W, Itoh S, Matsuda A, Ichinose S, Shinomiya K, Hata Y, *et al.* Influences of mechanical properties and permeability on chitosan nano/microfiber mesh tubes as a scaffold for nerve regeneration. *J Biomed Mater Res Part A* 2008;84A:557–66.
 - [139] Zhang D, Chang J. Electrospinning of three-dimensional nanofibrous tubes with controllable architectures. *Nano Lett* 2008;8:3283–7.
 - [140] Teo WE, Kotaki M, Mo XM, Ramakrishna S. Porous tubular structures with controlled fibre orientation using a modified electrospinning method.

Nanotechnology 2005;16:918–24.

- [141] Takagi R, Yamato M, Kanai N, Murakami D, Kondo M, Ishii T, *et al.* Cell sheet technology for regeneration of esophageal mucosa. *World J Gastroenterol* 2012;18:5145–50.
- [142] Iwasaki K, Kojima K, Kodama S, Paz AC, Chambers M, Umezumi M, *et al.* Bioengineered three-layered robust and elastic artery using hemodynamically-equivalent pulsatile bioreactor. *Circulation* 2008;118:S52–7.
- [143] Owida A, Chen R, Patel S, Morsi Y, Mo X. Artery vessel fabrication using the combined fused deposition modeling and electrospinning techniques. *Rapid Prototyp J* 2011;17:37–44.
- [144] Mäkitie AA, Korpela J, Elomaa L, Reivonen M, Kokkari A, Malin M, *et al.* Novel additive manufactured scaffolds for tissue engineered trachea research. *Acta Otolaryngol* 2013;133:412–7.
- [145] Norotte C, Marga FS, Niklason LE, Forgacs G. Scaffold-free vascular tissue engineering using bioprinting. *Biomaterials* 2009;30:5910–7.
- [146] Itoh M, Nakayama K, Noguchi R, Kamohara K, Furukawa K, Uchihashi K, *et al.* Scaffold-free tubular tissues created by a bio-3D printer undergo remodeling and endothelialization when implanted in rat aortae. *PLoS One* 2015;10:e0136681.
- [147] Ohki T, Yamato M, Okano T, Yamamoto M. Regenerative medicine: tissue-engineered cell sheet for the prevention of post-esophageal ESD stricture. *Gastrointest Endosc Clin N Am* 2014;24:273–81.
- [148] Takimoto Y, Nakamura T, Teramachi M, Kiyotani T, Shimizu Y. Replacement of long segments of the esophagus with a collagen-silicone composite tube. *ASAIO J* 1995;41:M605–8.
- [149] Kawamura I, Sato H, Ogoshi S, Nagao K, Akiyama T, Miyata T. Experimental studies on an artificial esophagus using a collagen-silicone copolymer. *Jpn J Surg* 1983;13:358–67.
- [150] Sato M, Ando N, Ozawa S, Miki H, Kitajima M. An artificial esophagus consisting of cultured human esophageal epithelial cells, polyglycolic acid

- mesh, and collagen. *ASAIO J* 1994;40:M389–92.
- [151] Shinhar D, Finaly R, Niska A, Mares AJ. The use of collagen-coated vicryl mesh for reconstruction of the canine cervical esophagus. *Pediatr Surg Int* 1998;13:84–7.
 - [152] Zhu Y, Chan-Park MB. Density quantification of collagen grafted on biodegradable polyester: its application to esophageal smooth muscle cell. *Anal Biochem* 2007;363:119–27.
 - [153] Zhu Y, Ong WF. Epithelium regeneration on collagen (IV) grafted polycaprolactone for esophageal tissue engineering. *Mater Sci Eng C* 2009;29:1046–50.
 - [154] Miki H, Ando N, Ozawa S, Sato M, Hayashi K, Kitajima M. An artificial esophagus constructed of cultured human esophageal epithelial cells, fibroblasts, polyglycolic acid mesh, and collagen. *ASAIO J* 1999;45:502–8.
 - [155] Zhu Y, Chan-Park MB, Chian KS. The growth improvement of porcine esophageal smooth muscle cells on collagen-grafted poly(DL-lactide-co-glycolide) membrane. *J Biomed Mater Res Part B Appl Biomater* 2005;75B:193–9.
 - [156] Badylak S, Meurling S, Chen M, Spievack A, Simmons-Byrd A. Resorbable bioscaffold for esophageal repair in a dog model. *J Pediatr Surg* 2000;35:1097–103.
 - [157] Oshima T, Gedda K, Koseki J, Chen X, Husmark J, Watari J, *et al.* Establishment of esophageal-like non-keratinized stratified epithelium using normal human bronchial epithelial cells. *Am J Physiol Physiol* 2011;300:C1422–9.
 - [158] Lv J, Chen L, Zhu Y, Hou L, Liu Y. Promoting Epithelium Regeneration for Esophageal Tissue Engineering through Basement Membrane Reconstitution. *ACS Appl Mater Interfaces* 2014;6:4954–64.
 - [159] Saxena AK, Kofler K, Ainödhofer H, Höllwarth ME. Esophagus tissue engineering: Hybrid approach with esophageal epithelium and unidirectional smooth muscle tissue component generation *in vitro*. *J*

Gastrointest Surg 2009;13:1037–43.

- [160] Paterson WG. Esophageal peristalsis. GI Motil Online, 2006.
- [161] Agrawal A, Lee BH, Irvine SA, An J, Bhuthalingam R, Singh V, *et al.* Smooth muscle cell alignment and phenotype control by melt spun polycaprolactone fibers for seeding of tissue engineered blood vessels. *Int J Biomater* 2015;2015:1–8.
- [162] Thakar RG, Cheng Q, Patel S, Chu JS, Nasir M, Liepmann D, *et al.* Cell-shape regulation of smooth muscle cell proliferation. *Biophys J* 2009;96:3423–32.
- [163] Chang S, Song S, Lee J, Yoon J, Park J, Choi S, *et al.* Phenotypic modulation of primary vascular smooth muscle cells by short-term culture on micropatterned substrate. *PLoS One* 2014;9:e88089.
- [164] Zhang Y, Lei Y, Chang J, Li L, He B, Gu Z. Guidance of myoblast migration on aligned electrospun PLGA nanofibrous meshes. *Mater Lett* 2012;68:218–21.
- [165] Griffin MA, Sen S, Sweeney HL, Discher DE. Adhesion-contractile balance in myocyte differentiation. *J Cell Sci* 2004;117:5855–63.
- [166] Cha JM, Park SN, Noh SH, Suh H. Time-dependent modulation of alignment and differentiation of smooth muscle cells seeded on a porous substrate undergoing cyclic mechanical strain. *Artif Organs* 2006;30:250–8.
- [167] Yang F, Murugan R, Wang S, Ramakrishna S. Electrospinning of nano/micro scale poly (L-lactic acid) aligned fibers and their potential in neural tissue engineering. *Biomaterials* 2005;26:2603–10.
- [168] Kurpinski KT, Stephenson JT, Janairo RRR, Lee H, Li S. The effect of fiber alignment and heparin coating on cell infiltration into nanofibrous PLLA scaffolds. *Biomaterials* 2010;31:3536–42.
- [169] Lam MT, Huang YC, Birla RK, Takayama S. Microfeature guided skeletal muscle tissue engineering for highly organized 3-dimensional free-standing constructs. *Biomaterials* 2009;30:1150–5.

- [170] Cardwell RD, Dahlgren LA, Goldstein AS. Electrospun fibre diameter, not alignment, affects mesenchymal stem cell differentiation into the tendon/ligament lineage. *J Tissue Eng Regen Med* 2014;8:937–45.
- [171] Chen M, Patra PK, Warner SB, Bhowmick S. Role of fiber diameter in adhesion and proliferation of NIH 3T3 fibroblast on electrospun polycaprolactone scaffolds. *Tissue Eng* 2007;13:579–87.
- [172] Hwang CM, Park Y, Park JY, Lee K, Sun K, Khademhosseini A, *et al.* Controlled cellular orientation on PLGA microfibers with defined diameters. *Biomed Microdevices* 2009;11:739–46.
- [173] Lipski AM, Pino CJ, Haselton FR, Chen IW, Shastri VP. The effect of silica nanoparticle-modified surfaces on cell morphology, cytoskeletal organization and function. *Biomaterials* 2008;29:3836–46.
- [174] Rowe SL, Lee S, Stegemann JP. Influence of thrombin concentration on the mechanical and morphological properties of cell-seeded fibrin hydrogels. *Acta Biomater* 2007;3:59–67.
- [175] Sciote JJ, Morris TJ. Skeletal muscle function and fibre types: the relationship between occlusal function and the phenotype of jaw-closing muscles in human. *J Orthod* 2000;27:15–30.
- [176] Charest JL, García AJ, King WP. Myoblast alignment and differentiation on cell culture substrates with microscale topography and model chemistries. *Biomaterials* 2007;28:2202–10.
- [177] Hwang CM, Khademhosseini A, Park Y, Sun K, Lee SH. Microfluidic chip-based fabrication of PLGA microfiber scaffolds for tissue engineering. *Langmuir* 2008;24:6845–51.
- [178] Liu Y, Ji Y, Ghosh K, Clark RAF, Huang L, Rafailovich MH. Effects of fiber orientation and diameter on the behavior of human dermal fibroblasts on electrospun PMMA scaffolds. *J Biomed Mater Res Part A* 2009;90A:1092–106.
- [179] Ohara PT, Buck RC. Contact guidance *in vitro*: A light, transmission, and scanning electron microscopic study. *Exp Cell Res* 1979;121:235–49.
- [180] Xu C. Y, Inai R, Kotaki M, Ramakrishna S. Aligned biodegradable

nanofibrous structure: a potential scaffold for blood vessel engineering. *Biomaterials* 2004;25:877–86.

- [181] Guex AG, Birrer DL, Fortunato G, Tevæearai HT, Giraud MN. Anisotropically oriented electrospun matrices with an imprinted periodic micropattern: a new scaffold for engineered muscle constructs. *Biomed Mater* 2013;8:21001.
- [182] Dunn GA, Heath JP. A new hypothesis of contact guidance in tissue cells. *Exp Cell Res* 1976;101:1–14.
- [183] Barnes CP, Sell SA, Boland ED, Simpson DG, Bowlin GL. Nanofiber technology: designing the next generation of tissue engineering scaffolds. *Adv Drug Deliv Rev* 2007;59:1413–33.
- [184] Shields KJ, Beckman MJ, Bowlin GL, Wayne JS. Mechanical properties and cellular proliferation of electrospun collagen type II. *Tissue Eng* 2004;10:1510–7.
- [185] Buttafoco L, Kolkman NG, Engbers-Buijtenhuijs P, Poot AA, Dijkstra PJ, Vermes I, *et al.* Electrospinning of collagen and elastin for tissue engineering applications. *Biomaterials* 2006;27:724–34.
- [186] Lee BR, Lee KH, Kang E, Kim D-S, Lee S-H. Microfluidic wet spinning of chitosan-alginate microfibers and encapsulation of HepG2 cells in fibers. *Biomicrofluidics* 2011;5:22208.
- [187] Ryadnov MG, Woolfson DN. Engineering the morphology of a self-assembling protein fibre. *Nat Mater* 2003;2:329–32.
- [188] Paakinaho K, Ellä V, Syrjälä S, Kellomäki M. Melt spinning of poly(l/d)lactide 96/4: Effects of molecular weight and melt processing on hydrolytic degradation. *Polym Degrad Stab* 2009;94:438–42.
- [189] Incardona SD, Fambri L, Migliaresi C. Poly-L-lactic acid braided fibres produced by melt spinning: characterization and *in vitro* degradation. *J Mater Sci Mater Med* 1996;7:387–91.
- [190] Wong SC, Baji A, Leng S. Effect of fiber diameter on tensile properties of electrospun poly(ϵ -caprolactone). *Polymer* 2008;49:4713–22.

- [191] Ghasemi-Mobarakeh L, Prabhakaran MP, Morshed M, Nasr-Esfahani M-H, Ramakrishna S. Electrospun poly(ϵ -caprolactone)/gelatin nanofibrous scaffolds for nerve tissue engineering. *Biomaterials* 2008;29:4532–9.
- [192] Leong MF, Toh JKC, Du C, Narayanan K, Lu HF, Lim TC, *et al.* Patterned prevascularised tissue constructs by assembly of polyelectrolyte hydrogel fibres. *Nat Commun* 2013;4:879–84.
- [193] Hulteen JC, Chen HX, Chambliss CK, Martin CR. Template synthesis of carbon nanotubule and nanofiber arrays. *Nanostructured Mater* 1997;9:133–6.
- [194] Hartgerink JD, Beniash E, Stupp SI. Peptide-amphiphile nanofibers: a versatile scaffold for the preparation of self-assembling materials. *Proc Natl Acad Sci* 2002;99:5133–8.
- [195] Ellison CJ, Phatak A, Giles DW, Macosko CW, Bates FS. Melt blown nanofibers: Fiber diameter distributions and onset of fiber breakup. *Polymer* 2007;48:3306–16.
- [196] Weitz RT, Harnau L, Rauschenbach S, Burghard M, Kern K. Polymer nanofibers via nozzle-free centrifugal spinning. *Nano Lett* 2008;8:1187–91.
- [197] Brown TD, Dalton PD, Huttmacher DW. Direct writing by way of melt electrospinning. *Adv Mater* 2011;23:5651–7.
- [198] Ohki T, Yamato M, Ota M, Takagi R, Murakami D, Kondo M, *et al.* Prevention of esophageal stricture after endoscopic submucosal dissection using tissue-engineered cell sheets. *Gastroenterology* 2012;143:582-8-2.
- [199] Ohki T, Yamato M, Murakami D, Takagi R, Yang J, Namiki H, *et al.* Treatment of oesophageal ulcerations using endoscopic transplantation of tissue-engineered autologous oral mucosal epithelial cell sheets in a canine model. *Gut* 2006;55:1704–10.
- [200] Shamir ER, Ewald AJ. Three-dimensional organotypic culture: experimental models of mammalian biology and disease. *Nat Rev Mol Cell Biol* 2014;15:647–64.
- [201] Bhrany AD, Beckstead BL, Lang TC, Farwell DG, Giachelli CM, Ratner

- BD. Development of an esophagus acellular matrix tissue scaffold. *Tissue Eng* 2006;12:319–30.
- [202] Siew S, Goldstein ML. Scanning electron microscopy of mucosal biopsies of the human upper gastrointestinal tract. *Scan Electron Microsc* 1981;4:173–81.
- [203] Liao D, Fan Y, Zeng Y, Gregersen H. Stress distribution in the layered wall of the rat oesophagus. *Med Eng Phys* 2003;25:731–8.
- [204] Lambert RK, Codd SL, Alley MR, Pack RJ. Physical determinants of bronchial mucosal folding. *J Appl Physiol* 1994;77.
- [205] Lee MML, Chien S. Morphologic effects of pressure changes on canine carotid artery endothelium as observed by scanning electron microscopy. *Anat Rec* 1979;194:1–14.
- [206] Li B, Cao YP, Feng XQ. Growth and surface folding of esophageal mucosa: A biomechanical model. *J Biomech* 2011;44:182–8.
- [207] Dalton BA, Evans MDM, McFarland GA, Steele JG. Modulation of corneal epithelial stratification by polymer surface topography. *J Biomed Mater Res* 1999;45:384–94.
- [208] Saxena AK, Ainoedhofer H, Höllwarth ME. Esophagus tissue engineering: *in vitro* generation of esophageal epithelial cell sheets and viability on scaffold. *J Pediatr Surg* 2009;44:896–901.
- [209] Hayashi K, Ando N, Ozawa S, Kitagawa Y, Miki H, Sato M, *et al.* A neo-esophagus reconstructed by cultured human esophageal epithelial cells, smooth muscle cells, fibroblasts, and collagen. *ASAIO J* 2004;50:261–6.
- [210] Horváth L, Umehara Y, Jud C, Blank F, Petri-Fink A, Rothen-Rutishauser B, *et al.* Engineering an *in vitro* air-blood barrier by 3D bioprinting. *Sci Rep* 2015;5:7974.
- [211] Wüst S, Godla ME, Müller R, Hofmann S. Tunable hydrogel composite with two-step processing in combination with innovative hardware upgrade for cell-based three-dimensional bioprinting. *Acta Biomater* 2014;10:630–40.

- [212] Skardal A, Zhang J, Prestwich GD. Bioprinting vessel-like constructs using hyaluronan hydrogels crosslinked with tetrahedral polyethylene glycol tetracrylates. *Biomaterials* 2010;31:6173–81.
- [213] Billiet T, Gevaert E, De Schryver T, Cornelissen M, Dubruel P. The 3D printing of gelatin methacrylamide cell-laden tissue-engineered constructs with high cell viability. *Biomaterials* 2014;35:49–62.
- [214] Jolly C, Morimoto RI. Role of the heat shock response and molecular chaperones in oncogenesis and cell death. *J Natl Cancer Inst* 2000;92:1564–72.
- [215] Miller JS. The billion cell construct: will three-dimensional printing get us there? *PLoS Biol* 2014;12:e1001882.
- [216] Rezende RA, Pereira FDAS, Kasyanov V, Ovsianikov A, Torgensen J, Gruber P, *et al.* Design, physical prototyping and initial characterisation of “lockyballs.” *Virtual Phys Prototyp* 2012;7:287–301.
- [217] Kang HW, Lee SJ, Ko IK, Kengla C, Yoo JJ, Atala A. A 3D bioprinting system to produce human-scale tissue constructs with structural integrity. *Nat Biotechnol* 2016;34:312–9.
- [218] Jung JW, Lee JS, Cho DW. Computer-aided multiple-head 3D printing system for printing of heterogeneous organ/tissue constructs. *Sci Rep* 2016;6:21685.
- [219] Roti RJL. Cellular responses to hyperthermia (40–46 ° C): Cell killing and molecular events. *Int J Hyperth* 2008;24:3–15.
- [220] Sun H, Mei L, Song C, Cui X, Wang P. The *in vivo* degradation, absorption and excretion of PCL-based implant. *Biomaterials* 2006;27:1735–40.
- [221] Oda D, Savard CE, Eng L, Sekijima J, Haigh G, Lee SP. Reconstituted human oral and esophageal mucosa in culture. *Vitr Cell Dev Biol - Anim* 1998;34:46–52.
- [222] Noguchi TK, Ninomiya N, Sekine M, Komazaki S, Wang P-C, Asashima M, *et al.* Generation of stomach tissue from mouse embryonic stem cells. *Nat Cell Biol* 2015;17:984–93.

- [223] Tan B, Wei RQ, Tan MY, Luo JC, Deng L, Chen XH, *et al.* Tissue engineered esophagus by mesenchymal stem cell seeding for esophageal repair in a canine model. *J Surg Res* 2013;182:40–8.
- [224] Nieponice A, Gilbert TW, Johnson SA, Turner NJ, Badylak SF. Bone marrow–derived cells participate in the long-term remodeling in a mouse model of esophageal reconstruction. *J Surg Res* 2013;182:e1–7.
- [225] Krause DS, Theise ND, Collector MI, Henegariu O, Hwang S, Gardner R, *et al.* Multi-organ, multi-lineage engraftment by a single bone marrow-derived stem cell. *Cell* 2001;105:369–77.
- [226] Ko J, Mohtaram NK, Ahmed F, Montgomery A, Carlson M, Lee PCD, *et al.* Fabrication of poly (ϵ -caprolactone) microfiber scaffolds with varying topography and mechanical properties for stem cell-based tissue engineering applications. *J Biomater Sci Polym Ed* 2014;25:1–17.
- [227] Ugartemendia JM, Muñoz ME, Sarasua JR, Santamaria A. Phase behavior and effects of microstructure on viscoelastic properties of a series of polylactides and polylactide/poly(ϵ -caprolactone) copolymers. *Rheol Acta* 2014;53:857–68.
- [228] Lu XL, Cai W, Gao ZY. Shape-memory behaviors of biodegradable poly(L-lactide-co- ϵ -caprolactone) copolymers. *J Appl Polym Sci* 2008;108: 1109–1115.
- [229] An J. Engineering scaffolds for restorative tissue repair of tendon via polycaprolactone microfiber and polycaprolactone membrane. Nanyang Technological University, 2012.
- [230] Loesberg WA, Riet J, Delft FCMJM, Schön P, Fidgor CG, Speller S, *et al.* The threshold at which substrate nanogroove dimensions may influence fibroblast alignment and adhesion. *Biomaterials* 2007;28: 3944-51.
- [231] Tawakoli PN, Al-Ahmad A, Hoth-Hannig W, Hannig M, Hannig C. Comparison of different live/dead stainings for detection and quantification of adherent microorganisms in the initial oral biofilm. *Clin Oral Investig* 2013;17:841–50.
- [232] Fan XJ, Lee SWR, Han Q. Experimental investigations and model study

- of moisture behaviors in polymeric materials. *Microelectron Reliab* 2009;49:861-71.
- [233] Ferracane JL. Hygroscopic and hydrolytic effects in dental polymer networks. *Dent Mater* 2006;22:211–22.
- [234] An J, Chua CK, Leong KF, Chen CH, Chen JP. Solvent-free fabrication of three dimensionally aligned polycaprolactone microfibers for engineering of anisotropic tissues. *Biomed Microdevices* 2012;14:863–72.
- [235] Reneker DH, Yarin AL, Zussman E, Xu H. Electrospinning of nanofibers from polymer solutions and melts. *Adv Appl Mech* 2007;41:43–346.
- [236] Yoshimoto H, Shin YM, Terai H, Vacanti JP. A biodegradable nanofiber scaffold by electrospinning and its potential for bone tissue engineering. *Biomaterials* 2003;24:2077–82.
- [237] Wang J, Porter RS. On the viscosity-temperature behavior of polymer melts. *Rheol Acta* 1995;34:496–503.
- [238] Liu CY, He J, Keunings R, Bailly C. New linearized relation for the universal viscosity–temperature behavior of polymer melts. *Macromolecules* 2006;39:8867–9.
- [239] Higuchi A, Ling QD, Hsu ST, Umezawa A. Biomimetic cell culture proteins as extracellular matrices for stem cell differentiation. *Chem Rev* 2012;112:4507–40.
- [240] Tay CY, Yu H, Pal M, Leong WS, Tan NS, Ng KW, *et al.* Micropatterned matrix directs differentiation of human mesenchymal stem cells towards myocardial lineage. *Exp Cell Res* 2010;316:1159–68.
- [241] Hossain KMZ, Parsons AJ, Rudd CD, Ahmed I, Thielemans W. Mechanical, crystallisation and moisture absorption properties of melt drawn polylactic acid fibres. *Eur Polym J* 2014;53:270–81.
- [242] Shazly T, Rachev A, Lessner S, Argraves WS, Ferdous J, Zhou B, *et al.* On the Uniaxial Ring Test of Tissue Engineered Constructs. *Exp Mech* 2014;55:41–51.
- [243] Kobayashi J, Asahi T, Ichiki M, Oikawa A, Suzuki H, Watanabe T, *et al.*

- Structural and optical properties of poly lactic acids. *J Appl Phys* 1995;77:2957–73.
- [244] Hoogsteen W, Postema AR, Pennings AJ, Ten Brinke G, Zugenmaier P. Crystal structure, conformation and morphology of solution-spun poly (L-lactide) fibers. *Macromolecules* 1990;23:634–42.
- [245] Middleton JC, Tipton AJ. Synthetic biodegradable polymers as orthopedic devices. *Biomaterials* 2000;21:2335–46.
- [246] Phillipson K, Hay JN, Jenkins MJ. Thermal analysis FTIR spectroscopy of poly (ϵ -caprolactone). *Thermochim Acta* 2014;595:74–82.
- [247] Huang MH, Li S, Vert M. Synthesis and degradation of PLA–PCL–PLA triblock copolymer prepared by successive polymerization of ϵ -caprolactone and dl-lactide. *Polymer* 2004;45:8675–81.
- [248] Turner JF, Riga A, O'Connor A, Zhang J, Collis J. Characterization of drawn and undrawn poly-L-lactide films by differential scanning calorimetry. *J Therm Anal Calorim* 2004;75:257–68.
- [249] Xu H, Teng C, Yu M. Improvements of thermal property and crystallization behavior of PLLA based multiblock copolymer by forming stereocomplex with PDLA oligomer. *Polymer* 2006;47:3922–8.
- [250] Ikada Y, Jamshidi K, Tsuji H, Hyon SH. Stereocomplex formation between enantiomeric poly (lactides). *Macromolecules* 1987;20:904–6.
- [251] Fisher EW, Sterzel HJ, Fischer EW, Sterzel HJ, Wegner G. Investigation of the structure of solution grown crystals of lactide copolymers by means of chemical reactions. *Kolloid-Z U Z Polym* 1973;251:980–90.
- [252] Sawai D, Takahashi K, Imamura T, Nakamura K, Kanamoto T, Hyon S. Preparation of oriented β -form poly (L-lactic acid) by solid-state extrusion. *J Polym Sci Part B Polym Phys* 2002;40:95–104.
- [253] Cicero JA, Dorgan JR, Janzen J, Garrett J, Runt J, Lin JS. Supramolecular morphology of two-step, melt-spun poly (lactic acid) fibers. *J Appl Polym Sci* 2002;86:2828–38.
- [254] Ball RC, Doi M, Edwards SF, Warner M. Elasticity of entangled networks.

Polymer 1981;22:1010–8.

- [255] Edwards SF, Vilgis T. The effect of entanglements in rubber elasticity. Polymer 1986;27:483–92.
- [256] Koelling AS, Ballintyn NJ, Salehi A, Darden DJ, Taylor ME, Varnavas J, *et al.* In vitro real-time aging and characterization of poly (L/D-lactic acid). Proc. 1997 16 South. Biomed. Eng. Conf., IEEE; p. 197–201.
- [257] Han F, Zhu C, Guo Q, Yang H, Li B. Cellular modulation by the elasticity of biomaterials. J Mater Chem B 2016;4:9–26.
- [258] Jeong SI, Kim BS, Kang SW, Kwon JH, Lee YM, Kim SH, *et al.* In vivo biocompatibility and degradation behavior of elastic poly (L-lactide-co- ϵ -caprolactone) scaffolds. Biomaterials 2004;25:5939–46.
- [259] Jeong SI, Kim BS, Lee YM, Ihn KJ, Kim SH, Kim YH. Morphology of elastic poly(l-lactide-co- ϵ -caprolactone) copolymers and *in vitro* and *in vivo* degradation behavior of their scaffolds. Biomacromolecules 2004;5:1303–9.
- [260] Vanderhoof JA, Rapoport PJ, Paxson CL. Manometric diagnosis of lower esophageal sphincter incompetence in infants: use of a small, single-lumen perfused catheter. Pediatrics 1978;62:805–8.
- [261] Teixeira AI, Abrams GA, Bertics PJ, Murphy CJ, Nealey PF. Epithelial contact guidance on well-defined micro-and nanostructured substrates. J Cell Sci 2003;116:1881–92.
- [262] Watts RL, Raiser CD, Stover NP, Cornfeldt ML, Schweikert AW, Allen RC, *et al.* Stereotaxic intrastriatal implantation of human retinal pigment epithelial (hRPE) cells attached to gelatin microcarriers: a potential new cell therapy for Parkinson's disease. J Neural Transm Suppl 2003:215–27.
- [263] Liu JY, Hafner J, Dragieva G, Seifert B, Burg G. Autologous cultured keratinocytes on porcine gelatin microbeads effectively heal chronic venous leg ulcers. Wound Repair Regen 2004;12:148–56.
- [264] Sun L, Xiong Z, Zhou W, Liu R, Yan X, Li J, *et al.* Novel konjac glucomannan microcarriers for anchorage-dependent animal cell culture. Biochem Eng J 2015;96:46–54.

- [265] Langer R. Drug delivery and targeting. *Nature* 1998;392:5–10.
- [266] Parsons-Wingerter PA, Saltzman WM. Growth versus function in the three-dimensional culture of single and aggregated hepatocytes within collagen gels. *Biotechnol Prog* 1993;9:600–7.
- [267] Stokols S, Tuszynski MH. Freeze-dried agarose scaffolds with uniaxial channels stimulate and guide linear axonal growth following spinal cord injury. *Biomaterials* 2006;27:443–51.
- [268] Aymard P, Martin DR, Plucknett K, Foster TJ, Clark AH, Norton IT. Influence of thermal history on the structural and mechanical properties of agarose gels. *Biopolymers* 2001;59:131–44.
- [269] Pernodet N, Maaloum M, Tinland B. Pore size of agarose gels by atomic force microscopy. *Electrophoresis* 1997;18:55–8.
- [270] Lake SP, Hald ES, Barocas VH. Collagen-agarose co-gels as a model for collagen-matrix interaction in soft tissues subjected to indentation. *J Biomed Mater Res Part A* 2011;99A:507–15.
- [271] O'Connor SM, Stenger DA, Shaffer KM, Ma W. Survival and neurite outgrowth of rat cortical neurons in three-dimensional agarose and collagen gel matrices. *Neurosci Lett* 2001;3:189–93.
- [272] Kansal AR, Torquato S, Stillinger FH. Computer generation of dense polydisperse sphere packings. *J Chem Phys* 2002;117:8212.
- [273] Hinton TJ, Jallerat Q, Palchesko RN, Park JH, Grodzicki MS, Shue H-J, *et al.* Three-dimensional printing of complex biological structures by freeform reversible embedding of suspended hydrogels. *Sci Adv* 2015;1:e1500758–e1500758.
- [274] Levato R, Visser J, Planell JA, Engel E, Malda J, Mateos-Timoneda MA. Biofabrication of tissue constructs by 3D bioprinting of cell-laden microcarriers. *Biofabrication* 2014;6:35020.
- [275] Poldervaart MT, Gremmels H, van Deventer K, Fledderus JO, Oner FC, Verhaar MC, *et al.* Prolonged presence of VEGF promotes vascularization in 3D bioprinted scaffolds with defined architecture. *J Control Release* 2014;184:58–66.

- [276] Poldervaart MT, Wang H, van der Stok J, Weinans H, Leeuwenburgh SCG, Öner FC, *et al.* Sustained release of BMP-2 in bioprinted alginate for osteogenicity in mice and rats. PLoS One 2013;8:e72610.
- [277] Gun S, Edirisinghe M, Stride E. Encapsulation of superparamagnetic iron oxide nanoparticles in poly-(lactide-co-glycolic acid) microspheres for biomedical applications. Mater Sci Eng C 2013;33:3129–37.
- [278] Kim BS, Mooney DJ. Development of biocompatible synthetic extracellular matrices for tissue engineering. Trends Biotechnol 1998;16:224–30.
- [279] Emans PJ, van Rhijn LW, Welting TJM, Cremers A, Wijnands N, Spaapen F, *et al.* Autologous engineering of cartilage. Proc Natl Acad Sci 2010;107:3418–23.
- [280] Matsuda T. Recent Progress of Vascular Graft Engineering in Japan. Artif Organs 2004;28:64–71.
- [281] Behr JM, Tan YJ, An J, Irvine SA, Leong KF, Chua CK, Zussman E, Venkatraman S, Non-linear elasticity and compliance matching of PLCL dip-coated tubes with melt-drawn fibers. Acta Biomater. Ready for submission.
- [282] Grikscheit TC, Ochoa ER, Ramsanahie A, Alsberg E, Mooney D, Whang EE, *et al.* Tissue-engineered large intestine resembles native colon with appropriate *in vitro* physiology and architecture. Ann Surg 2003;238:35–41.
- [283] Hecker L. Development of a three-dimensional physiological model of the internal anal sphincter bioengineered *in vitro* from isolated smooth muscle cells. AJP Gastrointest Liver Physiol 2005;289:G188–96.
- [284] Hotta R, Stamp LA, Foong JPP, McConnell SN, Bergner AJ, Anderson RB, *et al.* Transplanted progenitors generate functional enteric neurons in the postnatal colon. J Clin Invest 2013;123:1182–91.
- [285] Anitha M, Joseph I, Ding X, Torre ER, Sawchuk MA, Mwangi S, *et al.* Characterization of Fetal and Postnatal Enteric Neuronal Cell Lines With

Improvement in Intestinal Neural Function. *Gastroenterology*
2008;134:1424–35.

Appendices

Appendix A: Biomechanical properties of human esophagus

Biomechanical properties of the esophagi of four experimental groups were reported by Vanags *et al.* [29], which are Group I: 19-44 years old, Group II: 45–59 years old; Group III: 60–74 years; and Group IV: 75–89 years. Ultimate stress and strain were the greatest in the cervical part of the esophagus for all age groups. With the age the values of mechanical parameters of the esophagus wall reduced, but the modulus of elasticity increases. Difference in the tensile properties of the esophagus in different age groups is summarized:

Longitudinal direction:

- Mean ultimate stress: Group I: 2.19 ± 0.06 MPa (28%, 45% and 69.8% higher than in Group II, Group III, and Group IV)
- Mean strain: Group I: $70.0 \pm 7\%$ (13%, 12.5%, and 28% higher than Group II, Group III, and Group IV)
- Tangential moduli at 40% of relative strain 0.4MPa (E0.4): Group I (2.30 ± 0.09 MPa), other age groups (invariable between 1.95-1.98 MPa).

Circumferential direction:

- Mean ultimate stress: Group I: 1.41 ± 0.05 MPa (34.3%, 38.2%, and 42.4% higher than in Group II, Group III, and Group IV)
- Mean strain: Group I: $82.5 \pm 9\%$ (13.8%, 19.2%, and 28.1% higher than in Group II, Group III, and Group IV)
- E0.4: Group I (1.44 ± 0.06 MPa); Group II (1.31 ± 0.05 MPa); Group III (7.6% higher than in Group I); Group IV (10.4% higher than in Group I)

Appendix B: Rheological results for PLC at various temperatures

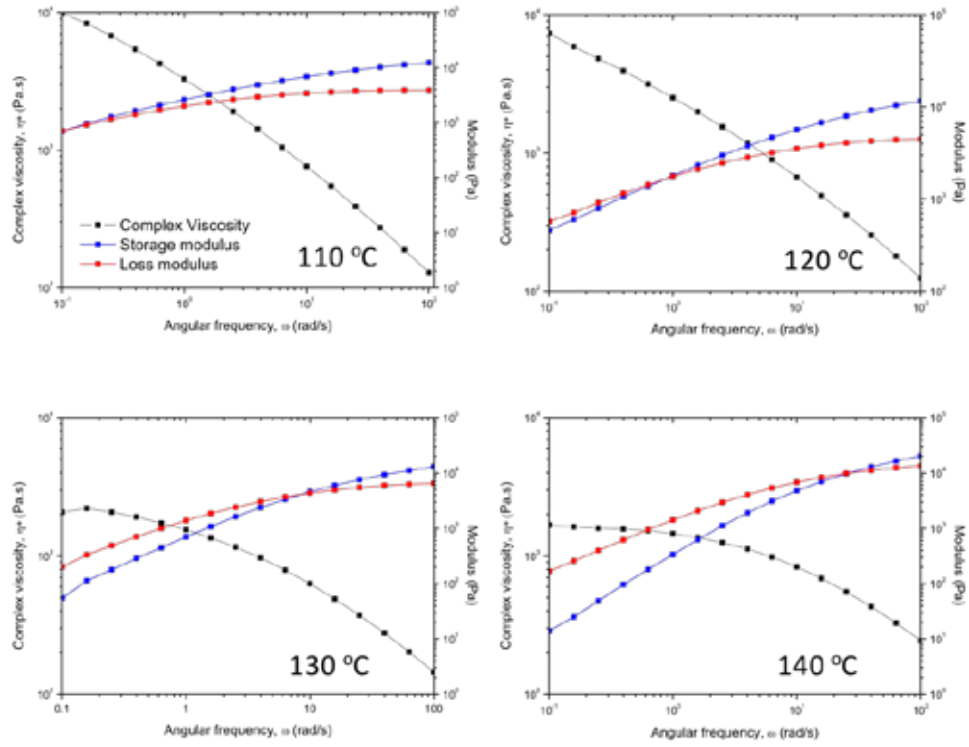
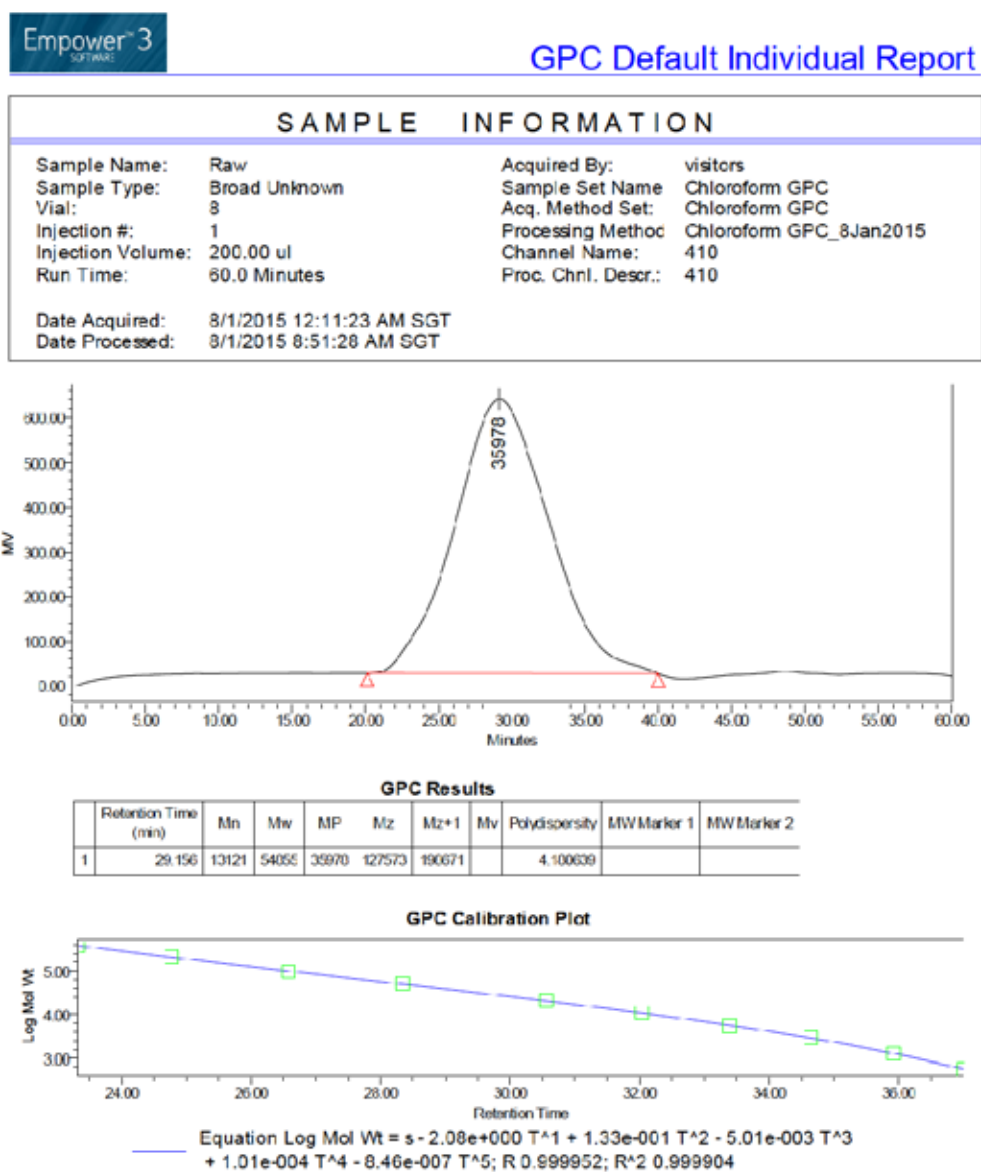


Figure B.1: Dynamic frequency sweep tests of PLC melt at various temperatures.

Appendix C: GPC report for pristine and melt-drawn PLC

(I) Pristine PLC pellets



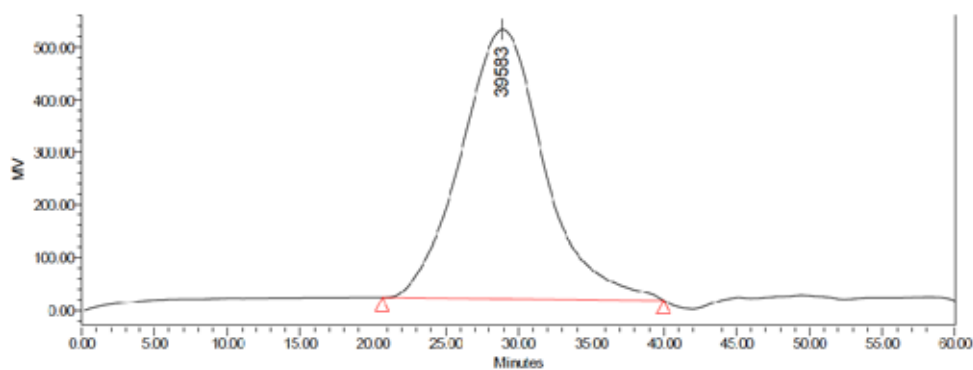
(II) Melt-drawn PLC, V3.77



GPC Default Individual Report

SAMPLE INFORMATION

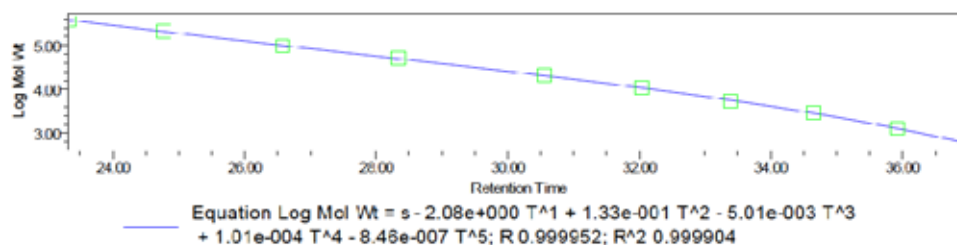
Sample Name:	MS_2400RPM	Acquired By:	visitors
Sample Type:	Broad Unknown	Sample Set Name:	Chloroform GPC
Vial:	10	Acq. Method Set:	Chloroform GPC
Injection #:	1	Processing Method:	Chloroform GPC_8Jan2015
Injection Volume:	200.00 ul	Channel Name:	410
Run Time:	60.0 Minutes	Proc. Chnl. Descr.:	410
Date Acquired:	8/1/2015 2:16:47 AM SGT		
Date Processed:	8/1/2015 8:51:34 AM SGT		



GPC Results

Retention Time (min)	Mn	Mw	MP	Mz	Mz+1	Mv	Polydispersity	MW/Marker 1	MW/Marker 2
28.915	15588	56660	36563	125621	192701		3.620966		

GPC Calibration Plot



Appendix D: L929 cell alignment on PLC scaffolds

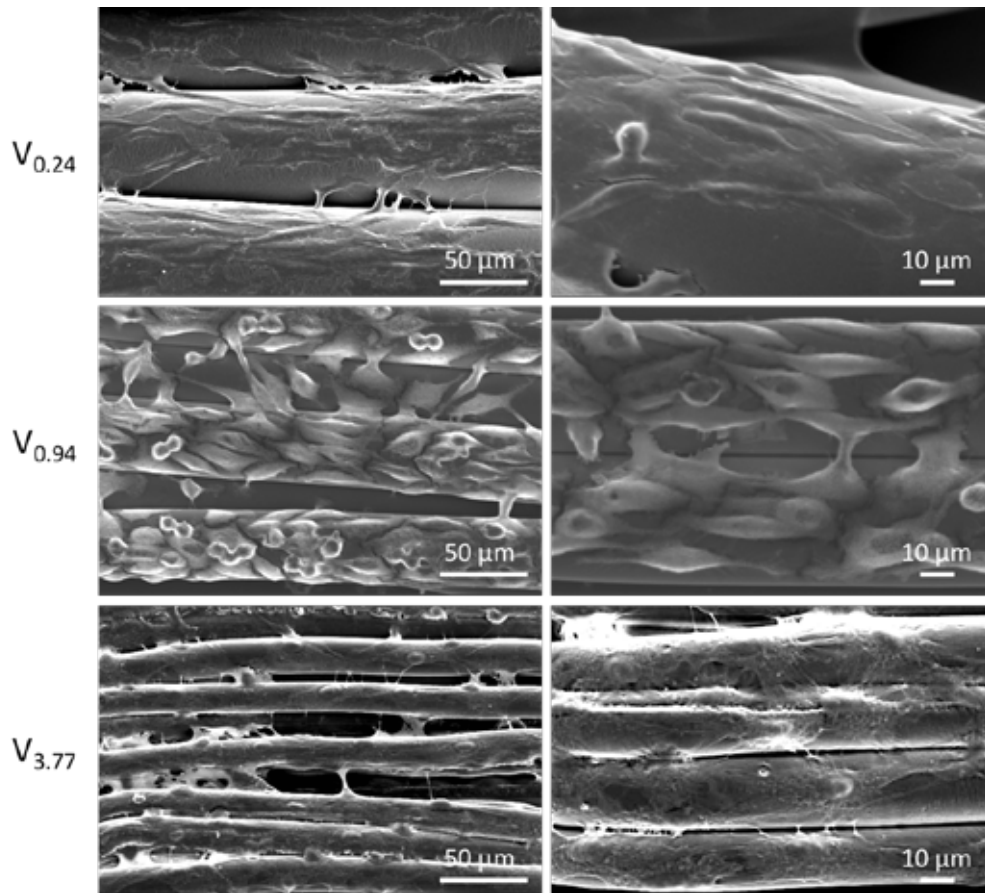


Figure D.1: L929 was aligned on all PLC scaffolds. In particular, high cell alignment was observed in $V_{0.94}$.

Appendix E: Calculations of the initial cell numbers needed before bioprinting of a 1 mm³ construct.

a) Calculation of cells needed to be seeded into microspheres for bioprinting of a 1 mm³ tissue construct. Overestimation as per reasons stated above. b) Calculations of cell numbers needed for bioprinting of a 1 mm³ tissue construct for cell-laden hydrogel-based and scaffold-free tissue spheroids-based bioprinting, according to closest packing of spheres inside a volume.

a)

Packing of dry spheres into a known volume was investigated.

Mass of dry spheres per unit volume is 4.08×10^{-4} g/mm³.

Cells seeding protocol:

3 mg/mL microspheres with 2×10^5 cells/mL.

No. of initial cells/mass of microspheres = 6.67×10^7 cells/g

No. of initial cells/volume = 2.7×10^4 cells/mm³

Grounds for overestimation:

Dry spheres were used in calculation.

Before printing, the microspheres were loaded with cells (form microtissues) where the value of microtissues/unit volume will be lower than the calculated value.

b)

Assumptions:

Cells are spherical with diameter (D) of 20 μ m; Spheroids are spherical with D of 200 μ m (min) or 600 μ m (max).

Cells and spheroids have negligible size distributions.

Closest spheres packing can be achieved (74% inside the cube)

Consider printing spheres (closely packed) into a cube with volume (V) of 1 mm³:

Cells (assume spherical) loaded in hydrogels

Cells: D = 20 mm

$$V_{\text{cell}} = 4.19 \times 10^{-6} \text{ mm}^3$$

To pack cells inside a cube with $V_{\text{cube}} = 1 \text{ mm}^3$

Closest sphere packing is 0.74.

$$V_{\text{sphere}} \text{ could be packed inside the cube} = 0.74 \text{ mm}^3$$

$$\begin{aligned} \text{No. of cells/volume} &= 0.74 / 4.19 \times 10^{-6} \\ &= 1.77 \times 10^5 \text{ cells/mm}^3 \end{aligned}$$

Or

$$\text{No. of cells/volume of hydrogel} = 1.77 \times 10^8 \text{ cells/ml}$$

Tissue spheroids printing in hydrogels

Spheroids: D = 200 mm to 600 mm

$$V_{\text{spheroid}} = 4.19 \times 10^{-3} \text{ mm}^3 \text{ to } 0.113 \text{ mm}^3$$

To pack spheroids inside a cube with $V_{\text{cube}} = 1 \text{ mm}^3$

Closest sphere packing is 0.74.

$$V_{\text{spheroids}} \text{ could be packed inside the cube} = 0.74 \text{ mm}^3$$

$$\begin{aligned} \text{No. of spheroids/volume} &= 0.74 / 4.19 \times 10^{-3} \text{ to } 0.74 / 0.113 \\ &= 6 \text{ to } 176 \end{aligned}$$

$$\text{No. of initial cells/Spheroids} = 2 \times 10^4 \text{ cells/spheroid}$$

$$\text{No. of initial cells/Volume} = 1.2 \times 10^5 \text{ cells/mm}^3 \text{ to } 3.5 \times 10^6 \text{ cells/mm}^3$$

$$\text{No. of initial cells/Volume (average)} = 1.8 \times 10^6 \text{ cells/mm}^3$$

Appendix F: 3D bioprinted constructs

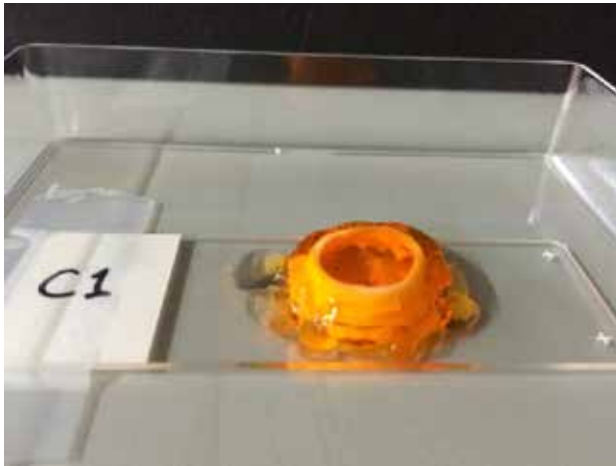


Figure F.1: Printing of tubular construct with gelatin as support structure

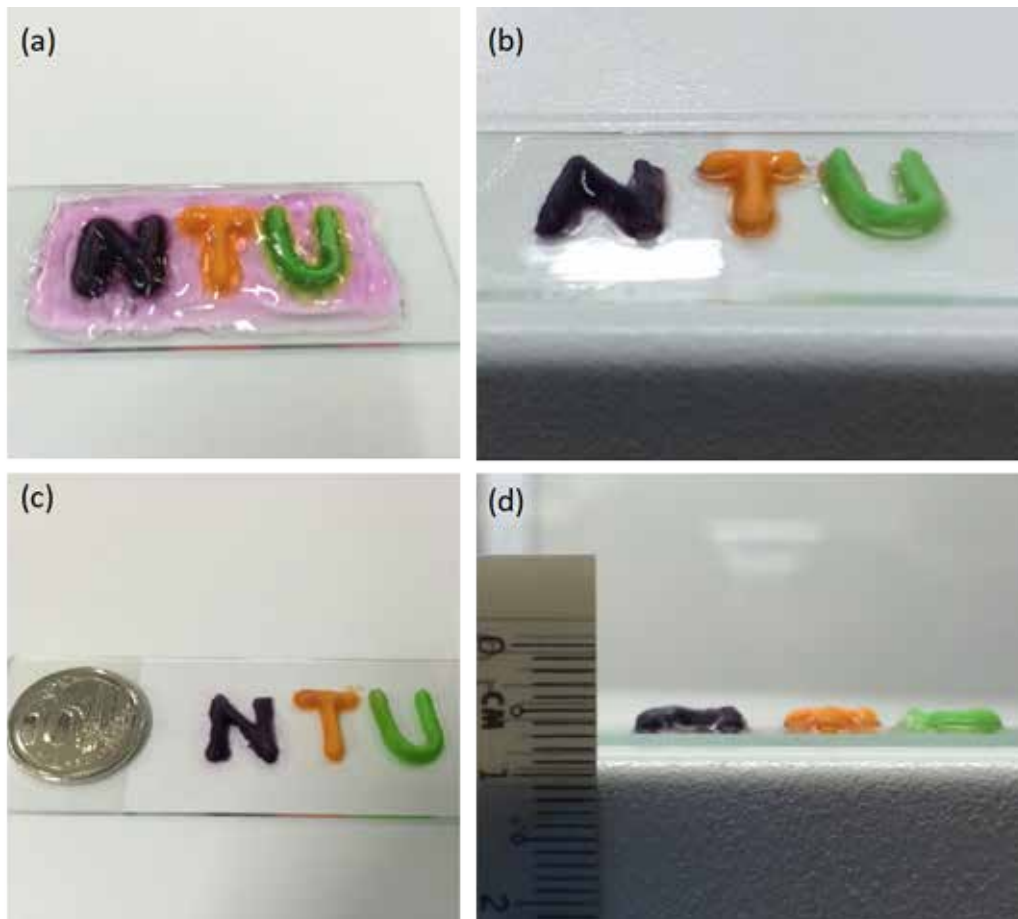


Figure F.2: Printing of “NTU” letters (a) with gelatin as support structure and (b-d) after support removal.